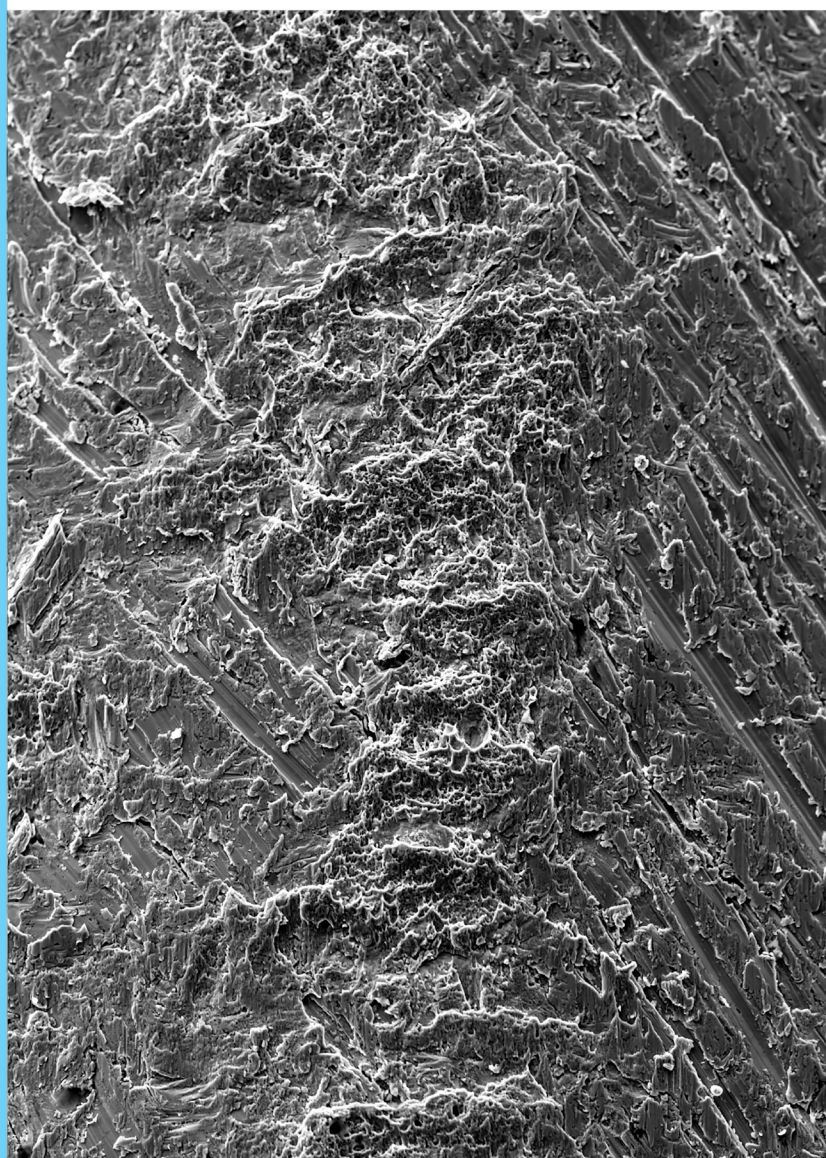


ISSN 2782-4039 (Print)
ISSN 2782-6074 (Online)

Frontier Materials & Technologies



2025
Nº 3

Frontier Materials & Technologies

Founded in 2008

No. 3

2025

16+

Quarterly
Scientific Journal

The Founder is
Togliatti State University

Editor-in-Chief

Mikhail M. Krishtal, DSc (Physics and Mathematics), Professor

Deputy Editor-in-Chief

for Metallurgy and Materials Science

Dmitry L. Merson, DSc (Physics and Mathematics), Professor

Deputy Editor-in-Chief

for Mechanical Engineering and Machine Science

Aleksandr P. Shaikin, DSc (Engineering), Professor

Deputy Editor-in-Chief

for Welding and Allied Processes and Technologies

Aleksandr I. Kovtunov, DSc (Engineering), Associate Professor

Editors:

Petr Yu. Bochkarev, DSc (Engineering), Professor

Boris M. Brzhozovskiy, DSc (Engineering), Professor

Aleksandr F. Denisenko, DSc (Engineering), Professor

Yuri Z. Estrin, DSc (Physics and Mathematics), Professor

Sergey S. Gavryushin, DSc (Engineering), Professor

Gregory Gerstein, DSc (Engineering)

Fedor V. Grechnikov, Academician of the Russian Academy of Sciences, DSc (Engineering), Professor

Mikhail I. Karpov, Corresponding Member of the Russian Academy of Sciences, DSc (Engineering), Professor

Aleksandr V. Katsman, PhD (Physics and Mathematics)

Aleksandr A. Kazakov, DSc (Engineering), Professor

Aleksandr V. Kudrya, DSc (Engineering), Professor

Sergey V. Kuzmin, Corresponding Member of the Russian Academy of Sciences, DSc (Engineering), Professor

Aleksey V. Makarov, Corresponding Member of the Russian Academy of Sciences, DSc (Engineering)

Radik R. Mulyukov, Corresponding Member of the Russian Academy of Sciences,

DSc (Physics and Mathematics), Professor

Oleg B. Naimark, DSc (Physics and Mathematics), Professor

Nikolay V. Nosov, DSc (Engineering), Professor

Aleksandr V. Pilinsky, PhD (Engineering), Associate Professor

Aleksey E. Romanov, DSc (Physics and Mathematics), Professor

Vasili V. Rubanik, Corresponding Member of the National Academy of Sciences of Belarus, DSc (Engineering)

Vladimir A. Shishkov, DSc (Engineering)

Tushar Madhukar Sonar, PhD (Engineering)

Ramasubbu Sunder, Fellow of the Indian Academy of Sciences, PhD (Engineering)

Vladimir P. Tabakov, DSc (Engineering), Professor

Alexey Yu. Vinogradov, DSc (Engineering), PhD (Physics and Mathematics), Professor

Until December 2021,
the journal was published under
the title
“**Science Vector**
of Togliatti State University”.

Indexed in Scopus.
Included in the List of HAC,
RSCI core, DOAJ,
“White List”.
Available in Crossref,
Google Scholar.

Registered by the Federal
Service for Supervision
of Communications,
Information Technology
and Mass Media
(Registration Certificate
ПН No. ФС77-83040
dated March 31, 2022).

Desktop publishing:

Natalya A. Nikitenko

*Responsible/technical
editor:*

Natalya A. Nikitenko

Mailing Address:

14, Belorusskaya St.,
Togliatti,

Russia, 445020

Phone: **(8482) 44-91-74**

E-mail:

vektornaukitgu@yandex.ru

Website:

<https://vektornaukitech.ru>

Passed for printing
26.09.2025.
Published 30.09.2025.
Format 60×84 1/8.
Digital printing.
Conventional printed sheets 17.0.
Circulation is 28 copies.
Order 3-270-25.
The price is free.

EDITORIAL BOARD INFORMATION

Editor-in-Chief

Mikhail M. Krishtal, Doctor of Sciences (Physics and Mathematics), Professor, Rector (Togliatti State University, Togliatti, Russia).

Scopus AuthorID: [14634063100](#)

ResearcherID: [AAD-7707-2019](#)

ORCID: <https://orcid.org/0000-0001-7189-0002>

Deputy Editor-in-Chief for Metallurgy and Materials Science

Dmitry L. Merson, Doctor of Sciences (Physics and Mathematics), Professor, Director of the Research and Development Institute of Advanced Technologies (Togliatti State University, Togliatti, Russia).

Scopus AuthorID: [6603449333](#)

ResearcherID: [M-7210-2016](#)

ORCID: <https://orcid.org/0000-0001-5006-4115>

Deputy Editor-in-Chief for Mechanical Engineering and Machine Science

Aleksandr P. Shaikin, Doctor of Sciences (Engineering), Professor, Professor of Chair “Energy-Converting Machines and Control Systems” (Togliatti State University, Togliatti, Russia).

Scopus AuthorID: [6602779899](#)

ORCID: <https://orcid.org/0000-0002-9832-4753>

Deputy Editor-in-Chief for Welding and Allied Processes and Technologies

Aleksandr I. Kovtunov, Doctor of Sciences (Engineering), Associate Professor, Professor of Chair “Welding, Pressure Treatment of Materials and Allied Processes” (Togliatti State University, Togliatti, Russia).

Scopus AuthorID: [36761987000](#)

ResearcherID: [B-4545-2016](#)

ORCID: <https://orcid.org/0000-0002-7705-7377>

Editorial board:

Petr Yu. Bochkarev, Doctor of Sciences (Engineering), Professor, Professor of Chair “Mechanical Engineering Technology and Applied Mechanics” (Kamyshin Technological Institute (Branch) of Volgograd State Technical University, Kamyshin, Russia), Professor of Chair “Technical Support of Agro-Industrial Complex” (Saratov State Vavilov Agrarian University, Saratov, Russia).

Scopus AuthorID: [57189893110](#)

Boris M. Brzhozovskiy, Doctor of Sciences (Engineering), Professor, chief researcher of Laboratory of Theory of Mechanisms and Machine Structure (Institute of Machines Science named after A.A. Blagonravov of the Russian Academy of Sciences, Moscow, Russia).

Scopus AuthorID: [55683317200](#)

Alexander F. Denisenko, Doctor of Sciences (Engineering), Professor, Professor of Chair “Technology of Mechanical Engineering, Machines and Tools” (Samara State Technical University, Samara, Russia).

Scopus AuthorID: [36131150100](#)

Yuri Z. Estrin, Doctor of Sciences (Physics and Mathematics), Professor, Professor of Chair of Engineering Materials (Monash University, Melbourne, Australia).

Scopus AuthorID: [7005031984](#)

Sergey S. Gavryushin, Doctor of Sciences (Engineering), Professor, Head of Chair “Computer Systems of Production Automation”, Head of the Theory & Machines Structure Laboratory (Bauman Moscow State Technical University, Moscow, Russia; Mechanical Engineering Research Institute of the Russian Academy of Sciences, Moscow, Russia).

Scopus AuthorID: [6507067486](#)

ResearcherID: [AAT-8610-2020](#)

ORCID: <https://orcid.org/0000-0002-6547-1351>

Gregory Gerstein, Doctor of Sciences (Engineering), Laboratory Head (Leibniz University Hannover, Hanover, Germany).

Scopus AuthorID: [55001912200](#)

Fedor V. Grechnikov, Academician of the Russian Academy of Sciences, Doctor of Sciences (Engineering), Professor, Head of the Chair of Forming Processes (Samara National Research University, Samara, Russia).

Scopus AuthorID: [6506174877](#)

ResearcherID: [P-2319-2016](#)

ORCID: <https://orcid.org/0000-0002-3767-4004>

Mikhail I. Karpov, Corresponding Member of the Russian Academy of Sciences, Doctor of Sciences (Engineering), Professor, Head of the Laboratory of Materials Science (Institute of Solid State Physics of the Russian Academy of Sciences, Chernogolovka, Russia).

Scopus AuthorID: [7004130343](#)

ResearcherID: [Q-9288-2016](#)

Aleksandr V. Katsman, PhD (Physics and Mathematics), Senior Research Associate (Technion – Israel Institute of Technology, Haifa, Israel).

Scopus AuthorID: [7004225554](#)

Aleksandr A. Kazakov, Doctor of Sciences (Engineering), Professor, Professor of Chair “Metallurgy and Casting Technologies”, Head of the Metallurgy Expertise Laboratory (Peter the Great Saint-Petersburg Polytechnic University, St. Petersburg, Russia).

Scopus AuthorID: [56037035400](#)

ResearcherID: [E-6090-2014](#)

ORCID: <https://orcid.org/0000-0001-6511-1228>

Aleksandr V. Kudrya, Doctor of Sciences (Engineering), Professor, Professor of Chair of Physical Metallurgy and Physics of Strength (National University of Science and Technology MISiS, Moscow, Russia).

Scopus AuthorID: [6603628218](#)

Sergey V. Kuzmin, Corresponding Member of the Russian Academy of Sciences, Doctor of Sciences (Engineering), Professor, First Prorector, Professor of Chair “Equipment and Technology of Welding Production” (Volgograd State Technical University, Volgograd, Russia).

Scopus AuthorID: [57217278342](#)

ResearcherID: [I-7424-2012](#)

ORCID: <https://orcid.org/0000-0003-2802-8497>

Aleksey V. Makarov, Corresponding Member of the Russian Academy of Sciences, Doctor of Sciences (Engineering), Chief Research Associate, Head of Chair of Materials Science, Head of the Laboratory of Mechanical Properties (M.N. Mikheev Institute of Metal Physics of Ural Branch of Russian Academy of Sciences, Ekaterinburg, Russia).

Scopus AuthorID: [57195590138](#)

ResearcherID: [D-5663-2016](#)

ORCID: <https://orcid.org/0000-0002-2228-0643>

Radik R. Mulyukov, Corresponding Member of the Russian Academy of Sciences, Doctor of Sciences (Physics and Mathematics), Professor, Director (Institute for Metals Superplasticity Problems of the Russian Academy of Sciences, Ufa, Russia).

Scopus AuthorID: [7003520439](#)

ResearcherID: [B-3800-2016](#)

ORCID: <https://orcid.org/0000-0002-0452-3816>

Oleg B. Naimark, Doctor of Sciences (Physics and Mathematics), Professor, Head of the Laboratory of Physical Foundations of Strength (Institute of Continuous Media Mechanics of Ural Branch of Russian Academy of Sciences, Perm, Russia).

Scopus AuthorID: [6701720806](#)

Nikolay V. Nosov, Doctor of Sciences (Engineering), Professor, Professor of Chair “Technology of Mechanical Engineering, Machines and Tools” (Samara State Technical University, Samara, Russia).

Scopus AuthorID: [6602506825](#)

Aleksandr V. Pilinsky, PhD (Engineering), Associate Professor, MSME (Master of Science in Mechanical Engineering), Los Angeles, USA.

ORCID: <https://orcid.org/0009-0009-8933-195X>

Aleksey E. Romanov, Doctor of Sciences (Physics and Mathematics), Professor, Professor of the Institute of Advanced Data Transfer Systems (ITMO University, St. Petersburg, Russia).

Scopus AuthorID: [7202768874](#)

Vasili V. Rubanik, Corresponding Member of the National Academy of Sciences of Belarus, Doctor of Sciences (Engineering), Head of the Laboratory of Metal Physics (Institute of Technical Acoustics of the National Academy of Sciences of Belarus, Vitebsk, Belarus).

Scopus AuthorID: [57215218253](#)

Vladimir A. Shishkov, Doctor of Sciences (Engineering), Head of the Technical Department (Palladio LLC, Togliatti, Russia).

RSCI AuthorID: [596086](#)

SPIN-code: [9504-4454](#)

Tushar Madhukar Sonar, PhD (Engineering), Senior Research Scientist of Chair “Welding Engineering”

(South Ural State University, Chelyabinsk, Russia).

Scopus AuthorID: [57200800257](#)

ResearcherID: [AAS-6037-2021](#)

ORCID: <https://orcid.org/0000-0002-3997-5337>

Ramasubbu Sunder, Fellow of the Indian Academy of Sciences, PhD (Engineering), Director (BISS (P) Ltd, Bangalore, India).

Scopus AuthorID: [7003530245](#)

ResearcherID: [H-6740-2016](#)

ORCID: <https://orcid.org/0000-0001-6143-0723>

Vladimir P. Tabakov, Doctor of Sciences (Engineering), Professor, Head of Chair “Innovative Technologies in Mechanical Engineering” (Ulyanovsk State Technical University, Ulyanovsk, Russia).

Scopus AuthorID: [6701501345](#)

ResearcherID: [E-1832-2017](#)

ORCID: <https://orcid.org/0000-0002-2568-9401>

Alexey Yu. Vinogradov, Doctor of Sciences (Engineering), PhD (Physics and Mathematics), Professor, Professor of Faculty of Mechanical and Industrial Engineering (Norwegian University of Science and Technology, Trondheim, Norway).

Scopus AuthorID: [7402889776](#)

ResearcherID: [A-7175-2009](#)

ORCID: <https://orcid.org/0000-0001-9585-2801>

СВЕДЕНИЯ О ЧЛЕНАХ РЕДКОЛЛЕГИИ

Главный редактор

Криштал Михаил Михайлович, доктор физико-математических наук, профессор, ректор (Тольяттинский государственный университет, Тольятти, Россия).

Scopus AuthorID: [14634063100](#)

ResearcherID: [AAD-7707-2019](#)

ORCID: <https://orcid.org/0000-0001-7189-0002>

Заместитель главного редактора по направлению «Металлургия и материаловедение»

Мерсон Дмитрий Львович, доктор физико-математических наук, профессор, директор Научно-исследовательского института перспективных технологий (Тольяттинский государственный университет, Тольятти, Россия).

Scopus AuthorID: [6603449333](#)

ResearcherID: [M-7210-2016](#)

ORCID: <https://orcid.org/0000-0001-5006-4115>

Заместитель главного редактора по направлению «Машиностроение и машиноведение»

Шайкин Александр Петрович, доктор технических наук, профессор, профессор кафедры «Энергетические машины и системы управления» (Тольяттинский государственный университет, Тольятти, Россия).

Scopus AuthorID: [6602779899](#)

ORCID: <https://orcid.org/0000-0002-9832-4753>

Заместитель главного редактора по направлению «Сварка, родственные процессы и технологии»

Ковтунов Александр Иванович, доктор технических наук, доцент, профессор кафедры «Сварка, обработка материалов давлением и родственные процессы» (Тольяттинский государственный университет, Тольятти, Россия).

Scopus AuthorID: [36761987000](#)

ResearcherID: [B-4545-2016](#)

ORCID: <https://orcid.org/0000-0002-7705-7377>

Редакционная коллегия:

Бочкарев Петр Юрьевич, доктор технических наук, профессор, профессор кафедры «Технология машиностроения и прикладная механика» (Камышинский технологический институт (филиал) Волгоградского государственного технического университета, Камышин, Россия), профессор кафедры «Техническое обеспечение АПК» (Саратовский государственный аграрный университет имени Н.И. Вавилова, Саратов, Россия).

Scopus AuthorID: [57189893110](#)

Бржозовский Борис Максимович, доктор технических наук, профессор, главный научный сотрудник лаборатории теории механизмов и структуры машин (Институт машиноведения им. А.А. Благонравова РАН, Москва, Россия).

Scopus AuthorID: [55683317200](#)

Виноградов Алексей Юрьевич, доктор технических наук, кандидат физико-математических наук, профессор факультета механической и промышленной инженерии (Норвежский университет науки и технологии, Тронхейм, Норвегия).

Scopus AuthorID: [7402889776](#)

ResearcherID: [A-7175-2009](#)

ORCID: <https://orcid.org/0000-0001-9585-2801>

Гавришин Сергей Сергеевич, доктор технических наук, профессор, заведующий кафедрой «Компьютерные системы автоматизации производства», заведующий лабораторией компьютерных систем автоматизации производства и цифровых технологий (Московский государственный технический университет имени Н.Э. Баумана (национальный исследовательский университет), Москва, Россия; Институт машиноведения им. А.А. Благонравова Российской академии наук, Москва, Россия).

Scopus AuthorID: [6507067486](#)

ResearcherID: [AAT-8610-2020](#)

ORCID: <https://orcid.org/0000-0002-6547-1351>

Герштейн Григорий, доктор технических наук, заведующий лабораторией (Ганноверский университет имени Готфрида Вильгельма Лейбница, Ганновер, Германия).

Scopus AuthorID: [55001912200](#)

Гречников Федор Васильевич, академик РАН, доктор технических наук, профессор, заведующий кафедрой обработки металлов давлением (Самарский национальный исследовательский университет имени академика С.П. Королева, Самара, Россия).

Scopus AuthorID: [6506174877](#)

ResearcherID: [P-2319-2016](#)

ORCID: <https://orcid.org/0000-0002-3767-4004>

Денисенко Александр Федорович, доктор технических наук, профессор, профессор кафедры «Технология машиностроения, станки и инструменты» (Самарский государственный технический университет, Самара, Россия).

Scopus AuthorID: [36131150100](#)

Казаков Александр Анатольевич, доктор технических наук, профессор, профессор кафедры «Металлургические и литейные технологии», руководитель научно-испытательной лаборатории «Металлургическая экспертиза» (Санкт-Петербургский политехнический университет Петра Великого, Санкт-Петербург, Россия).

Scopus AuthorID: [56037035400](#)

ResearcherID: [E-6090-2014](#)

ORCID: <https://orcid.org/0000-0001-6511-1228>

Карпов Михаил Иванович, член-корреспондент РАН, доктор технических наук, профессор, заведующий лабораторией материаловедения (Институт физики твердого тела Российской академии наук, Черноголовка, Россия).

Scopus AuthorID: [7004130343](#)

ResearcherID: [Q-9288-2016](#)

Кацман Александр Владимирович, кандидат физико-математических наук, PhD, старший научный сотрудник (Технион – Израильский технологический институт, Хайфа, Израиль).

Scopus AuthorID: [7004225554](#)

Кудря Александр Викторович, доктор технических наук, профессор, заместитель заведующего кафедрой металловедения и физики прочности (Национальный исследовательский технологический университет «МИСиС», Москва, Россия).

Scopus AuthorID: [6603628218](#)

Кузьмин Сергей Викторович, член-корреспондент РАН, доктор технических наук, профессор, первый проректор, профессор кафедры «Оборудование и технология сварочного производства» (Волгоградский государственный технический университет, Волгоград, Россия).

Scopus AuthorID: [57217278342](#)

ResearcherID: [I-7424-2012](#)

ORCID: <https://orcid.org/0000-0003-2802-8497>

Макаров Алексей Викторович, член-корреспондент РАН, доктор технических наук, главный научный сотрудник, заведующий отделом материаловедения и лабораторией механических свойств (Институт физики металлов имени М.Н. Михеева Уральского отделения Российской академии наук, Екатеринбург, Россия).

Scopus AuthorID: [57195590138](#)

ResearcherID: [D-5663-2016](#)

ORCID: <https://orcid.org/0000-0002-2228-0643>

Мулюков Радик Рафикович, член-корреспондент РАН, доктор физико-математических наук, профессор, директор (Институт проблем сверхпластичности металлов Российской академии наук, Уфа, Россия).

Scopus AuthorID: [7003520439](#)

ResearcherID: [B-3800-2016](#)

ORCID: <https://orcid.org/0000-0002-0452-3816>

Наймарк Олег Борисович, доктор физико-математических наук, профессор, заведующий лабораторией «Физические основы прочности» (Институт механики сплошных сред Уральского отделения Российской академии наук, Пермь, Россия).

Scopus AuthorID: [6701720806](#)

Носов Николай Васильевич, доктор технических наук, профессор, профессор кафедры «Технология машиностроения, станки и инструменты» (Самарский государственный технический университет, Самара, Россия).

Scopus AuthorID: [6602506825](#)

Пилинский Александр Вениаминович, кандидат технических наук, доцент, MSME (Master of Science in Mechanical Engineering), Лос-Анджелес, США.

ORCID: <https://orcid.org/0009-0009-8933-195X>

Романов Алексей Евгеньевич, доктор физико-математических наук, профессор Института перспективных систем передачи данных, руководитель научно-исследовательского центра перспективных функциональных материалов и лазерных коммуникационных систем (Национальный исследовательский университет ИТМО, Санкт-Петербург, Россия).

Scopus AuthorID: [7202768874](#)

Рубаник Василий Васильевич, член-корреспондент Национальной академии наук Беларуси, доктор технических наук, заведующий лабораторией физики металлов (Институт технической акустики Национальной академии наук Беларуси, Витебск, Республика Беларусь).

Scopus AuthorID: [57215218253](#)

Сонар Тушар Мадхукар, кандидат технических наук, старший научный сотрудник кафедры «Оборудование и технология сварочного производства» (Южно-Уральский государственный университет, Челябинск, Россия).

Scopus AuthorID: [57200800257](#)

ResearcherID: [AAS-6037-2021](#)

ORCID: <https://orcid.org/0000-0002-3997-5337>

Сундер Рамасуббу, член Индийской академии наук, кандидат технических наук, директор (“BISS (P) Ltd”, Бангалор, Индия).

Scopus AuthorID: [7003530245](#)

ResearcherID: [H-6740-2016](#)

ORCID: <https://orcid.org/0000-0001-6143-0723>

Табakov Владимир Петрович, доктор технических наук, профессор, заведующий кафедрой «Инновационные технологии в машиностроении» (Ульяновский государственный технический университет, Ульяновск, Россия).

Scopus AuthorID: [6701501345](#)

ResearcherID: [E-1832-2017](#)

ORCID: <https://orcid.org/0000-0002-2568-9401>

Шишков Владимир Александрович, доктор технических наук, начальник технического отдела (ООО «Палладио», Тольятти, Россия).

AuthorID РИНЦ: [596086](#)

SPIN-код: [9504-4454](#)

Эстрин Юрий Захарович, доктор физико-математических наук, профессор, профессор кафедры инженерных материалов (Университет им. Монаша, Мельбурн, Австралия).

Scopus AuthorID: [7005031984](#)

September 15–19, the XII International School-Conference of Physical Materials Science (hereinafter referred to as SPM-2025) took place in Togliatti. The school-conference focused on the issues of fundamental materials science, the development of new materials, including those for medical applications, micro- and macrostructure analysis, material behavior under the action of various fields, cyclically changing loads, hydrogen embrittlement, corrosion damage, and other current topics in materials science. As part of SPM-2025, a competition for the best scientific work was held among young scientists whose age at the time of SPM-2025 did not exceed 35 years. The competition was carried out in two stages. At the first stage, the works of participants executed as full-length papers and having passed the mandatory peer reviewing were recognized as winners of the first stage and recommended for publication in the Frontier Materials & Technologies scientific journal. At the second stage, the winners of the first stage presented their papers in person at the SPM-2025. Their works were judged by a panel of leading materials scientists. The winners of the second stage in the *Student*, *Postgraduate Student*, and *Researcher* categories were awarded diplomas and valuable prizes. This issue of the journal includes four papers by the authors who won the first stage of the competition. The remaining competition papers will be published in subsequent issues.

Co-chairman of the SPM-2025 organizing committee, Professor D.L. Merson

CONTENT

Features of arc surfacing of intermetallic alloys of the Fe–Al system on the surface of low-carbon steels Bochkarev A.G., Kovtunov A.I., Plakhotny D.I., Khokhlov Yu.Yu., Belonogov S.O., Vedeneev I.V.	11
Scheme for producing composite material based on structural aluminum alloy by the direct extrusion method Bushueva N.I., Loginov Yu.N.	27
Study of rigidity and frequency response of an end mill on a vertical milling centre Voronov R.D., Rastorguev D.A., Levashkin D.G.	39
Microstructure, properties and strengthening mechanisms of low-carbon steel subjected to equal-channel angular pressing Malinin A.V., Sitdikov V.D., Lebedev Yu.A.	51
Special aspects of microstructure formation in Cu–Cr–Zr–Y bronze under low-temperature friction stir processing Nikitin I.S., Kalinenko A.A., Malopheyev S.S., Mironov S.Yu., Bodyakova A.I.	67
Study of the influence of deformation temperature on the mechanical behaviour and fracturing behaviour of the cast TNM-B1 alloy Sokolovskiy V.S., Salishchev G.A.	81
Study of the temperature field formed in the process of milling with the use of ultrasonic vibrations under various processing modes Unyanin A.N., Chudnov A.V., Dimukhametov I.Z.	91
Influence of heat treatment on the structure and corrosion properties of microalloyed pipe steels with a chromium content of up to 1 % Chistopoltseva E.A., Kudashov D.V., Komissarov A.A., Yushchuk V.V., Muntin A.V., Chervonniy A.V., Dolgach E.D.	101
The influence of rotary swaging and subsequent annealing on the structure and mechanical properties of L68 single-phase brass Chistyukhina E.I., Martynenko N.S., Rybalchenko O.V., Nikitin I.S., Lukyanova E.A., Gorbenko A.D., Temralieva D.R., Straumal P.B., Andreev V.A., Dobatkin S.V.	113
Strength of joints produced by ultrasonic spot welding of copper plates using tools with different tooth heights Shayakhmetova E.R.	125
OUR AUTHORS	137

СОДЕРЖАНИЕ

Особенности дуговой наплавки интерметаллидных сплавов системы Fe–Al на поверхности низкоуглеродистых сталей Бочкарев А.Г., Ковтунов А.И., Плахотный Д.И., Хохлов Ю.Ю., Белоногов С.О., Веденеев И.В.	11
Схема получения композиционного материала на основе конструкционного алюминиевого сплава методом прямого прессования Бушуева Н.И., Логинов Ю.Н.	27
Исследование жесткости и частотных характеристик концевой фрезы на вертикальном фрезерном центре Воронов Р.Д., Расторгуев Д.А., Левашкин Д.Г.	39
Микроструктура, свойства и механизмы упрочнения низкоуглеродистой стали, подвергнутой равноканальному угловому прессованию Малинин А.В., Ситдилов В.Д., Лебедев Ю.А.	51
Особенности формирования микроструктуры в Cu–Cr–Zr–Y бронзе в условиях низкотемпературной обработки трением с перемешиванием Никитин И.С., Калинин А.А., Малофеев С.С., Миронов С.Ю., Бодякова А.И.	67
Исследование влияния температуры деформации на механическое поведение и особенности разрушения литого сплава TNM-B1 Соколовский В.С., Салищев Г.А.	81
Исследование температурного поля, формирующегося в процессе фрезерования с применением ультразвуковых колебаний, при различных режимах обработки Унянин А.Н., Чуднов А.В., Димухаметов И.З.	91
Влияние термической обработки на структуру и коррозионные свойства микролегированных трубных сталей с содержанием хрома до 1 % Чистопольцева Е.А., Кудашов Д.В., Комиссаров А.А., Ющук В.В., Мунтин А.В., Червонный А.В., Долгач Е.Д.	101
Влияние ротационнойковки и последующего отжига на структуру и механические свойства однофазной латуни Л68 Чистюхина Э.И., Мартыненко Н.С., Рыбальченко О.В., Никитин И.С., Лукьянова Е.А., Горбенко А.Д., Темралиева Д.Р., Страумал П.Б., Андреев В.А., Добаткин С.В.	113
Прочность соединений пластин меди, полученных точечной ультразвуковой сваркой инструментом с разной высотой зубцов Шаяхметова Э.Р.	125
НАШИ АВТОРЫ	137

Features of arc surfacing of intermetallic alloys of the Fe–Al system on the surface of low-carbon steels

Aleksandr G. Bochkarev^{*1,3}, PhD (Engineering),
assistant professor of Chair “Welding, Pressure Material Treatment and Related Processes”

Aleksandr I. Kovtunov^{1,4}, Doctor of Sciences (Engineering),
professor of Chair “Welding, Pressure Material Treatment and Related Processes”

Denis I. Plakhotny^{1,5}, senior lecturer
of Chair “Welding, Pressure Material Treatment and Related Processes”

Yuri Yu. Khokhlov^{1,6}, Head of the Laboratory
of Chair “Welding, Pressure Material Treatment and Related Processes”

Savely O. Belonogov^{2,7}, engineer
of the Laboratory of Destructive Inspection Methods

Ivan V. Vedeneev^{2,8}, engineer
of the Laboratory of Non-Destructive Inspection

¹Togliatti State University, Togliatti (Russia)

²LLC Middle Volga Certification and Diagnostic Center “Delta”, Togliatti (Russia)

*E-mail: a.bochkarev5@tltsu.ru,
a.bochkarev93@mail.ru

³ORCID: <https://orcid.org/0000-0002-7945-1634>

⁴ORCID: <https://orcid.org/0000-0002-7705-7377>

⁵ORCID: <https://orcid.org/0000-0003-2021-8974>

⁶ORCID: <https://orcid.org/0000-0002-5276-8957>

⁷ORCID: <https://orcid.org/0009-0007-9788-9967>

⁸ORCID: <https://orcid.org/0009-0009-4159-526X>

Received 17.04.2025

Revised 10.06.2025

Accepted 13.08.2025

Abstract: The durability of industrial components is largely determined by the materials they are made of. Often, the materials used must be resistant to wear, corrosion, and high temperatures. Advanced materials, such as high-strength alloy steels, are expensive and have limited weldability, which complicates the restoration of worn components. Fe–Al alloys having high corrosion resistance, wear resistance, and heat resistance at a lower cost are considered as an alternative. The objective of this study is to increase the wear resistance and heat resistance of low-carbon steel components by studying the processes of arc surfacing of iron aluminides and their properties. The study methodology included single-arc and double-arc surfacing using aluminium and steel electrode wires, analysis of the chemical composition of the deposited coatings, their hardness, wear resistance, and heat resistance. The results showed that single-arc surfacing forms alloys based on FeAl₃ and α -Al phases with Fe₂Al₅ and FeAl₃ inclusions, while double-arc surfacing produces alloys more saturated with iron with an α -Fe matrix phase and a Fe₃AlC_x carbide phase. The resulting alloys demonstrate a hardness of up to 58 HRC, a relative wear resistance of up to 2.5 units, and a weight loss of no more than 5 % with an aluminium content of up to 20 %, which indicates their potential for use under high loading conditions. The results confirm the feasibility of using iron aluminides as an inexpensive alternative to expensive coatings, which expands the possibilities for increasing the wear resistance and heat resistance of components in industry.

Keywords: arc surfacing; intermetallic alloys; iron aluminides; low-carbon steel; hardness; wear resistance; heat resistance.

For citation: Bochkarev A.G., Kovtunov A.I., Plakhotny D.I., Khokhlov Yu.Yu., Belonogov S.O., Vedeneev I.V. Features of arc surfacing of intermetallic alloys of the Fe–Al system on the surface of low-carbon steels. *Frontier Materials & Technologies*, 2025, no. 3, pp. 11–25. DOI: 10.18323/2782-4039-2025-3-73-1.

INTRODUCTION

The productivity and competitiveness of mining enterprises largely depend on the reliability and wear resistance of the equipment in operation. The main problems faced by enterprises are related to the reduction of the service life of components, increased downtime due to wear and tear and breakdowns, as well as increased costs for repairs and spare parts. The problem of increasing the wear resistance of parts subject to abrasive and corrosive wear, which directly affects the technical and economic indicators of enterprises

and the cost of products, is particularly relevant. Under conditions of intensive operational loads, the materials of the parts wear out quickly, which necessitates frequent repairs and replacement of equipment elements.

In recent decades, research has been actively conducted in the field of increasing the wear resistance of mining equipment. Thus, in works [1; 2] it is noted that about 50 % of equipment downtime is associated with the restoration of the surfaces of components damaged by abrasive wear. An important aspect is the use of materials with increased

corrosion and wear resistance. For example, high-strength medium-alloy steels (35HGS, 38H2NMA, 20HGSN2MFA) are used for parts operating under high loads, but their cost is quite high. In this regard, in most cases, more affordable carbon and low-alloy steels are used (3, 20, 10HSND, 12H1M steels), which have good wear resistance and are easy to repair [3].

Particular attention is paid to the application of protective coatings, which can significantly increase the wear resistance and corrosion resistance of parts. The literature describes spraying and surfacing methods, such as plasma, arc and gas-flame spraying, as well as arc metallisation [4; 5]. However, despite the effectiveness of these methods, due to the limited thickness of the protective layers (from 10 to 200 μm) and their tendency to failure under loads, their use requires further research.

An interesting direction is the use of intermetallic alloys of the Fe–Al system [6; 7], which have high corrosion [8] and heat resistance [9], as well as the ability to form protective coatings up to several millimeters thick. In [10; 11], it is shown that such materials can significantly increase the wear resistance of parts. In [12], the mechanical properties of iron aluminides are shown when heated to 600 $^{\circ}\text{C}$, in [13], the results of the study of intermetallic alloys of the Fe–Al system under high-temperature cyclic oxidation at temperatures of 800, 900 and 1000 $^{\circ}\text{C}$ are presented, which confirms the possibility of using these materials at elevated temperatures. In [14], the successful use of iron aluminides during operation at elevated temperatures (up to 950 $^{\circ}\text{C}$) is shown. However, at present, the possibilities of their use for the restoration of mining equipment parts have not been sufficiently studied, which makes further research relevant.

Known methods of applying iron aluminides to the surface of steel parts are friction application of aluminium and iron powder [15] or application of aluminium powder only [16] followed by annealing of the part in a furnace. Other known methods of applying iron aluminides are self-propagating high-temperature synthesis [17], laser cladding [18], various spraying methods (plasma spraying, vacuum plasma spraying, gas-flame spraying) [14].

The presented methods of applying protective coatings based on iron aluminides allow obtaining coatings with a limited layer thickness of up to 0.5 mm, which is clearly insufficient for mining equipment components operating under abrasive wear conditions. Another significant limitation is the impossibility of applying the coating in installation conditions and the lack of prospects for further restoration of the coating after wear. Therefore, despite a significant amount of research, issues related to the optimisation of the technologies of protective coating application, their durability and resistance to mechanical and chemical influences remain unresolved. In particular, the processes of formation of intermetallic coatings on parts made of low-carbon steels, as well as their behaviour under operating conditions of mining equipment, have not been sufficiently studied. Moreover, there is a necessity of developing inexpensive and effective methods for restoring worn surfaces that can ensure a long service life of parts.

The aim of this study is to increase the wear resistance and heat resistance of parts made of low-carbon steel by studying the processes of arc surfacing of iron aluminides and their properties.

METHODS

The study of the processes of surfacing of Fe–Al intermetallic alloys was carried out by single-arc surfacing using an aluminium electrode wire (Fig. 1) and double-arc surfacing using steel and aluminium electrode wires (Fig. 2).

The authors used SvA7 solid electrode wire according to GOST 7871-2019 as surfacing material for single-arc surfacing and Sv-08G2S wire according to GOST 2246-70 and SvA7 wire according to GOST 7871-2019 for double-arc surfacing. The diameter of the wires used was 1.2 mm. High-grade argon according to GOST 10157-2016 was used as a gas shield. Surfacing was carried out on plates made of steel 20 according to GOST 1577-2022 with overall dimensions of 160 \times 80 mm and a thickness of 10 mm. As the welding equipment, Megatron BDH 550 (Denmark) was used.

The single-arc surfacing modes were varied in a wide range: arc voltage ($U_{\text{arc Al}}$) – from 10 to 30 V; surfacing speed (V_s) – from 0.1 to 0.2 m/min; speed of aluminium electrode wire feed ($V_f/w \text{ Al}$) – from 3 to 6 m/min; shielding gas flow rate – from 10 to 14 l/min. The torch tilt angle (α) during single-arc surfacing was varied from 90 to 30 $^{\circ}$ with a step of 15 $^{\circ}$. The double-arc surfacing modes were varied in the following ranges: arc voltage when using aluminium electrode wire ($U_{\text{arc Al}}$) – from 14 to 18 V; arc voltage when using Sv-08G2S electrode wire ($U_{\text{arc St}}$) – from 23.5 to 27.5 V; surfacing speed (V_s) – 0.1 to 0.2 m/min; speed of aluminium electrode wire feed ($V_f/w \text{ Al}$) – from 3 to 5 m/min; speed of Sv-08G2S electrode wire feed ($V_f/w \text{ St}$) – from 3 to 4 m/min; shielding gas flow rate – from 10 to 14 l/min. The angle of inclination of the torches (α) for double-arc surfacing was 55 $^{\circ}$.

The geometric parameters of the welding beads were determined on pre-etched samples (in a 20 % HNO_3 solution) cut in cross section (Fig. 3). The measurement was carried out using the Universal Desktop Ruler program by setting the scale factor and subsequent measurement of the width of the welding bead (e), the height of the welding bead reinforcement (g), and the depth of fusion penetration (h) (Fig. 3).

The influence of the electrode wire feed angle on the stability of the surfacing process and the geometric parameters of the deposited alloys, such as the width of the welding bead (e), the height of the welding bead reinforcement (g) and the depth of fusion penetration (h) were assessed by changing the torch tilt angle from 30 to 90 $^{\circ}$ with a step of 15 $^{\circ}$.

The volume of intermetallic inclusions in the matrix alloy was assessed using microstructure images obtained with a microscope. Taking into account the scale factor, the volume of all inclusions in the image was measured and compared with the total volume of the matrix in the same image.

The chemical composition was analysed by scanning electron microscopy (SEM) using a LEO 1455 VP scanning

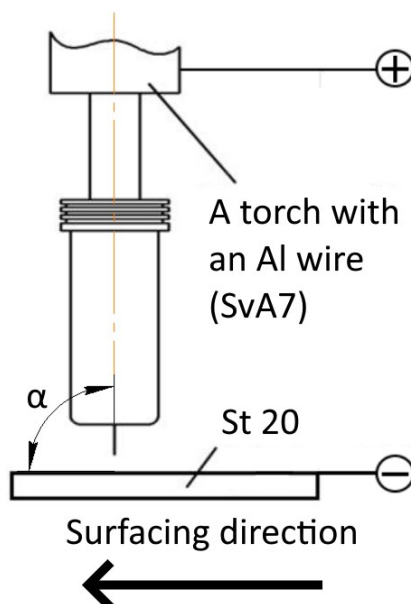


Fig. 1. Scheme of single-arc surfacing of Fe–Al system intermetallic alloys with a consumable electrode in a shielding gas environment. α is wire feed angle

Рис. 1. Схема одnodуговой наплавки плавящимся электродом в среде защитных газов интерметаллидных сплавов системы Fe–Al. α – угол ввода проволоки

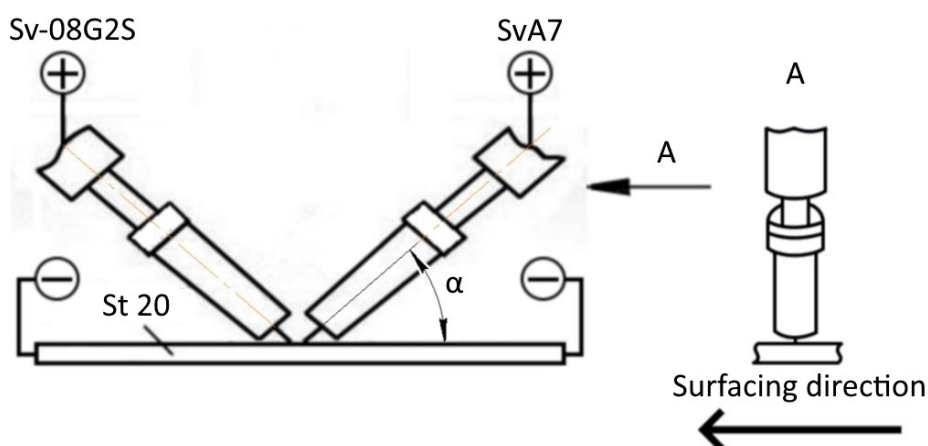


Fig. 2. Scheme of double-arc surfacing with the feed of steel and aluminium electrode wires. α is wire feed angle

Рис. 2. Схема двухдуговой наплавки с подачей стальной и алюминиевой электродных проволок. α – угол ввода проволоки

electron microscope (ZEISS, Germany) with INCA Energy-300 X-ray energy spectrometer (UK) and INCA Wave-500 X-ray wave spectrometer (UK) units and an HKL Premium EBSD System (UK) electron backscatter diffraction recording and analysis system. The samples for the studies were ground cross-sectional surfaces after surfacing Fe–Al beads onto grade 20 steel plates. Due to the insufficient quality of grinding for implementing the electron backscatter diffraction technique and reliably determining the elemental composition of the deposited metal in its various areas, chemical etching of the grinding surface was performed with a reagent of

3 ml HF + 3 ml HNO₃ + 94 ml H₂O. Fig. 4 shows a diagram of the selection of points for determining the chemical composition of the deposited metal.

X-ray diffraction analysis (XRD) was performed on a Bruker D8 Advance Eco X-ray diffractometer (Bruker AXS GmbH) (Germany) with a vertical θ – θ goniometer. For deposited samples with an uneven surface, it is preferable to use a parallel-beam geometry shooting scheme. To implement it, a Goebel mirror was installed on the primary beam using the linear focus of the X-ray tube. Goebel mirror is a multilayer heterostructure on a parabolically curved substrate that transforms the diverging beam into a parallel

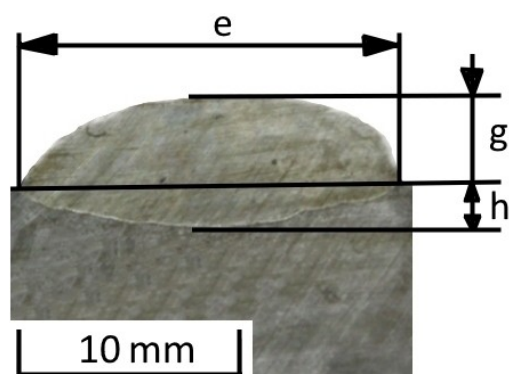


Fig. 3. Cross-section of the deposited metal for measuring geometric parameters

Рис. 3. Поперечное сечение наплавленного металла для измерения геометрических параметров

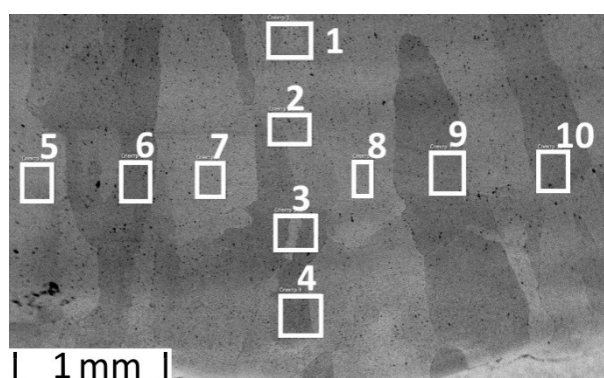


Fig. 4. Scheme of selection of points for chemical composition study

Рис. 4. Схема выбора точек для исследования химического состава

quasi-monochromatic one with a divergence angle of 0.03° . A collimator with a diameter of 1.0 mm was used to truncate the X-ray radiation "spot". The shooting point was preliminarily cleaned with sandpaper. The samples under study were shot in copper anode radiation ($\lambda=1.54060 \text{ \AA}$). The tube voltage was 40 kV; the heating current was 25 mA. The exposure time was 1 s; the scanning step was 0.02° . Focusing on the test area and bringing the sample surface to the centre of the focusing circle were performed using a laser guidance system. The samples were examined for reflection; the intensity of the diffraction pattern was recorded using an SSD160 linear-type position-sensitive detector (Germany) with 160 channels. Phase identification was performed in the software for the Diffrac EVA diffractometer (version 4.2.1) (USA) using the licensed Powder Diffraction File-2 database (The International Center for Diffraction Data).

Rockwell hardness of the deposited alloys was measured according to GOST 9013-59. The measurements were carried out using the HRC scale on an ITBRV-187.5-A hardness tester.

The wear resistance of the deposited alloys was assessed by testing samples for friction against fixed abrasive particles according to GOST 17367-71. For a more

accurate assessment of the relative wear resistance, the comparison of the test and reference samples was carried out by measuring the linear and weight wear according to the formula:

$$\varepsilon = \frac{\Delta l_s}{\Delta l_m},$$

where l_s is the wear of the standard;

Δl_m is the wear of the test material.

Steel 45 was used as the reference material to determine the degree of wear.

To study wear resistance, an installation that ensures a stable load on the test sample was used (Fig. 5). The installation consists of a frame with a fixed drive connected to a metal disk. The metal disk is equipped with clamps using which abrasive paper is attached to it. A vice for installing test samples is located on the frame under the disk. The installation is equipped with a timer that allows setting the required test time. The pressure on the sample during testing is regulated by installing weights on the lever.

Thermal resistance was determined by holding the samples in a SNOL 30/1100 muffle furnace at a temperature

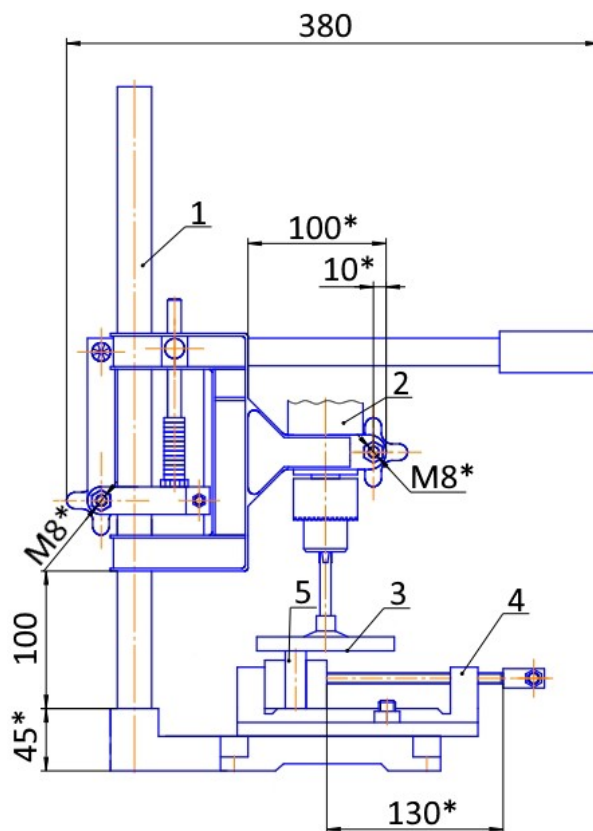


Fig. 5. Installation for testing wear resistance of deposited samples:
1 – frame; 2 – drive; 3 – metal disk with clamps; 4 – vice; 5 – test sample

Рис. 5. Установка для испытания износостойкости наплавленных образцов:
1 – станина; 2 – привод; 3 – металлический диск с зажимами; 4 – тиски; 5 – испытуемый образец

of 950 °C, then weighing them at equal intervals. Based on the data obtained, diagrams were compiled showing the dependence of the change in the mass of the samples on the time spent in the furnace at a certain temperature (950 °C).

RESULTS

Studies of single-arc surfacing of aluminium electrode wire on steel 20 have shown that in the selected range of modes, beads with different geometric parameters and stability of the surfacing process are formed. It is possible to conditionally divide the ranges of modes in which beads with low, medium and high stability of the surfacing process are formed. As a criterion for the stability of the surfacing process, the homogeneity of the geometric parameters of the surfacing beads in height and width was chosen. This criterion indicates the stability of droplet transfer during the formation of welding beads, and is necessary for surfacing and ensuring a more uniform distribution of chemical elements and the absence of defects in the form of inter-bead lack of fusion during multi-pass surfacing.

Low stability of the surfacing processes (Fig. 6) is observed in the following modes: feed rate of the aluminium electrode wire ($V_f/w\text{ Al}$) is 3 m/min with an arc voltage

range ($U_{\text{arc Al}}$) from 10 to 20 V. The surfacing speed (V_s) in this case is from 0.1 to 0.2 m/min. With an increase in voltage indicators in the specified range of modes, fusion of the current-carrying tip of the torch is observed. With an increase in the feed rate of the aluminium electrode wire to 4 m/min, with all other parameters specified above being equal, medium stability of the surfacing process is observed (Fig. 7). In this range of modes, a more uniform formation of welding beads is observed.

Increasing the arc voltage ($U_{\text{arc Al}}$) to 22.5 V at a feed rate of the aluminium electrode wire ($V_f/w\text{ Al}$) of 4 m/min in the surfacing speed range (V_s) from 0.1 to 0.2 m/min leads to a decrease in the stability of the surfacing process (Fig. 8), and an arc voltage above 22.5 V leads to melting of the current-carrying tip.

At a feed rate of the aluminium electrode wire ($V_f/w\text{ Al}$) from 5 to 6 m/min with an arc voltage ($U_{\text{arc Al}}$) from 15 to 25 V and a surfacing speed (V_s) from 0.1 to 0.2 m/min, beads with stable geometric parameters are observed (Fig. 9).

The stability of the surfacing process is determined primarily by the surfacing modes, however, the stability of the surfacing process and the quality of the formation of the deposited alloys are also affected by the angle of the electrode wire feed relative to the surface being surfacing.

It is noted that by changing the torch tilt angle (α) from 30 to 90°, one can observe a slight decrease in the width (e)



Fig. 6. External appearance of the welding bead produced in the following mode:

$V_{f/w} Al=3$ m/min; $U_{arc} Al=20$ V; $V_s=0.15$ m/min

Рис. 6. Внешний вид наплавленного валика, полученного при следующем режиме:

$V_{n/n} Al=3$ м/мин; $U_{\partial} Al=20$ В; $V_n=0,15$ м/мин

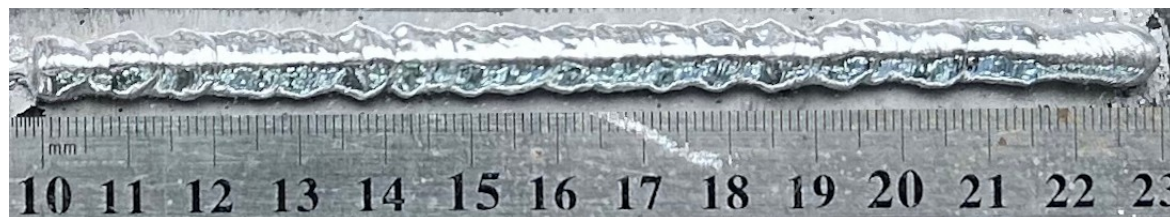


Fig. 7. External appearance of the welding bead produced in the following mode:

$V_{f/w} Al=4$ m/min; $U_{arc} Al=12.5$ V; $V_s=0.15$ m/min

Рис. 7. Внешний вид наплавленного валика, полученного при следующем режиме:

$V_{n/n} Al=4$ м/мин; $U_{\partial} Al=12,5$ В; $V_n=0,15$ м/мин



Fig. 8. External appearance of the welding bead produced in the following mode:

$V_{f/w} Al=4$ m/min; $U_{arc} Al=22.5$ V; $V_s=0.1$ m/min

Рис. 8. Внешний вид наплавленного валика, полученного при следующем режиме:

$V_{n/n} Al=4$ м/мин; $U_{\partial} Al=22,5$ В; $V_n=0,1$ м/мин

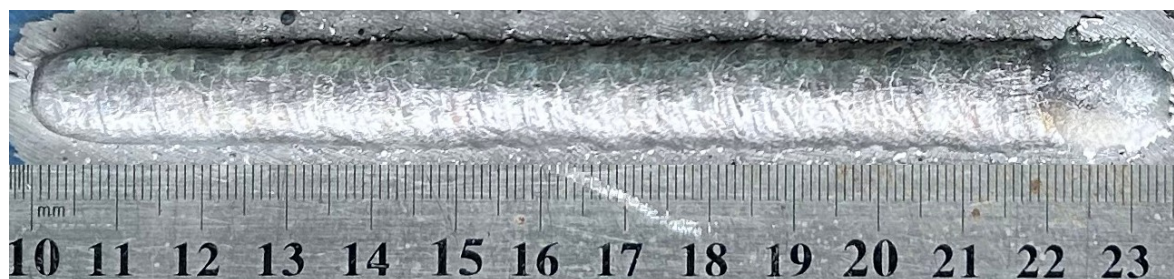


Fig. 9. External appearance of the welding bead produced in the following mode:

$V_{f/w} Al=6$ m/min; $U_{arc} Al=25$ V; $V_s=0.15$ m/min

Рис. 9. Внешний вид наплавленного валика, полученного при следующем режиме:

$V_{n/n} Al=6$ м/мин; $U_{\partial} Al=25$ В; $V_n=0,15$ м/мин

of the welding beads and a slight increase in the height of the welding beads (g) and the weld penetration depth (h). An increase in the torch tilt angle by 1° leads to a decrease in the weld width by approximately 0.038 mm, an increase in the weld height by 0.016 mm and an increase in the weld penetration depth by approximately 0.003 mm. To the greatest extent, a change in the torch tilt angle from 90 to 30° leads to an increase in the electrode wire losses due to spatter (Fig. 10).

The geometric parameters of the welding beads depend on the surfacing modes. An increase in the arc voltage ($U_{arc\ Al}$) in the specified range of modes leads to an increase in the width of the welding beads (e) and an insignificant increase in the weld penetration depth (h), while the height of the welding beads (g) decreases. An increase in the surfacing speed (V_s) in the specified range of modes leads to a decrease in the width (e) and height (g) of the welding beads, while the weld penetration depth (h) increases slightly. An increase in the rate of the aluminium electrode wire feed ($Vf/w\ Al$) in the specified range of modes leads to an increase in the geometric parameters of the welding alloys, such as the width (e) and height (g) of the welding beads and the weld penetration depth (h) of the base metal. The geometric parameters of the deposited alloys in single-arc surfacing are described by regression equations:

$$e = -0.542 + 0.557 \times U_{arc\ Al} - 22.437 \times V_s + 1.258 \times Vf/w\ Al - 0.098 \times \alpha;$$

$$g = 7.309 - 0.136 \times U_{arc\ Al} - 16.460 \times V_s + 0.281 \times Vf/w\ Al + 0.016 \times \alpha;$$

$$h = -1.703 + 0.044 \times U_{arc\ Al} + 0.476 \times V_s + 0.146 \times Vf/w\ Al + 0.003 \times \alpha.$$

It was found that from the wide range of surfacing modes considered, intermetallic alloys of the Fe–Al system are formed in a narrower range of modes. Intermetallic alloys are formed under the following surfacing modes: rate of the aluminium electrode wire feed ($Vf/w\ Al$) is 5–6 m/min; arc voltage ($U_{arc\ Al}$) is 20–25 V; surfacing speed (V_s) is 0.1–0.2 m/min. At an arc voltage above 25 V, melting of the current-carrying tip is observed, and at a voltage below 20 V, no weld penetration of the base metal is observed (Fig. 11), and the deposited alloy is pure aluminium, which is not suitable for use as a protective coating on steel parts. At a rate of the aluminium electrode wire feed less than 5 m/min in the entire range of modes, the deposited metal is an aluminium coating on steel.

The aluminium content in the welding intermetallic beads varies in the range from 71.49 to 94.21 wt. % at a torch tilt angle of 90° (angle of electrode wire feed relative to the product surface).

The aluminium content in the deposited metal depends on the surfacing modes. The rate of the aluminium electrode wire feed ($Vf/w\ Al$) (Fig. 12) and the speed of surfacing (V_s) (Fig. 13) exert the greatest influence. Arc voltage, all other parameters being

equal, reduces the aluminium content in the deposited metal, but the effect of arc voltage ($U_{arc\ Al}$) is statistically insignificant in its value and has virtually no effect on the chemical composition. With an increase in arc voltage by 1 V, all other parameters being equal, a decrease in the aluminium content in the deposited metal by 0.3 wt. % is observed.

The study of the chemical composition of iron aluminides and its structural components showed that the deposited metal is represented by a matrix alloy based on the $FeAl_3 + \alpha\text{-Al}$ phases with inclusions of the Fe_2Al_5 and $FeAl_3$ intermetallic phases (Fig. 14). However, producing deposited alloys with the Fe_2Al_5 and $FeAl_3$ phases is undesirable due to high brittleness. As the research results showed, the deposited metal is destroyed (peels off from the substrate) along the fusion line, where the content of brittle intermetallic inclusions based on the Fe_2Al_5 and $FeAl_3$ phases is maximal (Fig. 15).

It becomes obvious that it is necessary to produce deposited alloys based on more plastic phases, namely Fe_3Al and $FeAl$. To reduce the aluminium content in the deposited metal, double-arc surfacing using Sv-08G2S steel electrode wire and SvA7 aluminium electrode wire was proposed.

The double-arc surfacing modes were changed in the following ranges: arc voltage when using aluminium electrode wire ($U_{arc\ Al}$) – from 14 to 18 V; arc voltage when using Sv-08G2S electrode wire ($U_{arc\ St}$) – from 23.5 to 27.5 V; surfacing speed (V_s) – from 0.1 to 0.2 m/min; speed of aluminium electrode wire feed ($Vf/w\ Al$) – from 3 to 5 m/min; speed of Sv-08G2S electrode wire feed ($Vf/w\ St$) – from 3 to 4 m/min. As the studies have shown, beads with stable geometric parameters are formed in the selected range of modes (Fig. 16).

The chemical composition of the deposited alloys varied depending on the surfacing modes within the range from 7 to 27.5 wt. % of aluminium and from 71.5 to 92 wt. % of iron, the content of impurities did not exceed 1 wt. %. The dependence of the content of aluminium and iron in the welding bead on the surfacing modes is described by regression equations:

$$Al = 32.45 + 2.01 \times Vf/w\ Al + 0.17 \times Vf/w\ Fe + 1.64 \times V_s - 0.33 \times U_{arc\ Al} - 0.83 \times U_{arc\ Fe};$$

$$Fe = 66.8 - 1.99 \times Vf/w\ Al - 0.18 \times Vf/w\ Fe - 1.56 \times V_s + 0.33 \times U_{arc\ Al} + 0.82 \times U_{arc\ Fe}.$$

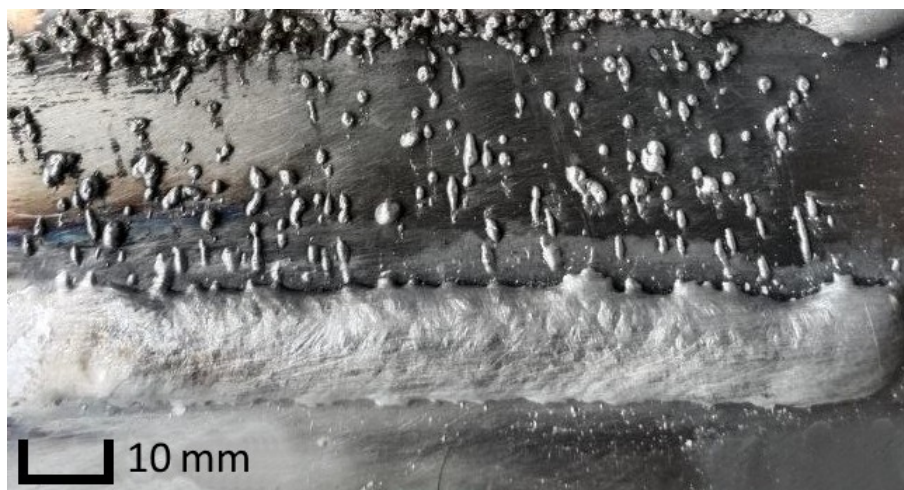
The heterogeneity of the chemical composition across the section of the deposited metal did not exceed 3 %.

The structure of the deposited alloys is represented by the $\alpha\text{-Fe}$ matrix phase with partial ordering according to the B2 type, and the inclusions are the Fe_3AlC_x carbide phase (Fig. 17). The volume of inclusions in the matrix phase varies from 3.26 to 18.95 %.

The hardness of the deposited metal varies in the range from 20 to 58 HRC (Fig. 18). It is noted that with an increase in the aluminium content, the hardness increases, which is associated with an increase in the proportion of solid intermetallic phases in the coating structure.



a



b

Fig. 10. External appearance of the welding bead produced in the following mode:
 $V_f/w\text{ Al}=6\text{ m/min}$; $U_{arc}\text{ Al}=25\text{ V}$; $V_s=0.15\text{ m/min}$. A torch tilt angle: *a* – 90° ; *b* – 30°
Рис. 10. Внешний вид наплавленного валика, полученного при следующем режиме:
 $V_n/n\text{ Al}=6\text{ м/мин}$; $U_{\partial}\text{ Al}=25\text{ В}$; $V_n=0,15\text{ м/мин}$.
 Угол наклона горелки: *a* – 90° ; *b* – 30°

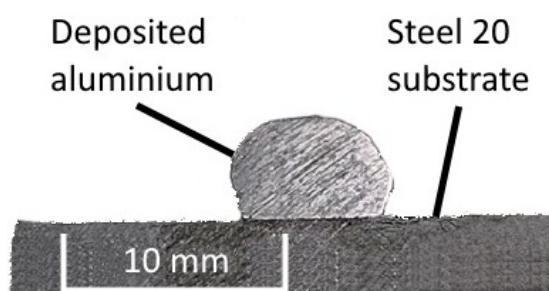


Fig. 11. Cross-section of the deposited aluminium bead produced in the following mode:
 $V_f/w\text{ Al}=5\text{ m/min}$; $U_{arc}\text{ Al}=17.5\text{ V}$; $V_s=0.2\text{ m/min}$
Рис. 11. Поперечное сечение наплавленного алюминиевого валика, полученного при следующем режиме:
 $V_n/n\text{ Al}=5\text{ м/мин}$; $U_{\partial}\text{ Al}=17,5\text{ В}$; $V_n=0,2\text{ м/мин}$

The relative wear resistance of the deposited metal varies in the range from 1.6 to 2.5 units. Maximum wear resistance is observed with an aluminium content of about 20 % (Fig. 19).

Heat resistance tests for 3000 h at a temperature of 950°C showed that the deposited metal has high heat resistance. An increase in the aluminium content “re-

fines” the surface of the welding bead; the presence of an oxide film ensures reliable protection of the metal from contact with the atmosphere. The loss of mass of the samples during heat resistance tests gradually decreases with an increase in the aluminium content from 9 to 20 %. With an aluminium content of 9–10 %,

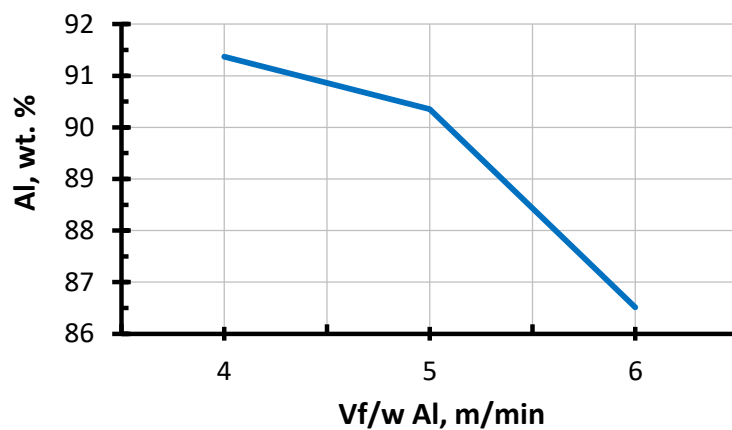


Fig. 12. Effect of the feed rate of the aluminium electrode wire on the aluminium content in the deposited metal ($U_{arc} Al=22.5$ V; $V_s=0.1$ m/min)

Рис. 12. Влияние скорости подачи алюминиевой электродной проволоки на содержание алюминия в наплавленном металле ($U_{\partial} Al=22,5$ В; $V_n=0,1$ м/мин)

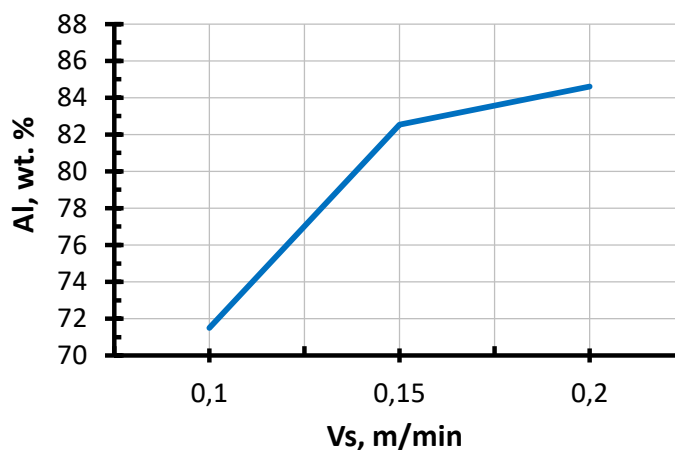


Fig. 13. Effect of surfacing speed on the aluminium content in the deposited metal ($U_{arc} Al=25$ V; $V_f/w Al=5$ m/min)

Рис. 13. Влияние скорости наплавки на содержание алюминия в наплавленном металле ($U_{\partial} Al=25$ В; $V_n/n Al=5$ м/мин)

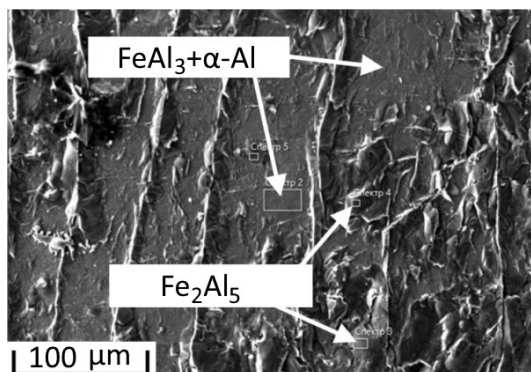


Fig. 14. Microstructure of the deposited sample of the Fe–Al system ($V_f/w Al=5$ m/min; $U_{arc} Al=20$ V; $V_s=0.15$ m/min)

Рис. 14. Микроструктура наплавленного образца системы Fe–Al ($V_n/n Al=5$ м/мин; $U_{\partial} Al=20$ В; $V_n=0,15$ м/мин)

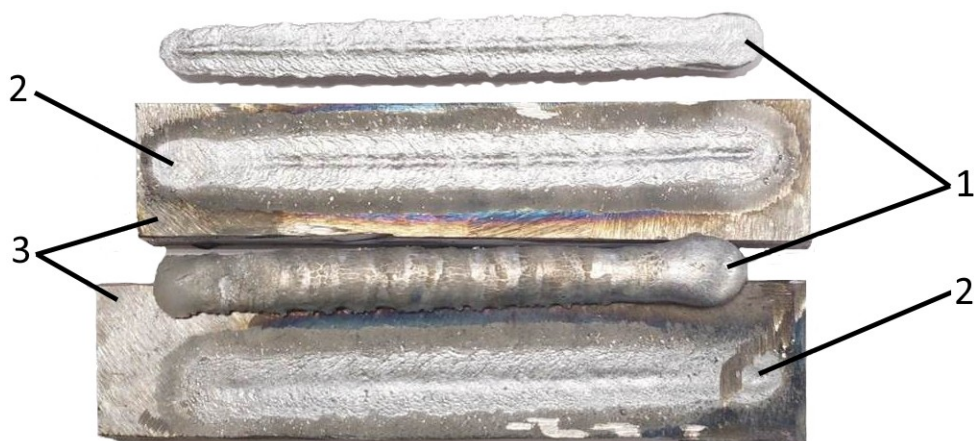


Fig. 15. External appearance of deposited alloys peeled off from the substrates:
1 – deposited alloys; 2 – fracture boundaries; 3 – base metal

Рис. 15. Внешний вид наплавленных сплавов, отслоившихся от подложки:
1 – наплавленные сплавы; 2 – граница разрушения; 3 – основной металл



Fig. 16. External appearance of the welding bead produced by double-arc surfacing in the following mode:
 $V_{f/w} Al=3$ m/min; $V_{f/w} Fe=3$ m/min; $V_s=0.15$ m/min; $U_{arc} Al=17$ V; $U_{arc} Fe=27.5$ V

Рис. 16. Внешний вид наплавленного валика, полученного двухдуговой наплавкой при следующем режиме:
 $V_{n/n} Al=3$ м/мин; $V_{n/n} Fe=3$ м/мин; $V_n=0,15$ м/мин; $U_{\partial} Al=17$ В; $U_{\partial} Fe=27,5$ В

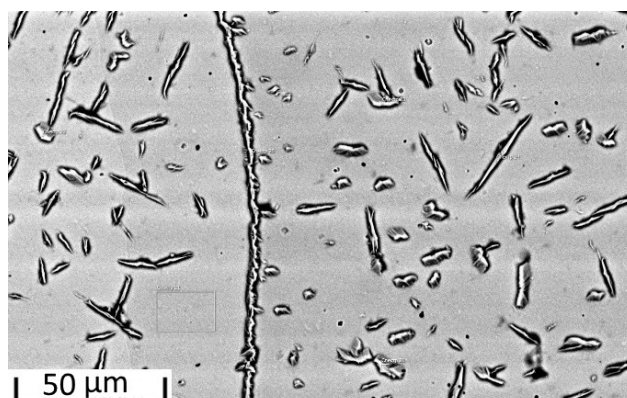


Fig. 17. Microstructure of the deposited sample with the α -Fe matrix phase and 6 % of Fe_3AlC_x phase inclusions
Рис. 17. Микроструктура наплавленного образца с матричной фазой α -Fe и 6 % включений фазы Fe_3AlC_x

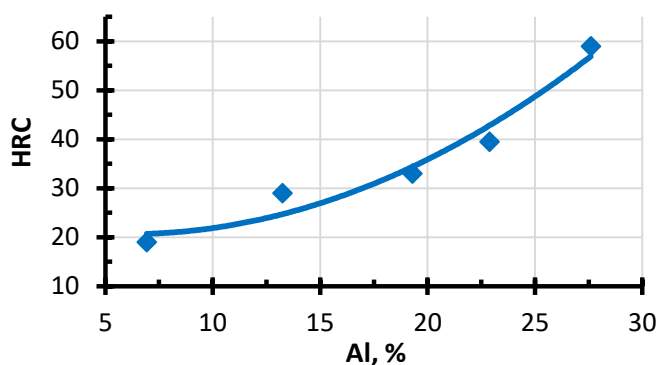


Fig. 18. Dependence of the hardness of the deposited metal on the percentage content of aluminium
Рис. 18. Зависимость твердости наплавленного металла от процентного содержания алюминия

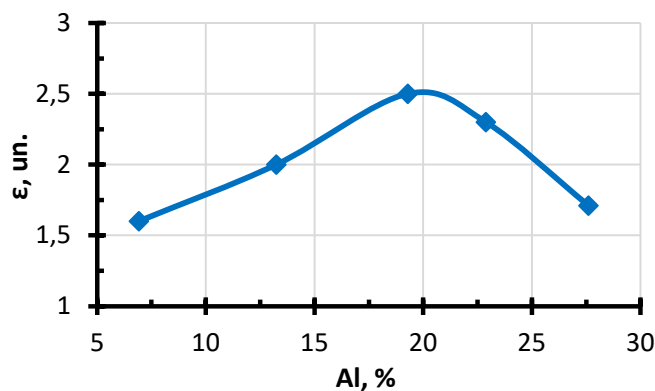


Fig. 19. Dependence of relative wear resistance under abrasive wear on the percentage content of aluminium
Рис. 19. Зависимость относительной износостойкости при абразивном изнашивании от процентного содержания алюминия

the mass loss was about 5 %, and with an aluminium content of 17–20 % – no more than 1 %. The aluminium content in the welding bead of more than 20 % leads to the appearance of a significant number of cracks and microcracks in the welding bead, which sharply reduces the heat resistance of the metal during tests. The loss of mass of samples with an aluminium content of more than 25 % during holding for 3000 h was more than 75 %. Thus, alloys containing 15 to 20 % aluminium have maximum heat resistance (Fig. 20).

DISCUSSION

The study found that single-arc surfacing of intermetallic alloys of the Fe–Al system using aluminium electrode wire does not provide a stable and predictable composition and properties of coatings based on iron aluminides. This is related to the high aluminium content in the deposited metal and the formation of alloys based on the FeAl_3 and $\alpha\text{-Al}$ phases, as well as Fe_2Al_5 and FeAl_3 intermetallic inclusions,

which, according to observations, leads to delamination of the deposited layer from the substrate.

This phenomenon is apparently determined by the uneven distribution of intermetallic phases and the high FeAl_3 concentration, which contributes to the formation of microcracks and a decrease in the ductility of the deposited layer, especially along the fusion line. In [6; 7], the authors consider the properties and work for the formation of coatings based on the Fe_3Al or FeAl intermetallic phases due to their better ductility and resistance to cracking at room temperature. In this regard, for producing wear-resistant and durable coatings on steel parts, methods that allow forming coatings with a chemical and phase composition based on the Fe_3Al and FeAl phases are more promising. However, the known methods of applying protective coatings based on iron aluminides allow producing coatings with a limited layer thickness of up to 0.5 mm, which is clearly insufficient for mining equipment components operating under abrasive wear conditions. Another significant limitation of existing

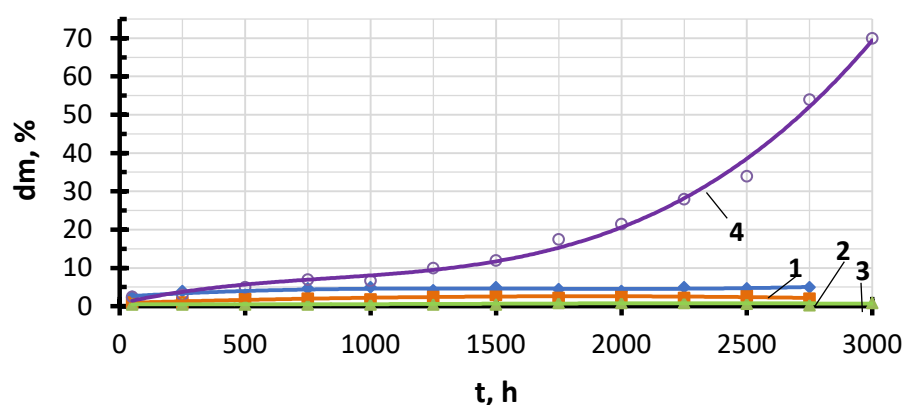


Fig. 20. Dependence of the change in the mass of samples on the time of their holding at a temperature of 950 °C with an aluminium content of:
1 – 7 %; 2 – 14 %; 3 – 17 %; 4 – 25 %

Рис. 20. Зависимость изменения массы образцов от времени их выдержки при температуре 950 °C с содержанием алюминия: 1 – 7 %; 2 – 14 %; 3 – 17 %; 4 – 25 %

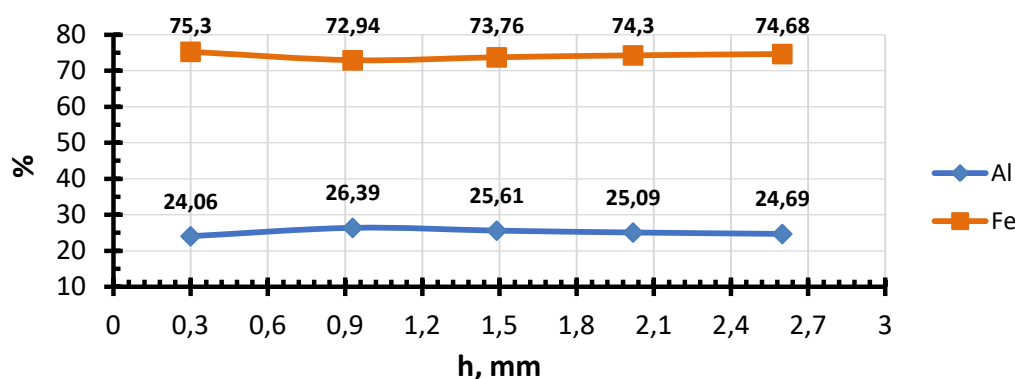


Fig. 21. Graph of the percentage content of aluminium and iron in the cross-section of the deposited metal (Uarc Al=14 V; Vf/w Al=5 m/min; Uarc Fe=23.5 V; Vf/w Fe=3 m/min; Vs=0.1 m/min)

Рис. 21. График процентного содержания алюминия и железа по сечению наплавленного металла (U_д Al=14 В; V_{н/н} Al=5 м/мин; U_д Fe=23,5 В; V_{н/н} Fe=3 м/мин; V_н=0,1 м/мин)

methods is the impossibility of applying coatings under installation conditions and the lack of prospects for further restoration of the coating after wear.

Therefore, for mining parts operating in tough environment, it is necessary to apply methods that combine the possibilities of producing coatings with a phase composition based on Fe₃Al or FeAl, as well as the possibility of producing coatings thicker than 0.5 mm. Such methods may include automatic argon-arc surfacing with a nonconsumable electrode [19] or double-arc surfacing using steel and aluminium electrode wires. In particular, the double-arc technology allows achieving better homogeneity of the chemical composition (Fig. 21).

A study of the effect of double-arc surfacing modes showed that changing the wire feed speed, voltage and torch angle significantly affects the properties of the resulting layers. In particular, an increase in the aluminium content to 27 wt. % contributes to an increase in the hardness of the deposited alloys to 58 HRC. How-

ever, this is accompanied by a decrease in ductility and an increase in the risk of cracking.

Wear tests showed that maximum wear resistance is achieved with an aluminium content of about 20 %, which is associated with an optimal ratio of hardness and microstructural stability. These results coincide with the data of [10; 11], where it is noted that the content of intermetallic phases and their distribution significantly affect the wear resistance of coatings. At the same time, there is no direct correlation between hardness and wear resistance, which indicates the importance of microstructural factors such as the size and distribution of intermetallic inclusions.

As for heat resistance, the results show that the aluminium content in the range of 15–20 % provides the maximum resistance to high temperatures. This is due to the formation of an oxide film, which serves as a protective barrier and prevents metal oxidation. However, an increase in the aluminium content above 20 % leads to the appearance of microcracks and a decrease in heat resistance, which is

consistent with the data of [14; 16; 17], where it is noted that excess aluminium contributes to the formation of internal stresses and defects.

The obtained results allow recommending double-arc surfacing as a method for applying wear-resistant coatings based on iron aluminides for low-carbon steel parts used in the mining industry or as a substitute for expensive coatings, since it allows producing coatings with a thickness of up to 5 mm. The discovered patterns allow concluding that the optimal composition for wear-resistant and heat-resistant coatings of the Fe–Al system is in the range of 15–20 % of aluminium. An important direction for further research is the development of methods for monitoring and stabilising the microstructure, as well as studying the effect of additional alloying elements on the properties of coatings. Moreover, it is necessary to study in more detail the mechanisms of formation of intermetallic phases and their influence on the adhesion and durability of coatings.

A limitation of this study is the limited range of modes and the lack of long-term tests under operating conditions. In the future, it is planned to expand the range of modes, as well as conduct wear and heat resistance tests under real operating loads.

CONCLUSIONS

1. Double-arc surfacing allows creating wear-resistant coatings of the Fe–Al system on low-carbon steel products used under conditions of abrasive wear and high temperatures reaching 950 °C.

2. By controlling the parameters of the double-arc surfacing process, it is possible to create deposited layers of intermetallic alloys with specified properties adapted to specific operating conditions due to the variation of their chemical and phase composition.

3. The chemical composition of the deposited alloys is characterised by an aluminium content in the range from 7 to 27.5 wt. %. The basis of the structure is the α -Fe matrix partially ordered according to the B2 type, and the inclusions present are the Fe_3AlC_x carbide phase. The volume of carbide inclusions varies from 3.26 to 18.95 %.

4. Fe–Al system alloys produced by double-arc surfacing have high hardness (20–58 HRC), wear resistance and heat resistance.

REFERENCES

- Grechneva M.V., Tolkachev S.A., Vladimirtsev I.K. Increasing wear resistance of mining machinery parts. *Proceedings of Irkutsk State Technical University*, 2011, no. 12, pp. 26–29. EDN: [ONXUEZ](#).
- Isagulov A.Z., Kvon S.S., Kulikov V.Yu. Improving wear resistance of elements of mining and processing equipment. *Ferrous Metallurgy. Bulletin of Scientific, Technical and Economic Information*, 2020, vol. 76, no. 6, pp. 609–613. DOI: [10.32339/0135-5910-2020-6-609-613](#).
- Nikitenko M.S., Knyazkov K.V., Ababkov N.V., Ozhiganov E.A. Development of diagnostic, restoration and strengthening complex for mining equipment. *Mining Informational and Analytical Bulletin*, 2013, no. S6, pp. 447–456. EDN: [RYYJAP](#).
- Korotkova V.A., Zamotina V.A. Restoration of mining equipment components. *Gornyi zhurnal*, 2001, no. 8, pp. 53–58.
- Ivanov A.V., Priezorskaya O.L. Promising methods of welding deposition and machining of parts restored. *Technico-tehnologicheskie problemy servisa*, 2010, no. 3, pp. 7–9. EDN: [MVHIZL](#).
- Palm M., Stein F., Dehm G. Iron aluminides. *Annual Review of Materials Research*, 2019, vol. 49, pp. 297–326. DOI: [10.1146/annurev-matsci-070218-125911](#).
- Mosznier F., Peng J., Suutala J., Jasnau U., Damayi M., Palm M. Application of iron aluminides in the combustion chamber of large bore 2-stroke marine engines. *Metals*, 2019, vol. 9, no. 8, article number 847. DOI: [10.3390/met9080847](#).
- Kumar A., Nayak S.K., Laha T. Comparative Study on Wear and Corrosion Behavior of Plasma Sprayed $\text{Fe}_{73}\text{Cr}_2\text{Si}_{11}\text{B}_{11}\text{C}_3$ and $\text{Fe}_{63}\text{Cr}_9\text{P}_5\text{B}_{16}\text{C}_7$ Metallic Glass Composite Coatings. *Journal of Thermal Spray Technology*, 2022, vol. 31, pp. 1302–1316. DOI: [10.1007/s11666-021-01280-1](#).
- Metidji N., Younes A., Allou D., Dilmi N. Effect of zirconium on the corrosion behavior of $\text{FeAl}_{40}\text{Ti}_3\text{B}$ intermetallic compounds for use in solar water heaters. *Journal of Applied Electrochemistry*, 2024, vol. 54, pp. 1267–1277. DOI: [10.1007/s10800-023-02033-4](#).
- Ravi K., Batra U., Prakash U. Investigation of mechanical and wear characteristics of forged Fe–Al–C intermetallic quaternary alloyed with Zr/Ti. *Journal of Materials Engineering and Performance*, 2022, vol. 31, pp. 3127–3135. DOI: [10.1007/s11665-021-06424-6](#).
- Metidji N., Younes A. Effects of boron, nickel and molybdenum content on the microstructure, mechanical behaviour and wear properties of FeAl alloy made by vacuum arc melting. *Transactions of the Indian Institute of Metals*, 2022, vol. 75, pp. 2691–2699. DOI: [10.1007/s12666-022-02639-w](#).
- De Sousa Malafaia A.M., Maestro C.A.R., de Oliveira M.F. Alternative air induction melt–remelt processing of an Fe_3Al –C intermetallic alloy: part I – mechanical properties and the effects of loading rate, heat treatment and test temperatures. *International Journal of Metalcasting*, 2022, vol. 16, pp. 1265–1275. DOI: [10.1007/s40962-021-00679-4](#).
- De Sousa Malafaia A.M., Maestro C.A.R., de Oliveira M.F. Alternative air induction melt–remelt processing of an Fe_3Al –C intermetallic alloy: part II – high temperature cyclic oxidation behavior. *International Journal of Metalcasting*, 2023, vol. 17, pp. 1673–1680. DOI: [10.1007/s40962-022-00881-y](#).
- Deevi S.C. Advanced intermetallic iron aluminide coatings for high temperature applications. *Progress in Materials Science*, 2021, vol. 118, article number 100769. DOI: [10.1016/j.pmatsci.2020.100769](#).
- Martins N., Silva A.P., Cordeiro Da Silva G., Dos Santos I.B., Santos C.E.D., Troysi F., Brito P. Characterization of Iron Aluminide Diffusion Coatings Obtained after Friction Surfacing. *Metals*, 2023, vol. 13, article number 461. DOI: [10.3390/met13030461](#).

16. Troysi F.D., Brito P.P. Development and characterization of an iron aluminide coating on mild steel substrate obtained by friction surfacing and heat treatment. *The International journal of Advanced Manufacturing Technology*, 2020, vol. 111, no. 9, pp. 2569–2576. DOI: [10.1007/s00170-020-06310-w](https://doi.org/10.1007/s00170-020-06310-w).
17. Mohammadkhani S., Bondar N., Vahdati-Khaki J., Haddad-Sabzevar M. Fabrication of Iron Aluminide Coatings (Fe_3Al and FeAl_3) on Steel Substrate by Self-Propagating High Temperature Synthesis (SHS) Process. *Journal of Coating Science and Technology*, 2017, vol. 4, no. 2, pp. 40–44. DOI: [10.6000/2369-3355.2017.04.02.2](https://doi.org/10.6000/2369-3355.2017.04.02.2).
18. Chen Maolong, Yang Xuefeng, Zhang Zhiqiang, Gu Yanguang, Li Kunjie, Liu Yansheng, Ma Junbei. Research status of laser cladding technology on aluminum alloy surface. *The International journal of Advanced Manufacturing Technology*, 2025, vol. 137, no. 1-2, pp. 1–21. DOI: [10.1007/s00170-025-15204-8](https://doi.org/10.1007/s00170-025-15204-8).
19. Kovtunov A.I., Bochkarev A.G., Plakhotnyy D.I. Study of the processes of formation of deposited alloys of the Fe–Al system alloyed with Si. *Svarochnoe proizvodstvo*, 2017, no. 12, pp. 3–7. EDN: [YRIBHU](https://elibrary.ru/yribhu).
9. Metidji N., Younes A., Allou D., Dilmi N. Effect of zirconium on the corrosion behavior of $\text{FeAl}_{40}\text{Ti}_3\text{B}$ intermetallic compounds for use in solar water heaters // *Journal of Applied Electrochemistry*. 2024. Vol. 54. P. 1267–1277. DOI: [10.1007/s10800-023-02033-4](https://doi.org/10.1007/s10800-023-02033-4).
10. Ravi K., Batra U., Prakash U. Investigation of mechanical and wear characteristics of forged Fe–Al–C intermetallic quaternary alloyed with Zr/Ti // *Journal of Materials Engineering and Performance*. 2022. Vol. 31. P. 3127–3135. DOI: [10.1007/s11665-021-06424-6](https://doi.org/10.1007/s11665-021-06424-6).
11. Metidji N., Younes A. Effects of boron, nickel and molybdenum content on the microstructure, mechanical behaviour and wear properties of FeAl alloy made by vacuum arc melting // *Transactions of the Indian Institute of Metals*. 2022. Vol. 75. P. 2691–2699. DOI: [10.1007/s12666-022-02639-w](https://doi.org/10.1007/s12666-022-02639-w).
12. De Sousa Malafaia A.M., Maestro C.A.R., de Oliveira M.F. Alternative air induction melt–remelt processing of an Fe_3Al –C intermetallic alloy: part I – mechanical properties and the effects of loading rate, heat treatment and test temperatures // *International Journal of Metalcasting*. 2022. Vol. 16. P. 1265–1275. DOI: [10.1007/s40962-021-00679-4](https://doi.org/10.1007/s40962-021-00679-4).
13. De Sousa Malafaia A.M., Maestro C.A.R., de Oliveira M.F. Alternative air induction melt–remelt processing of an Fe_3Al –C intermetallic alloy: part II – high temperature cyclic oxidation behavior // *International Journal of Metalcasting*. 2023. Vol. 17. P. 1673–1680. DOI: [10.1007/s40962-022-00881-y](https://doi.org/10.1007/s40962-022-00881-y).
14. Deevi S.C. Advanced intermetallic iron aluminide coatings for high temperature applications // *Progress in Materials Science*. 2021. Vol. 118. Article number 100769. DOI: [10.1016/j.pmatsci.2020.100769](https://doi.org/10.1016/j.pmatsci.2020.100769).
15. Martins N., Silva A.P., Cordeiro Da Silva G., Dos Dantos I.B., Santos C.E.D., Troysi F., Brito P. Characterization of Iron Aluminide Diffusion Coatings Obtained after Friction Surfacing // *Metals*. 2023. Vol. 13. Article number 461. DOI: [10.3390/met13030461](https://doi.org/10.3390/met13030461).
16. Troysi F.D., Brito P.P. Development and characterization of an iron aluminide coating on mild steel substrate obtained by friction surfacing and heat treatment // *The International journal of Advanced Manufacturing Technology*. 2020. Vol. 111. № 9. P. 2569–2576. DOI: [10.1007/s00170-020-06310-w](https://doi.org/10.1007/s00170-020-06310-w).
17. Mohammadkhani S., Bondar N., Vahdati-Khaki J., Haddad-Sabzevar M. Fabrication of Iron Aluminide Coatings (Fe_3Al and FeAl_3) on Steel Substrate by Self-Propagating High Temperature Synthesis (SHS) Process // *Journal of Coating Science and Technology*. 2017. Vol. 4. № 2. P. 40–44. DOI: [10.6000/2369-3355.2017.04.02.2](https://doi.org/10.6000/2369-3355.2017.04.02.2).
18. Chen Maolong, Yang Xuefeng, Zhang Zhiqiang, Gu Yanguang, Li Kunjie, Liu Yansheng, Ma Junbei. Research status of laser cladding technology on aluminum alloy surface // *The International journal of Advanced Manufacturing Technology*. 2025. Vol. 137. № 1-2. P. 1–21. DOI: [10.1007/s00170-025-15204-8](https://doi.org/10.1007/s00170-025-15204-8).
19. Ковтунов А.И., Бочкарев А.Г., Плахотный Д.И. Исследование процессов формирования наплавленных сплавов системы Fe–Al легированных Si // *Сварочное производство*. 2017. № 12. С. 3–7. EDN: [YRIBHU](https://elibrary.ru/yribhu).

СПИСОК ЛИТЕРАТУРЫ

1. Гречнева М.В., Толкачев С.А., Владимирцев И.К. Повышение износостойкости деталей горных машин // *Вестник Иркутского государственного технического университета*. 2011. № 12. С. 26–29. EDN: [ONXUEZ](https://elibrary.ru/onxuez).
2. Исагулов А.З., Квон С.С., Куликов В.Ю. Повышение износостойкости элементов горно-обогатительного оборудования // *Черная металлургия. Бюллетень научно-технической и экономической информации*. 2020. Т. 76. № 6. С. 609–613. DOI: [10.32339/0135-5910-2020-6-609-613](https://doi.org/10.32339/0135-5910-2020-6-609-613).
3. Никитенко М.С., Князьков К.В., Абабков Н.В., Ожиганов Е.А. Разработка комплекса средств технической диагностики, восстановления и упрочнения элементов горнодобывающего оборудования // *Горный информационно-аналитический бюллетень (научно-технический журнал)*. 2013. № S6. С. 447–456. EDN: [RYYJAP](https://elibrary.ru/ryyjap).
4. Короткова В.А., Замотина В.А. Восстановление деталей горного оборудования // *Горный журнал*. 2001. № 8. С. 53–58.
5. Иванов А.В., Приозерская О.Л. Перспективные способы наплавки и механической обработки восстанавливаемых деталей // *Технико-технологические проблемы сервиса*. 2010. № 3. С. 7–9. EDN: [MVHIIZL](https://elibrary.ru/mvhiizl).
6. Palm M., Stein F., Dehm G. Iron aluminides // *Annual Review of Materials Research*. 2019. Vol. 49. P. 297–326. DOI: [10.1146/annurev-matsci-070218-125911](https://doi.org/10.1146/annurev-matsci-070218-125911).
7. Moszner F., Peng J., Suutala J., Jasna U., Damayi M., Palm M. Application of iron aluminides in the combustion chamber of large bore 2-stroke marine engines // *Metals*. 2019. Vol. 9. № 8. Article number 847. DOI: [10.3390/met9080847](https://doi.org/10.3390/met9080847).
8. Kumar A., Nayak S.K., Laha T. Comparative Study on Wear and Corrosion Behavior of Plasma Sprayed $\text{Fe}_{73}\text{Cr}_2\text{Si}_{11}\text{B}_{11}\text{C}_3$ and $\text{Fe}_{63}\text{Cr}_9\text{P}_5\text{B}_{16}\text{C}_7$ Metallic Glass Composite Coatings //

Особенности дуговой наплавки интерметаллидных сплавов системы Fe–Al на поверхности низкоуглеродистых сталей

Бочкарев Александр Геннадьевич^{*1,3}, кандидат технических наук,

доцент кафедры «Сварка, обработка материалов давлением и родственные процессы»

Ковтунов Александр Иванович^{1,4}, доктор технических наук,

профессор кафедры «Сварка, обработка материалов давлением и родственные процессы»

Плахотный Денис Иванович^{1,5}, старший преподаватель

кафедры «Сварка, обработка материалов давлением и родственные процессы»

Хохлов Юрий Юрьевич^{1,6}, заведующий лабораторией

кафедры «Сварка, обработка материалов давлением и родственные процессы»

Белоногов Савелий Олегович^{2,7}, инженер лаборатории разрушающих методов контроля

Веденеев Иван Вячеславович^{2,8}, инженер лаборатории неразрушающего контроля

¹Тольяттинский государственный университет, Тольятти (Россия)

²ООО «Средневолжский сертификационно-диагностический центр «Дельта», Тольятти (Россия)

*E-mail: a.bochkarev5@tltsu.ru,
a.bochkarev93@mail.ru

³ORCID: <https://orcid.org/0000-0002-7945-1634>

⁴ORCID: <https://orcid.org/0000-0002-7705-7377>

⁵ORCID: <https://orcid.org/0000-0003-2021-8974>

⁶ORCID: <https://orcid.org/0000-0002-5276-8957>

⁷ORCID: <https://orcid.org/0009-0007-9788-9967>

⁸ORCID: <https://orcid.org/0009-0009-4159-526X>

Поступила в редакцию 17.04.2025

Пересмотрена 10.06.2025

Принята к публикации 13.08.2025

Аннотация: Долговечность деталей, используемых в промышленности, во многом определяется материалами, из которых они изготовлены. Зачастую применяемые материалы должны быть устойчивыми к износу, коррозии и высоким температурам. Современные материалы, такие как высокопрочные легированные стали, обладают высокой стоимостью и ограниченной свариваемостью, что усложняет восстановление изношенных деталей. В качестве альтернативы рассматриваются сплавы системы Fe–Al, обладающие высокой коррозионной стойкостью, износостойкостью и жаростойкостью при меньшей стоимости. Цель исследования – повышение износостойкости и жаростойкости деталей из низкоуглеродистой стали путем исследования процессов дуговой наплавки алюминидов железа и их свойств. Методика исследования включала одnodуговую и двухдуговую наплавку с использованием алюминиевой и стальной электродных проволок, анализ химического состава наплавленных покрытий, их твердости, износостойкости и жаростойкости. Результаты показали, что одnodуговая наплавка формирует сплавы на основе фаз FeAl₃ и α-Al с включениями Fe₂Al₅ и FeAl₃, а двухдуговая – более насыщенные железом сплавы с матричной фазой α-Fe и карбидной фазой Fe₃AlC_x. Полученные сплавы демонстрируют твердость до 58 HRC, относительную износостойкость до 2,5 ед. и потерю массы не более 5 % при содержании алюминия до 20 %, что говорит об их перспективности для применения в условиях повышенных нагрузок. Результаты подтверждают целесообразность использования алюминидов железа как недорогой альтернативы дорогостоящим покрытиям, что расширяет возможности повышения износостойкости и жаростойкости деталей в промышленности.

Ключевые слова: дуговая наплавка; интерметаллидные сплавы; алюминиды железа; низкоуглеродистая сталь; твердость; износостойкость; жаростойкость.

Для цитирования: Бочкарев А.Г., Ковтунов А.И., Плахотный Д.И., Хохлов Ю.Ю., Белоногов С.О., Веденеев И.В. Особенности дуговой наплавки интерметаллидных сплавов системы Fe–Al на поверхности низкоуглеродистых сталей // Frontier Materials & Technologies. 2025. № 3. С. 11–25. DOI: 10.18323/2782-4039-2025-3-73-1.

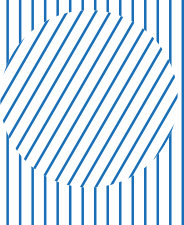
Togliatti State University is a participant in the Priority-2030 program of strategic academic leadership, a flagship university in the Samara region, a center for innovative and technological development of the region.

Togliatti State University was created in 2001 by merging Togliatti Polytechnic Institute (founded in 1951 as a branch of Kuibyshev Industrial Institute) and Togliatti branch of Samara State Pedagogical University (founded in 1987).

Togliatti State University today

- More than 22,000 students of all modes of study.
- Ten institutes implementing more than 170 higher education programs for 25 integrated groups of training areas, advanced technologies research institute, Zhiguli Valley Institute of Additional Education, military training center.
- 38 resource centers with up-to-date facilities and equipment created since 2011.
- Accreditation in eight systems for standard testing, research, and engineering.
- Main areas: advanced digital, intelligent manufacturing technologies, robotic systems, advanced materials and design methods, environmentally friendly and resource-saving energy engineering, personalized medicine, countering industrial threats.

University main achievements

- Ongoing project and professional practical activity was introduced for 100 % of full-time undergraduate/specialist students.
 - Four mega-grants were implemented according to the Resolutions of the Government of the Russian Federation dated April 9, 2010 No. 219 and No. 220 – three laboratories in the field of physical materials science and nanotechnology (with the invitation of leading scientists), as well as an innovation technology center were created. The latter was transformed into a university innovation technopark.
 - A member of the extraterritorial scientific and educational center “Engineering of the Future”.
 - An initiator of the formation of eight consortiums, which brought together 69 organizations, including 36 universities, six scientific partners, among which there are three organizations of the Russian Academy of Sciences.
 - A twice winner of the RF Government award in the field of quality (2009, 2019).
 - An Online Higher Education System promoted under the Rosdistant brand was created. The project is the winner of the Project Olympus competition of the Analytical Center under the Government of the Russian Federation in the Project Management in the System of Higher Education and Science nomination (2019).
- 

Scheme for producing composite material based on structural aluminum alloy by the direct extrusion method

Natalia I. Bushueva^{*1}, postgraduate student, research engineer of scientific laboratory “Metal Forming”

Yury N. Loginov², Doctor of Science (Engineering), professor of Chair of Metal Forming

Ural Federal University named after the first President of Russia B.N. Yeltsin, Yekaterinburg (Russia)

***E-mail:** n.i.bushueva@urfu.ru

¹ORCID: <https://orcid.org/0000-0002-0603-8785>

²ORCID: <https://orcid.org/0000-0002-7222-2521>

Received 30.06.2025

Revised 19.08.2025

Accepted 01.09.2025

Abstract: The work covers the development of a technology for producing a bimetallic rod from high-strength 7075 alloy with a cladding layer of 1100 aluminum, which is aimed at improving corrosion resistance while maintaining mechanical properties. A special feature of the proposed technology is the use of an additional front pure aluminum workpiece for the process of direct extrusion of a rod from 7075 alloy. The direct extrusion process for a composite workpiece was simulated with the DEFORM software package's finite element method. The influence of process temperature and speed on the formation of the cladding layer was analyzed. For this purpose, four problems were formulated with varying heating modes of workpieces and tools. It was found that it is possible to produce a thin cladding layer at a heating temperature of the base 7075 alloy equal to 360 °C and a cladding layer temperature equal to 20 °C, which ensures a uniform distribution of the coating along the length of the rod without signs of delamination. Stress-strain analysis during extrusion showed that a cold additional workpiece ensures continuity for cladding coating formation. However, heating above 300 °C leads to rupture from deformation localization. The developed approach can be used to reduce the cost of products by reducing the consumption of expensive 7075 alloy while simultaneously increasing corrosion resistance due to the use of pure aluminum cladding. Prospects for the development of further research are associated with the optimization of extrusion modes for various rod sizes.

Keywords: extrusion; finite element method; composite materials; 7075 aluminum alloy; cladding layer.

Acknowledgments: The paper was written on the reports of the participants of the XII International School of Physical Materials Science (SPM-2025), Togliatti, September 15–19, 2025.

For citation: Bushueva N.I., Loginov Yu.N. Scheme for producing composite material based on structural aluminum alloy by the direct extrusion method. *Frontier Materials & Technologies*, 2025, no. 3, pp. 27–37. DOI: 10.18323/2782-4039-2025-3-73-2.

INTRODUCTION

Modern requirements for increasing fuel efficiency, reducing the weight of structures and minimizing harmful carbon dioxide emissions justify the search for and development of promising lightweight materials and technologies for their processing. In this aspect, aluminum and aluminum alloys are of interest as promising structural materials, which is caused by the optimal combination of their physical and mechanical characteristics [1; 2]. However, to develop new types of products operating, for example, in extreme conditions, it is necessary to predict accurately their behavior at various stages of production (in particular, during metal forming).

The relevance of predicting properties at the stage of design of product manufacturing technologies is also caused by the continuing growth in metal prices. According to sources from the Fastmarkets database, the indicators of which are used in contracts, exchange trading and financial calculations, the cost of a cast ingot of 5000 and 6000 series alloys varies in the range of \$ 2.5–4 per kg. For 7000 series alloys, the price is significantly higher, since these alloys belong to the class of high-

strength and hard-to-deform. The 7075 alloy has high strength characteristics. Nevertheless, the aerospace industry's adoption of this metal is limited by poor corrosion resistance and fatigue life.

Manufacturers are interested in reducing costs, especially in the areas of production of goods from expensive metals, where even small savings per ton of material provide significant financial benefits. Primary aluminum with a minimum content of impurities is traditionally used as raw material to produce 6061, 6065 and 7075 alloys. In the current reality, there is a problem with the supply of this type of raw material due to the geopolitical situation in the world. This specifically concerns the introduction of new increased customs duty rates on goods. Manufacturers of metal products express concerns, since they will now have to pay a significantly higher amount for high-purity material. Custom tariffs are ultimately included in the cost of metal. This has a negative impact on all types of production whether the enterprise is a manufacturer of machining tools or sheet metal. For the case considered in this paper, the cost of the product includes both the manufacture of

cast metal and the further production of extruded semi-finished product, which has a significant impact on the final cost of the product. Moreover, the dynamics of prices for aluminum products continues to grow. According to data for 2024, prices for 7075 alloy consistently exceed \$ 20 per kg¹, which is dictated, among other things, by high demand in the aerospace sector. One solution aimed at improving productivity while maintaining product quality may be the use of composite workpieces, where functionally loaded areas contain expensive metals and the remaining parts are made of cheaper aluminum alloys or pure aluminum.

Although experimental methods remain the main research tool, numerical simulation provides significant advantages, including time and cost savings, as well as deeper analysis compared to experimental approaches [3]. This makes it important to study the properties of expensive alloys such as 7000 series alloys.

Recent studies of the corrosion behavior of 7075 aluminum alloy have revealed susceptibility to various aggressive environments: in NaCl solutions, intense intercrystalline corrosion is observed with the formation of surface roughness and grain embrittlement to a depth of 150 µm [4]. The corrosion rate is minimal at neutral pH due to the formation of a protective oxide layer, while acidic and alkaline environments accelerate the process [5]. Biological factors also have a significant impact. For example, the *Aspergillus niger* fungus increases the rate of uniform and localized corrosion by 3.7 and 22.4 times, respectively, compared to abiotic conditions [6]. The sulfate-reducing bacteria in seawater accelerate corrosion, completely destroying the protective film after 14 days [7]. These data demonstrate the complex interaction of environmental factors affecting the corrosion behavior of 7075 alloy and emphasize the need to develop specialized protection methods for different operating conditions.

The 7000 series alloys have high strength. This high strength makes them difficult to deform during metal forming [8]. Therefore, the traditional extrusion method is usually limited to a speed of 1–2 m/min due to the risk of surface defects [9]. In foreign practice, the development of new extrusion methods is very popular. For example, scientists from the Pacific Northwest National Laboratory (PNNL, USA) created the Shear Assisted Processing and Extrusion (ShAPE) technology, which allows achieving an extrusion speed of 12.2 m/min for 7075 alloy without the formation of surface ruptures, providing high mechanical properties after T6 heat treatment [10].

The 7075 alloy has a high sensitivity to various types of corrosion. Therefore, developing composite modifications for this material is highly relevant. For example, technologies for producing composites from aluminum alloys using rolling are known. This method is a more cost-effective alternative to applying protective coatings using chemical or galvanic methods. In [11; 12], a mathe-

matical model of grain evolution and dislocation density during cold asymmetric rolling of pure aluminum (Al 99.5 %) and 7075 alloy under severe plastic deformation conditions was developed.

Research has shown that reinforcing 7075 alloy with ceramic particles such as SiC and Al₂O₃ significantly increases corrosion resistance in various environments [13]. The stir casting method has proven effectiveness for the production of metal matrix composites based on 7075 alloy with ceramic nanoparticles, providing a significant improvement in mechanical properties [14], which is especially important in view of the growing demand for lightweight materials in the aerospace industry.

In manufacturing practice, it is common to apply cladding with pure aluminum to reduce the likelihood of cracking and increase corrosion resistance. Several methods exist for applying cladding to aluminum alloys including combined hot rolling for sheet products; friction stir welding, particularly for aerospace alloys [15]; the rolling of aluminum powder onto a substrate [16]; and a technique where an aluminum alloy cylinder is compressed into a pure aluminum shell followed by swaging, rolling, and cold drawing [17]. In this case, the cladding process allows producing a composite with improved characteristics. For example, clad wire demonstrates higher electrical conductivity compared to the determined values while maintaining strength properties.

The objective of this study is to develop a method for producing a composite rod based on 7075 alloy with a cladding layer of 1100 aluminum by direct extrusion to ensure increased corrosion resistance.

METHODS

The feasibility of implementing a technology to produce a rod from 7075 alloy with a pure 1100 aluminum cladding was predicted via numerical simulation using the DEFORM-2D software package based on the finite element method.

A plastic type of deformable material was used. The number of grid elements for the main workpiece is 12,000; for the additional one – 1,700 (the grid size was selected taking into account the element size in accordance with the volume of the workpieces). Fig. 1 shows a CAD model of the original geometry in 3D visualization. The original diameter of the workpiece is 750 mm. The final diameter of the rod is 360 mm. The diameter of the container is 800 mm. The taper angle of the matrix extrusion die is 75°. The dimensions and other parameters were selected from the practice of one of the enterprises.

Fig. 2 shows the hardening curves of the materials for the considered temperature ranges.

The Siebel's friction index was set to 0.5 at the workpiece-die contact and 1 for the other contact pairs². The extrusion speed was 4.27 mm/s. The parameter for accounting heat exchange between the workpieces materials

¹ Aluminium reliant industries not spared from the impact of tariffs. Fastmarkets.
URL: <https://www.fastmarkets.com/insights/us-aluminium-tariffs-impact-prices/>.

² Loginov Yu.N. *Pressovanie kak metod intensivnoy deformatsii metallov i splavov* [Pressing as a Method of Intensive Deformation of Metals and Alloys]. Ekaterinburg, UrFU Publ., 2016. 156 p.

and the tool was included when solving the problems in DEFORM.

According to the data from the DEFORM materials library, the thermal conductivity for the materials under consideration was $180 \text{ W/(m}\cdot\text{°C)}$. The heat capacity of the material was $2.43 \text{ MJ/(m}^3\cdot\text{°C)}$.

According to the MatWeb database, pure aluminum has the following thermodynamic parameters: specific heat of fusion is $q_f=387 \text{ kJ/kg}$, specific heat capacity is $c=900 \text{ J/(kg}\cdot\text{°C)}$, melting point is $t_m=660 \text{ °C}$.

Each series of alloys is characterized by certain ranges of thermodynamic properties, which is caused by the inconsistency of the chemical composition even within a single grade. For example, 1000 series alloys contain over 99 % aluminum. However, trace impurities cause their phase diagrams to demonstrate both liquidus and solidus lines. This can lead to a melting point decrease compared to pure aluminum. The lowest melting point values are characteristic of 7000 series alloys, which is explained by the presence of low-melting zinc in their composition.

Table 1 shows the average values of specific heat capacity c_m and melting point t_m to simplify engineering analysis [18]. In addition, the parameter $\Delta(\%)$ characterizing the deviation of the average melting point of the alloy from the melting point of aluminum of the 1000 series was determined. The greatest discrepancy (up to 13 %) is observed in 7000 series alloys. This indicator allows estimating the potential error when determining energy costs if the parameters of pure aluminum are taken as a basis, and the alloy is actually processed.

Considering the specific thermodynamic properties of aluminum alloys of different series is critical for accurate simulation of technological processes and minimizing errors in engineering analysis.

The successful implementation of a cladding technology for extruded rod requires an additional front workpiece made of pure aluminum and the correct selection of process boundary conditions. In particular, the selection of temperature conditions is difficult, since pure aluminum obviously has greater plasticity than 7075 alloy.

Several variations of temperature conditions for the process were selected (Table 2). The choice of temperature conditions for 7075 alloy was carried out in accordance with the recommendations from the manual³, which notes that the optimal temperature range is 360–430 °C.

Several variations of temperature conditions for the process were selected (Table 2). The choice of temperature conditions for 7075 alloy was carried out in accordance with the recommendations from the manual, which notes that the optimal temperature range is 360–430 °C.

RESULTS

During the simulation for temperature modes No. 1–3 (Table 2), unsuccessful results were obtained. When the product leaves the drawing cylinder of the matrix extru-

sion die parallel land, the cladding material is torn off from the main workpiece. For modes No. 1 and 3, a similar effect of cladding delamination is observed.

At temperature mode No. 2, the cladding material is intensively heated in the deformation zone – more than 100 °C from the initial temperature of 300 °C. The heating rate of the additional workpiece material does not allow achieving the desired result. At the same time, it is unreasonable to reduce the heating temperature of the tools, since 7075 alloy is difficult to deform and such a solution will obviously lead to a negative result.

Based on the results shown in Fig. 3 and 4, it was decided to attempt extruding without heating the additional workpiece (Table 2, option No. 4). For this temperature mode option, it was possible to obtain a rod with a thin uniform cladding layer. In this case, the material of the additional workpiece does not peel off.

As can be seen from Fig. 5, the cladding layer of pure aluminum is applied to the rod throughout the extrusion process. At the steady state stage of the extrusion process, the thickness of the cladding layer is 5 mm, which is 1.38 % of the diameter of the resulting product. The flow rate of the cladding metal is restrained by high friction forces at the container contact. This phenomenon is characteristic of the direct extrusion process and illustrated in Fig. 6.

It is evident from Fig. 7 that in the absence of heating of the additional workpiece, heat transfer occurs with moderate intensity. The flow stresses of the additional workpiece material are slightly lower (Fig. 2 b) than those of the base metal (Fig. 2 a), which prevents the separation from the main workpiece during extrusion.

Based on the distribution of the strain rate (Fig. 8), it can be concluded that the highest value of the strain rate is characteristic of the zone adjacent to the matrix extrusion die parallel land. The strain rate reaches the value of $\dot{\epsilon}=0.5 \text{ s}^{-1}$.

DISCUSSION

The result of the composite rod extrusion process, shown in Fig. 3, was obtained for the first three variants of the problem statement (Table 2, No. 1–3). For variant No. 2, the maximum possible extrusion temperature of 7075 alloy was selected 470 °C. This choice was caused by the existence of works that described the process of extruding rods from 7075 alloy at a heating temperature of 450 °C and higher [19]. When choosing this temperature mode, the possible chilling of the main workpiece metal during the extrusion process was considered. The heating temperature of the additional workpiece made of 1100 alloy was set to 300 °C in order to try to create conditions for more intense deformation of 7075 alloy.

As a result of the analysis, the optimal process parameters were identified: the heating temperature of the base 7075 alloy is 360 °C, the temperature of the cladding layer is 20 °C, and the heating temperature of the tools is 430 °C (Table 2, No. 4).

The difference in the heating temperatures of the workpieces creates an optimal balance of the plasticity

³ Loginov Yu.N. *Pressovanie kak metod intensivnoy deformatsii metallov i splavov [Pressing as a Method of Intensive Deformation of Metals and Alloys]*. Ekaterinburg, UrFU Publ., 2016. 156 p.

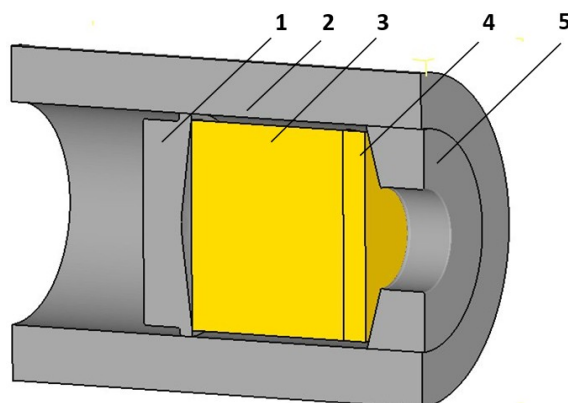
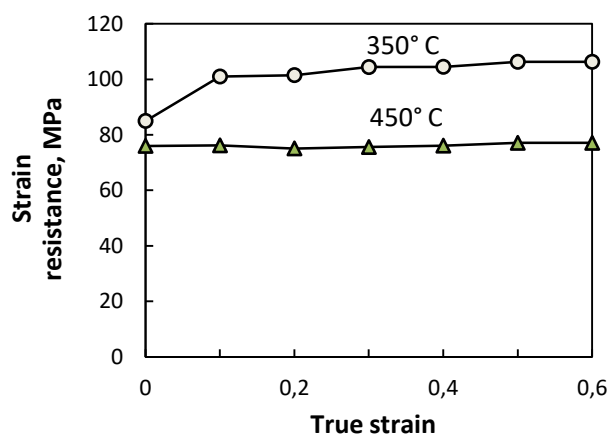
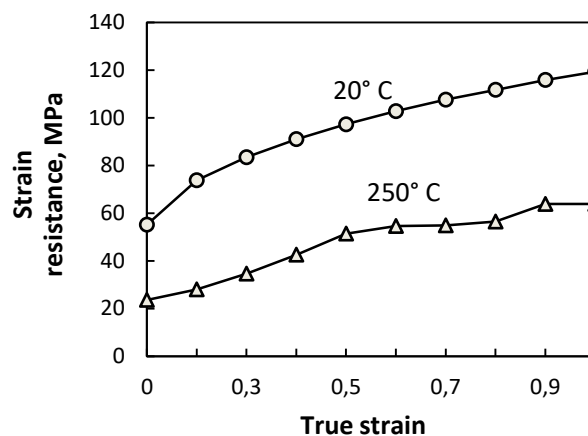


Fig. 1. Assembly for setting the task in 3D visualization: 1 – pressing disk; 2 – container; 3 – main workpiece; 4 – additional workpiece; 5 – matrix extrusion die

Рис. 1. Сборка для постановки задачи в 3D-визуализации: 1 – пресс-шайба; 2 – контейнер; 3 – основная заготовка; 4 – дополнительная заготовка; 5 – матрица



a



b

Fig. 2. Hardening curves for materials at a strain rate of $\dot{\epsilon}=0.1 \text{ s}^{-1}$:

a – for 7075 alloy; **b** – for 1100 aluminum

Рис. 2. Кривые упрочнения для материалов при скорости деформации $\dot{\epsilon}=0,1 \text{ с}^{-1}$:

a – для сплава 7075; **b** – для алюминия 1100

Table 1. Thermal properties of aluminum alloys by series [Reference: 18, p. 68]

Таблица 1. Теплотехнические свойства сплавов алюминия по сериям [Привод. по: 18, с. 68]

Alloy series	System	c , J/(kg·deg)	c_m , J/(kg·deg)	t_m , °C	t_{mm} , °C	Δ , %
1000	Al	900–904	902	643–660	652	0
7000	Al–Zn–Mg	856–960	858	476–657	567	–13

Table 2. Temperature modes for setting problems
Таблица 2. Температурные режимы для постановки задач

No.	Heating temperature of the main workpiece (AL7075), °C	Heating temperature of the additional workpiece (AL1100), °C	Heating temperature of tools, °C
1	450	430	360
2	470	300	430
3	430	430	430
4	360	20	430

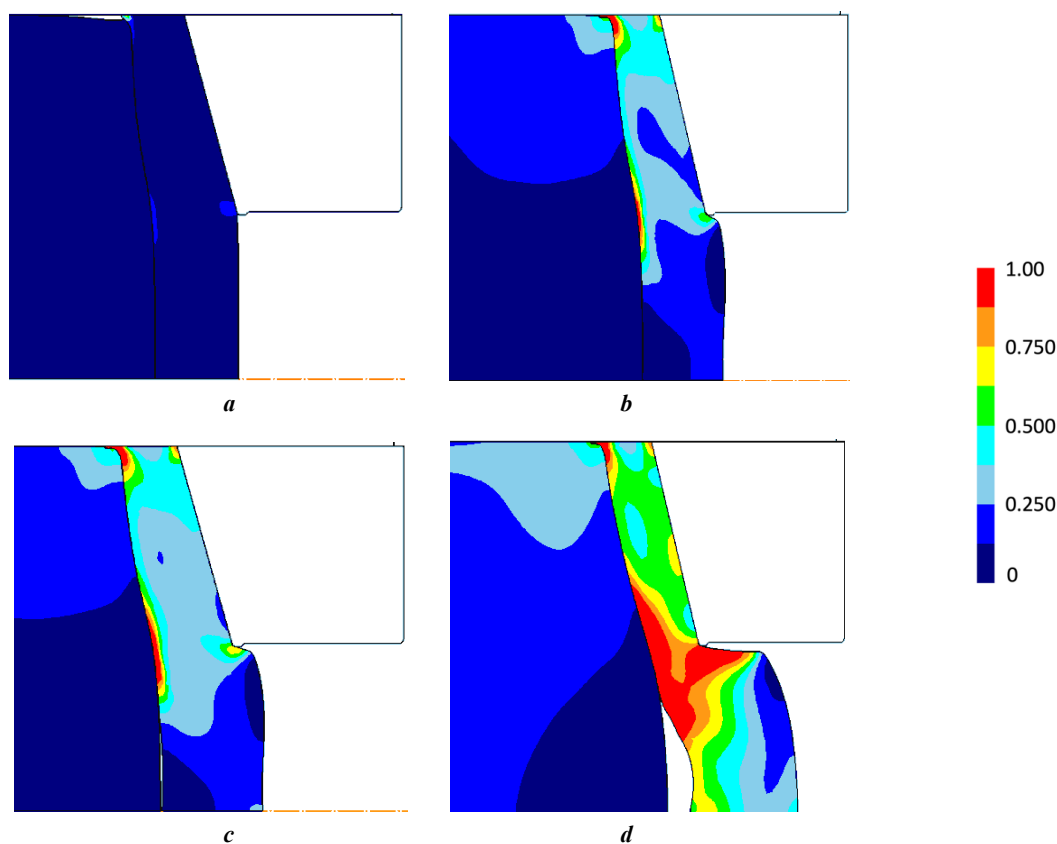


Fig. 3. The course of the extrusion process with the display of effective strain color levels for temperature mode No. 2: **a** – the stage of pressing out; **b** – the beginning of extrusion; **c** – the beginning of cladding peeling off; **d** – the development of the process of cladding peeling off
Рис. 3. Ход процесса прессования с отображением цветовых уровней эффективной деформации для температурного режима № 2:
a – стадия распрессовки; **b** – начало прессования; **c** – начало отслоения плакировки; **d** – развитие хода отслоения плакировки

of the components, which is a critically important factor. Heating the tool to 430 °C maintains the plasticity of the 7075 alloy. However, if the 1100 alloy heats up, it sticks to the tool. Therefore, a suitable result is only achieved by combining a cold 1100 alloy with a hot 7075 alloy.

An additional advantage of the proposed technology may be the possibility of using process waste in the form of scraps as a front workpiece, which increases the re-

source efficiency of production. A promising direction for further research is the optimization of the technology for rods of different diameters. This material's combination of high strength and corrosion resistance meets a critical requirement for structural materials in the aerospace industry.

To verify the obtained results, other works related to this topic were considered. In [20], a scheme for extrusion a rod

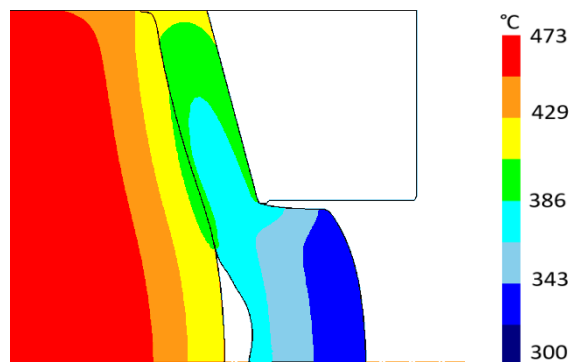


Fig. 4. Temperature field at the stage of additional workpiece peeling off for the extrusion option No. 2, °C

Рис. 4. Температурное поле на этапе отслоения дополнительной заготовки для варианта прессования № 2, °C

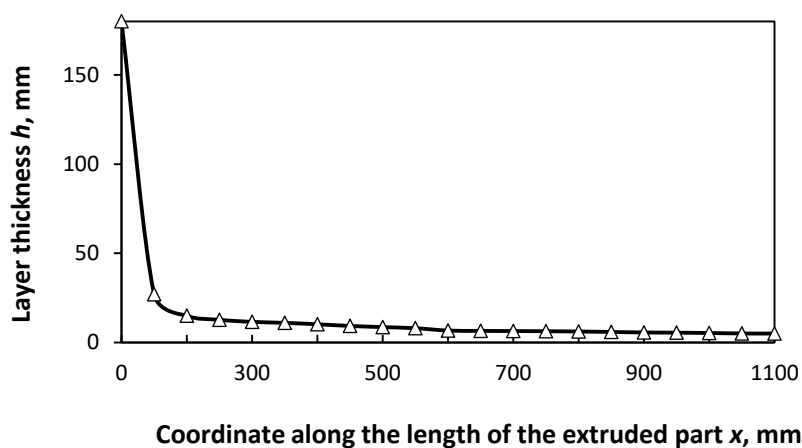


Fig. 5. Graph of the dependence of the cladding layer thickness h on the coordinate along the length of the extruded part of the product x

Рис. 5. График зависимости толщины плакирующего слоя h от координаты по длине отпрессованной части изделия x

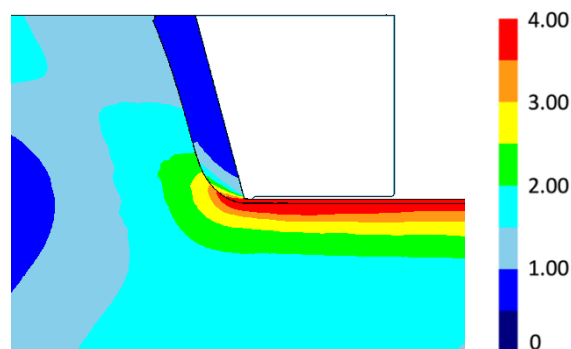


Fig. 6. The effective strain color levels for the temperature mode No. 4

Рис. 6. Цветовые уровни эффективной деформации для температурного режима № 4

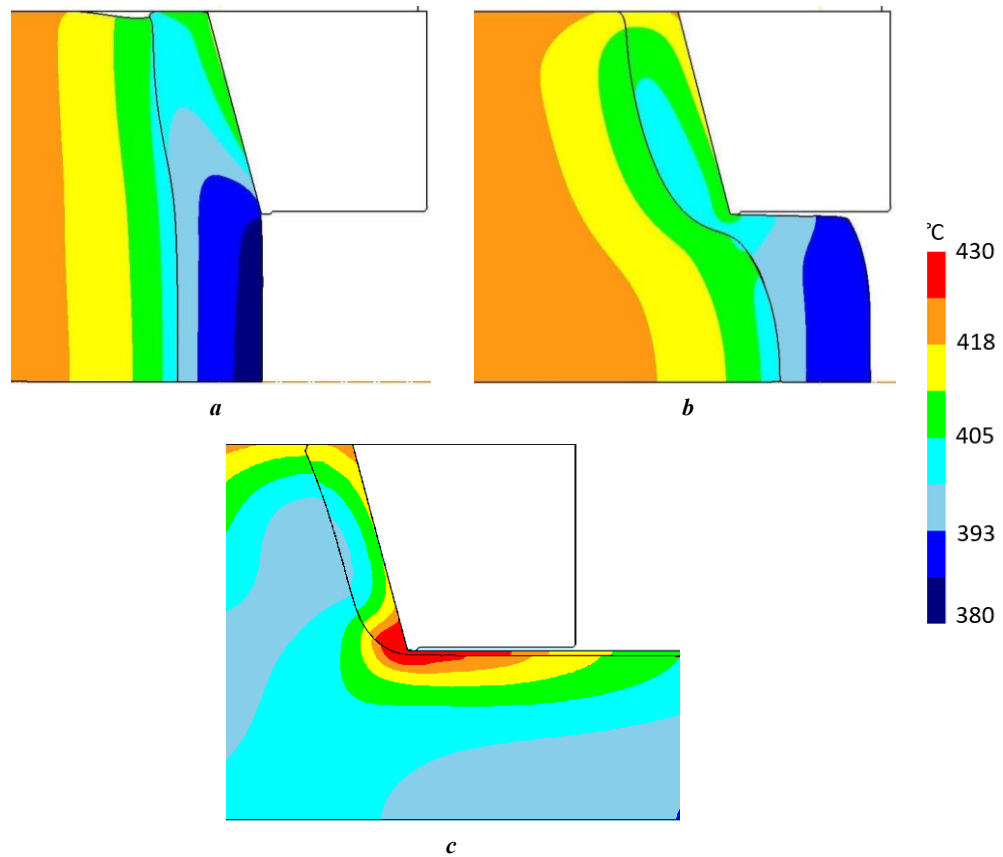


Fig. 7. Temperature field during the extrusion process, °C:
a – pressing out stage; *b* – beginning of extrusion; *c* – steady state stage

Рис. 7. Температурное поле по ходу процесса прессования, °C:
a – стадия распрессовки; *b* – начало прессования; *c* – стационарная стадия

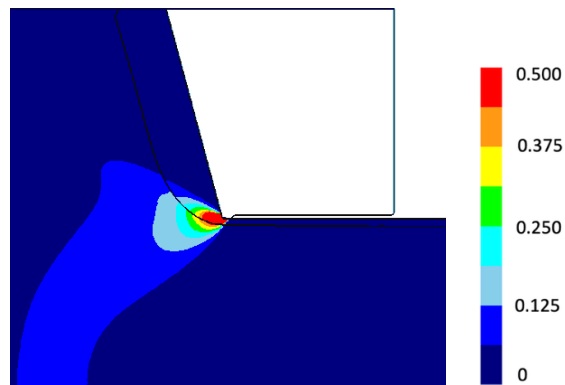


Fig. 8. Color levels of effective strain rate for the temperature mode No. 4, ξ , c^{-1}

Рис. 8. Цветовые уровни эффективной скорости деформации для температурного режима № 4, ξ , c^{-1}

made of a 6000 series aluminum alloy using an additional rear workpiece made of a less expensive alloy in order to reduce the loss of the base metal was considered. Three temperature modes for implementing the extrusion process were studied. It was found that the optimal mode is the one without heating the pressing disk and the additional workpiece. This confirms the result obtained in the course of the current study,

where it was found that it is possible to implement the technology of extruding a composite rod without heating the additional workpiece.

The implementation of the analogous composite rod production technology in [21] utilized a hot extrusion process wherein both workpieces were heated to a temperature of 380 °C. The technology proposed in this work implies the possibility of using process waste in

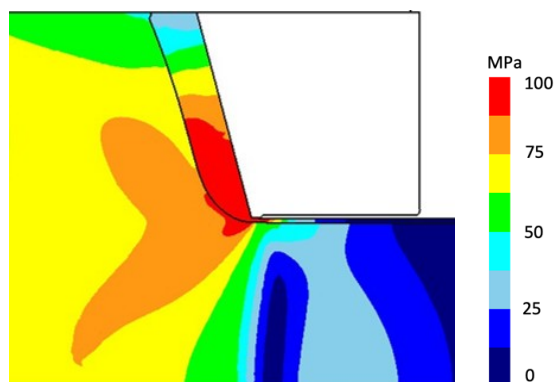


Fig. 9. Color levels of effective stresses for the temperature mode No. 4, $\sigma_{\text{effective}}$, MPa

Рис. 9. Цветовые уровни эффективных напряжений для температурного режима № 4, $\sigma_{\text{effective}}$ МПа

the form of extrusion discard as an additional front workpiece, which is intended to reduce losses of the base metal.

The feasibility of the technology was assessed through numerical simulation of the direct and inverted extrusion processes for a large-sized rod. The model incorporated a softer aluminum alloy as an additional workpiece. Using the tracing point function, a comparative study of the flow rates of the materials of the main and additional workpieces during plastic deformation was performed. For both extrusion options, graphical dependencies of the cladding layer thickness on the length of the rod extruded part were constructed. It was found that the direct extrusion method is preferable for solving the problem of producing a bimetallic rod. Experimental modeling of the extrusion process on model materials was carried out. As a result, a bimetallic rod with a thin cladding layer was produced.

At the same time, a defect of local delamination of the additional workpiece material after exiting the matrix extrusion die parallel land was detected. In the study conducted within this work, the effect of peeling of the cladding layer material is not observed.

The study's key task was to develop resource-saving recommendations for setting experimental conditions. This was essential because running the experiment on the targeted industrial equipment would have been prohibitively expensive.

The verification of the obtained data is substantiated in the literature. For example, the reference manual⁴ presents hardening curves for pure aluminum for various types of tests. The values of effective stresses vary in the range of 50–100 MPa depending on the state of the material for which the curves are given. In the course of solving the problem in DEFORM, the distribution of effective stresses shown in Fig. 9 was obtained.

As can be seen from the figure, no abnormal growth of stresses in the deformation zone is observed, therefore, it can be concluded that the extrapolation of stress values for the materials under consideration (Fig. 2) in the course of solving the problem occurs correctly.

⁴ Burkin S.P., Babaylov N.A., Ovsyannikov B.V. *Soprotivlenie deformatsii splavov Al i Mg [Resistance of deformation of Al and Mg alloys]*. Ekaterinburg, UrFU Publ, 2010. 344 p.

CONCLUSIONS

The study allowed predicting the possibility of implementing the developed technology for producing bimetallic rods from high-strength 7075 alloy with a cladding layer of 1100 aluminum by direct extrusion using an additional front workpiece. The optimal extrusion temperature mode was identified, which makes it possible to produce a rod with a thin uniform cladding layer, amounting to 1.38 % of the diameter of the final rod. For this mode, the heating temperature of 7075 alloy is 360 °C, and the temperature of pure aluminum is 20 °C.

REFERENCES

1. Elagin V.I. Ways of developing high-strength and high-temperature structural aluminum alloys in the 21st century. *Metal Science and Heat Treatment*, 2007, vol. 49, no. 9-10, pp. 427–434. DOI: [10.1007/s11041-007-0081-y](https://doi.org/10.1007/s11041-007-0081-y).
2. Parveez B., Kittur M.I., Badruddin I.A., Kamangar S., Hussien M., Umarfarooq M.A. Scientific advancements in composite materials for aircraft applications: a review. *Polymers*, 2022, vol. 14, no. 22, article number 5007. DOI: [10.3390/polym14225007](https://doi.org/10.3390/polym14225007).
3. Lei Kong. Computer Simulation Study on the Relationship between the Tensile Fracture Behavior of Aircraft Composites and the Fiber Strength Distribution. *2022 6th International Conference on Intelligent Computing and Control Systems (ICICCS)*, 2022, pp. 664–667. DOI: [10.1109/ICICCS53718.2022.9788372](https://doi.org/10.1109/ICICCS53718.2022.9788372).
4. Dzakyprasetyo R.Q., Anawati A. Corrosion Behaviour of Aluminum Alloy AA7075-T651. *IOP Conference Series: Materials Science and Engineering*, 2019, vol. 541, article number 012006. DOI: [10.1088/1757-899X/541/1/012006](https://doi.org/10.1088/1757-899X/541/1/012006).
5. Raza S.A., Karim M.R.A., Shehbaz T., Taimoor A.A., Ali R., Khan M.I. Effect of pH and Concentration on Electrochemical Corrosion Behavior of Aluminum Al-7075 T6 Alloy in NaCl Aqueous Environment. *Journal of Electrochemical Science and Technology*, 2022, vol. 13, no. 2, pp. 213–226. DOI: [10.33961/jecst.2020.01214](https://doi.org/10.33961/jecst.2020.01214).
6. Wang Junlei, Xiong Fuping, Liu Hongwei, Zhang Tiansui, Li Yanyan, Li Chenjing, Xia Wu, Wang Haitao, Liu

- Hongfang. Study of the corrosion behavior of *Aspergillus niger* on 7075-T6 aluminum alloy in a high salinity environment. *Bioelectrochemistry*, 2019, vol. 129, pp. 10–17. DOI: [10.1016/j.bioelechem.2019.04.020](https://doi.org/10.1016/j.bioelechem.2019.04.020).
7. Feng Zhiyuan, Li Jiao, Ma Jincai, Su Yongjin, Zheng Xiaoyuan, Mao Yu, Zhao Zilong. EBSD Characterization of 7075 Aluminum Alloy and Its Corrosion Behaviors in SRB Marine Environment. *Journal of Marine Science and Engineering*, 2022, vol. 10, no. 6, article number 740. DOI: [10.3390/jmse10060740](https://doi.org/10.3390/jmse10060740).
8. Rajamuthamilselvan M., Ramanathan S. Hot deformation behaviour of 7075 alloy. *Journal of Alloys and Compounds*, 2011, vol. 509, no. 3, pp. 948–952. DOI: [10.1016/j.jallcom.2010.09.139](https://doi.org/10.1016/j.jallcom.2010.09.139).
9. Whalen S., Reza-E-Rabby Md., Wang Tianhao, Ma Xiaplong, Roosendaal T., Herling D., Overman N., Taysom B. Shear Assisted Processing and Extrusion of Aluminum Alloy 7075 Tubing at High Speed. *The Minerals, Metals & Materials Series*, 2021, vol. 6, pp. 277–280. DOI: [10.1007/978-3-030-65396-5_41](https://doi.org/10.1007/978-3-030-65396-5_41).
10. Whalen S., Olszta M., Reza-E-Rabby Md., Roosendaal T., Wang Tianhao, Herling D., Taysom B.S., Suffield S., Overman N. High speed manufacturing of aluminum alloy 7075 tubing by Shear Assisted Processing and Extrusion (ShAPE). *Journal of Manufacturing Processes*, 2021, vol. 71, pp. 699–710. DOI: [10.1016/j.jmapro.2021.10.003](https://doi.org/10.1016/j.jmapro.2021.10.003).
11. Pustovoytov D.O., Pesin A.M., Sverdlik M.K. Mathematical simulation of grain evolution during asymmetric rolling of pure aluminum and 7075 alloy. *Vestnik of Novosibirsk State Technical University*, 2015, no. 4, pp. 81–88. EDN: [VAUJJP](https://www.edn.ru/VAUJJP).
12. Pustovoytov D.O., Pesin A.M., Vafin R.K. Simulation of temperature fields in a deformation zone during asymmetric rolling of aluminum alloys. *Vestnik of Novosibirsk State Technical University*, 2015, no. 4, pp. 75–81. EDN: [VAUJJE](https://www.edn.ru/VAUJJE).
13. Karthikraja M., Ramanathan K., Loganathan K.T., Selvaraj S. Corrosion behaviour of SiC and Al₂O₃ reinforced Al 7075 hybrid aluminium matrix composites by weight loss and electrochemical methods. *Journal of the Indian Chemical Society*, 2023, vol. 100, no. 5, article number 101002. DOI: [10.1016/j.jics.2023.101002](https://doi.org/10.1016/j.jics.2023.101002).
14. Khalid M.Y., Umer R., Khan K.A. Review of recent trends and developments in aluminium 7075 alloys and metal matrix composites (MMCs) for aircraft applications. *Results in Engineering*, 2023, vol. 20, article number 101372. DOI: [10.1016/j.rineng.2023.101372](https://doi.org/10.1016/j.rineng.2023.101372).
15. Stelt A.A., Bor T.C., Geijselaers H.J.M., Akkerman R., Boogaard A.H. Cladding of Advanced Al Alloys Employing Friction Stir Welding. *Key Engineering Materials*, 2013, vol. 554–557, pp. 1014–1021. DOI: [10.4028/www.scientific.net/KEM.554-557.1014](https://doi.org/10.4028/www.scientific.net/KEM.554-557.1014).
16. Otsubo F., Era H. Cladding of Al Layer onto Mild Steel Substrate Using Al Powder and Its Structure and Properties. *Materials Transactions*, 2018, vol. 59, no. 10, pp. 1585–1590. DOI: [10.2320/matertrans.P-M2018835](https://doi.org/10.2320/matertrans.P-M2018835).
17. Hou Jiapeng, Chen Qingyin, Wang Qiang, Yu Hongyun, Zhang Zhenjun, Li Rui, Li Xiaowu, Zhang Zhefeng. Interface Characterization and Performances of a Novel Pure Al Clad Al Alloy Wire. *Advanced Engineering Materials*, 2018, vol. 20, no. 8, article number 1800082. DOI: [10.1002/adem.201800082](https://doi.org/10.1002/adem.201800082).
18. Loginov Yu.N., Zagirov N.N., Ivanov E.V. Energy efficiency of processing of chips from aluminum and its alloys without the use of remelting. *Technology of light alloys*, 2023, no. 4, pp. 66–72. DOI: [10.24412/0321-4664-2023-4-66-72](https://doi.org/10.24412/0321-4664-2023-4-66-72).
19. Deryabin A.Yu., Kargin V.R. Final stage modeling of large-size bars extrusion by low stretch ratio while creation of central back-end extrusion defect. *Izvestiya of Samara Scientific Center of the Russian Academy of Sciences*, 2018, vol. 20, no. 1, pp. 5–10. EDN: [OUSTNP](https://www.edn.ru/OUSTNP).
20. Loginov Yu.N., Razinkin A.V., Shimov G.V., Bushueva N.I. Aluminum alloy extrusion scheme and model with reduction of basis metal waste. *Non-ferrous metals*, 2023, no. 11, pp. 83–88. DOI: [10.17580/tsm.2023.11.11](https://doi.org/10.17580/tsm.2023.11.11).
21. Bushueva N.I., Loginov Yu.N., Shimov G.V. Pressing of clad rods from aluminum alloys using a front deformable washer. *Non-ferrous metals*, 2024, no. 7, pp. 89–95. DOI: [10.17580/tsm.2024.07.12](https://doi.org/10.17580/tsm.2024.07.12).

СПИСОК ЛИТЕРАТУРЫ

1. Елагин В.И. Пути развития высокопрочных и жаропрочных конструкционных алюминиевых сплавов в XXI столетии // *Металловедение и термическая обработка металлов*. 2007. № 9. С. 3–11. EDN: [KVXJZB](https://www.edn.ru/KVXJZB).
2. Parveez B., Kittur M.I., Badruddin I.A., Kamangar S., Hussien M., Umarfarooq M.A. Scientific advancements in composite materials for aircraft applications: a review // *Polymers*. 2022. Vol. 14. № 22. Article number 5007. DOI: [10.3390/polym14225007](https://doi.org/10.3390/polym14225007).
3. Lei Kong. Computer Simulation Study on the Relationship between the Tensile Fracture Behavior of Aircraft Composites and the Fiber Strength Distribution // 2022 6th International Conference on Intelligent Computing and Control Systems (ICICCS). 2022. P. 664–667. DOI: [10.1109/ICICCS53718.2022.9788372](https://doi.org/10.1109/ICICCS53718.2022.9788372).
4. Dzakyprasetyo R.Q., Anawati A. Corrosion Behaviour of Aluminum Alloy AA7075-T651 // *IOP Conference Series: Materials Science and Engineering*. 2019. Vol. 541. Article number 012006. DOI: [10.1088/1757-899X/541/1/012006](https://doi.org/10.1088/1757-899X/541/1/012006).
5. Raza S.A., Karim M.R.A., Shehbaz T., Taimoor A.A., Ali R., Khan M.I. Effect of pH and Concentration on Electrochemical Corrosion Behavior of Aluminum Al-7075 T6 Alloy in NaCl Aqueous Environment // *Journal of Electrochemical Science and Technology*. 2022. Vol. 13. № 2. P. 213–226. DOI: [10.33961/jecst.2020.01214](https://doi.org/10.33961/jecst.2020.01214).
6. Wang Junlei, Xiong Fuping, Liu Hongwei, Zhang Tiansui, Li Yanyan, Li Chenjing, Xia Wu, Wang Haitao, Liu Hongfang. Study of the corrosion behavior of *Aspergillus niger* on 7075-T6 aluminum alloy in a high salinity environment // *Bioelectrochemistry*. 2019. Vol. 129. P. 10–17. DOI: [10.1016/j.bioelechem.2019.04.020](https://doi.org/10.1016/j.bioelechem.2019.04.020).
7. Feng Zhiyuan, Li Jiao, Ma Jincai, Su Yongjin, Zheng Xiaoyuan, Mao Yu, Zhao Zilong. EBSD Characterization of 7075 Aluminum Alloy and Its Corrosion Behaviors in SRB Marine Environment // *Journal of Marine Science and Engineering*. 2022. Vol. 10. № 6. Article number 740. DOI: [10.3390/jmse10060740](https://doi.org/10.3390/jmse10060740).

8. Rajamuthamilselvan M., Ramanathan S. Hot deformation behaviour of 7075 alloy // *Journal of Alloys and Compounds*. 2011. Vol. 509. № 3. P. 948–952. DOI: [10.1016/j.jallcom.2010.09.139](https://doi.org/10.1016/j.jallcom.2010.09.139).
9. Whalen S., Reza-E-Rabby Md., Wang Tianhao, Ma Xiaplong, Roosendaal T., Herling D., Overman N., Taysom B. Shear Assisted Processing and Extrusion of Aluminum Alloy 7075 Tubing at High Speed // *The Minerals, Metals & Materials Series*. 2021. Vol. 6. P. 277–280. DOI: [10.1007/978-3-030-65396-5_41](https://doi.org/10.1007/978-3-030-65396-5_41).
10. Whalen S., Olszta M., Reza-E-Rabby Md., Roosendaal T., Wang Tianhao, Herling D., Taysom B.S., Suffield S., Overman N. High speed manufacturing of aluminum alloy 7075 tubing by Shear Assisted Processing and Extrusion (ShAPE) // *Journal of Manufacturing Processes*. 2021. Vol. 71. P. 699–710. DOI: [10.1016/j.jmapro.2021.10.003](https://doi.org/10.1016/j.jmapro.2021.10.003).
11. Пустовойтов Д.О., Песин А.М., Свердлик М.К. Математическое моделирование эволюции зерна при асимметричной прокатке чистого алюминия и сплава 7075 // *Вестник Магнитогорского государственного технического университета им. Г.И. Носова*. 2015. № 4. С. 81–87. EDN: [VAUJJP](https://elibrary.ru/vaujup).
12. Пустовойтов Д.О., Песин А.М., Вафин Р.К. Моделирование температурных полей в очаге деформации при асимметричной прокатке алюминиевых сплавов // *Вестник Магнитогорского государственного технического университета им. Г.И. Носова*. 2015. № 4. С. 75–81. EDN: [VAUJJE](https://elibrary.ru/vaujje).
13. Karthikraja M., Ramanathan K., Loganathan K.T., Selvaraj S. Corrosion behaviour of SiC and Al₂O₃ reinforced Al 7075 hybrid aluminium matrix composites by weight loss and electrochemical methods // *Journal of the Indian Chemical Society*. 2023. Vol. 100. № 5. Article number 101002. DOI: [10.1016/j.jics.2023.101002](https://doi.org/10.1016/j.jics.2023.101002).
14. Khalid M.Y., Umer R., Khan K.A. Review of recent trends and developments in aluminium 7075 alloys and metal matrix composites (MMCs) for aircraft applications // *Results in Engineering*. 2023. Vol. 20. Article number 101372. DOI: [10.1016/j.rineng.2023.101372](https://doi.org/10.1016/j.rineng.2023.101372).
15. Stelt A.A., Bor T.C., Geijselaers H.J.M., Akkerman R., Boogaard A.H. Cladding of Advanced Al Alloys Employing Friction Stir Welding // *Key Engineering Materials*. 2013. Vol. 554–557. P. 1014–1021. DOI: [10.4028/www.scientific.net/KEM.554-557.1014](https://doi.org/10.4028/www.scientific.net/KEM.554-557.1014).
16. Otsubo F., Era H. Cladding of Al Layer onto Mild Steel Substrate Using Al Powder and Its Structure and Properties // *Materials Transactions*. 2018. Vol. 59. № 10. P. 1585–1590. DOI: [10.2320/matertrans.P-M2018835](https://doi.org/10.2320/matertrans.P-M2018835).
17. Hou Jiapeng, Chen Qingyin, Wang Qiang, Yu Hongyun, Zhang Zhenjun, Li Rui, Li Xiaowu, Zhang Zhefeng. Interface Characterization and Performances of a Novel Pure Al Clad Al Alloy Wire // *Advanced Engineering Materials*. 2018. Vol. 20. № 8. Article number 1800082. DOI: [10.1002/adem.201800082](https://doi.org/10.1002/adem.201800082).
18. Логинов Ю.Н., Загиров Н.Н., Иванов Е.В. Энергоэффективность переработки стружки из алюминия и его сплавов без применения переплава // *Технология легких сплавов*. 2023. № 4. С. 66–72. DOI: [10.24412/0321-4664-2023-4-66-72](https://doi.org/10.24412/0321-4664-2023-4-66-72).
19. Дерябин А.Ю., Каргин В.Р. Моделирование заключительной стадии прессования крупногабаритных прутков при малых вытяжках в момент образования центральной пресс-утяжины // *Известия Самарского научного центра Российской академии наук*. 2018. Т. 20. № 1. С. 5–10. EDN: [OUSTNP](https://elibrary.ru/oustnp).
20. Логинов Ю.Н., Разинкин А.В., Шимов Г.В., Бушуева Н.И. Схема и модель прессования алюминиевого сплава с уменьшением потерь основного металла // *Цветные металлы*. 2023. № 11. С. 83–88. DOI: [10.17580/tsm.2023.11.11](https://doi.org/10.17580/tsm.2023.11.11).
21. Бушуева Н.И., Логинов Ю.Н., Шимов Г.В. Прессование плакированных прутков из алюминиевых сплавов с применением передней деформируемой шайбы // *Цветные металлы*. 2024. № 7. С. 89–95. DOI: [10.17580/tsm.2024.07.12](https://doi.org/10.17580/tsm.2024.07.12).

УДК 669.715

doi: 10.18323/2782-4039-2025-3-73-2

Схема получения композиционного материала на основе конструкционного алюминиевого сплава методом прямого прессования

Бушуева Наталья Игоревна^{*1}, аспирант,

инженер-исследователь научной лаборатории «Обработка металлов давлением»

Логинов Юрий Николаевич², доктор технических наук,

профессор кафедры обработки металлов давлением

*Уральский федеральный университет имени первого Президента России Б.Н. Ельцина, Екатеринбург (Россия)**E-mail: n.i.bushueva@urfu.ru¹ORCID: <https://orcid.org/0000-0002-0603-8785>²ORCID: <https://orcid.org/0000-0002-7222-2521>

Поступила в редакцию 30.06.2025

Пересмотрена 19.08.2025

Принята к публикации 01.09.2025

Аннотация: Исследование посвящено разработке технологии получения биметаллического прутка из высокопрочного сплава 7075 с плакирующим слоем из алюминия 1100, которая направлена на улучшение коррозионной стойкости при сохранении механических свойств. Особенностью предложенной технологии является применение дополнительной передней заготовки из чистого алюминия для процесса прямого прессования прутка из сплава

7075. Проведено численное моделирование процесса прямого прессования композитной заготовки в программном комплексе DEFORM с использованием метода конечных элементов. Проведен анализ влияния температурно-скоростных условий процесса на формирование плакирующего слоя. Для этого была выполнена постановка четырех задач с варьированием режимов нагрева заготовок и инструментов. Установлено, что получить тонкий плакирующий слой удастся при температуре нагрева основного сплава 7075, равной 360 °С, и температуре плакирующего слоя, равной 20 °С, что обеспечивает равномерное распределение покрытия по длине прутка без признаков расслоения. Анализ напряженно-деформированного состояния материалов в ходе прессования показал, что вариант использования дополнительной заготовки в холодном состоянии позволяет сохранять достаточную сплошность для формирования непрерывного плакирующего покрытия, в то время как нагрев до 300 °С и выше приводит к его разрыву из-за локализации деформации. Разработанный подход может быть использован для снижения себестоимости изделий за счет уменьшения расхода дорогостоящего сплава 7075 при одновременном повышении коррозионной стойкости за счет применения плакировки из чистого алюминия. Перспективы развития дальнейших исследований связаны с оптимизацией режимов прессования для различных типоразмеров прутков.

Ключевые слова: прессование; метод конечных элементов; композиционные материалы; алюминиевый сплав 7075; плакирующий слой.

Благодарности: Статья подготовлена по материалам докладов участников XII Международной школы «Физическое материаловедение» (ШФМ-2025), Тольятти, 15–19 сентября 2025 года.

Для цитирования: Бушуева Н.И., Логинов Ю.Н. Схема получения композиционного материала на основе конструкционного алюминиевого сплава методом прямого прессования // Frontier Materials & Technologies. 2025. № 3. С. 27–37. DOI: 10.18323/2782-4039-2025-3-73-2.

The Publishing Center (until November 1, 2011 – the Editorial and Publishing Center) is a structural subdivision of Togliatti State University, which takes an important place in providing the educational process with high-quality instructional, educational, methodological, and scientific literature.

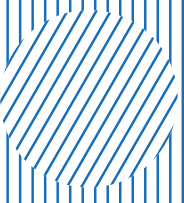
TSU Publishing Center today

- Publishing center includes an editorial office and a printing shop. In recent years, the base of computer equipment, printing and post-printing equipment has been almost completely updated.
- It publishes books and electronic textbooks for students, graduate students, lecturers, and specialists in almost all branches of modern scientific knowledge, as well as popular science and reference literature, fiction, books of reports (papers) of conferences. Published literature corresponds to all areas of the educational cycles of the university disciplines.
- A considerable volume of printing job is the prompt execution of promotional and information products.
- The publishing center team is a collaboration of highly skilled professionals with wide work experience and young motivated employees.
- Publishing center employees participate in practical seminars to become acquainted with new opportunities in the field of printing technologies and equipment, as well as with advanced materials for digital printing.

Main areas of activity

- Publication of paper-based educational and scientific literature, production of electronic educational and scientific aids.
- Implementation of editorial and publishing cycle stages: editing, production of original layouts, replication, pre-printing and post-printing treatment.
- Methodological and advisory work with the university departments on the issue of educational and scientific publications.
- Interaction with the Russian Book Chamber on the assignment of ISBNs to publications issued by Togliatti State University.
- Preparation of publications issued by Togliatti State University for state registration and sending of statutory copies.
- Markup of papers published in the TSU journals in the Articulus program to place on the eLibrary platform.

Main achievements

- The results of the work were awarded with diplomas of the winners of the annual interregional and all-Russian University Book competitions.
 - Publishing center regularly participates in the academic book exhibition of publishing activities “University – Science – City”.
- 

Study of rigidity and frequency response of an end mill on a vertical milling centre

Roman D. Voronov*, teacher of Chair “Equipment and Technologies of Machinery Production”

Dmitry A. Rastorguev¹, PhD (Engineering), Associate Professor,
assistant professor of Chair “Equipment and Technologies of Machinery Production”

Denis G. Levashkin², PhD (Engineering), Associate Professor,
assistant professor of Chair “Equipment and Technologies of Machinery Production”

Togliatti State University, Togliatti (Russia)

*E-mail: smr.rom@yandex.ru

¹ORCID: <https://orcid.org/0000-0001-6298-1068>

²ORCID: <https://orcid.org/0009-0007-2704-4635>

Received 21.04.2025

Revised 11.08.2025

Accepted 04.09.2025

Abstract: The study covers the problem of early elimination of tool resonant vibrations through preliminary mathematical modelling. In particular, the problem is considered for the case of milling with an end mill on a vertical milling centre. The paper presents processed experimental data and results of mathematical modelling containing information on the rigidity of the FKC 4257 mill, its natural frequencies on the spectrum and vibration modes. The constructed finite element mathematical model covers the mill itself, the gripping collet and the collet chuck attachment. The model describes the static rigidity of the mill with an error of 2.2 %, and the position of its natural frequencies on the spectrum – with an error of about 7 % relative to the experimental results. By constructing the amplitude-frequency characteristic and conducting a modal analysis, it is shown that the first two vibration modes (80 and 112 Hz) are the most critical for the mill, both in terms of the amplitude of vibrations and in terms of their shape. The vibration shapes in the first modes are bending. During the modal analysis, the vibration shapes in the remaining modes are considered and estimated. To improve the convergence of the frequency analysis results, it is proposed to introduce the coefficient $K_{k1}=0.9$, which takes into account the lower rigidity of a real mill in comparison with an idealized mathematical model, when applying which the convergence is improved to 2.5 %. Thanks to the applied technique, it is possible to obtain reliable data on the frequency zones of instability used in practice to avoid resonance phenomena. In the future, based on such data, taking into account the correction factors, it is possible to train neural network models predicting the tool response under specific processing conditions and solving the inverse problem of selecting rational tool geometry for specific tasks.

Keywords: end mill; rigidity; modal analysis; frequency analysis; mathematical modelling; amplitude-frequency characteristic; resonance.

Acknowledgments: The study was carried out within the state contract for R&D No. 125011300177-8.

For citation: Voronov R.D., Rastorguev D.A., Levashkin D.G. Study of rigidity and frequency response of an end mill on a vertical milling centre. *Frontier Materials & Technologies*, 2025, no. 3, pp. 39–49. DOI: 10.18323/2782-4039-2025-3-73-3.

INTRODUCTION

During milling with end mills on large-sized high-rigidity milling machines, the limiting elastic deformations are the release of the cutting tool itself, its vibrations with a certain amplitude and frequency [1; 2]. In cases when the frequencies of these vibrations do not resonate with the frequencies of other components of the “machine – fixture – tool – part” system (hereinafter referred to as MFTP), there is only a deviation from the specified shaping [3; 4] to one degree or another, i.e. a decrease in the processing accuracy [5; 6]. However, it is widely known that when resonance phenomena occur during milling, vibrations of increased amplitude occur, which can lead to accelerated wear [7], tool breakage [8; 9] due to fatigue failure and microchipping of its cutting edges, as well as to failure of spindle bearings and other machine components [10; 11]. It should be noted that

the above-mentioned negative consequences of the mill operation in the resonant or near-resonant frequency range are visible both when milling difficult-to-machine materials along complex spatial curved trajectories and when processing relatively pliable materials along simple flat trajectories. In particular, this is expressed in the unsatisfactory quality of the machined surfaces and the discrepancy between the obtained dimensions and shapes of the part and the initial machining tolerances [12].

In this regard, the ability to abstract from the resonant frequency zones in advance remains relevant for mechanical machining; for this purpose, the vibration component of the machining is often analyzed and the frequency response of the mills are constructed [13; 14]. To solve this problem, both empirical methods [15; 16], based on the readings of eddy current sensors, and mathematical modelling, including the finite element

analysis method [17; 18], are widely used. Moreover, to reduce and prevent the influence of tool vibrations, the results of modal analysis [19; 20] can be used, which provides an idea of the vibration forms [21] on the frequency spectrum.

The great majority of studies of cutting tools, in particular end mills, do not contain comprehensive consideration of the object in terms of both modal and frequency analyses and, as a result, no corresponding mathematical models with confirmed convergence are presented. Among the studies provided, when considering end mills, there are estimates of both the modes and amplitudes of vibrations on the frequency range, but separately from each other. Consequently, it is difficult to make an unambiguous conclusion about the criticality of a particular tool vibration frequency for milling. Therefore, an approach is required that combines an assessment by both the amplitude criterion and the vibration mode criterion.

The purpose of this study is to develop and test a method for end-to-end mathematical modelling, including static, modal and frequency analyses, using the example of the FKC 4257 mill installed on the MILLSTAR LMV 800 vertical milling centre; in this case, the modelling results should correlate with the experimental data.

METHODS

The end mill – collet chuck pair consisting of an FKC 4257 end mill with a diameter of 10 mm and a BT-40-ER32-100 collet chuck with a corresponding collet was investigated. The material of the mill is high-speed R6M5 steel. Modelling was carried out using the finite element method with Femap with NX Nastran v11. A static force of 400 N was used for static analysis and a unit force to obtain frequency responses. The MatLab package was used to process and visualize the experimental data.

The experimental part of the study includes measuring the static rigidity of the mill, as well as obtaining its frequency response. To conduct the experiment, a Z-shaped compression sensor was attached to the thread on the one side of the vertical plate fixed in a vice inside the working volume of the LMV 800 centre, and a screw was installed on the other side to load the mill. An indicator was mounted in a magnetic stand fixed to the machine spindle body. Measurements were taken using a DEP1 portable electronic dynamometer.

During this experiment, a series of measurements were carried out with different forces applied to the mill – from 50 to 400 N. Direct measurement of deformation was carried out using a strain-gauge dynamometer with displacement control by a clock-type indicator with a measurement error of 0.01 mm (right side of Fig. 1).

The natural frequencies of the end mill on the LMV 800 machine were obtained using the pulse method – by striking a dynamometric hammer with recording the response with a Bentley Nevada eddy current sensor.

As will be shown below, it is the first two vibration modes that have the largest amplitudes, as well as the most dangerous natural vibration modes. In this regard, when considering the peaks in the frequency spectrum, we will make comparisons based on the first two peaks obtained experimentally.

For the mathematical model, the conditions of fixing (boundary conditions) and loading were set according to the experiment, taking into account the materials of the bodies and the nature of their contact.

Obviously, the limiting deformations will be observed at the maximum extension of the mill from the chuck, and the chuck itself will practically not undergo deformation. In this regard, a proportional finite element mesh for various bodies was set, which allows reducing the time required for analysis.

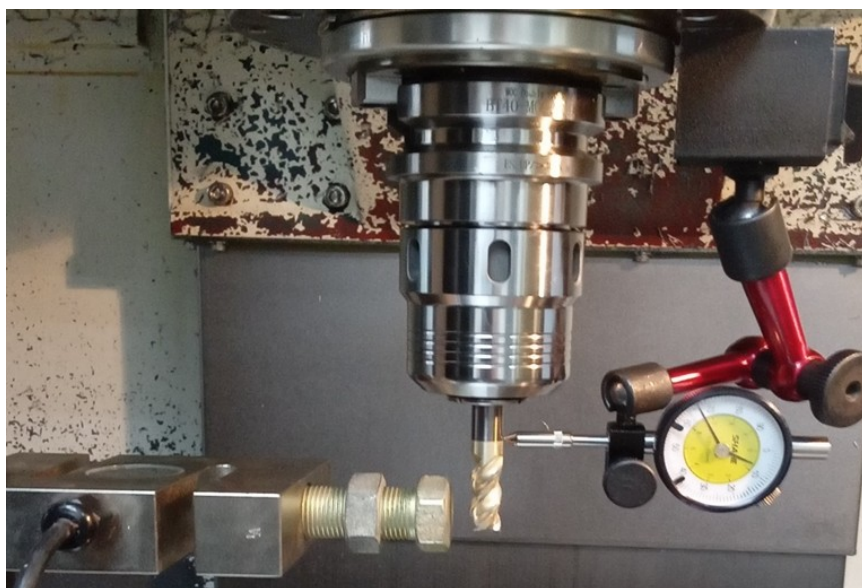


Fig. 1. General view of the experimental installation inside the machine
Рис. 1. Общий вид экспериментальной установки внутри станка

RESULTS

Since deformations occur deep in the elastic region, then, as expected, the compliance graph (Fig. 2) is a straight line with a certain coefficient responsible for its slope. Let us determine the rigidity at the measurement point (approximately 19 mm from the chuck) using the known relationship:

$$j = \frac{F}{\Delta};$$

$$j_{exp} = \frac{F}{\Delta} = \frac{400}{0.0513} \approx 7797.3 \frac{\text{N}}{\text{mm}}.$$

The vibration analyzer allowed obtaining the amplitude-frequency characteristic (hereinafter referred to as the AFC)

of the mill with pronounced peaks (Fig. 3). The first two peaks are located at frequencies of 80 and 112 Hz, respectively. The parameters that were identified during measurements in these experiments are decisive in terms of forming accuracy through elastic deformations.

As can be seen from the static calculation (Fig. 4), under a load of 400 N, the greatest displacements are about 0.2 mm at the end of the mill. It is possible to visualize more clearly the distribution of deformations along the length of the mill using a graph. The graph (Fig. 5) shows the displacements along the Z-axis (the longitudinal axis of the mill), with the zero reference point being the point of zero mill extension from the chuck (the edge of the chuck). The obtained dependence, in accordance with expectations, is close to linear.

According to the calculation results, displacements of 0.05 mm obtained experimentally were recorded at

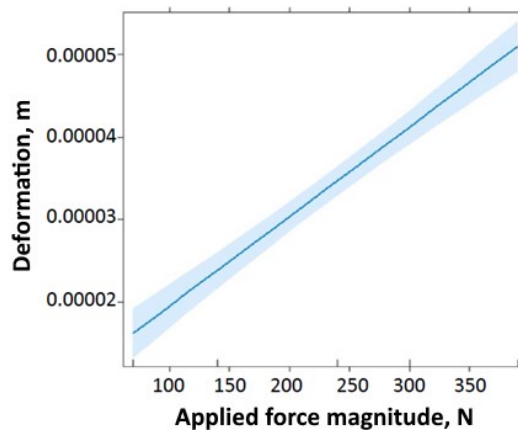


Fig. 2. Experimental graph of the dependence of deformations (m) on the applied force (N).

The highlighted area located along the graph line visualizes the 95 % confidence interval

Рис. 2. Экспериментальный график зависимости деформаций (м) от прикладываемой силы (Н).

Выделенная область, расположенная вдоль линии графика, визуализирует 95%-й доверительный интервал

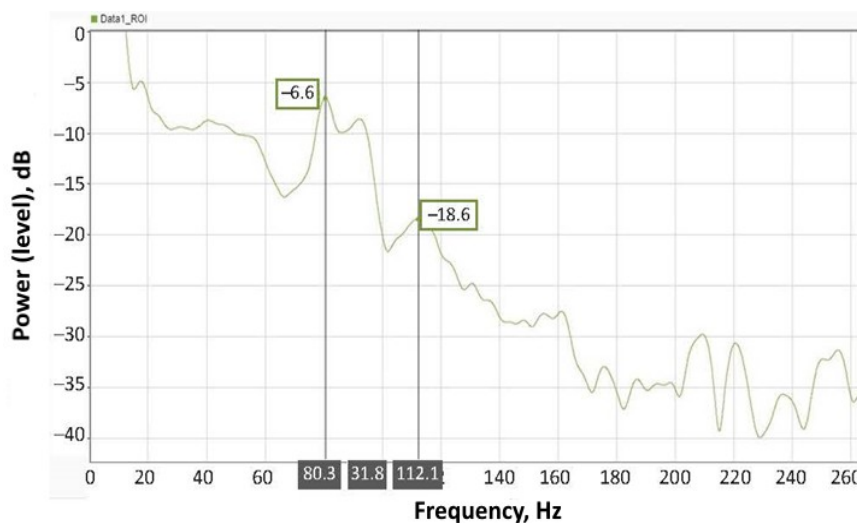


Fig. 3. The amplitude-frequency characteristic obtained experimentally with the peaks marked

Рис. 3. Амплитудно-частотная характеристика, полученная экспериментально, с отмеченными пиками

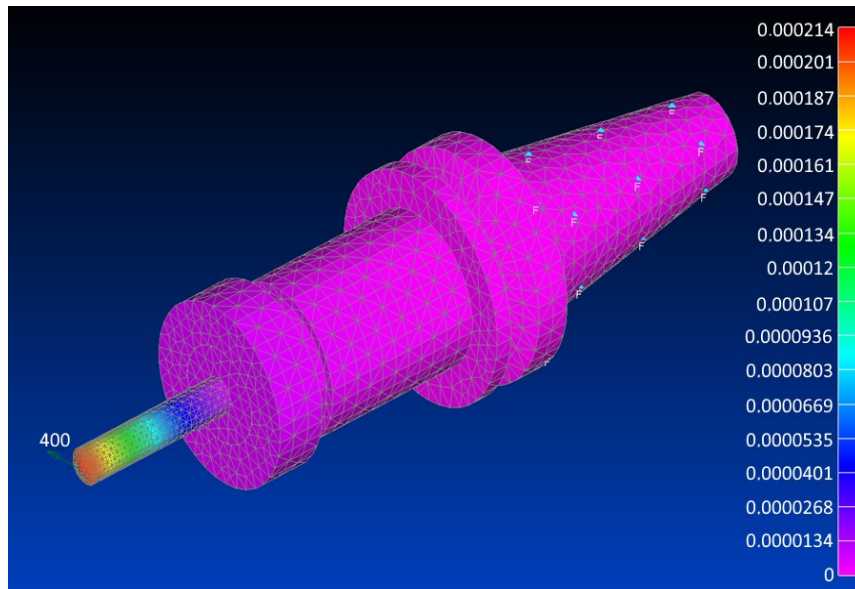


Fig. 4. Result of static calculation for rigidity
Рис. 4. Результат статического расчета на жесткость

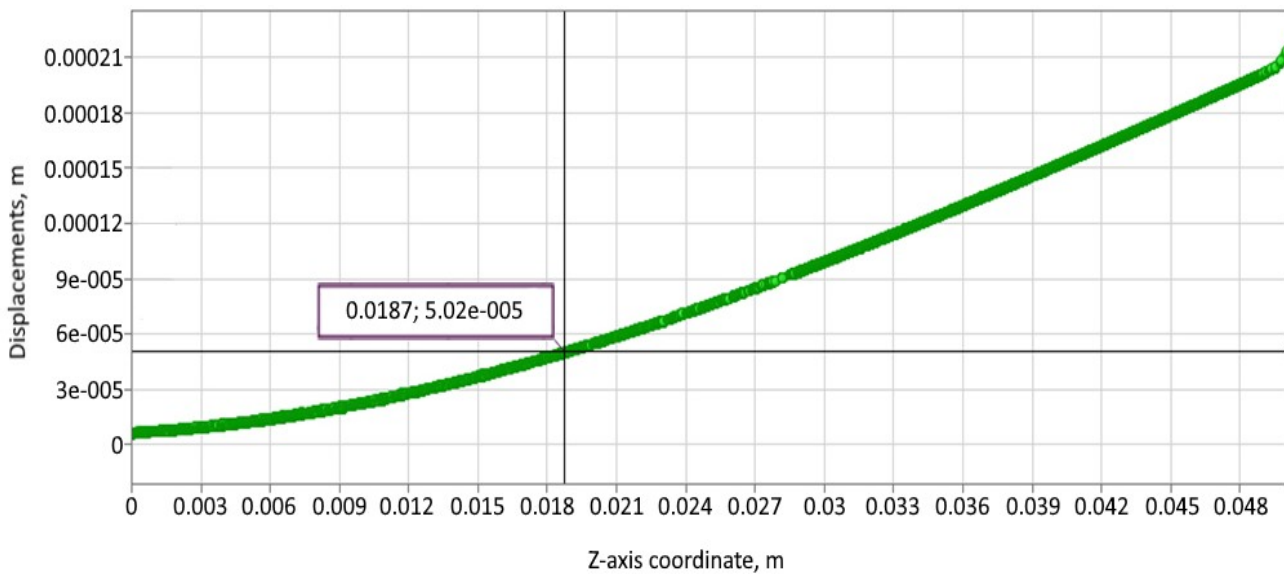


Fig. 5. Graph of the dependence of displacements on the coordinate of the mill longitudinal axis (modelling)
Рис. 5. График зависимости перемещений от координаты продольной оси фрезы (моделирование)

a distance of approximately 19 mm (Fig. 5) from the edge of the chuck (mill extension). This value coincides with the distance from the edge of the chuck to the measurement point during the experiment, which allows concluding that the created mathematical model for determining static rigidity is correct.

Then the rigidity at the measurement point is equal to

$$j_{model} = \frac{F}{\Delta} = \frac{400}{0.0502} \approx 7968 \frac{\text{N}}{\text{mm}}.$$

The obtained modelled rigidity value differs from that calculated from the experimental data by 2.2 %, which confirms the correlation.

To find the natural forms and frequencies of the structure, we will conduct a modal analysis for the same fixing conditions as in the case of a static calculation. The result of the modal analysis can be presented both as a set of modes (Fig. 6) and graphically on a frequency interval (Fig. 7), where the peaks of natural frequencies are clearly visible. On the graph (Fig. 7), the dimensionless coefficient, which does not show the amplitude of vibrations at resonant frequencies, is plotted along the ordinate axis, and the interval

Mode order number	Frequency, Hz
1	86.282
2	86.314
3	119.853
4	119.917
5	275.697
6	407.808
7	407.826
8	427.403
9	596.541
10	596.969

Fig. 6. *Vibration modes of the end mill – collet chuck pair*
Рис. 6. *Моды колебаний пары «концевая фреза – цанговый патрон»*

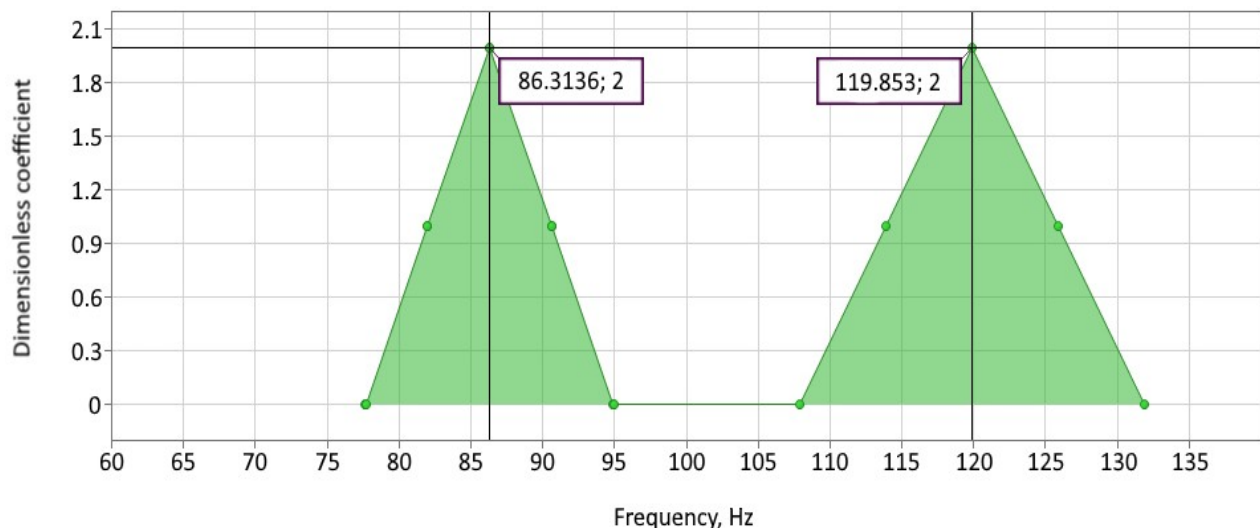


Fig. 7. *The location of the first two natural frequencies of the mill on the spectrum (modelling)*
Рис. 7. *Расположение первых двух собственных частот фрезы на спектре (моделирование)*

of the frequencies under consideration is plotted along the abscissa axis. The desired peaks are located at 86 and 120 Hz, respectively. When comparing the position of the peaks on the spectrum with the experimental data (Fig. 3), a discrepancy of approximately 6–8 Hz is noticeable.

As the modal analysis shows, in the first and second vibration modes (≈ 86 and 120 Hz), the natural form is bending, and in the instability zone there is only the mill itself, deviating from its axis to the side, which fully corresponds to the real direction of elastic deformations during milling with an end mill.

Note that modes 1 and 2, 3 and 4, 6 and 7, 9 and 10 have practically the same frequencies (Fig. 6), which is expressed graphically as a “merger” into a single peak of modes with serial numbers of 1 and 2, 3 and 4, respectively. Moreover, the natural forms of the mill at these frequencies are identical and they are bending (Fig. 8).

Therefore, we will consider such close modes as a single natural frequency.

In the fifth mode of vibrations (≈ 276 Hz), the natural form is twisting around the longitudinal axis of the mill, and the collet chuck itself is mostly in the zone of instability (Fig. 9). The next, sixth and seventh modes (≈ 408 Hz), correspond to the form of spatial bending of the entire structure around the nodes indicated by the violet-coloured zones (Fig. 10). This form of vibrations is dangerous due to the presence of an inflection, where the form of vibrations changes its direction. In this case, both the mill itself and the chuck body are still in the vibration antinode zones. The natural form in the eighth mode (≈ 427 Hz) is compressive along the longitudinal axis of the tool, covering both the tool and the collet chuck (Fig. 11). The vibration antinode in this mode is concentrated on the mill.

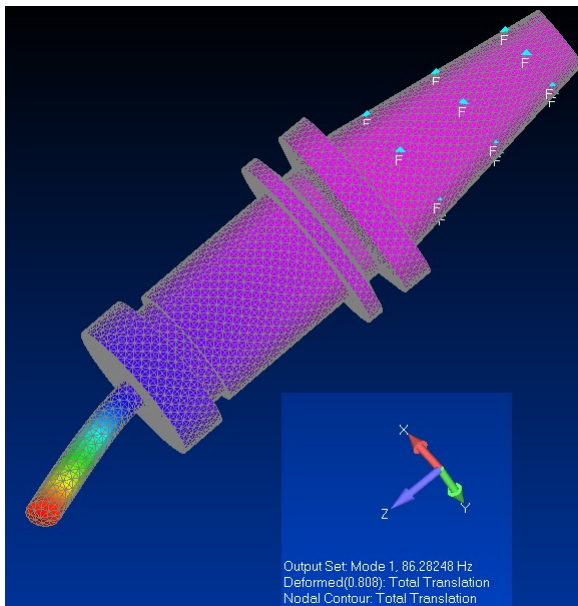


Fig. 8. *Vibration mode shape in the first mode for the case of a solid end mill*

Рис. 8. *Собственная форма колебаний на первой моде для случая цельной концевой фрезы*

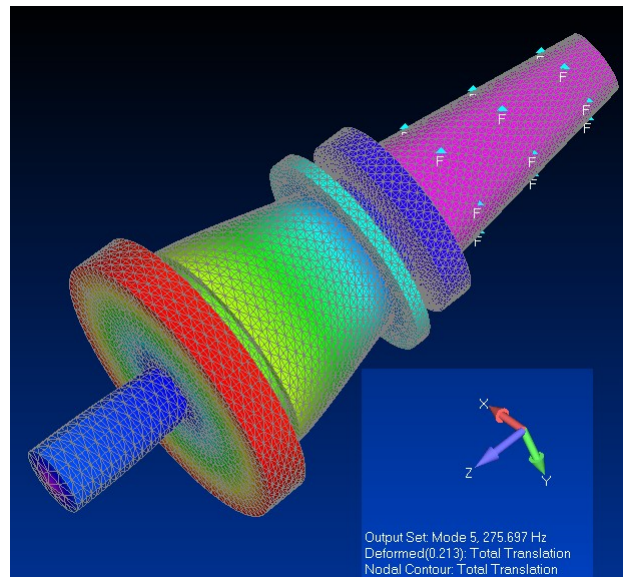


Fig. 9. *Vibration mode shape in the fifth mode for the case of a solid end mill*

Рис. 9. *Собственная форма колебаний на пятой моде для случая цельной концевой фрезы*

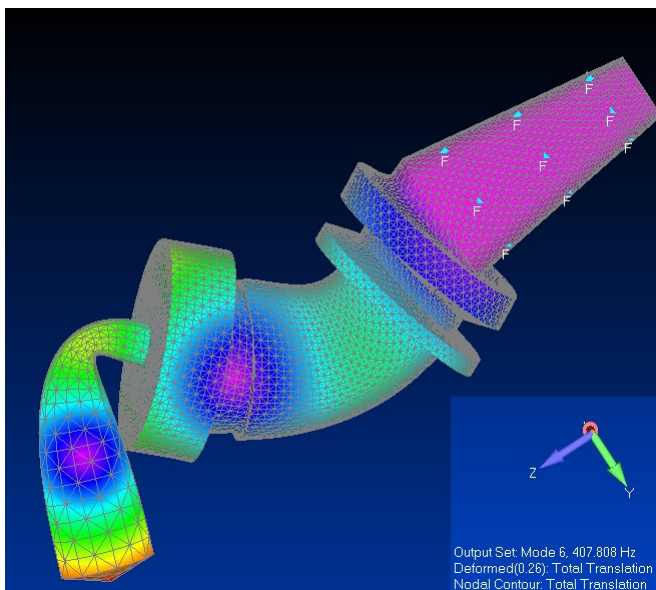


Fig. 10. *Vibration mode shape in the sixth mode for the case of a solid end mill*

Рис. 10. *Собственная форма колебаний на шестой моде для случая цельной концевой фрезы*

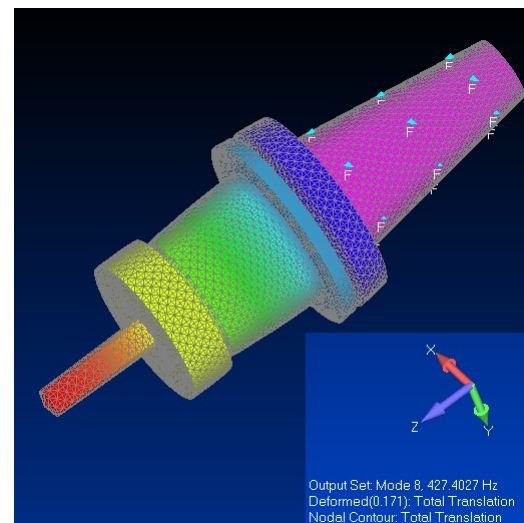


Fig. 11. *Vibration mode shape in the eighth mode for the case of a solid end mill*

Рис. 11. *Собственная форма колебаний на восьмой моде для случая цельной концевой фрезы*

The last, ninth and tenth vibration modes (≈ 596 Hz), correspond to the form of the spatial bending of the mill itself exclusively (Fig. 12), similar to the natural form in the sixth mode (Fig. 10). Here, the bend and nodes on the mill body are also traced.

Since the coefficient on the ordinate axis (Fig. 7) does not give any idea of the degree of criticality of a particular fre-

quency according to the vibration amplitude criterion, it is necessary to carry out a frequency analysis next. Frequency analysis implies taking into account the damping of the vibrating system through the damping coefficient determined experimentally. For the case of a solid end mill, the logarithmic damping decrement was 0.06 according to empirical data obtained from the graph of the transient process of vibration

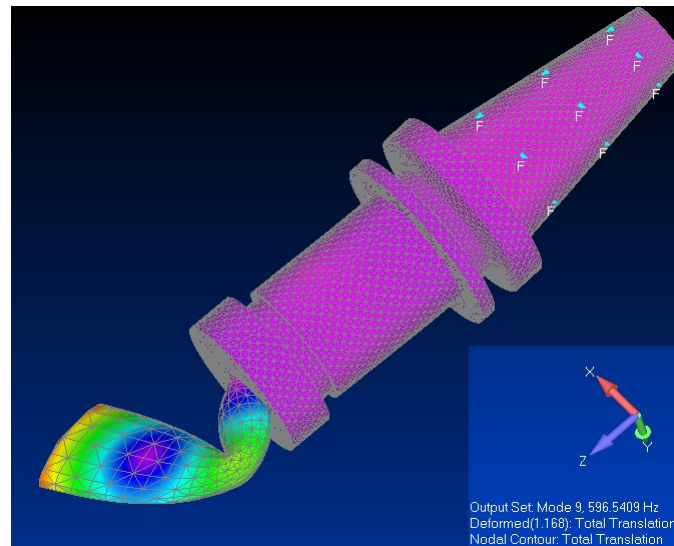


Fig. 12. *Vibration mode shape in the tenth mode for the case of a solid end mill*

Рис. 12. *Собственная форма колебаний на девятой моде для случая цельной концевой фрезы*

damping. Let us assume that this coefficient remains constant over the entire range of frequencies under consideration and is equal to the logarithmic damping decrement of vibrations.

The result of frequency analysis is the amplitude – frequency dependence in the relevant direction in space. In this case, we consider the transverse direction of the mill loading, i.e. the direction perpendicular to its axis. The frequency response (AFC) is obtained with a damping coefficient taken equal to 6 %. For a more demonstrative display of all amplitudes, we will use a logarithmic scale on the ordinate axis (Fig. 13).

According to the constructed AFC, it can be concluded that, according to the vibration amplitude criterion, the most dangerous are the first two natural frequencies of vibrations corresponding to frequencies of about 86 and 120 Hz (according to the simulation results). They are also the most dangerous according to the vibration form criterion, as shown by the modal analysis.

Thus, the results of static, modal and frequency analyses correlating with the experimental results are obtained.

DISCUSSION

The obtained results on the position of natural frequencies on the spectrum correlate with the experimental data within $\approx 7\%$. Such a significant percentage of error is caused by the shift of the theoretical frequency response to the right in comparison with the empirical frequency response, which, in turn, occurs due to the idealization of the mathematical model. In particular, in the model subjected to finite element analysis, there are no mill chip grooves, which makes it more rigid and overstates the natural frequencies. Moreover, the type of frequency response and natural frequencies of a solid body is also affected by its geometric shape. Therefore, in the absence of wide and deep chip grooves, the result is somewhat distorted. In this regard, to improve convergence in such cases, it is possible

to introduce a clarifying coefficient that will correct the rigidity of the mill and allow avoiding labour-intensive refinement of its model.

It is important to note that since the force action during the experiment was exerted on the mill, which is kinematically connected to the collet chuck, and the chuck, in turn, to the machine spindle, etc., the obtained frequency response is the resultant with respect to the machine itself and its rigidity. This contributed undoubtedly to the shape of the curve and the absolute values of the amplitudes [22]. This explains the inevitable external difference between the experimental frequency response and the frequency response obtained during the modelling.

For the case of a solid end mill, we introduce a dimensionless K_k coefficient, taking into account the presence of chip grooves in the section undergoing deformations. Obviously, the presence of chip grooves affects the movements along each of the coordinate axes differently, so the values of the coefficients should differ. Since for an axial tool in this work, the rigidity in the transverse direction (perpendicular to the tool axis) is considered, we define the corresponding coefficient $K_{k1}=0.9$. This coefficient value for each specific tool can be obtained as the ratio of the deformations of a solid cylindrical body (rod) and the considered real tool with chip grooves, all other things being equal.

When changing the rigidity of the model by 0.9 times, we obtain the following position of the peaks of the first two natural frequencies (Fig. 14). The first peak has shifted to the left to 82.2 Hz, the second one – to 114.3 Hz. Convergence with the experiment has been improved to 2.5 % (Fig. 3).

It is important to note that the introduction of a clarifying coefficient may not always be justified, since finding the peaks of natural frequencies is used in practice to avoid resonance phenomena, i.e. to separate operating modes and natural frequencies further from each other on the frequency spectrum. In this case, from a practical point of view, in some cases it is not necessary to know the position

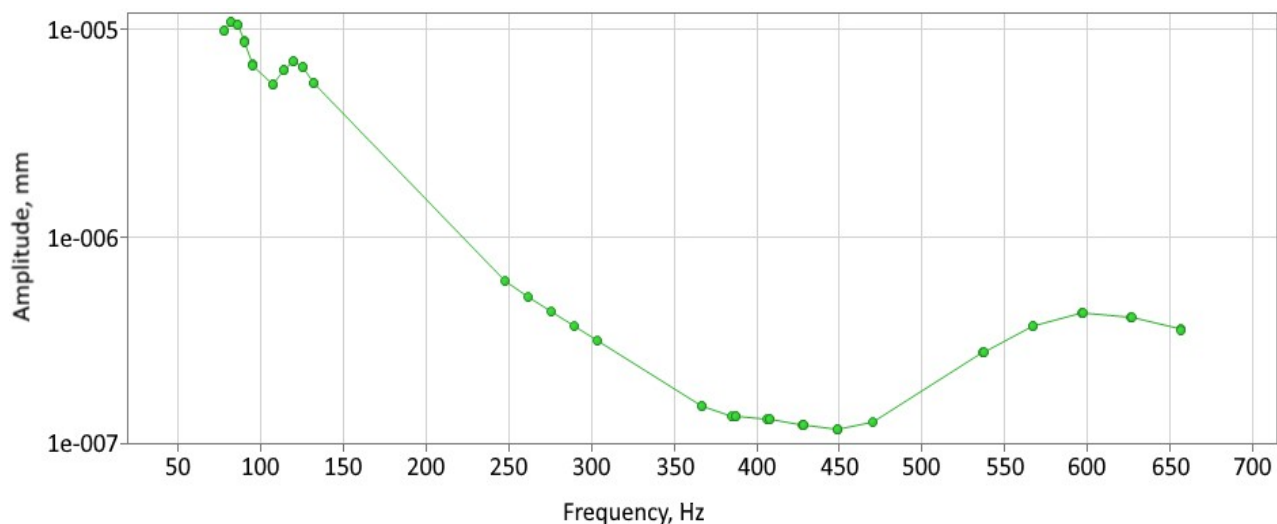


Fig. 13. Amplitude-frequency characteristic in the cross direction with amplitude logarithmic scale (modelling)
Рис. 13. Амплитудно-частотная характеристика в поперечном направлении с логарифмической шкалой амплитуды (моделирование)

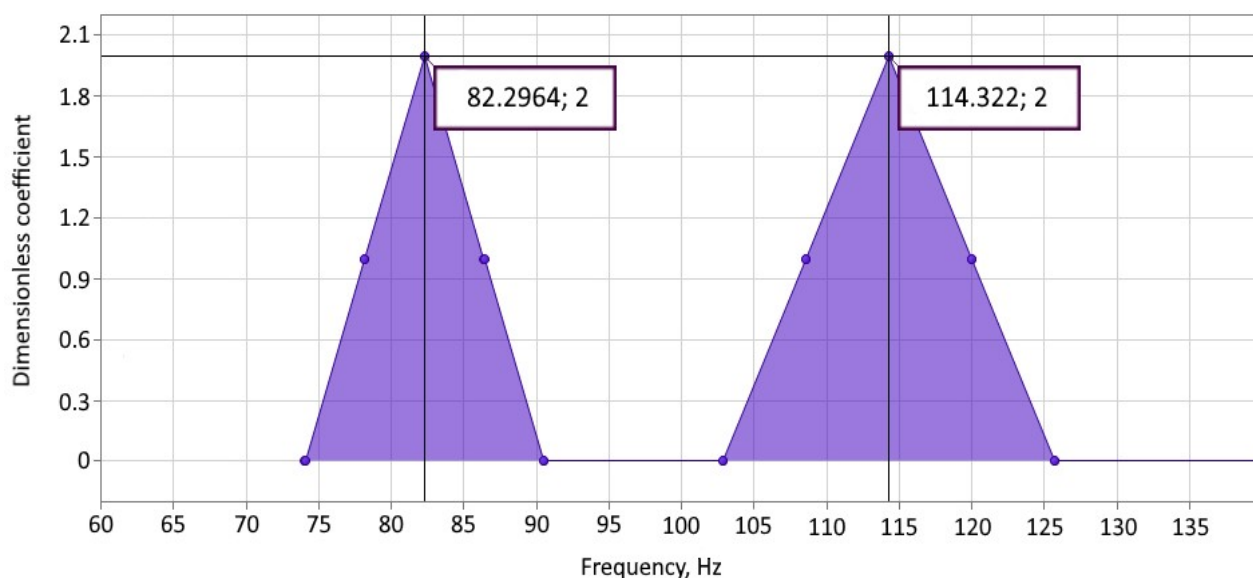


Fig. 14. The location of the first two natural frequencies of the mill on the spectrum taking into account the correction factor (modelling)

Рис. 14. Расположение первых двух собственных частот фрезы на спектре с учетом поправочного коэффициента (моделирование)

of the peak on the spectrum with an accuracy of 1–3 Hz. Knowing the presence of a peak in the range of about 10–15 Hz may be sufficient. The results of the static analysis (rigidity calculation) do not require clarification, initially, a convergence of 2.2 % is provided.

One of the directions for further development of the subject of this study is the expansion of the modelled system, i.e. the inclusion of a blank, a device, and the machine itself in the mathematical model, which will ultimately allow obtaining a model of a closed-loop “machine – fixture – tool – part” system. When maintaining the model-

ling methodology, it is expected to obtain convergence with the experiment, which will allow reflecting more fully and in detail the state of the technological processing system both in dynamics and in statics.

CONCLUSIONS

The presented rigidity modelling technique together with frequency analysis allows calculating force displacements and elastic deformations of the tool for its state at critical loading frequencies. It is the search for rigidity

balance within the "machine – tool – part" system that forces us to evaluate the critical states of the tool, and then the machine, since it is the level of damping, rigidity and natural frequencies of the elements of the "machine – fixture – tool – part" (MFTP) system that determines the possibility and duration of the tool operation, which is the closing link (relatively low-rigidity and vulnerable) in the MFTP system.

The real response of the tool in the "machine – fixture – tool – part" system for individual cases, taking into account the geometry of the tool used, can be modelled with a convergence of 7 %. In this case, the results of mathematical modelling can be clarified using a coefficient that allows taking into account the chip grooves of the tool, which makes it possible to save time for the detailed development of a 3D model. When using the coefficient, the convergence of the peaks on the spectrum with the experiment reaches 2.5 %. Since the obtained calculated values of frequencies and deformations correlate with the experimental data, it can be stated that the goal of the work has been achieved.

Based on differential equations with a coefficient adopted in the first approximation, it becomes possible to train neural network models that will allow obtaining output data on the amplitude of tool deformation for any input data on the expected processing conditions. Moreover, this will allow the neural network and the user to formulate specific proposals for changing (improving) the input data to ensure optimal cutting conditions for a predetermined target function or for a whole set of target functions. In other words, it is possible to solve both the direct and inverse problems. With a sufficiently high level of training of such a neural network model, all the modal, frequency and rigidity characteristics of the tool of interest can be obtained from its output data without experiments or any modelling.

REFERENCES

1. Dovnar S.S., Yakimovich A.M. FEM analysis of the concept of a post-resonant portal multi-purpose machine. *Mashinostroenie: respublikanskiy mezhvedomstvennyy sbornik nauchnykh trudov*. Minsk, BNTU Publ., 2023. Vyp. 34, pp. 155–165.
2. Sazonov M.B., Zhidyaev A.N. Research on end mill vibration in machining of VT9 titanium alloy. *Vestnik of Samara University. Aerospace and Mechanical Engineering*, 2021, vol. 20, no. 4, pp. 89–99. DOI: [10.18287/2541-7533-2021-20-4-89-99](https://doi.org/10.18287/2541-7533-2021-20-4-89-99).
3. Kalmykov V.V., Barkov A.V. Analytical and statistical assessment elastic deformation along the contour at milling. *Fundamental research*, 2016, no. 8-1, pp. 34–38. EDN: [WHOECF](https://www.elibrary.ru/whoecp).
4. Nurkenov A.Kh., Guzeev V.I., Batuev V.V., Nesteruk E.V., Pavlov S.A. Experimental study of rigidity of a technological system on the basis of industrial robot KUKA KR 300 R2500 ULTRA. *Bulletin of the South Ural State University. Series "Mechanical engineering industry"*, 2022, vol. 22, no. 1, pp. 48–58. DOI: [10.14529/engin220104](https://doi.org/10.14529/engin220104).
5. Kozlov A.M., Kuznetsov S.F., Kozlov A.A. Application of the active damper to reduce vibration when milling. *Actual problems in machine building*, 2021, vol. 8, no. 3–4, pp. 81–86. EDN: [MOXJMI](https://www.elibrary.ru/moxjmi).
6. Markova E.V. Causes of vibration and methods of vibration extinguishing. *Izvestiya Tula State University. Tekhnicheskie nauki*, 2021, no. 5, pp. 428–432. EDN: [CISDFC](https://www.elibrary.ru/cisdfc).
7. Yang Bin, Wang Min, Liu Zhihao, Che Changjia, Zan Tao, Gao Xiangsheng, Gao Peng. Tool wear process monitoring by damping behavior of cutting vibration for milling process. *Journal of Manufacturing Processes*, 2023, vol. 102, pp. 1069–1084. DOI: [10.1016/j.jmapro.2023.07.077](https://doi.org/10.1016/j.jmapro.2023.07.077).
8. Ponomarev B.B., Nguen V.D. Computing stresses in the wear zone of a radius end mill cutter. *BMSTU Journal of Mechanical Engineering*, 2025, no. 1, pp. 61–75. EDN: [GFYZYA](https://www.elibrary.ru/gfyzya).
9. Lukyanov A.V., Aleynikov D.P., Kostin P.N. Investigation of oscillations in the forces of interaction of the milling cutter with the workpiece during passing and counter milling. *Modern Technologies. System analysis. Modeling*, 2022, no. 3, pp. 38–49. DOI: [10.26731/1813-9108.2022.3\(75\).38-49](https://doi.org/10.26731/1813-9108.2022.3(75).38-49).
10. Aleynikov D.P., Lukyanov A.V., Kostin P.N. Cutting data effect on machine tool vibrational state and surface roughness when machining. *Systems. Methods. Technologies. Bratsk State University Scientific Journal*, 2021, no. 3, pp. 14–19. DOI: [10.18324/2077-5415-2021-3-14-19](https://doi.org/10.18324/2077-5415-2021-3-14-19).
11. Kozlov A.M., Kiryushchenko E.V., Kozlov A.A. Expansion of technological capabilities of mobile milling equipment. *Bulletin of Voronezh State Technical University*, 2019, vol. 15, no. 4, pp. 140–145. DOI: [10.25987/VSTU.2019.15.4.022](https://doi.org/10.25987/VSTU.2019.15.4.022).
12. Gimadeev M.R., Li A.A., Berkun V.O., Stelmakov V.A. Experimental study of the dynamics of the machining process by ball-end mills. *Obrabotka metallov. Metal working and material science*, 2023, vol. 25, no. 1, pp. 44–56. DOI: [10.17212/1994-6309-2023-25.1-44-56](https://doi.org/10.17212/1994-6309-2023-25.1-44-56).
13. Lukyanov A.V., Aleynikov D.P. Analysis of oscillations of cutting forces between a mill and a workpiece when increasing the spindle rotation speed. *Modern Technologies. System analysis. Modeling*, 2017, no. 4, pp. 70–82. EDN: [YLXFFI](https://www.elibrary.ru/ylxffi).
14. Altintas Y., Lee P. Mechanics and dynamics of ball end milling. *Journal of manufacturing science and engineering*, 1998, vol. 120, no. 4, pp. 684–692. DOI: [10.1115/1.2830207](https://doi.org/10.1115/1.2830207).
15. Sazonov M.B., Zhidyaev A.N. Research on end mill vibration in machining of VT9 titanium alloy. *Vestnik of Samara University. Aerospace and Mechanical Engineering*, 2021, vol. 20, no. 4, pp. 89–99. DOI: [10.18287/2541-7533-2021-20-4-89-99](https://doi.org/10.18287/2541-7533-2021-20-4-89-99).
16. Kravchenko K.Yu., Kugaevskiy S.S., Zhuravlev M.P., Elkind D.M. Natural frequencies estimation using operational modal analysis. *Bulletin of Perm National Research Polytechnic University. Mechanical engineering, materials science*, 2017, vol. 19, no. 2, pp. 21–35. DOI: [10.15593/2224-9877/2017.2.02](https://doi.org/10.15593/2224-9877/2017.2.02).
17. Zhuravlev M.P., Kravchenko K.Yu., Elkind D.M. Vibration resistance at processing by end mills with variable pitch. *Bulletin of Bryansk State Technical University*, 2018, no. 8, pp. 14–24. DOI: [10.30987/article_5bb5e69727bb41.28471955](https://doi.org/10.30987/article_5bb5e69727bb41.28471955).

18. Yatsun E.I., Zubkova O.S. Investigation of the tool system during boring and milling with a large departure. *Izvestiya Tula State University. Tekhnicheskie nauki*, 2024, no. 3, pp. 627–631. EDN: [AXRLQN](#).
19. Matlygin G.V., Savilov A.V., Pyatykh A.S., Timofeev S.A. Study of the effect of cutting modes on output parameters under high-speed steel turn-milling. *Advanced Engineering Research (Rostov-on-Don)*, 2022, vol. 22, no. 2, pp. 99–106. DOI: [10.23947/2687-1653-2022-22-2-99-106](#).
20. Pyatykh A.S., Shaparev P.P. Investigating the impact of chucks on the stability of a milling process. *iPolytech Journal*, 2021, vol. 25, no. 5, pp. 549–558. DOI: [10.21285/1814-3520-2021-5-549-558](#).
21. Berthold J., Kolouch M., Regel J., Dix M. Identification of natural frequencies of machine tools during milling: comparison of the experimental modal analysis and the operational modal analysis. *Production Engineering*, 2024, vol. 18, no. 5, pp. 853–862. DOI: [10.1007/s11740-024-01270-6](#).
22. Berthold J., Regel J., Dix M., Drossel W.-G. Operational modal analysis used to identify dynamic behaviour of machine tools during milling. *Procedia CIRP*, 2023, vol. 118, pp. 128–133. DOI: [10.1016/j.procir.2023.06.023](#).
23. Lukyanov A.V., Aleynikov D.P., Kostin P.N. Investigation of the rigidity and frequency response of an end mill. *Journal of Manufacturing Processes*, 2023. Vol. 102. P. 1069–1084. DOI: [10.1016/j.jmapro.2023.07.077](#).
24. Пономарев Б.Б., Нгуен В.Д. Расчет напряжений в зоне износа режущей части концевой радиусной фрезы // Известия высших учебных заведений. Машиностроение. 2025. № 1. С. 61–75. EDN: [GFYZYA](#).
25. Лукьянов А.В., Алейников Д.П., Костин П.Н. Исследование колебаний сил взаимодействия фрезы с заготовкой при попутном и встречном фрезеровании // Современные технологии. Системный анализ. Моделирование. 2022. № 3. С. 38–49. DOI: [10.26731/1813-9108.2022.3\(75\).38-49](#).
26. Алейников Д.П., Лукьянов А.В., Костин П.Н. Влияние параметров резания на вибрационное состояние станка и шероховатость обработанных поверхностей при механообработке // Системы. Методы. Технологии. 2021. № 3. С. 14–19. DOI: [10.18324/2077-5415-2021-3-14-19](#).
27. Козлов А.М., Кирющенко Е.В., Козлов А.А. Расширение технологических возможностей мобильного фрезерного оборудования // Вестник Воронежского государственного технического университета. 2019. Т. 15. № 4. С. 140–145. DOI: [10.25987/VSTU.2019.15.4.022](#).
28. Гимадеев М.Р., Ли А.А., Беркун В.О., Стельмаков В.А. Экспериментальное исследование динамики процесса механообработки концевыми сфероцилиндрическими фрезами // Обработка металлов (технология, оборудование, инструменты). 2023. Т. 25. № 1. С. 44–56. DOI: [10.17212/1994-6309-2023-25.1-44-56](#).
29. Лукьянов А.В., Алейников Д.П. Исследование колебаний сил взаимодействия фрезы с заготовкой при повышении скорости вращения шпинделя // Современные технологии. Системный анализ. Моделирование. 2017. № 4. С. 70–82. EDN: [YLXFFI](#).
30. Altintas Y., Lee P. Mechanics and dynamics of ball end milling // *Journal of manufacturing science and engineering*. 1998. Vol. 120. № 4. P. 684–692. DOI: [10.1115/1.2830207](#).
31. Сазонов М.Б., Жидяев А.Н. Исследование вибраций концевых фрез при обработке титанового сплава BT9 // Вестник Самарского университета. Аэрокосмическая техника, технологии и машиностроение. 2021. Т. 20. № 4. С. 89–99. DOI: [10.18287/2541-7533-2021-20-4-89-99](#).
32. Кравченко К.Ю., Кугаевский С.С., Журавлев М.П., Элькинд Д.М. Операционный модальный анализ для определения собственных частот колебаний // Вестник Пермского национального исследовательского политехнического университета. Машиностроение, материаловедение. 2017. Т. 19. № 2. С. 21–35. DOI: [10.15593/2224-9877/2017.2.02](#).
33. Журавлев М.П., Кравченко К.Ю., Элькинд Д.М. Виброустойчивость при обработке торцевыми фрезами с переменным шагом // Вестник Брянского государственного технического университета. 2018. № 8. С. 14–24. DOI: [10.30987/article_5bb5e69727bb41.28471955](#).
34. Яцун Е.И., Зубкова О.С. Исследование инструментальной системы при растачивании и фрезеровании с большим вылетом // Известия Тульского государственного университета. Технические науки. 2024. № 3. С. 627–631. EDN: [AXRLQN](#).

СПИСОК ЛИТЕРАТУРЫ

1. Довнар С.С., Якимович А.М. МКЭ-анализ концепции пострезонансного портального многоцелевого станка // Машиностроение: республиканский межведомственный сборник научных трудов. Минск: БНТУ, 2023. Вып. 34. С. 155–165.
2. Сазонов М.Б., Жидяев А.Н. Исследование вибраций концевых фрез при обработке титанового сплава BT9 // Вестник Самарского университета. Аэрокосмическая техника, технологии и машиностроение. 2021. Т. 20. № 4. С. 89–99. DOI: [10.18287/2541-7533-2021-20-4-89-99](#).
3. Калмыков В.В., Барков А.В. Аналитическое и статистическое оценивание упругих деформаций при фрезеровании по контуру // Фундаментальные исследования. 2016. № 8-1. С. 34–38. EDN: [WHOESP](#).
4. Нуркенов А.Х., Гузеев В.И., Батуев В.В., Нестерук Е.В., Павлов С.А. Экспериментальное исследование жесткости технологической системы на базе промышленного робота KUKA KR 300 R2500 ULTRA // Вестник Южно-Уральского государственного университета. Серия: Машиностроение. 2022. Т. 22. № 1. С. 48–58. DOI: [10.14529/engin220104](#).
5. Козлов А.М., Кузнецов С.Ф., Козлов А.А. Применение активного демпфера для снижения колебаний при фрезеровании // Актуальные проблемы в машиностроении. 2021. Т. 8. № 3-4. С. 81–86. EDN: [MQXJMI](#).
6. Маркова Е.В. Причины возникновения вибраций и способы виброгашения // Известия Тульского государственного университета. Технические науки. 2021. № 5. С. 428–432. EDN: [CISDFC](#).
7. Yang Bin, Wang Min, Liu Zhihao, Che Changjia, Zan Tao, Gao Xiangsheng, Gao Peng. Tool wear process monitoring by damping behavior of cutting vibration for milling pro-

19. Матлыгин Г.В., Савилов А.В., Пятых А.С., Тимофеев С.А. Исследование влияния режимов резания на выходные параметры при точении фрезерованием быстрорежущей стали // Advanced Engineering Research (Rostov-on-Don). 2022. Т. 22. № 2. С. 99–106. DOI: [10.23947/2687-1653-2022-22-2-99-106](https://doi.org/10.23947/2687-1653-2022-22-2-99-106).
20. Пятых А.С., Шапарев П.П. Исследование влияния зажимных патронов на устойчивость процесса фрезерования // iPolytech Journal. 2021. Т. 25. № 5. С. 549–558. DOI: [10.21285/1814-3520-2021-5-549-558](https://doi.org/10.21285/1814-3520-2021-5-549-558).
21. Berthold J., Kolouch M., Regel J., Dix M. Identification of natural frequencies of machine tools during milling: comparison of the experimental modal analysis and the operational modal analysis // Production Engineering. 2024. Vol. 18. № 5. P. 853–862. DOI: [10.1007/s11740-024-01270-6](https://doi.org/10.1007/s11740-024-01270-6).
22. Berthold J., Regel J., Dix M., Drossel W.-G. Operational modal analysis used to identify dynamic behaviour of machine tools during milling // Procedia CIRP. 2023. Vol. 118. P. 128–133. DOI: [10.1016/j.procir.2023.06.023](https://doi.org/10.1016/j.procir.2023.06.023).

УДК 621.9.022.2

doi: 10.18323/2782-4039-2025-3-73-3

Исследование жесткости и частотных характеристик концевой фрезы на вертикальном фрезерном центре

*Воронов Роман Дмитриевич**, преподаватель

кафедры «Оборудование и технологии машиностроительного производства»

*Расторгуев Дмитрий Александрович*¹, кандидат технических наук, доцент,

доцент кафедры «Оборудование и технологии машиностроительного производства»

*Левашкин Денис Геннадьевич*², кандидат технических наук, доцент,

доцент кафедры «Оборудование и технологии машиностроительного производства»

Тольяттинский государственный университет, Тольятти (Россия)

*E-mail: smr.rom@yandex.ru

¹ORCID: <https://orcid.org/0000-0001-6298-1068>²ORCID: <https://orcid.org/0009-0007-2704-4635>

Поступила в редакцию 21.04.2025

Пересмотрена 11.08.2025

Принята к публикации 04.09.2025

Аннотация: Исследование посвящено проблеме заблаговременного исключения резонансных колебаний инструмента путем предварительного математического моделирования. В частности, проблема рассмотрена для случая процесса фрезерования концевой фрезой на вертикальном фрезерном центре. В работе приведены обработанные экспериментальные данные и результаты математического моделирования, содержащие сведения о жесткости фрезы ФКЦ 4257, ее собственных частотах на спектре и формах колебаний. Построенная конечно-элементная математическая модель охватывает саму фрезу, зажимную цангу и цанговый патрон. Модель описывает статическую жесткость фрезы с погрешностью 2,2 %, а положение ее собственных частот на спектре – с погрешностью около 7 % относительно результатов эксперимента. Посредством построения амплитудно-частотной характеристики и проведения модального анализа показано, что наиболее критичными для фрезы являются первые две моды колебаний (80 и 112 Гц), как по критерию величины амплитуды колебаний, так и по критерию их формы. Формы колебаний на первых модах являются изгибными. В рамках модального анализа рассмотрены и оценены формы колебаний на остальных модах. Для улучшения сходимости результатов частотного анализа предложено ввести коэффициент $K_{k1}=0,9$, учитывающий меньшую жесткость реальной фрезы в сравнении с идеализированной математической моделью, при применении которого сходимость улучшена до 2,5 %. Благодаря примененной методике можно получать достоверные данные о частотных зонах неустойчивости, используемые на практике для уходов от резонансных явлений. В перспективе на основе таких данных с учетом поправочных коэффициентов возможно обучение нейросетевых моделей, предсказывающих отклик инструмента при конкретных условиях обработки и решающих обратную задачу подбора рациональной геометрии инструмента под определенные задачи.

Ключевые слова: концевая фреза; жесткость; модальный анализ; частотный анализ; математическое моделирование; амплитудно-частотная характеристика; резонанс.

Благодарности: Исследование выполнено в рамках государственного контракта по НИОКТР № 125011300177-8.

Для цитирования: Воронов Р.Д., Расторгуев Д.А., Левашкин Д.Г. Исследование жесткости и частотных характеристик концевой фрезы на вертикальном фрезерном центре // Frontier Materials & Technologies. 2025. № 3. С. 39–49. DOI: 10.18323/2782-4039-2025-3-73-3.

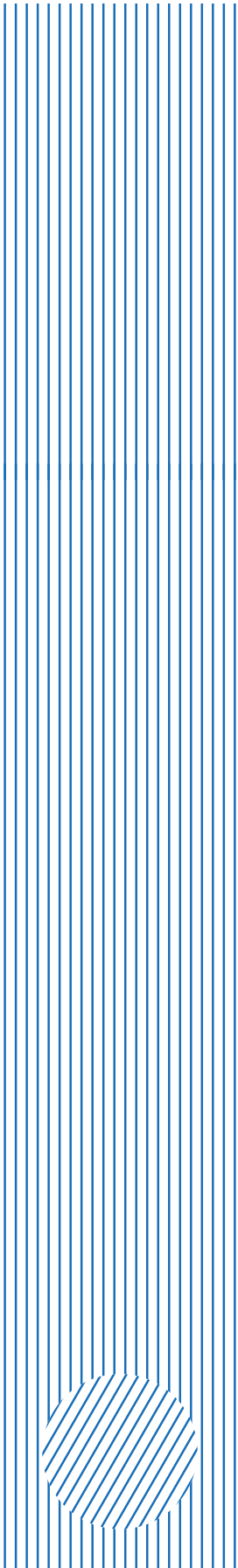
The Research and Development Institute of Advanced Technologies is a structural division of Togliatti State University.

The Research and Development Institute of Advanced Technologies today

- More than 60 employees, including seven Doctors of Sciences and fourteen PhDs.
- Three centers, four departments, nineteen laboratories equipped with the up-to-date testing and research facilities for amount over 500 million roubles.
- Accreditation in three systems for testing and research, including in the ILAC international system (laboratory accreditation authority – Association of Analytical Centers “Analitika”, a full member and participant of the ILAC and APLAC mutual recognition agreements).
- Basic areas: fundamental research in the field of physical materials science (the development of the promising materials design, the issues of strength, plasticity, corrosion resistance, fatigue strength, stress corrosion cracking, improving the surface functional properties) and chemistry (methods for synthesis of molecules with the properties of selective fluorescent probes); applied research and inventions in the field of non-destructive control, micro-arc oxidation, manufacturing of cast products, etc.; services for testing and research of various materials, metallographic evaluations, environmental analyses, chemical monitoring of the environment.

Main achievements of the Research and Development Institute of Advanced Technologies

– Three mega-grants were implemented according to the Resolution of the Government of the Russian Federation dated April 9, 2010 No. 220; five projects within the Federal Targeted Programme for Research and Development in Priority Areas of Development of the Russian Scientific and Technological Complex for 2014–2020, including three international ones; in 2023, nine projects of the Russian Science Foundation and two state assignments are being implemented; under the auspices of the extraterritorial scientific and educational center “Engineering of the Future”, a youth Laboratory for the design of magnesium alloys was created.

- Annually:
 - the number of papers is more than 35, half of them are in specialized journals of the Q1 and Q2 levels;
 - more than 1,500 test reports and conclusions at the request of enterprises, arbitration courts, and the prosecutor’s office
 - An initiator and organizer of 11 Physical Materials Science international schools with the participation of leading scientists-material engineers and metal physicists, the lectures of which became the basis for publishing nine volumes of the Advanced Materials textbook
 - International cooperation with the universities of Kumamoto (Japan), Seoul (South Korea), Prague (Czech Republic), and Freiberg (Germany), academic cooperation with IMP UB RAS (Yekaterinburg), IMSP RAS (Ufa), ISPMS SB RAS (Tomsk) and others; technical cooperation with more than 150 organizations in the real sector of the economy.
- 

Microstructure, properties and strengthening mechanisms of low-carbon steel subjected to equal-channel angular pressing

Andrey V. Malinin^{*1,3}, PhD (Engineering),

Deputy General Director for Research

Vil D. Sitdikov^{1,4}, Doctor of Sciences (Physics and Mathematics),
senior expert

Yuri A. Lebedev², PhD (Physics and Mathematics),
senior researcher

¹LLC RN-BashNIPIneft, Ufa (Russia)

²Institute of Physics of Molecules and Crystals of Ufa Federal Research Center of RAS, Ufa (Russia)

*E-mail: MalininAV@bnipi.rosneft.ru

³ORCID: <https://orcid.org/0000-0003-1185-5648>

⁴ORCID: <https://orcid.org/0000-0002-9948-1099>

Received 22.07.2025

Revised 29.07.2025

Accepted 20.08.2025

Abstract: In the work, an ultrafine-grained (UFG) state was formed in a low-carbon steel by equal-channel angular pressing (ECAP) (8 passes, 200 °C), demonstrating high mechanical properties (yield strength is 1021 MPa, tensile strength is 1072 MPa, ductility is 10.7 %) along with satisfactory corrosion resistance (0.345 mm/year). To explain the reasons for improvement of strength properties and changes in corrosion properties, UFG steel microstructure was analysed using electron microscopy and X-ray scattering methods. Specifically, electron microscopy methods revealed structural refinement of ECAP-processed steel, resulting in the formation of equiaxed grains averaged ~240 nm in size. Modified Williamson–Hall and Warren–Averbach X-ray procedures were applied to find the patterns of changes in coherent scattering domains size, density ρ and fraction f_s of screw-type dislocations, effective outer cut-off radius R_e of dislocations and some other parameters of low-carbon steel depending on a number of ECAP passes (degree of deformation). X-ray diffraction analysis and small-angle X-ray scattering methods were used to determine evolution trends of mass fraction, size and morphology of various precipitates depending on the number of ECAP passes. Based on the obtained data, a model of microstructure transformation during UFG state formation in steel was proposed. Furthermore, strengthening mechanisms of both coarse-grained and UFG steels were discussed. It was found that in initial state, steel strength was primarily ensured by grain-boundary strengthening and precipitation of small Me_{23}C_6 and Me_3C_2 precipitates. It was shown that during UFG structure formation, steel strength increases due to grain-boundary strengthening and dislocation density increase. The contribution of precipitates in the UFG state to the strengthening decreases and this is due to their growth during ECAP processing. It was found that an increase in corrosion rate of UFG steel results from a decrease in ferrite grain size, an increase in grain-boundary dislocations density and a cellular structure formation.

Keywords: low-carbon steel; ferrite; equal-channel angular pressing; ultrafine-grained structure; microstructure; strengthening mechanisms; X-ray diffraction analysis; corrosion rate; small-angle X-ray scattering.

Acknowledgments: The authors express their gratitude to PJSC Rosneft Oil Company and LLC RN-BashNIPIneft for the opportunity to conduct the research. The authors also thank A.I. Voloshin, Doctor of Sciences (Chemistry), Yu.B. Lind, PhD (Physics and Mathematics), and N.R. Yarkeeva, PhD (Engineering) (LLC RN-BashNIPIneft) for discussing the results obtained and valuable comments during the preparation of the paper.

For citation: Malinin A.V., Sitdikov V.D., Lebedev Yu.A. Microstructure, properties and strengthening mechanisms of low-carbon steel subjected to equal-channel angular pressing. *Frontier Materials & Technologies*, 2025, no. 3, pp. 51–65. DOI: 10.18323/2782-4039-2025-3-73-4.

INTRODUCTION

Currently, low-carbon steels are widely used in the automotive, construction, aerospace and oil and gas industries due to their high industrial application potential. Nevertheless, further enhancement of the set of physical, mechanical and performance properties of low-carbon steels through the optimisation of alloying elements and/or the implementation of various thermo-mechanical processing modes remains a significant fundamental and applied challenge in materials science. To

date, among the various methods for improving the physical and mechanical properties of metallic materials and alloys, the methods of severe plastic deformation (SPD) are among the most popular [1–4]. As a result of SPD processing, an ultrafine-grained (UFG) structure is formed in the initial coarse-grained (CG) metallic materials due to the refinement of the initial grains [1–4]. Moreover, UFG structures produced by SPD methods in metals and alloys are characterised by an increased density of introduced defects, products of various phase

transformations, the formation of equiaxed grains of nanometric size and highly non-equilibrium grain boundaries [5; 6]. Furthermore, in the case of SPD effects on alloys, dynamic strain ageing may occur in them, resulting in the precipitation of particles of different morphology, sizes and chemical compositions in the main phase [7; 8]. All these microstructural changes in metals and alloys processed by such techniques lead to the formation of high-strength states due to the activation of various strengthening mechanisms [9; 10]. In this regard, the creation of high-strength steels through targeted control of their structure and phase composition represents a pressing issue in modern materials science.

The main SPD methods include equal-channel angular pressing (ECAP) and high-pressure torsion (HPT) [1; 2]. Previously, these methods have been successfully applied to obtain high-strength states in a number of low-carbon steels [11–13]. In particular, the authors of [11] applied the ECAP method to AISI 1010 steel with three passes at a temperature range of 150–300 °C. By varying the ECAP temperature, they obtained a high-strength state of the steel at 200 °C, characterised by high yield strength σ_{YS} of 778 MPa and ultimate tensile strength σ_{UTS} of 819 MPa, significantly exceeding those of the CG steel (σ_{YS} =252 MPa, σ_{UTS} =307 MPa) [11]. At the same time, ductility decreased by more than half. The improvement in strength characteristics was attributed by the authors to the formation of a ferritic UFG structure in the steel [11]. In [12], the authors managed to increase the number of ECAP passes (degree of deformation) in ferritic steel up to six by raising the temperature to 300 °C. It was shown [12] that increasing the ECAP deformation degree further raised the yield strength to 851 MPa and the ultimate tensile strength to 857 MPa. However, the ductility value did not exceed 9 %. Based on microstructural analysis, it was concluded that the formation of a banded structure consisting of submicrocrystalline grains with high dislocation density enhances the mechanical properties of ferritic steel [12]. Furthermore, hot rolling of low-carbon steel prior to ECAP processing allowed increasing the number of passes up to ten [13]. Thanks to such combined processing, the authors succeeded in forming a banded structure composed of elongated grains with a width of 200–300 nm, thereby raising the ultimate tensile strength to record-high values (over 1200 MPa) [13].

When determining the reasons for the improvement of strength characteristics in ECAP-processed steels, the authors [11–13] relied solely on electron microscopy

data. Meanwhile, X-ray scattering methods are a powerful tool for providing an integrated characterisation of the steel microstructure through other structural parameters [14–16]. Recently modified Williamson–Hall and modified Warren–Averbach techniques have been successfully applied to the structural characterisation of steels [17; 18]. In particular, the reasons for the destruction of the near-surface layer of martensitic steel were identified, which included the reduction in dislocation density, a change in the dislocation type and an increase in the coherent scattering domain (CSD) size [17]. In [18], X-ray scattering was used to study the changes in microstructural parameters during the tensile deformation of Fe–26Mn–1Al–0.14C steel. It was found that tensile deformation leads to an increase in dislocation density, suppression of the screw dislocations shares, the emergence of a strong dislocation dipole field indicative of cell structure formation and the activation of dynamic recovery (growth of the effective outer cut-off radius of dislocations) [18].

The above examples demonstrate that the combined use of X-ray scattering and electron microscopy methods enables a more detailed characterisation of steel structures during thermomechanical processing. Accordingly, in the present study, these methods were jointly applied to determine the reasons for the enhancement of strength properties and changes in corrosion behaviour in a medium-carbon steel upon the formation of a UFG state.

Objective of the study is to form a high-strength state in medium-carbon steel using the ECAP method, to analyse strengthening mechanisms and to identify possible reasons for changes in corrosion properties based on microstructural data obtained by X-ray scattering and electron microscopy methods.

METHODS

Methodology for the UFG structure formation

A widely used low-carbon steel was selected for the formation of UFG structure by ECAP method. The chemical composition of the steel measured by optical emission spectrometry is presented in Table 1. Before ECAP processing, the cylindrical steel specimens (9 mm in diameter and 30 mm in length) were annealed at a temperature of 200 °C for 1 h. ECAP was performed using tooling with a channel intersection angle of 120°. The ECAP processing temperature was maintained at 200 °C, the deformation route used was route B_C and the number of passes was 4, 6, and 8.

Table 1. Chemical composition of the studied steel (wt. %)
 Таблица 1. Элементный состав исследуемой низкоуглеродистой стали (мас. %)

C	Si	Mn	Cr	Ni	Cu	P	S	Fe
0.108	0.195	0.397	0.135	0.216	0.087	0.003	0.012	balance

Methodology for carrying out mechanical and corrosion tests

Tensile mechanical tests were carried out using a universal testing machine Instron 8801. The following mechanical properties were determined: yield strength σ_{YS} , ultimate tensile strength σ_{UTS} and elongation δ . In order to exclude the influence of the heterogeneity of the formed structure and the effects of poor processing of the peripheral areas, tests were carried out on small samples cut from the central area of the rod relative to its longitudinal axis [1; 3]. The dimensions of the flat samples: length 4 mm, sides of the working part $1 \times 1 \text{ mm}^2$. The strain rate during tensile testing was $1 \cdot 10^{-3} \text{ s}^{-1}$. The steel hardness after various numbers of ECAP passes was measured using the Vickers method on a universal hardness tester Shimadzu HMV-G with an indenter load of 100 g and a dwell time of 10 s.

Corrosion rate V_c was determined by mass loss after exposure to a corrosive environment. For corrosion testing, disks 9 mm in diameter and 2 mm thick were cut from the as-received and ECAP-processed specimens. Samples were kept in a test solution prepared from 5.0 wt. % sodium chloride, 0.5 wt. % acetic acid and distilled water for 100 h.

Methodology for studying microstructure using electron microscopy

The microstructure of the as-received and ECAP-processed specimens was analysed using a scanning electron microscope (SEM) Thermo Scientific Q250 (USA). Microstructure analysis was performed on cross-sectional metallographic specimens cut from ECAP-processed samples. Specimens were prepared for SEM by grinding, followed by polishing with diamond paste and etching in a nital solution. The steel microstructure was also examined by transmission electron microscopy (TEM) to obtain information on the size of structural elements, with an accelerating voltage of 200 kV. Thin foils for TEM studies were prepared by twin-jet electropolishing using an electrolyte based on *n*-butyl alcohol.

Methodology for carrying out X-ray structural analysis

X-ray diffraction analysis (XRD) was performed on steel samples using a Tongda TD-3000 diffractometer (China) operating in Bragg–Brentano geometry. X-ray patterns were recorded within a 2θ scattering angle range from 25° to 140° in continuous scanning mode at a scanning speed of $0.5^\circ/\text{min}$. Cu anode tube was used to generate radiation ($\lambda=0.154060 \text{ nm}$) at an operating voltage of 40 kV and a current of 35 mA. Diffracted beams were detected using a Mythen 2D multichannel detector (Switzerland). Parasitic β and W_L lines from copper radiation were suppressed using a $30 \mu\text{m}$ thick nickel foil. The use of a high-precision multichannel detector and nickel foil in the registration of diffracted copper radiation reduced fluorescence levels on the X-ray patterns, enabling the measurement of clear (hkl) reflections both from ferritic steel and from secondary phases.

The calculation of fine structure parameters (CSD average size D , dislocation density ρ , fraction of screw-type dislocations, effective outer cut-off radius R_e and dislocation type) was carried out using the modified Wil-

liamson–Hall (mW-H) and Warren–Averbach (mW-A) techniques [19]. In the mW-H method, CSD size D_{W-H} was determined based on the full width at half maximum (FWHM) broadening according to the dependence of

$$\Delta K = FWHM \frac{\cos\theta}{\lambda} \text{ on } K = \frac{2\sin\theta}{\lambda}:$$

$$\Delta K = \frac{0,9}{D} + \left(\frac{\pi M^2 b^2}{2} \right)^{\frac{1}{2}} \rho^{\frac{1}{2}} \left(K \bar{C}^{\frac{1}{2}} \right) + O(K^2 \bar{C}), \quad (1)$$

where K is the scattering vector;

M is the Wilkens parameter depending on the effective outer cut-off radius R_e of dislocations;

\bar{C} is the average dislocation contrast factor;

b is the value of the Burgers vector (0.204 nm).

By squaring equation (1) and considering that $(O(K^2 \bar{C}))^2 \approx 0$, the following expression for calculating D_{W-H} was obtained:

$$\frac{\Delta K^2 - \alpha}{K^2} = \frac{\pi M^2 b^2}{2} \rho \bar{C}_{h00} (1 - qH), \quad (2)$$

where \bar{C}_{h00} is the average dislocation contrast factor in the $\{h00\}$ plane;

q is a constant related to the type of dislocations and the elastic constants of steel;

H for an arbitrary $\{hkl\}$ plane was determined using the expression

$$H = \frac{h^2 k^2 + h^2 l^2 + k^2 l^2}{h^2 + k^2 + l^2};$$

$$\alpha = \left(\frac{0,9}{D} \right)^2.$$

The dislocation density ρ used in equation (2) was found from the real $A(L)$ and size $A^s(L)$ parts of the Fourier coefficients (where L is Fourier length) using the mW-A method:

$$\ln A(L) = \ln A^s(L) - \frac{\pi b^2 \rho}{2} L^2 \ln \left(\frac{R_e}{L} \right) (K^2 \bar{C}) = \ln A^s(L) - Y K^2 \bar{C}, \quad (3)$$

$$\text{where } Y = \frac{\pi b^2 \rho}{2} L^2 \ln \left(\frac{R_e}{L} \right).$$

By transforming equation (3), a relation for determining ρ was obtained:

$$\frac{Y}{L^2} = \frac{\pi b^2 \rho}{2} L^2 \ln \left(\frac{R_e}{L} \right) - \rho \frac{\pi b^2}{2} \ln(L). \quad (4)$$

Equations (3) and (4) are similar to the expression $y = m + (-k)x$. Accordingly, $A^s(L)$ values were determined by approximating the dependence of $\ln A(L)$ on $K^2 \bar{C}$ to the point of intersection with the OY -axis (i. e.,

the $\ln A(L)$ axis). From this dependence (4), values of Y were also determined via the tangent of the curve slope. Dislocation density ρ values used in the right part of equation (4) were found from the graph of Y/L^2 versus $\ln(L)$ based on the tangent of the curve slope. R_e value for each state was determined by approximating the graph of relation (4) to the point of intersection with the OY axis. Instrumental broadening of steel (hkl) reflections was taken into account by recording and analysing the X-ray pattern of LaB_6 powder.

Small-angle X-ray scattering technique

To obtain information about the morphology and size of precipitates, thin foils were prepared from thin sections (5 mm long, 10 mm wide, $\sim 20 \mu\text{m}$ thick). Small-angle X-ray scattering (SAXS) curves were recorded in the scattering vector q range from 0.01 to 1.4 nm^{-1} using Tongda TD-3000 diffractometer (China) equipped with a single-channel detector. The diameter of the analysed foil surface was $\sim 3.5 \text{ mm}$. When analysing the steel precipitates, the resulting scattering intensity $I(q)$ was expressed as:

$$I(q) = I(q)_1 + I(q)_2 + \dots + I(q)_n = \sum_{i=1}^n |F(q)_i|^2 |S(q)_i|^2,$$

where $I(q)_i$ is the scattering intensity from precipitates with the i -th shape;

$F(q)_i$ is the form factor defining the morphology of the i -th precipitates;

$S(q)_i$ is the structure factor determining the spatial distribution of the i -th precipitates.

The morphology of the precipitates was defined according to the expressions given in [20].

RESULTS

Tensile and corrosion resistance tests

The results of mechanical tests and corrosion rate data for the studied steel states are presented in Table 2. It can be seen that ECAP processing of the initial steel leads to

an increase in its hardness and strength characteristics (Table 2). In particular, after 4 ECAP passes, the steel hardness increases by 1.4 times, yield strength σ_{YS} increases by 2.9 times and ultimate tensile strength σ_{UTS} increases by 2.3 times compared to the initial CG state. At the same time, an inverse effect is observed: the steel ductility decreases by approximately 2.7 times. This state is also characterised by an increase in corrosion rate by 0.03 mm/year. An increase in the number of ECAP passes to 6 results in a further growth of microhardness, tensile strength, yield strength, and corrosion rate (Table 2). The steel ductility in this state slightly improves. After 8 ECAP passes, the steel exhibits very high strength properties, with ductility reaching $\sim 11\%$ (Table 2). The corrosion rate after 8 ECAP passes increases by 0.046 mm/year.

Microstructure studies using electron microscopy

SEM images of the microstructure of the initial and ECAP-processed steels are shown in Fig. 1. In the initial state, the steel microstructure is characterised by the presence of ferrite grains (Fig. 1 a). In some ferrite grains, needle-like cementite particles are also visible. The average ferrite grain size, based on the analysis of no fewer than ten images, was $\sim 4 \mu\text{m}$. As a result of ECAP processing (4 passes), a banded structure is formed in the steel (Fig. 1 b). The bands contain heavily refined grains (average size $\sim 270 \text{ nm}$ according to TEM data), in which a high density of defects in the form of dislocation tangles can also be observed (Fig. 1 b, inset). After 6 ECAP passes, the banded structure becomes less pronounced (Fig. 1 c). The average ferrite grain size in this state, based on TEM investigations, was $\sim 250 \text{ nm}$ (Fig. 1 c, inset). After 8 ECAP passes, the steel forms an equiaxed structure with an average grain size of $\sim 240 \text{ nm}$ (Fig. 1 d). Additionally, a cellular structure is observed in some grains (Fig. 1 d, inset).

Microstructure studies using X-ray diffraction analysis

Experimental X-ray patterns of the steel in various structural states are presented in Fig. 2. It is evident that the X-ray patterns for the initial and ECAP-processed states

Table 2. Mechanical properties and corrosion rate of low-carbon steel in coarse-grained and ultrafine-grained states
Таблица 2. Механические свойства и скорость коррозии низкоуглеродистой стали в крупнокристаллическом и ультрамелкозернистом состояниях

State	HV, GPa	σ_{YS} , MPa	σ_{UTS} , MPa	δ , %	V_c , mm/year
CG	1.89 \pm 0.08	343 \pm 9	454 \pm 8	26.1 \pm 1.3	0.299 \pm 0.006
ECAP, 4 passes	2.66 \pm 0.06	995 \pm 10	1033 \pm 6	9.7 \pm 0.5	0.329 \pm 0.008
ECAP, 6 passes	2.77 \pm 0.04	1012 \pm 8	1061 \pm 9	9.9 \pm 0.4	0.336 \pm 0.006
ECAP, 8 passes	2.85 \pm 0.05	1021 \pm 9	1072 \pm 12	10.7 \pm 0.4	0.345 \pm 0.005

Note. HV is Vickers hardness; σ_{YS} is yield strength; σ_{UTS} is ultimate strength; δ is plasticity; V_c is corrosion rate.

Примечание. HV – твердость по Виккерсу; σ_{YS} – предел текучести; σ_{UTS} – предел прочности; δ – пластичность; V_c – скорость коррозии.

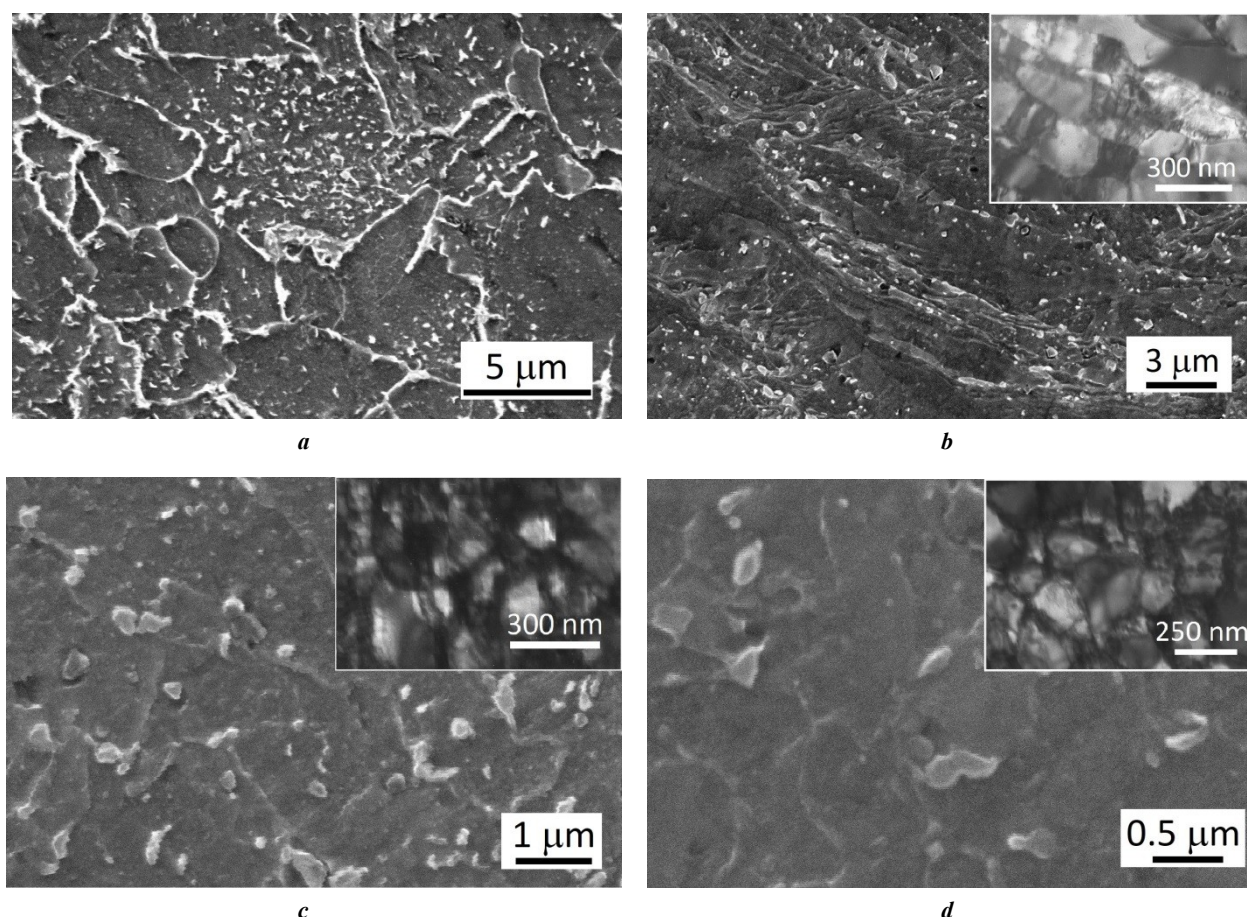


Fig. 1. SEM images of the microstructure of the steel under study:
a – in the coarse-grained state; **b** – after 4 ECAP passes; **c** – after 6 ECAP passes;
d – after 8 ECAP passes. The insets contain TEM images

Рис. 1. РЭМ-изображения микроструктуры исследуемой стали:
a – крупнокристаллическое состояние; **b** – после 4 проходов РКУП; **c** – после 6 проходов РКУП;
d – после 8 проходов РКУП. Во вставках изображения, полученные ПЭМ

are characterised by the presence of ferrite (α -Fe) reflections and cementite (Fe_3C) particles (Fig. 2 a). At the same time, new reflections appear on the X-ray pattern of a sample after ECAP (4 passes) (Fig. 2 a).

Phase identification revealed that these new reflections belong to Me_{23}C_6 - and Me_3C_2 -type precipitates. An increase in the number of ECAP passes leads to a growth in the intensity of Me_{23}C_6 and Me_3C_2 reflections on the X-ray patterns (Fig. 2 a). To evaluate the mass fraction of the identified phases, Rietveld refinement was performed on the X-ray patterns. An example of such refinement is shown in Fig. 2 b. Minor fluctuations in the difference curve (grey) between the measured (black) and the simulated (red) X-ray patterns indicate a good correlation between them. The results of the X-ray analysis regarding the content of identified phases are presented in Table 3.

The initial steel is characterised by a relatively high content of cementite Fe_3C particles and a low mass fraction of Me_{23}C_6 precipitates. During the formation of the UFG structure in steel, the mass fractions of Me_{23}C_6 and Me_3C_2 precipitates increase, while the cementite particle content remains practically unchanged (Table 3).

Precise analysis of the X-ray patterns revealed that, in addition to the appearance and growth of Me_{23}C_6 and Me_3C_2 reflec-

tions, an increase in broadening of the ferrite (hkl) reflections and a shift toward higher angles occur as a result of ECAP processing. These changes are clearly illustrated in Fig. 3 using the (110) and (210) ferrite reflections as examples.

Additionally, the insets in Fig. 3 b show the (200) and (320) reflections of lanthanum hexaboride used to take into account the contribution of instrumental broadening of the (110) and (211) ferrite peaks. As is known [21], an increase in peak broadening indicates a rise in defect density in the fine structure and a decrease in the CSD size D , while a peak shift toward large angles leads to a decrease in the lattice parameter. In this regard, these microstructural changes were further analysed by means of XRD analysis. To estimate the CSD size and dislocation type, the mW-H technique (Equation (2)) was used, and for the evaluation of the effective outer cut-off radius of dislocations and Wilkens parameter, the mW-A technique was used (Equation (4)).

In order to find the \bar{C}_{h00} value in Equation (2), contrast factors \bar{C}_{hkl}^e for edge and screw \bar{C}_{hkl}^s dislocations were calculated according to [22]. For the investigated steel grade, the elastic constants C_{11} , C_{12} and C_{44} are 245, 139 and 122 GPa, respectively [23]. The calculated values of \bar{C}_{hkl}^e and \bar{C}_{hkl}^s are presented in Table 4. Based on these

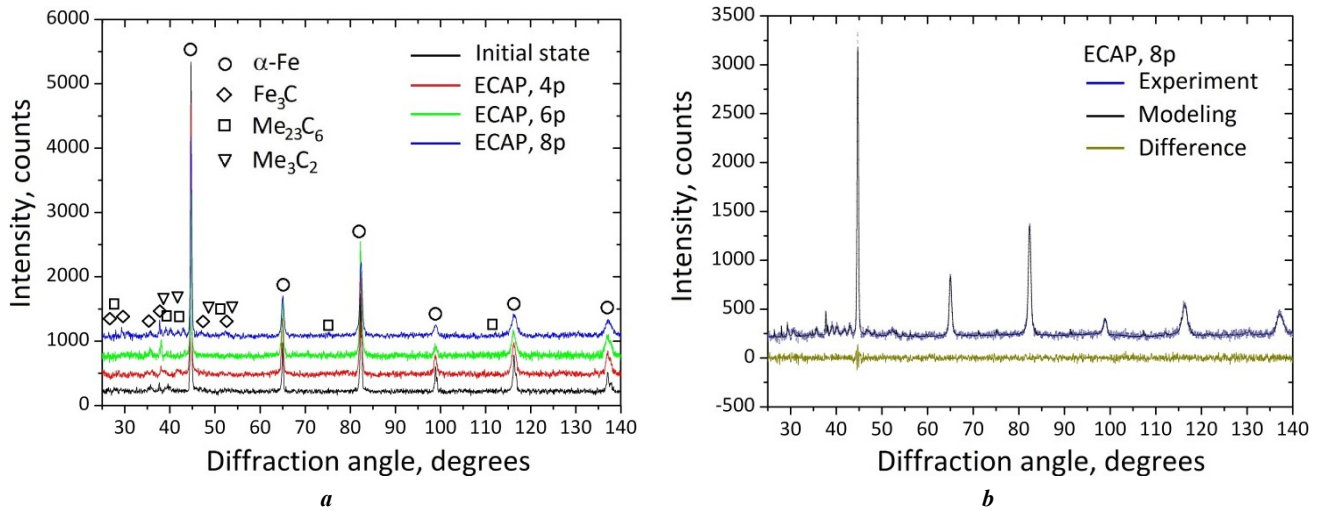


Fig. 2. Experimental diffraction patterns of steel in different structural states:

a – general view; **b** – processed diffraction pattern of steel after 8 ECAP passes

Рис. 2. Экспериментальные дифрактограммы стали в различных структурных состояниях:

a – общий вид; **b** – обработанная дифрактограмма стали после 8 проходов ПКВП

Table 3. Identified phases and their mass fraction in the original and ultrafine-grained low-carbon steel

Таблица 3. Обнаруженные фазы и их массовая доля в исходной и ультрамелкозернистой низкоуглеродистой стали

State	Mass fraction of phases, %			
	α -Fe	Fe_3C	Me_{23}C_6	Me_3C_2
CG	99.24±0.54	0.76±0.07	0.13±0.07	—
ECAP, 4 passes	98.72±0.61	0.82±0.06	0.34±0.05	0.12±0.05
ECAP, 6 passes	98.45±0.49	0.85±0.04	0.54±0.06	0.16±0.05
ECAP, 8 passes	98.36±0.55	0.81±0.04	0.62±0.05	0.21±0.06

data, theoretical values of q_{th}^e and q_{th}^s were estimated, which turned out to be 1.29 and 2.44, respectively. To determine the value of q , the parameter α in Equation (2) was optimised to obtain a linear relationship, as shown in Fig. 4 a. By approximating the dependencies shown in Fig. 4 a to the intersection with the OX axis, the values of $1/q$ were obtained for each state ($q=2.25$, 1.94, 1.81, and 1.66 for the initial CG state, and after 4, 6, and 8 ECAP passes, respectively). The fractions f_e of edge and f_s of screw dislocations were then determined according to the expression

$$q = (1 - f_s)q_{th}^e + f_s q_{th}^s.$$

The obtained values made it possible to find \bar{C}_{h00} using the formula

$$\bar{C}_{h00} = (1 - f_s)\bar{C}_{h00}^e + f_s\bar{C}_{h00}^s.$$

The averaged \bar{C}_{hkl} values were calculated according to formula (Table 4)

$$\bar{C}_{hkl} = \bar{C}_{h00}(1 - qH).$$

Based on the obtained data, the dependence $\Delta K(K\bar{C}^{1/2})$ was plotted as shown in Fig. 4 b. Extrapolation of $\Delta K(K\bar{C}^{1/2})$ dependence to its intersection with the OY axis allowed estimating the D_{W-H} CSD size according to the mW-H technique. Resulting D_{W-H} CSD size values and the fractions of screw dislocations for the studied states are summarised in Table 5.

To assess the dislocation density in the mW-A technique, Fourier coefficients were first determined by analysing each reflection on the X-ray pattern of the initial and ECAP-processed steel.

Examples of the obtained Fourier coefficients $\ln A(L)$ as functions of $K^2\bar{C}$ (equation 3) for the initial and UFG steel (8 ECAP passes) are shown in Fig. 5 a, b. Subsequently, based on the $\ln A(L)$ vs $K^2\bar{C}$ dependencies and by approximating the lines to their intersection with the OY axis (see insets in the figures), the dimensional values $A^s(L)$ of the Fourier coefficients were determined. These coefficients for the studied steel states are presented in Fig. 5 c as $A^s(L)$ dependencies.

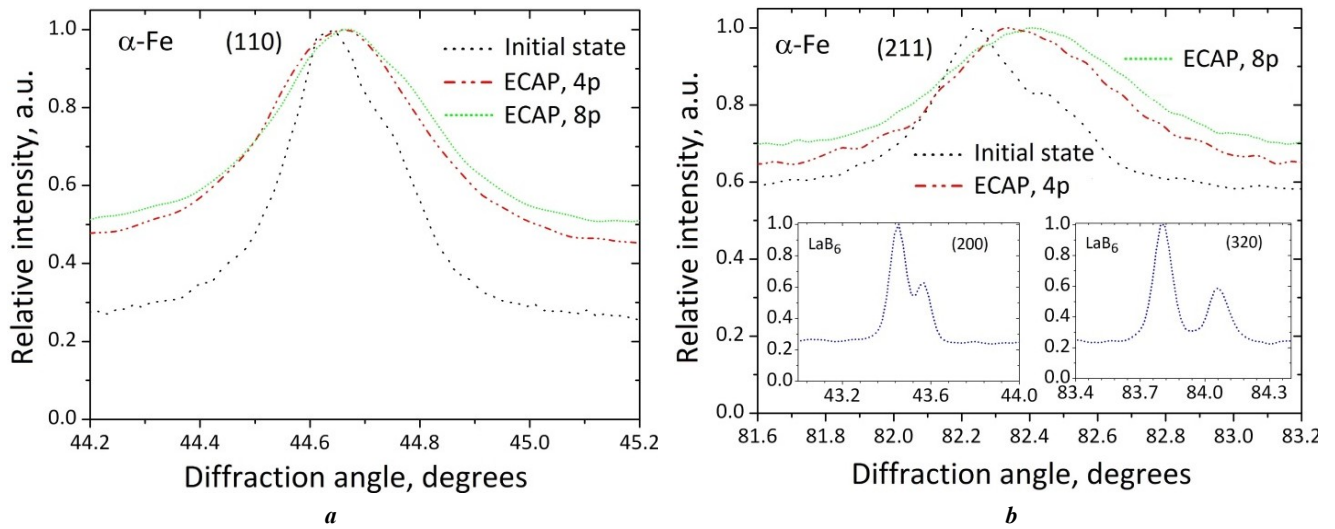


Fig. 3. Normalised reflections of steel demonstrating the change in their width and angular position on the diffraction pattern: **a** – reflection (110); **b** – (211).

The insets show some reflections of LaB₆, which were used to take into account the instrumental broadening of the peaks

Рис. 3. Нормализованные рефлексы стали, демонстрирующие изменение их ширины

и угловой позиции на дифрактограмме: **a** – отражение (110); **b** – (211).

Во вставках приведены некоторые рефлексы LaB₆, по которым учитывали инструментальные уширения пиков

Table 4. Calculated values of \bar{C}_{hkl}^e , \bar{C}_{hkl}^s and \bar{C}_{hkl} for coarse-grained and ECAP steel

Таблица 4. Рассчитанные для крупнокристаллической и подвергнутой РКУП стали значения \bar{C}_{hkl}^e , \bar{C}_{hkl}^s и \bar{C}_{hkl}

Plane (<i>hkl</i>)	\bar{C}_{hkl}^e	\bar{C}_{hkl}^s	\bar{C}_{hkl}			
			CG	ECAP, 4 passes	ECAP, 6 passes	ECAP, 8 passes
(110)	0.172182	0.118142	0.05568	0.06202	0.06469	0.06776
(200)	0.252323	0.37929928	0.35786	0.32378	0.30949	0.29300
(211)	0.172182	0.118138	0.05568	0.33083	0.06468	0.06776
(220)	0.172182	0.118142	0.05568	0.33084	0.05797	0.06776
(310)	0.223471	0.204317	0.16551	0.16960	0.17132	0.17330
(222)	0.145468	0.0732345	0.02200	0.02699	0.02908	0.03150

By drawing tangents to the obtained curves in the domain of small L values, D_{W-A} CSD size for the different structural states of steel was determined. Further, using the obtained Fourier coefficients $A^s(L)$, the dependence Y/L^2 vs $\ln L$ (Fig. 5 d) was plotted. From this dependence, in accordance with equation 4, the dislocation density was calculated. By approximating the curves (Fig. 5 d) to their intersection with the OY axis (at $\ln L=0$), the effective outer cut-off radius of dislocations R_e was determined. The resulting information on the fine structure parameters is presented in Table 5.

Analysis of Table 5 shows that an increase in the number of ECAP passes leads to a decrease in the lattice parameter, a decrease in the CSD parameter, an increase in the dislocation density, and a decrease in the proportion of screw-type disloca-

tions. At the same time, a decrease in the R_e and M values indicates an increase in dislocation dipole fields, and the nature of the mutual arrangement of dislocations becomes ordered.

Microstructure studies using small-angle X-ray scattering

To obtain dimensional characteristics of the precipitates (Fe_3C , $Me_{23}C_6$, Me_3C_2) identified during phase analysis, measurement and analysis of SAXS curves were carried out for the investigated states. Experimental SAXS curves for CG and UFG states of the steel, as well as an example of processed scattering curve after 8 ECAP passes, are shown in Fig. 6. Unlike the scattering curve for CG steel, the UFG SAXS curves are characterised by pronounced inflection

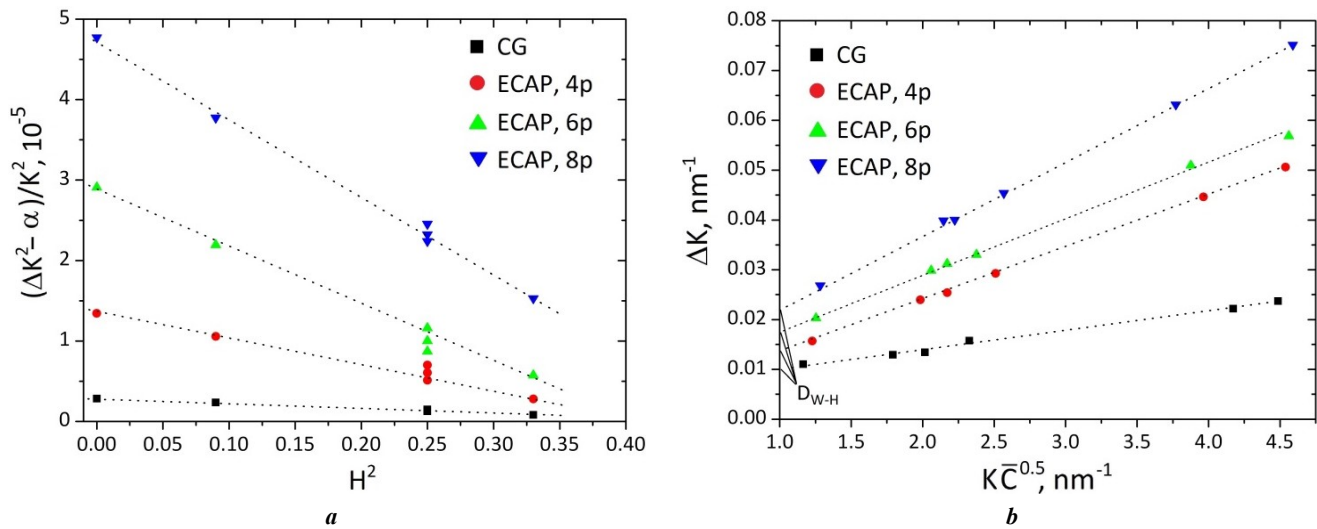


Fig. 4. Experimental dependencies for various structural states of steel

in the modified Williamson–Hall method: $a - \frac{\Delta K^2 - \alpha}{K^2}$ vs H^2 ; $b - \Delta K$ vs $K\bar{C}^{1/2}$

Рис. 4. Экспериментальные зависимости для различных структурных состояний стали

по модифицированной методике Вильямсона – Холла: $a - \frac{\Delta K^2 - \alpha}{K^2}$ от H^2 ; $b - \Delta K$ от $K\bar{C}^{1/2}$

Table 5. Fine structure parameters of steel in the initial state and after ECAP

Таблица 5. Параметры тонкой структуры стали в исходном состоянии и в состояниях после РКМП

State	a, nm	D _{W-H} , nm	D _{W-A} , nm	ρ , 10^{15} m^{-2}	f_s , %	R_e , nm	M
CG	0.286808±0.000012	229±20	356±24	0.11±0.03	83±4	184±15	1.94±0.11
ECAP, 4 passes	0.286769±0.000009	88±5	53±3	1.93±0.02	56±3	14±2	0.63±0.05
ECAP, 6 passes	0.286732±0.000011	79±4	48±2	2.68±0.02	45±3	8±1	0.41±0.04
ECAP, 8 passes	0.286692±0.000013	61±4	43±2	3.32±0.03	32±2	6±1	0.33±0.03

Note. a is the lattice parameter;

D_{W-H} is the CSD size found in modified Williamson–Hall (mW-H);

D_{W-A} is the CSD size found in modified Warren–Averbach (mW-A) technique; ρ is the dislocation density;

f_s is the fraction of screw-type dislocations; R_e is the effective outer radius of the dislocation cross-section;

M is the Wilkens parameter.

Примечание. a – параметр решетки;

D_{W-H} – размер ОКР, найденный по модифицированной методике Вильямсона – Холла;

D_{W-A} – размер ОКР, найденный по модифицированной методике Уоррена – Авербаха;

ρ – плотность дислокаций; f_s – доля дислокаций винтового типа; R_e – эффективный внешний радиус сечения дислокаций;

M – параметр Вилкенса.

points concentrated in the Guinier region (range 0.05 to 0.5 nm^{-1}) (Fig. 6 a). Moreover, in this region, the UFG steel scattering curves show a sharp decrease in intensity depending on scattering vector (Fig. 6 a).

It is known that the particle size is determined by the position of the Guinier region on the SAXS curve and particle morphology is determined through the dependence $I \sim q^{-\alpha}$, where α parameter equals 1, 2, 3, or 4 (particle shapes: $\alpha=1$ (cylinder), 2 (disk), 3 and 4 (sphere)) [24]. Analysis showed that, in the CG state,

the Guinier region is characterised by a dependence $I \sim 1/q$, indicating that the initial steel mainly contains particles of cylindrical shape. In the case of ECAP steel, it was found that the area from 0.05 to 0.5 nm^{-1} does not conform to the known dependences described above. Therefore, when analysing the SAXS curves of ECAP-processed steel, three types of particles differing in morphology (Table 3) were simultaneously fitted into the model. The result of such processing, e. g. for the 8 ECAP state, is shown in Fig. 6 b. It is evident that

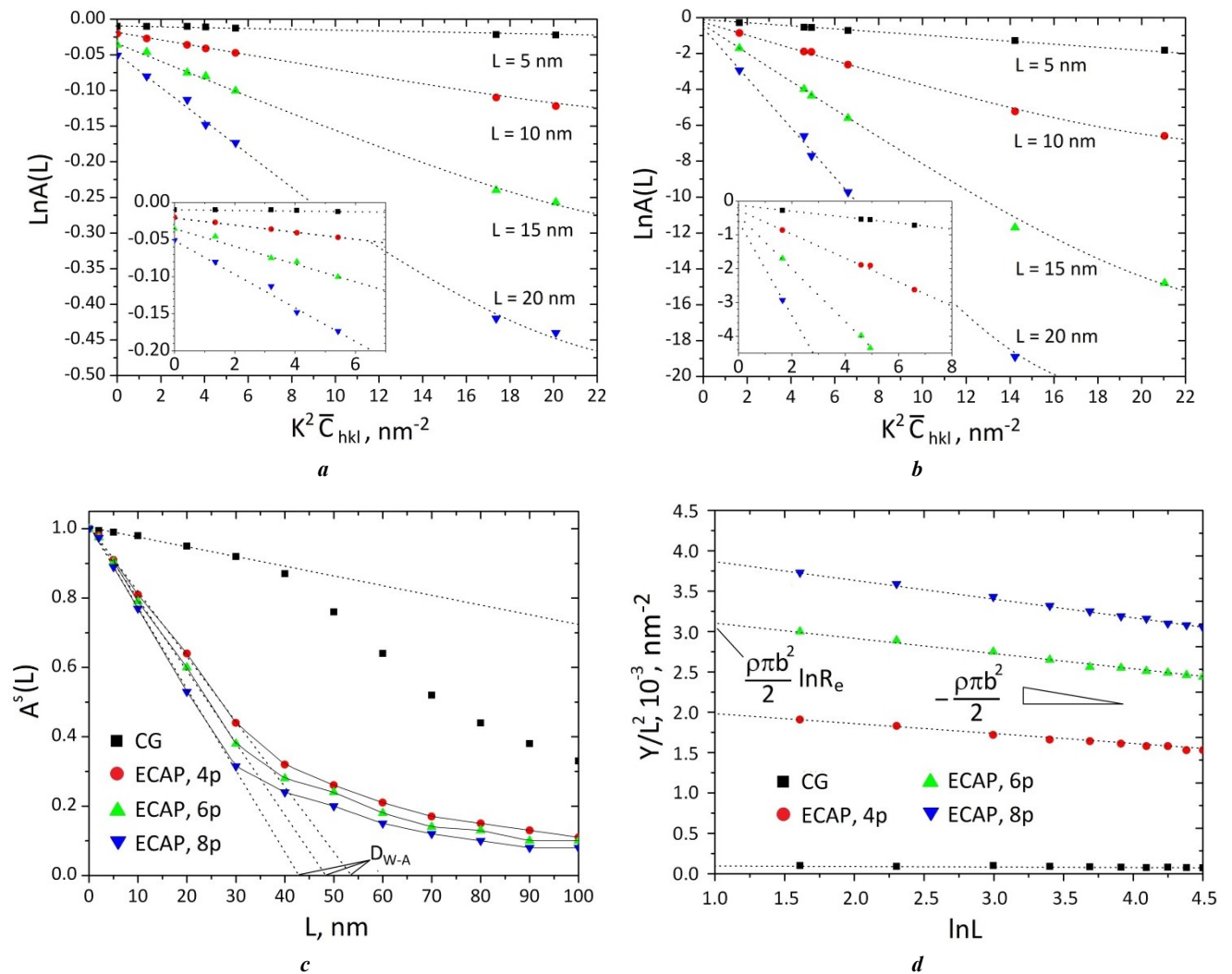


Fig. 5. Experimental dependencies for various structural states of steel in the modified Warren–Averbach method: **a** – $\ln A(L)$ on $K^2 \bar{C}$ for the initial steel; **b** – $\ln A(L)$ on $K^2 \bar{C}$ for UFG steel (8 ECAP passes); **c** – $A^s(L)$ patterns; **d** – $Y/L^2(\ln L)$ dependence for different structural states of steel.

The insets show enlarged areas where the $A^s(L)$ coefficients were found

Рис. 5. Экспериментальные зависимости для различных структурных состояний стали по модифицированной методике Уоррена – Авербаха:

a – $\ln A(L)$ от $K^2 \bar{C}$ для исходной стали; **b** – $\ln A(L)$ от $K^2 \bar{C}$ для ультрамелкозернистой стали (8 проходов ПКВП); **c** – закономерности $A^s(L)$; **d** – зависимость $Y/L^2(\ln L)$ для различных структурных состояний стали.

Во вставках показаны увеличенные области, по которым находили коэффициенты $A^s(L)$

this approach allows modelling satisfactory the experimental SAXS curves of the UFG steel leading to the determination of particle size and shape (Table 6).

Moreover, this analysis makes it possible to determine the contributions of individual particle types to the resulting SAXS intensity. Specifically, in Fig. 5 b, one can see that the SAXS intensity from cylindrical Fe_3C particles is higher than that from spherical Me_3C_2 -type particles. This fact indicates a higher fraction of cementite particles compared to Me_3C_2 -type particles, which is consistent with the data in Table 3.

The SAXS analysis revealed that the particle sizes in CG steel are significantly smaller than those in UFG steel (Table 6). Furthermore, an increase in the number of ECAP passes is accompanied by a growth in the sizes of cylindrical, elliptical and spherical particles.

DISCUSSION

The studies conducted on the steel subjected to ECAP demonstrated a significant increase in strength, a decrease in ductility and an increase in corrosion rate, which were caused directly by structural changes. In particular, it was found that ECAP treatment led to a reduction in ferrite grain size down to the nanometer range. Moreover, at higher degrees of ECAP processing, the grains themselves acquired an equiaxed shape. The grain refinement observed by microscopy methods during ECAP treatment is consistent with the reduction of the CSD size obtained by the mW-H and mW-A techniques (Table 5). The investigations also revealed that, along with structural refinement, a dynamic ageing process occurred after ECAP treatment of the steel. This fact is corroborated by evidence that, during the formation of the UFG structure of steel, the precipitation

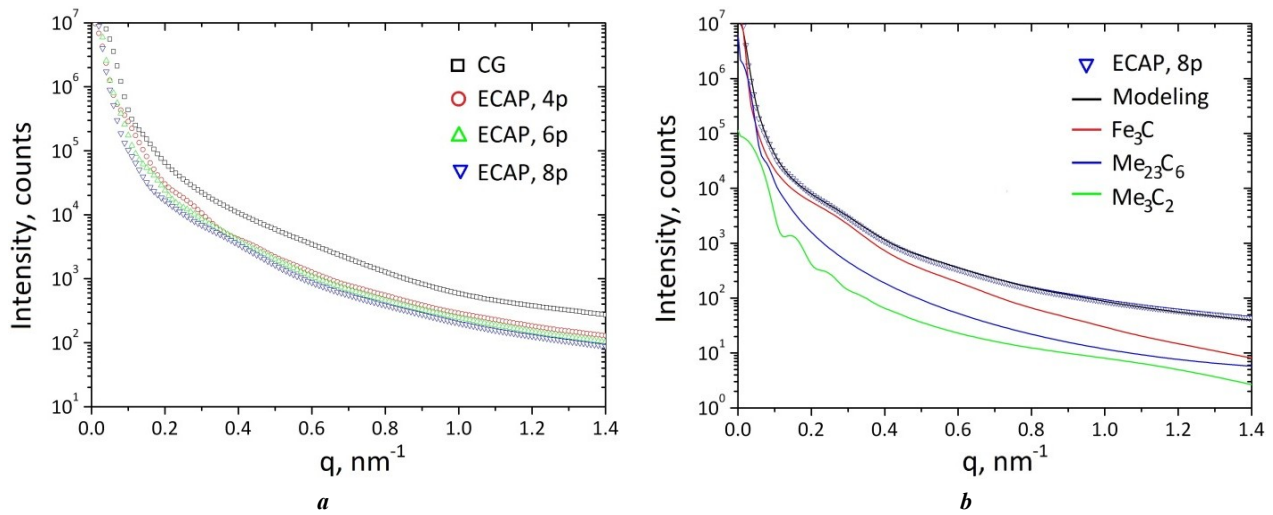


Fig. 6. Experimental small-angle X-ray scattering curves of steel:

a – general view of curves for different structural states;

b – processed small-angle X-ray scattering curve of steel (8 ECAP passes)

Рис. 6. Экспериментальные кривые малоуглового рентгеновского рассеяния стали:

a – общий вид кривых для различных структурных состояний;

b – обработанная кривая малоуглового рентгеновского рассеяния стали (8 проходов РКУП)

Table 6. Average size and morphology of precipitates obtained by small-angle X-ray scattering method.

Particle sizes are given in nanometers

Таблица 6. Средний размер и форма преципитатов, полученных методом малоуглового рентгеновского рассеяния.

Размерность частиц указана в нанометрах

State	Fe_3C	Me_{23}C_6	Me_3C_2
	Cylinder d/l	Ellipse a_1/a_2	Sphere d
CG	113/384	10/6	–
ECAP, 4 passes	157/431	57/34	31
ECAP, 6 passes	223/458	94/69	49
ECAP, 8 passes	259/460	139/98	72

and growth of Me_{23}C_6 - and Me_3C_2 -type precipitates, as well as a slight increase in the mass fraction of cementite particles were observed (Table 3). As a rule, the dynamic ageing process in steel should lead to the purification of the ferrite crystal lattice from impurity elements, which should be accompanied by a change in the lattice parameter of the base matrix. Indeed, the observed decrease in the ferrite lattice parameter confirms this (Table 5). It is known that the tabular value of the pure ferrite lattice parameter is 0.286 nm [25]. In the initial state, the presence of impurity elements in ferrite led to an increase in the lattice parameter up to 0.286808 nm (Table 5). However, after 8 ECAP passes, the lattice parameter decreased to 0.286692 nm, bringing it closer to the value characteristic of pure ferrite.

Along with the aforementioned changes, the microstructure of the steel after ECAP was characterised by a high density of introduced defects (Table 5). In particular, compared to the initial state, the dislocation density increased

significantly after 8 ECAP passes. At the same time, the dislocation type changed as well. Whereas in the initial state the dislocations were mainly of screw type, after 8 ECAP passes they predominantly consisted of edge-type dislocations (Table 5). The obtained data on the degree and type of structural defectiveness is consistent with previous studies [26; 27], according to which, under conditions of severe plastic deformation, an intense annihilation process of screw dislocations within the grain interiors occurs, while the accumulation of edge dislocations at grain boundaries increases and sometimes they form cell walls. To verify this theory, changes in R_e and M parameters were evaluated (Table 5). It is known [28] that R_e parameter characterises the degree of screening of the long-range strain fields of dislocations by adjacent dislocations. In this regard, the decrease in R_e value during ECAP indicates an increase in the degree of screening of dislocation long-range fields, which can result in the formation of dipoles. This phenom-

enon leads to correlated dislocation interactions, which, as is known, cause the formation of a cellular structure [29].

At the same time, the dimensionless Wilkens parameter $M = R_e \sqrt{\rho}$ characterises the mutual arrangement of dislocations within the grains and determines the strength of the dislocation dipole field [28]. In the initial CG state, the M parameter was close to 2, indicating a chaotic arrangement of dislocations and a weak dipole field. Conversely, after ECAP, this parameter dropped sharply ($M < 1$), indicating an ordered arrangement of dislocations in the steel structure. In general, the decrease in the Wilkens parameter after ECAP treatment indicates the formation of dislocation tangles and dislocation walls in the steel structure leading to the formation of a cellular structure [18]. Some areas of cellular structures within the ferrite grains were also revealed by TEM investigations (Fig. 1).

Thus, according to the obtained data, ECAP treatment leads to an increase in dislocation density, dipole field strength and the degree of dislocation ordering, which ultimately results in the formation of a cellular structure. Subsequently, the cellular structure transforms into grain boundaries [1]. In this context, ferrite grain refinement during ECAP proceeds according to the mechanism schematically shown in Fig. 7.

The conducted structural studies also make it possible to analyse and identify the causes of the increase in the corrosion rate of the steel subjected to ECAP. It is well known [1; 3] that UFG metallic materials are characterised by an increased volumetric fraction of grain boundaries due to grain refinement. The analysis showed that the grain boundaries in the UFG steel contain a high density of dislocations, predominantly of edge type. It is known that the diffusion coefficient along dislocation cores is several orders of magnitude higher compared to the lattice diffusion coefficient [30]. This circumstance leads to the fact that grain boundaries in the UFG steel should exhibit an enhanced diffusion coefficient. As a result, impurity atoms (H, O, S, etc.), which chemically react with Fe, may diffuse

along grain boundaries in the UFG steel much faster than in its CG analogue. Accordingly, it can be expected that the formation of the UFG structure with a high density of grain-boundary dislocations is the reason for the increased corrosion rate of the steel subjected to ECAP.

The obtained data on the microstructural parameters of the steel also enable the assessment of the contribution of individual strengthening mechanisms after ECAP processing. It is known that the tensile strength of steels is determined by the action of various strengthening mechanisms, including strengthening due to the initial yield stress σ_0 , grain-boundary strengthening σ_{gb} , precipitation strengthening σ_{pp} , solid solution strengthening σ_{ss} and dislocation strengthening σ_d [31]. Based on the obtained microscopy and XRD analysis data, a theoretical evaluation of individual strengthening mechanisms was performed and the resulting tensile strength was calculated. The comparative contribution of individual strengthening components to the resulting tensile strength is presented in Table 7.

When calculating the steel precipitation strengthening σ_{pp} in the CG state, two types of particles were considered, while three types were considered after ECAP processing and the total strengthening $\Sigma\sigma_{pp}$ was determined (Table 3, 6). As previously shown in [31], a theoretical evaluation of the resulting tensile strength requires the use of the root-mean-square $\sqrt{\sum \sigma_i^2}$ summation of the strengthening components. Accordingly, in the present study, the resulting tensile strength was calculated using this summation method. The calculated resulting tensile strength values for the studied states are given in Table 7. As can be seen from Table 7, the resulting tensile strength $\sqrt{\sum \sigma_i^2}$ values for the CG and ECAP-processed states of the steel are in good agreement with the experimental data (Table 2). The analysis of the strengthening mechanisms showed that in the UFG state, the increase in the tensile strength of the steel is primarily due to grain-boundary strengthening σ_{gb} (Table 7). The increase in the contribution of grain-boundary

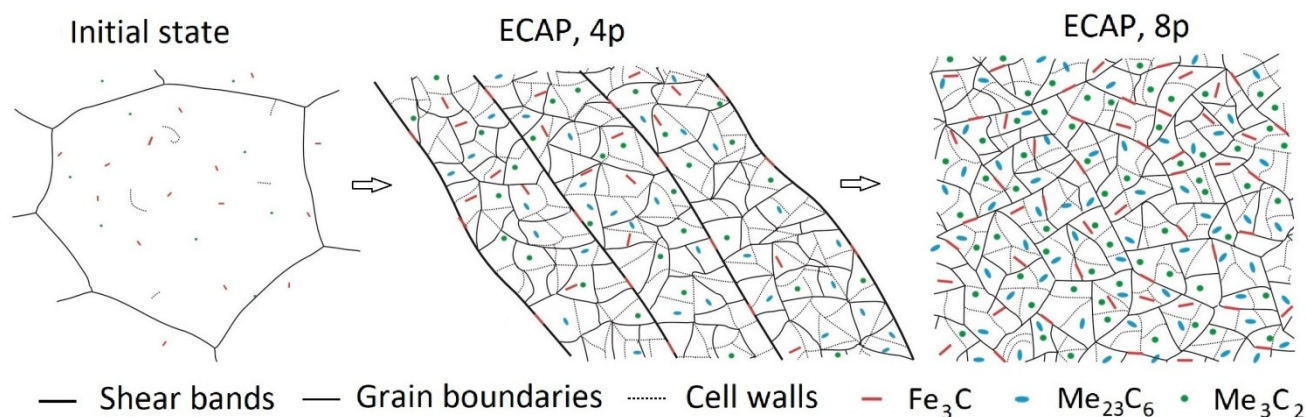


Fig. 7. Schematic representation of structure transformation during the formation of an ultrafine-grained state in low-carbon steel

Рис. 7. Схематичное изображение трансформации структуры при формировании ультрамелкозернистого состояния в низкоуглеродистой стали

Table 7. Contribution of different strengthening mechanisms in coarse-grained and ultrafine-grained states of low-carbon steel
Таблица 7. Вклад различных механизмов упрочнения в крупнокристаллическом и ультрамелкозернистом состояниях низкоуглеродистой стали

State	Calculated data, MPa					
	σ_o	σ_{gb}	$\Sigma\sigma_{pp}$	σ_{ss}	σ_d	$\sqrt{\Sigma\sigma_i^2}$
CG	50	300	268	75	88	419
ECAP, 4 passes	50	916	222	75	366	1015
ECAP, 6 passes	50	946	179	75	431	1059
ECAP, 8 passes	50	951	147	75	480	1079

Note. σ_o is yield stress; σ_{gb} is grain-boundary strengthening; σ_{pp} is precipitation strengthening; σ_{ss} is solid solution strengthening; σ_d is dislocation hardening.

Примечание. σ_o – напряжение течения; σ_{gb} – зернограницная прочность; σ_{pp} – дисперсионная прочность; σ_{ss} – прочность твердого раствора; σ_d – дислокационная прочность.

strengthening σ_{gb} after ECAP processing is realised, according to microscopy data, as a result of grain refinement down to the nanometric scale. Moreover, the dislocation strengthening mechanism σ_d also contributes to the enhancement of the tensile strength due to the increased dislocation density after ECAP (Table 5, 7). On the other hand, the contribution of precipitation strengthening $\Sigma\sigma_{pp}$ decreases during the formation of the UFG structure. The analysis showed that in the case of CG steel, the high value of $\Sigma\sigma_{pp}$ is achieved due to the presence of small-sized ellipsoidal Me_{23}C_6 particles (Table 6, 7). Meanwhile, the decrease in $\Sigma\sigma_{pp}$ during ECAP is explained by the growth of cementite, Me_{23}C_6 and Me_3C_2 particles.

CONCLUSIONS

A high-strength state (ultimate tensile strength of 1072 MPa) with satisfactory ductility (10.7 %) and a corrosion rate of 0.345 mm/year was achieved in the steel using the ECAP method. TEM and XRD analysis identified that the formation of the UFG state is accompanied by grain refinement down to 240 nm, an increase in the dislocation density (predominantly of edge type), precipitation and growth of Me_{23}C_6 and Me_3C_2 precipitates and the formation of a dislocation cell structure (reduction of the M parameter). In the CG state, steel strengthening is primarily provided by grain-boundary strengthening and the precipitation of relatively small-sized particles (cementite, Me_{23}C_6). The increase in the strength of UFG steel is mainly achieved as a result of grain refinement to the nanometric size and an increase in the dislocation density up to $3 \cdot 10^{15} \text{ m}^{-2}$. Precipitation strengthening in the UFG state decreases due to the growth in the mass fraction and size of Me_{23}C_6 and Me_3C_2 particles. The increase in the corrosion rate of the UFG steel is explained by the small size of ferrite grains containing a high density of grain-boundary dislocations and the presence of a dislocation cell structure.

REFERENCES

1. Zayed E.M., Shazly M., El-Sabbagh A., El-Mahallawy N.A. Deformation behavior and properties of severe plastic deformation techniques for bulk materials: A review. *Heliyon*, 2023, vol. 9, no. 6, article number e16700. DOI: [10.1016/j.heliyon.2023.e16700](https://doi.org/10.1016/j.heliyon.2023.e16700).
2. Enikeev N.A., Abramova M.M., Smirnov I.V., Mavlyutov A.M., Kim J.G., Lee C.S., Kim H.S. Performance of twinning-induced plasticity steel processed by multipass equal channel angular pressing at high temperatures. *Physical mesomechanics*, 2024, vol. 27, no. 6, pp. 698–709. DOI: [10.1134/S1029959924060079](https://doi.org/10.1134/S1029959924060079).
3. Figueiredo R.B., Langdon T.G. Deformation mechanisms in ultrafine-grained metals with an emphasis on the Hall–Petch relationship and strain rate sensitivity. *Journal of Materials Research and Technology*, 2021, vol. 14, pp. 137–159. DOI: [10.1016/j.jmrt.2021.06.016](https://doi.org/10.1016/j.jmrt.2021.06.016).
4. Kasaeian-Naeini M., Sedighi M., Hashemi R. Severe plastic deformation (SPD) of biodegradable magnesium alloys and composites: A review of developments and prospects. *Journal of Magnesium and Alloys*, 2022, vol. 10, no. 4, pp. 938–955. DOI: [10.1016/j.jma.2021.11.006](https://doi.org/10.1016/j.jma.2021.11.006).
5. Li Changsheng, Shao Zhibao, Li Kun, Peng Lianggui, Dong Jingbo. Mechanical properties and plastic deformation mechanisms of Fe–Cr–Ni–Mn–Mo–0.37/0.47 N low magnetic stainless-steel plates. *Materials Chemistry and Physics*, 2025, vol. 344, article number 131114. DOI: [10.1016/j.matchemphys.2025.131114](https://doi.org/10.1016/j.matchemphys.2025.131114).
6. Levitas V.I. Steady states in severe plastic deformations and microstructure at normal and high pressure. *Journal of Materials Research and Technology*, 2025, vol. 36, pp. 382–397. DOI: [10.1016/j.jmrt.2025.03.060](https://doi.org/10.1016/j.jmrt.2025.03.060).
7. Ranaware P.G. Effect of severe plastic deformation on aging kinetics of precipitation hardening 17–4 stainless steel. *Materials Today: Proceedings*, 2022, vol. 62, part 14, pp. 7600–7604. DOI: [10.1016/j.matpr.2022.04.783](https://doi.org/10.1016/j.matpr.2022.04.783).
8. Usmanov E.I., Rezyapova L.R., Valiev R.Z. High-strength state and strengthening mechanisms of ultrafine-grained

- titanium. *Physical Mesomechanics*, 2023, vol. 26, no. 5, pp. 483–494. DOI: [10.1134/s1029959923050016](https://doi.org/10.1134/s1029959923050016).
9. Cho Yeonggeun, Cho Hyung-Jun, Noh Han-Seop, Kim Sung-Ho, Kim Sung-Joon. Strengthening mechanism and martensite transformation behavior in grain-refined low-Ni austenitic stainless steel. *Materials Science and Engineering: A*, 2024, vol. 916, article number 147368. DOI: [10.1016/j.msea.2024.147368](https://doi.org/10.1016/j.msea.2024.147368).
10. Mohd Yusuf Sh., Chen Ying, Yang Shoufeng, Gao Nong. Microstructural evolution and strengthening of selective laser melted 316L stainless steel processed by high-pressure torsion. *Materials Characterization*, 2019, vol. 159, article number 110012. DOI: [10.1016/j.matchar.2019.110012](https://doi.org/10.1016/j.matchar.2019.110012).
11. Zrník J., Kraus L., Dobatkin S.V. Influence of Thermal Condition of ECAP on Microstructure Evolution in Low Carbon Steel. *Materials Science Forum*, 2007, vol. 558–559, part 1, pp. 611–616. DOI: [10.4028/0-87849-443-x.611](https://doi.org/10.4028/0-87849-443-x.611).
12. Zrník J., Lapovok R., Raab G.I. Prior thermo-mechanical processing to modify structure and properties of severely deformed low carbon steel. *IOP Conference Series: Materials Science and Engineering*, 2014, vol. 63, article number 012066. DOI: [10.1088/1757-899X/63/1/012066](https://doi.org/10.1088/1757-899X/63/1/012066).
13. Wang Jing Tao, Xu Cheng, Du Zhong Ze, Qu Guo Zhong, Langdon T.G. Microstructure and properties of a low-carbon steel processed by equal-channel angular pressing. *Materials Science and Engineering: A*, 2005, vol. 410–411, pp. 312–315. DOI: [10.1016/j.msea.2005.08.111](https://doi.org/10.1016/j.msea.2005.08.111).
14. Hajizadeh K., Kurzydowski K.J. On the possibility of fabricating fully austenitic sub-micron grained AISI 304 stainless steel via equal channel angular pressing. *Material Today Communications*, 2023, vol. 35, article number 105641. DOI: [10.1016/j.mtcomm.2023.105641](https://doi.org/10.1016/j.mtcomm.2023.105641).
15. Wauthier-Monnin A., Chauveau T., Castelnau O., Réglé H., Bacroix B. The evolution with strain of the stored energy in different texture components of cold-rolled IF steel revealed by high resolution X-ray diffraction. *Materials Characterization*, 2015, vol. 104, pp. 31–41. DOI: [10.1016/j.matchar.2015.04.005](https://doi.org/10.1016/j.matchar.2015.04.005).
16. Hao Ting, Tang Haiyin, Luo Guangnan, Wang Xianping, Liu Changsong, Fang Qianfeng. Enhancement effect of inter-pass annealing during equal channel angular pressing on grain refinement and ductility of 9Cr1Mo steel. *Materials Science and Engineering: A*, 2016, vol. 667, pp. 454–458. DOI: [10.1016/j.msea.2016.04.098](https://doi.org/10.1016/j.msea.2016.04.098).
17. Das Bakshi S., Sinha D., Ghosh Chowdhury S. Anisotropic broadening of XRD peaks of α' -Fe: Williamson–Hall and Warren–Averbach analysis using full width at half maximum (FWHM) and integral breadth (IB). *Materials Characterization*, 2018, vol. 142, pp. 144–153. DOI: [10.1016/j.matchar.2018.05.018](https://doi.org/10.1016/j.matchar.2018.05.018).
18. Das S.R., Shyamal S., Shee S.K., Kömi J.I., Sahu P. X-ray line profile analysis of the deformation microstructure in a medium-grained Fe–Mn–Al–C austenitic steel. *Materials Characterization*, 2021, vol. 172, article number 110833. DOI: [10.1016/j.matchar.2020.110833](https://doi.org/10.1016/j.matchar.2020.110833).
19. Schafner E., Zehetbauer M.J., Ungár T. Measurement of screw and edge dislocation density by means of X-ray Bragg profile analysis. *Materials Science and Engineering: A*, 2001, vol. 319–321, pp. 220–223. DOI: [10.1016/S0921-5093\(01\)00979-0](https://doi.org/10.1016/S0921-5093(01)00979-0).
20. Sitdikov V.D., Murashkin M.Yu., Valiev R.Z. Full-scale use of X-ray scattering techniques to characterize aged Al–2wt.%Cu alloy. *Journal of Alloys and Compounds*, 2018, vol. 735, pp. 1792–1798. DOI: [10.1016/j.jallcom.2017.11.282](https://doi.org/10.1016/j.jallcom.2017.11.282).
21. Gubicza J., Ungár T. Characterization of defect structures in nanocrystalline materials by X-ray line profile analysis. *Zeitschrift für Kristallographie – Crystalline Materials*, 2007, vol. 222, no. 11, pp. 567–579. DOI: [10.1524/zkri.2007.222.11.567](https://doi.org/10.1524/zkri.2007.222.11.567).
22. Ungár T., Dragomir I., Révész Á., Borbély A. The contrast factors of dislocations in cubic crystals: the dislocation model of strain anisotropy in practice. *Journal of Applied Crystallography*, 1999, vol. 32, pp. 992–1002. DOI: [10.1107/s0021889899009334](https://doi.org/10.1107/s0021889899009334).
23. Park Soon-Dong, Kim Sung Youb, Kim Daeyong. Ab initio investigations of the interfacial bond of Fe(001)/Al(001). *Materials Today Communications*, 2021, vol. 26, article number 102107. DOI: [10.1016/j.mtcomm.2021.102107](https://doi.org/10.1016/j.mtcomm.2021.102107).
24. Ren Yang, Zuo Xiaoding. Synchrotron X-Ray and Neutron Diffraction, Total Scattering, and Small-Angle Scattering Techniques for Rechargeable Battery Research. *Small Methods*, 2018, vol. 2, no. 8, article number 1800064. DOI: [10.1002/smt.201800064](https://doi.org/10.1002/smt.201800064).
25. Huan F., Larker R., Rubin P., Hedström P. Effect of Solute Silicon on the Lattice Parameter of Ferrite in Ductile Irons. *ISIJ International*, 2014, vol. 54, no. 1, pp. 248–250. DOI: [10.2355/isijinternational.54.248](https://doi.org/10.2355/isijinternational.54.248).
26. Mughrabi H. Dislocation wall and cell structures and long-range internal stresses in deformed metal crystals. *Acta Metallurgica*, 1983, vol. 31, no. 9, pp. 1367–1379. DOI: [10.1016/0001-6160\(83\)90007-x](https://doi.org/10.1016/0001-6160(83)90007-x).
27. Zehetbauer M. Cold work hardening in stages IV and V of F.C.C. metals – II. Model fits and physical results. *Acta Metallurgica et Materialia*, 1993, vol. 41, no. 2, pp. 589–599. DOI: [10.1016/0956-7151\(93\)90089-b](https://doi.org/10.1016/0956-7151(93)90089-b).
28. Ungár T., Révész Á., Borbély A. Dislocations and Grain Size in Electrodeposited Nanocrystalline Ni Determined by the Modified Williamson–Hall and Warren–Averbach Procedures. *Journal of Applied Crystallography*, 1998, vol. 31, pp. 554–558. DOI: [10.1107/S0021889897019559](https://doi.org/10.1107/S0021889897019559).
29. Wu R., Zaiser M. Cell structure formation in a two-dimensional density-based dislocation dynamics model. *Journal of Materials Science: Materials Theory*, 2021, vol. 5, article number 3. DOI: [10.1186/s41313-020-00025-x](https://doi.org/10.1186/s41313-020-00025-x).
30. Sauvage X., Enikeev N.A., Valiev R.Z., Nasedkina Y., Murashkin M.Yu. Atomic-scale analysis of the segregation and precipitation mechanisms in a severely deformed Al–Mg alloy. *Acta Materialia*, 2014, vol. 72, pp. 125–136. DOI: [10.1016/j.actamat.2014.03.033](https://doi.org/10.1016/j.actamat.2014.03.033).
31. Islamgaliev R.K., Nikitina M.A., Ganeev A.V., Sitdikov V.D. Strengthening mechanisms in ultrafine-grained ferritic/martensitic steel produced by equal channel angular pressing. *Materials Science and Engineering: A*, 2019, vol. 744, pp. 163–170. DOI: [10.1016/j.msea.2018.11.141](https://doi.org/10.1016/j.msea.2018.11.141).

СПИСОК ЛИТЕРАТУРЫ

1. Zayed E.M., Shazly M., El-Sabbagh A., El-Mahalawy N.A. Deformation behavior and properties of severe plastic deformation techniques for bulk materials: A review // *Heliyon*. 2023. Vol. 9. № 6. Article number e16700. DOI: [10.1016/j.heliyon.2023.e16700](https://doi.org/10.1016/j.heliyon.2023.e16700).
2. Еникеев Н.А., Абрамова М.М., Смирнов И.В., Мавлютов А.М., Ким Ю.Г., Ли Х.С., Ким Х.С. Поведение стали с пластичностью, наведенной двойнико-

- ванием, при многопроходном равноканальном угловом прессовании при повышенных температурах // Физическая мезомеханика. 2024. Т. 27. № 4. С. 85–99. DOI: [10.55652/1683-805X_2024_27_4_85-99](https://doi.org/10.55652/1683-805X_2024_27_4_85-99).
3. Figueiredo R.B., Langdon T.G. Deformation mechanisms in ultrafine-grained metals with an emphasis on the Hall–Petch relationship and strain rate sensitivity // *Journal of Materials Research and Technology*. 2021. Vol. 14. P. 137–159. DOI: [10.1016/j.jmrt.2021.06.016](https://doi.org/10.1016/j.jmrt.2021.06.016).
 4. Kasaeian-Naeini M., Sedighi M., Hashemi R. Severe plastic deformation (SPD) of biodegradable magnesium alloys and composites: A review of developments and prospects // *Journal of Magnesium and Alloys*. 2022. Vol. 10. № 4. P. 938–955. DOI: [10.1016/j.jma.2021.11.006](https://doi.org/10.1016/j.jma.2021.11.006).
 5. Li Changsheng, Shao Zhibao, Li Kun, Peng Lianggui, Dong Jingbo. Mechanical properties and plastic deformation mechanisms of Fe–Cr–Ni–Mn–Mo–0.37/0.47 N low magnetic stainless-steel plates // *Materials Chemistry and Physics*. 2025. Vol. 344. Article number 131114. DOI: [10.1016/j.matchemphys.2025.131114](https://doi.org/10.1016/j.matchemphys.2025.131114).
 6. Levitas V.I. Steady states in severe plastic deformations and microstructure at normal and high pressure // *Journal of Materials Research and Technology*. 2025. Vol. 36. P. 382–397. DOI: [10.1016/j.jmrt.2025.03.060](https://doi.org/10.1016/j.jmrt.2025.03.060).
 7. Ranaware P.G. Effect of severe plastic deformation on aging kinetics of precipitation hardening 17–4 stainless steel // *Materials Today: Proceedings*. 2022. Vol. 62. Part 14. P. 7600–7604. DOI: [10.1016/j.matpr.2022.04.783](https://doi.org/10.1016/j.matpr.2022.04.783).
 8. Усманов Э.И., Резяпова Л.Р., Валиев Р.З. Высокопрочное состояние и механизмы упрочнения титана с ультрамелкозернистой структурой // Физическая мезомеханика. 2023. Т. 26. № 3. С. 5–17. DOI: [10.55652/1683-805X_2023_26_3_5](https://doi.org/10.55652/1683-805X_2023_26_3_5).
 9. Cho Yeongeun, Cho Hyung-Jun, Noh Han-Seop, Kim Sung-Ho, Kim Sung-Joon. Strengthening mechanism and martensite transformation behavior in grain-refined low-Ni austenitic stainless steel // *Materials Science and Engineering: A*. 2024. Vol. 916. Article number 147368. DOI: [10.1016/j.msea.2024.147368](https://doi.org/10.1016/j.msea.2024.147368).
 10. Mohd Yusuf Sh., Chen Ying, Yang Shoufeng, Gao Nong. Microstructural evolution and strengthening of selective laser melted 316L stainless steel processed by high-pressure torsion // *Materials Characterization*. 2019. Vol. 159. Article number 110012. DOI: [10.1016/j.matchar.2019.110012](https://doi.org/10.1016/j.matchar.2019.110012).
 11. Zrník J., Kraus L., Dobatkin S.V. Influence of Thermal Condition of ECAP on Microstructure Evolution in Low Carbon Steel // *Materials Science Forum*. 2007. Vol. 558–559. Part 1. P. 611–616. DOI: [10.4028/0-87849-443-x.611](https://doi.org/10.4028/0-87849-443-x.611).
 12. Zrník J., Lapovok R., Raab G.I. Prior thermo-mechanical processing to modify structure and properties of severely deformed low carbon steel // *IOP Conference Series: Materials Science and Engineering*. 2014. Vol. 63. Article number 012066. DOI: [10.1088/1757-899X/63/1/012066](https://doi.org/10.1088/1757-899X/63/1/012066).
 13. Wang Jing Tao, Xu Cheng, Du Zhong Ze, Qu Guo Zhong, Langdon T.G. Microstructure and properties of a low-carbon steel processed by equal-channel angular pressing // *Materials Science and Engineering: A*. 2005. Vol. 410–411. P. 312–315. DOI: [10.1016/j.msea.2005.08.111](https://doi.org/10.1016/j.msea.2005.08.111).
 14. Hajizadeh K., Kurzydowski K.J. On the possibility of fabricating fully austenitic sub-micron grained AISI 304 stainless steel via equal channel angular pressing // *Material Today Communications*. 2023. Vol. 35. Article number 105641. DOI: [10.1016/j.mtcomm.2023.105641](https://doi.org/10.1016/j.mtcomm.2023.105641).
 15. Wauthier-Monnin A., Chauveau T., Castelnau O., Réglé H., Bacroix B. The evolution with strain of the stored energy in different texture components of cold-rolled IF steel revealed by high resolution X-ray diffraction // *Materials Characterization*. 2015. Vol. 104. P. 31–41. DOI: [10.1016/j.matchar.2015.04.005](https://doi.org/10.1016/j.matchar.2015.04.005).
 16. Hao Ting, Tang Haiyin, Luo Guangnan, Wang Xianping, Liu Changsong, Fang Qianfeng. Enhancement effect of inter-pass annealing during equal channel angular pressing on grain refinement and ductility of 9Cr1Mo steel // *Materials Science and Engineering: A*. 2016. Vol. 667. P. 454–458. DOI: [10.1016/j.msea.2016.04.098](https://doi.org/10.1016/j.msea.2016.04.098).
 17. Das Bakshi S., Sinha D., Ghosh Chowdhury S. Anisotropic broadening of XRD peaks of α' -Fe: Williamson–Hall and Warren–Averbach analysis using full width at half maximum (FWHM) and integral breadth (IB) // *Materials Characterization*. 2018. Vol. 142. P. 144–153. DOI: [10.1016/j.matchar.2018.05.018](https://doi.org/10.1016/j.matchar.2018.05.018).
 18. Das S.R., Shyamal S., Shee S.K., Kömi J.I., Sahu P. X-ray line profile analysis of the deformation microstructure in a medium-grained Fe–Mn–Al–C austenitic steel // *Materials Characterization*. 2021. Vol. 172. Article number 110833. DOI: [10.1016/j.matchar.2020.110833](https://doi.org/10.1016/j.matchar.2020.110833).
 19. Schafner E., Zehetbauer M.J., Ungár T. Measurement of screw and edge dislocation density by means of X-ray Bragg profile analysis // *Materials Science and Engineering: A*. 2001. Vol. 319–321. P. 220–223. DOI: [10.1016/S0921-5093\(01\)00979-0](https://doi.org/10.1016/S0921-5093(01)00979-0).
 20. Sitdikov V.D., Murashkin M.Yu., Valiev R.Z. Full-scale use of X-ray scattering techniques to characterize aged Al–2wt.%Cu alloy // *Journal of Alloys and Compounds*. 2018. Vol. 735. P. 1792–1798. DOI: [10.1016/j.jallcom.2017.11.282](https://doi.org/10.1016/j.jallcom.2017.11.282).
 21. Gubicza J., Ungár T. Characterization of defect structures in nanocrystalline materials by X-ray line profile analysis // *Zeitschrift für Kristallographie - Crystalline Materials*. 2007. Vol. 222. № 11. P. 567–579. DOI: [10.1524/zkri.2007.222.11.567](https://doi.org/10.1524/zkri.2007.222.11.567).
 22. Ungár T., Dragomir I., Révész Á., Borbély A. The contrast factors of dislocations in cubic crystals: the dislocation model of strain anisotropy in practice // *Journal of Applied Crystallography*. 1999. Vol. 32. P. 992–1002. DOI: [10.1107/s0021889899009334](https://doi.org/10.1107/s0021889899009334).
 23. Park Soon-Dong, Kim Sung Youb, Kim Daeyong. Ab initio investigations of the interfacial bond of Fe(001)/Al(001) // *Materials Today Communications*. 2021. Vol. 26. Article number 102107. DOI: [10.1016/j.mtcomm.2021.102107](https://doi.org/10.1016/j.mtcomm.2021.102107).
 24. Ren Yang, Zuo Xiaoding. Synchrotron X-Ray and Neutron Diffraction, Total Scattering, and Small-Angle Scattering Techniques for Rechargeable Battery Research // *Small Methods*. 2018. Vol. 2. № 8. Article number 1800064. DOI: [10.1002/smt.201800064](https://doi.org/10.1002/smt.201800064).
 25. Huyen F., Larker R., Rubin P., Hedström P. Effect of Solute Silicon on the Lattice Parameter of Ferrite in Ductile Irons // *ISI International*. 2014. Vol. 54. № 1. P. 248–250. DOI: [10.2355/isijinternational.54.248](https://doi.org/10.2355/isijinternational.54.248).
 26. Mughrabi H. Dislocation wall and cell structures and long-range internal stresses in deformed metal crystals // *Acta Metallurgica*. 1983. Vol. 31. P. 1367–1379. DOI: [10.1016/0001-6160\(83\)90007-x](https://doi.org/10.1016/0001-6160(83)90007-x).
 27. Zehetbauer M. Cold work hardening in stages IV and V of F.C.C. metals – II. Model fits and physical results // *Acta Metallurgica et Materialia*. 1993. Vol. 41. № 2. P. 589–599. DOI: [10.1016/0956-7151\(93\)90089-b](https://doi.org/10.1016/0956-7151(93)90089-b).

28. Ungár T., Révész Á., Borbély A. Dislocations and Grain Size in Electrodeposited Nanocrystalline Ni Determined by the Modified Williamson–Hall and Warren–Averbach Procedures // Journal of Applied Crystallography. 1998. Vol. 31. P. 554–558. DOI: [10.1107/S0021889897019559](https://doi.org/10.1107/S0021889897019559).
29. Wu R., Zaiser M. Cell structure formation in a two-dimensional density-based dislocation dynamics model // Journal of Materials Science: Materials Theory. 2021. Vol. 5. Article number 3. DOI: [10.1186/s41313-020-00025-x](https://doi.org/10.1186/s41313-020-00025-x).
30. Sauvage X., Enikeev N.A., Valiev R.Z., Nasedkina Y., Murashkin M.Yu. Atomic-scale analysis of the segregation and precipitation mechanisms in a severely deformed Al–Mg alloy // Acta Materialia. 2014. Vol. 72. P. 125–136. DOI: [10.1016/j.actamat.2014.03.033](https://doi.org/10.1016/j.actamat.2014.03.033).
31. Islamgaliev R.K., Nikitina M.A., Ganeev A.V., Sitdikov V.D. Strengthening mechanisms in ultrafine-grained ferritic/martensitic steel produced by equal channel angular pressing // Materials Science and Engineering: A. 2019. Vol. 744. P. 163–170. DOI: [10.1016/j.msea.2018.11.141](https://doi.org/10.1016/j.msea.2018.11.141).

УДК 691.714, 539.26

doi: 10.18323/2782-4039-2025-3-73-4

Микроструктура, свойства и механизмы упрочнения низкоуглеродистой стали, подвергнутой равноканальному угловому прессованию

Малинин Андрей Владимирович^{*1,3}, кандидат технических наук,
заместитель генерального директора по исследованиям

Ситдигов Виль Даянович^{1,4}, доктор физико-математических наук,
старший эксперт

Лебедев Юрий Анатольевич², кандидат физико-математических наук,
старший научный сотрудник

¹ООО «РН-БашНИПИнефть», Уфа (Россия)

²Институт физики молекул и кристаллов Уфимского федерального исследовательского центра РАН, Уфа (Россия)

*E-mail: MalininAV@bnipi.rosneft.ru

³ORCID: <https://orcid.org/0000-0003-1185-5648>

⁴ORCID: <https://orcid.org/0000-0002-9948-1099>

Поступила в редакцию 22.07.2025

Пересмотрена 29.07.2025

Принята к публикации 20.08.2025

Аннотация: В работе методом равноканального углового прессования (РКУП) (8 проходов, 200 °С) сформировано ультрамелкозернистое (УМЗ) состояние в низкоуглеродистой стали, демонстрирующее высокие механические свойства (предел текучести 1021 МПа, предел прочности 1072 МПа, пластичность 10,7 %) наряду с удовлетворительной коррозионной стойкостью (0,345 мм/год). Для объяснения причин повышения прочностных и изменения коррозионных свойств проанализирована микроструктура УМЗ стали методами электронной микроскопии и рентгеновского рассеяния. В частности, методами электронной микроскопии установлено измельчение структуры подвергнутой РКУП стали, в результате которого формируются равноосные зерна со средним размером ~240 нм. Модифицированные рентгеновские методики Вильямсона – Холла и Уоррена – Авербаха применены для получения закономерностей изменения размера областей когерентного рассеяния, плотности ρ и доли f_s дислокаций винтового типа, внешнего эффективного радиуса R_e сечения дислокаций и ряда других параметров в низкоуглеродистой стали в зависимости от числа проходов (степени деформации) РКУП. Методами рентгенофазового анализа и малоуглового рентгеновского рассеяния найдены закономерности изменения массовой доли, размера и морфологии различных преципитатов от числа проходов РКУП. На основе полученных данных предложена модель трансформации микроструктуры стали при формировании в ней УМЗ состояния. Обсуждаются механизмы упрочнения крупнокристаллической и УМЗ стали. Обнаружено, что в исходном состоянии прочность стали в основном обеспечивается за счет зернограницного упрочнения и выпадения преципитатов $Me_{23}C_6$ и Me_3C_2 малого размера. Показано, что при формировании УМЗ структуры стали прочность возрастает в результате зернограницного упрочнения и роста плотности дислокаций. Вклад в упрочнение преципитатов в УМЗ состоянии понижается, и это обусловлено их ростом при обработке РКУП. Выявлено, что увеличение скорости коррозии УМЗ стали объясняется уменьшением размера ферритных зерен, повышением плотности зернограницных дислокаций и формированием ячеистой структуры.

Ключевые слова: низкоуглеродистая сталь; феррит; равноканальное угловое прессование; ультрамелкозернистая структура; микроструктура; механизмы упрочнения; рентгеноструктурный анализ; скорость коррозии; малоугловое рентгеновское рассеяние.

Благодарности: Авторы выражают благодарность ПАО «НК «Роснефть» и ООО «РН-БашНИПИнефть» за предоставленную возможность проведения исследований. Авторы также благодарят доктора химических наук А.И. Волошина, кандидата физико-математических наук Ю.Б. Линд, кандидата технических наук Н.Р. Яркееву (ООО «РН-БашНИПИнефть») за обсуждение полученных результатов и ценные замечания при подготовке статьи.

Для цитирования: Малинин А.В., Ситдигов В.Д., Лебедев Ю.А. Микроструктура, свойства и механизмы упрочнения низкоуглеродистой стали, подвергнутой равноканальному угловому прессованию // Frontier Materials & Technologies. 2025. № 3. С. 51–65. DOI: 10.18323/2782-4039-2025-3-73-4.

In 2003, at the initiative of D. Merson and A. Vikarchuk and upon the recommendation of the Interstate Coordination Council for Physics of Strength and Plasticity, it was decided, every two years starting from 2004, to hold the "Physical Materials Science" International School (hereinafter – SPhM) hosted by Togliatti State University (TSU) in order to solve the issues of training and rejuvenation of personnel.

The need for the SPhM was justified by the fact that "at present, there is no scientific event where young scientists, employees of factory laboratories, postgraduate students, university professors, and other relevant skill profile employees could attend a course of lectures on the hottest issues of physical materials science and receive a competent advice of leading metal physicists".

Over the past 20 years, twelve SPhMs have taken place. During this time, dozens of prominent scientists from Russia (E. Kozlov, Yu. Golovin, A. Glezer, V. Betekhtin, R. Andrievsky), Ukraine (Yu. Milman, V. Gavriluk, D. Orlov), as well as V. Rubanik (Belarus), A. Vinogradov (Japan), Yu. Estrin (Australia), A. Weidner (Germany) and many others participated in it as visiting lecturers. The audience was more than one thousand specialists, among which at least 50 % are young researchers.

A distinctive feature of the SPhM is that following the results of each of them, based on the lecture materials, a new volume of the "Advanced Materials" educational guidance is published under the general editorship of D. Merson. Consequently, by the beginning of the 11th SPhM in September, 2023, the 10th volume was published, where A. Romanov, A. Kazakov, A. Makarov, M. Vyboyshchik, A. Kudrya, and other well-known scientists are the authors of the chapters.

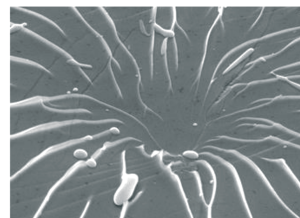
Another feature of the SPhM is the competition of works by young scientists, the winners of which (about 40 people) are granted relief both from the registration fee and from the residence fee. Moreover, each time the employees of the Research Institute of Advanced Technologies of TSU organize master classes for the SPhM participants, demonstrating the possibilities of the unique application of research equipment to solve materials science problems.

The SPhM is also famous for its remarkable performances, which are organized by efforts of its participants, who are talented in all respects.

Министерство образования Российской Федерации
Научный Совет РАН по физике конденсированных сред
Межгосударственный координационный совет
по физике прочности и пластичности материалов
Тольяттинский государственный университет

I Международная школа

«Физическое материаловедение»



**22–26 ноября 2004 года
Тольятти, Россия**

First information message

Special aspects of microstructure formation in Cu–Cr–Zr–Y bronze under low-temperature friction stir processing

Ivan S. Nikitin^{*1}, PhD (Engineering), junior researcher

of the Laboratory of Mechanical Properties of Nanostructured Materials and Superalloys

Aleksandr A. Kalinenko², PhD (Physics and Mathematics), junior researcher

of the Laboratory of Mechanical Properties of Nanostructured Materials and Superalloys

Sergey S. Malopheyev³, PhD (Engineering), senior researcher of the Laboratory

of Mechanical Properties of Nanostructured Materials and Superalloys

Sergey Yu. Mironov⁴, Doctor of Sciences (Physics and Mathematics), leading researcher

of the Laboratory of Mechanical Properties of Nanostructured Materials and Superalloys

Anna I. Bodyakova⁵, PhD (Physics and Mathematics), researcher

of the Laboratory of Mechanical Properties of Nanostructured Materials and Superalloys

Belgorod State University, Belgorod (Russia)

*E-mail: nikitin_i@bsuedu.ru

¹ORCID: <https://orcid.org/0000-0002-5417-9857>

²ORCID: <https://orcid.org/0000-0001-7534-0542>

³ORCID: <https://orcid.org/0000-0001-9145-3723>

⁴ORCID: <https://orcid.org/0000-0003-2202-1518>

⁵ORCID: <https://orcid.org/0000-0002-9378-0338>

Received 15.07.2025

Revised 26.08.2025

Accepted 09.09.2025

Abstract: The use of friction stir processing (FSP) to modify the physical and mechanical properties of age-hardenable low-alloyed bronzes is a promising and at the same time complex task due to the wide temperature range of its implementation. The difficulty is that friction stir processing of bronzes can result in the formation of fundamentally different types of microstructures with a wide range of grain sizes and various combinations of types of strengthening phases and their various morphologies. Moreover, options are possible when friction stir processing leads to degradation of properties of bronzes. A favorable combination of properties can be achieved by low-temperature friction stir processing. In this work, the main microstructural changes in promising Cu–Cr–Zr–Y bronze were analyzed during low-temperature friction stir processing with a tool rotation speed of 1000 rpm and a feed rate of 25 mm/min (ensuring a temperature in the stir zone of ≈ 350 °C). Scanning electron microscopy and EBSD analysis revealed the mechanisms of formation of an ultrafine-grained structure with predominantly high-angle boundaries, as well as the development of two types of simple shear crystallographic textures. It is shown that the Cu_x(Y,Zr) phase observed in the initial structure can undergo mechanical destruction or retain its geometric parameters depending on its initial morphology and location. It is shown for the first time that excess Cr particles (the equilibrium fraction at the heating temperature for quenching) may not be destroyed, but plastically deformed with a strong change in their morphology. During friction stir processing of the bronze under study, particles of a new Y-containing phase are released. The paper considered the relationship of the distribution of microhardness and electrical conductivity and the observed changes in the microstructure of a new promising material.

Keywords: friction stir processing; low-alloyed bronzes; recrystallization; secondary phases; electrical conductivity.

Acknowledgments: The study was supported by grant No. 24-29-00628 from the Russian Science Foundation (<https://rscf.ru/project/24-29-00628/>) using the equipment of the Common Use Center “Technology and materials of BSU”.

The paper was written on the reports of the participants of the XII International School of Physical Materials Science (SPM-2025), Togliatti, September 15–19, 2025.

For citation: Nikitin I.S., Kalinenko A.A., Malopheyev S.S., Mironov S.Yu., Bodyakova A.I. Special aspects of microstructure formation in Cu–Cr–Zr–Y bronze under low-temperature friction stir processing. *Frontier Materials & Technologies*, 2025, no. 3, pp. 67–80. DOI: 10.18323/2782-4039-2025-3-73-5.

© Nikitin I.S., Kalinenko A.A.,
Malopheyev S.S., Mironov S.Yu.,
Bodyakova A.I., 2025

INTRODUCTION

Friction stir processing (FSP) is one of the methods for increasing the strength characteristics of metallic materials by modifying the microstructure mainly due to grain refinement during dynamic recrystallization processes. Optimization of the FSP parameters of single-phase alloys aims to achieve a combination of two main characteristics: (1) to obtain a defect-free region and (2) to achieve grain refinement. The greatest difficulties arise with respect to alloys strengthened by particles of second phases, in particular by low-alloyed bronzes. For bronzes, defect-free processing zones can be obtained in a relatively wide temperature range ($0.27\text{--}0.77 T_{\text{melt}}$) [1–3], i.e. the process of friction stir processing can occur at various combinations of temperatures and deformation values. In this case, the process temperature will control the precipitation/dissolution and coarsening of particles of strengthening phases, as well as the size of dynamically recrystallized grains. In the works [2; 4], it is shown that a favorable combination of mechanical properties and electrical conductivity of Cu–Cr–Zr bronzes is achieved under the condition of carrying out the friction stir processing at temperatures near $0.27\text{--}0.40 T_{\text{melt}}$, which is close to the temperatures of artificial aging of bronzes [5–7]. Thus, a favorable combination of bronze properties can be obtained after friction stir processing at fairly low temperatures limiting the size of recrystallized grains and ensuring the precipitation or stability (within acceptable limits) of strengthening particles. Considering the rather narrow range of FSP temperatures ($0.27\text{--}0.40 T_{\text{melt}}$), at which favorable combinations of physical and mechanical properties are achievable, it is worth mentioning that, in addition to the FSP parameters, the second equally important factor is the initial state of the bronze microstructure. The possibility of refining Cu–Cr–Zr bronze grains to a range of ≈ 160 nm approaching the nanoscale was demonstrated in [8], while the formation of ultrafine grains of ≈ 300 nm was demonstrated in [4]. In the first case, quenched plates were used as the processed material [8], while in the second case, the alloy was aged to maximum strength [4]. In both studies, an increase in the hardness and strength of the alloys was observed; however, the effect of friction stir processing on the electrical conductivity was significantly different. Friction stir processing of quenched bronze increased the electrical conductivity from 34 to 38–50 % IACS [8]. This increase is relatively small compared to the effect of aging. Probably, in this case, the process temperature was lower than the temperatures of intense decomposition of the solid solution (the temperature was not measured). Friction stir processing of aged bronze led to a slight decrease in electrical conductivity from 80 to 70–74 % IACS due to partial dissolution of Cr particles and an increase in its content in the matrix [4]. As a result, the most promising idea is to conduct low-temperature friction stir processing of quenched bronze, which in the long term can eliminate the procedure of subsequent aging aimed at the formation of hardening phases.

Low-alloyed bronzes of the Cu–Cr–Zr system are used in a wide range of applications, for example, in

the manufacture of electrodes for contact welding, contact wires for railways, crystallizers for continuous casting of steel, liners in combustion chambers of rocket engines, blanket modules of thermonuclear reactors. A wide variety of applications allows believing that solid-phase FSP technology is promising in terms of modifying the structure, as well as the physical and mechanical characteristics of a number of critical parts.

Bronzes of the Cu–Cr–Zr–Y system are a new material; little research has been conducted on them. Therefore, it is very difficult to predict the behavior of this material during friction stir processing: to estimate the kinetics of grain refinement, phase composition, response of physical and mechanical characteristics to the evolution of the microstructure, which justifies significant scientific and practical interest in this work. Additional alloying of the Cu–Cr–Zr system bronze with Y was used for refining [9] and additional dispersion strengthening – in the Cu–Y system at temperatures below ≈ 900 °C, the solubility of Y in the matrix decreases [10]. It means that in quenched bronze with the addition of Y, upon subsequent heating to temperatures below ≈ 900 °C (during aging or heating during friction stir processing), the precipitation of strengthening phases is possible.

The aim of this work is to identify the main patterns of microstructure formation in bronze of the Cu–Cr–Zr–Y system under low-temperature friction stir processing and to assess the influence of microstructural changes on hardness and electrical conductivity.

METHODS

The material for the study was Cu–0.9%Cr–0.17%Zr–0.05%Y (wt. %) bronze. The initial state was obtained by forging a cast billet at temperatures of 850–1000 °C in air and cooling followed by heating to 920 °C (holding for 1 h) and cooling in water. After that, the billet was cut into 3 mm thick plates. Friction stir processing was carried out using a hemispherical tool with a pin diameter of 5 mm and flat shoulders with a diameter of 12 mm made of WC+Co hard alloy.

The FSP experiments were carried out on an AccuStir 1004 installation (USA) at a tool rotation speed of 1000 rpm and a feed rate of 25 mm/min with a tool tilt of $\approx 2.5^\circ$ and a penetration depth of 2.8 mm. The selected parameters are determined by the results of temperature measurements in a number of experiments on the friction stir processing at a rotation speed of 1000 rpm and varying feed rates (the mode with the lowest temperature and without external defects was selected). A sheet of 09G2S steel with a thickness of 4 mm was used as a substrate (a material under the bronze sheet).

Temperatures (thermal cycle) at the edge of the stir zone (SZ) were measured using a FLUKE 54 II B thermometer (USA) using chromel–alumel thermocouples. The temperature was measured at the middle of the sheet thickness. The measured maximum temperature of the friction stir processing did not exceed 350 °C.

Macro- and microstructure were studied on a transverse section after vibration polishing on a Buehler VibroMet 2 installation (USA) in an OP-U suspension for 24 h.

The macrostructure was analyzed after etching the polished sample in a mixture of 100 ml of 30 % H₂O₂ and 5 ml of H₂SO₄ using an Olympus GX51 optical microscope (Japan). The microstructure (in the Z-contrast mode) was studied using a Quanta 600 FEG scanning electron microscope (SEM) (USA) equipped with an attachment for energy-dispersive analysis of the composition and an EBSD attachment (an attachment for analyzing electron backscatter diffraction patterns).

In this work, two areas of the sample were studied: (1) the top of the SZ – at a distance of 50 µm from the surface of the processed zone and (2) the center of the SZ. For each of the states, EBSD maps of 50×50 µm in size with a scanning step of 0.1 µm were obtained. The data were processed and analyzed using TSL OIM Analysis 8 software. For texture analysis, EBSD maps were cleaned by removing all points with a CI (confidence index) of less than 0.1. To estimate the average grain size and grain misorientations, cleaning was performed using the standard "grain dilation" function with a minimum grain misorientation threshold of 15° and a minimum grain size of 3 pixels.

Vickers microhardness profiles were obtained in the middle of the FSP zone thickness using a Wolpert 402MVD microhardness tester (Netherlands) with a load of 100 g, a holding time of 10 s, and a measurement step of 0.25 mm.

The IACS relative conductivity (according to the International Annealed Copper Standard) was estimated as a percentage of the annealed copper conductivity of 58.1 mS/m at 20 °C:

$$\text{IACS} = \frac{100 \% \times \text{Bronze electrical conductivity}}{58.1}.$$

The relative conductivity profiles were obtained by the eddy current method using a Constant K-6 installation (RF) by taking measurements with a step of 1 mm from the surface of the plate perpendicular to the FSP direction after grinding on 1000 grit sandpaper.

Thermodynamic modeling of the equilibrium phase composition was carried out using the Thermo-Calc software package using the TCHEA4: High Entropy alloys v. 4.2 database.

RESULTS

Microstructure in the initial state

The microstructure of bronze in the initial state is represented by large grains with an average size of 64±35 µm (excluding twin boundaries), within which multiple annealing twins were observed (Fig. 1).

Most of the grain boundaries were decorated with a second phase interlayer, which stood out strongly against the matrix background in the Z-contrast mode in the form of light contrasting areas (Fig. 1 a). The composition assessment showed that these areas are enriched in Cu, Zr and Y with a total content of (Y+Zr) in the range of 8–15 at. %, as shown in Fig. 1 c. The detected phase can be designated by the formula Cu_x(Y,Zr), where *x* varies from 5.6 to 9.7. The study at high magnifications (Fig. 1 b) showed that

the light areas have an uneven contrast, which is associated with the heterogeneity of the Zr distribution (Fig. 1 b, d). In addition to the grain boundary arrangement, a (Y+Zr)-rich phase in the form of spherical inclusions with sizes from 4 to 18 µm (Fig. 1 c) was observed in the grain body. In some cases, the inclusions were located on black particles.

The microstructure also contained multiple homogeneously distributed particles with an average size of 1.02±0.78 µm with a black contrast, which were enriched with 78–98 at. % of Cr (Fig. 1).

Macrostructure after friction stir processing

The macrostructure of the sample after the friction stir processing is represented by different zones, which include the stir zone (SZ), the thermo-mechanically affected zone (TMAZ), and the base material zone, which is schematically shown in Fig. 2. Fig. 2 a shows the location of the stirring tip relative to the observed zones showing that the stir zone is not limited by the pin size, but expands towards the edges of the tool shoulders. Along the entire periphery of the stir zone, there is a TMAZ (Fig. 2 b, d) represented by fibers of elongated grains, followed by the main material zone with large grains.

Three types of inclusions are observed in all macrostructural zones of the treated area (Fig. 2 e, f, g): (1) gray spherical particles, (2) black areas of irregular morphology and (3) black spherical particles with internal inclusions and a contrast close to the matrix.

Microstructure and crystallographic texture after friction stir processing

The microstructure of bronze after FSP is represented by submicron grains with a fraction of high-angle boundaries of about 0.85 both at the top and in the center of the SZ – Fig. 3, 4 and Table 1. According to the data obtained by SEM, the average grain size in both areas of the SZ was ≈0.28 µm, while according to the EBSD results – ≈0.35–0.40 µm. Comparison of the size distribution shows that the measured values fall into the same size range from 0.15 to 0.8–1.0 µm and differ only in the intensities of each of the size groups, which is also reflected in the overlap of the average sizes taking into account the standard deviation of the value (Table 1). It means that the presented data are representative and reliable. The grains have a deviation from equiaxiality, as evidenced by the shape factor (SF) value equal to 1.99 for the top and 1.82 for the center of the SZ. In general, the friction stir processing leads to a decrease in the average grain size by 200 times.

The obtained experimental distributions of the misorientation angles of the top and center of the SZ are qualitatively similar to each other (Fig. 5). The distribution is characterized by the presence of two main maxima at small (≈2.5°) and large (≈45°) angles of misorientations with an intensity of up to 4 %. The experimental distribution of misorientation angles, random distribution and texture-induced distribution show the presence of a maximum in the angle range near ≈45°.

It is believed that the deformation scheme under FSW/FSP is close to the simple shear scheme [15], in this case, the shear surface can be the surface of the hemispherical

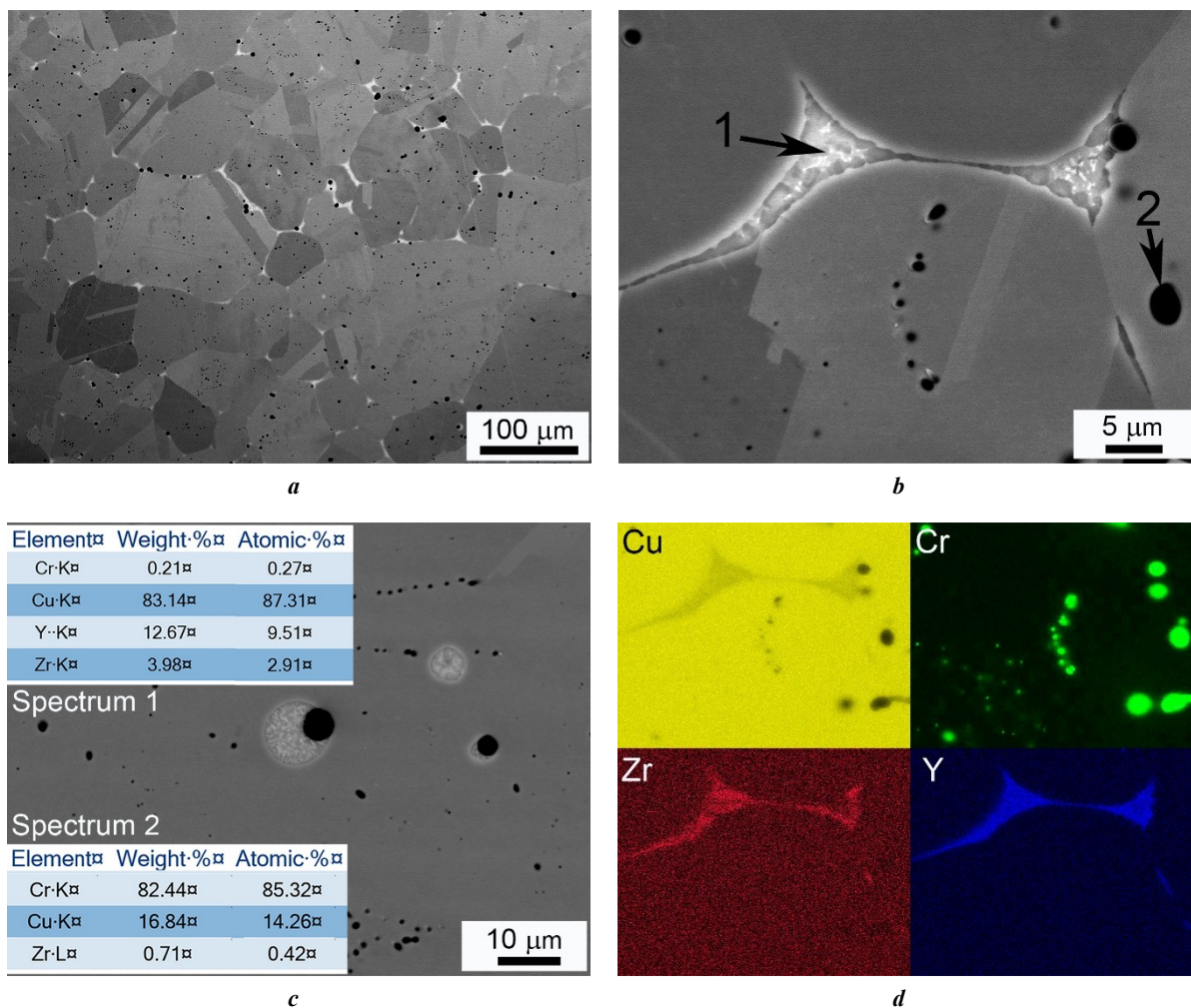


Fig. 1. Microstructure of bronze in initial state:

a – general view at $\times 500$ magnification; **b** – grain boundary phase and particles in the grain body at $\times 6000$ magnification; **c** – (Y+Zr)-enriched inclusions in the grain body and chemical compositions of the grain boundary phase (spectrum 1) and particles in the grain body (spectrum 2); **d** – distribution of elements in Fig. 1 b between phases

Рис. 1. Микроструктура бронзы в исходном состоянии:

a – общий вид при увеличении $\times 500$; **b** – зернограничная фаза и частицы в теле зерна при увеличении $\times 6000$; **c** – (Y+Zr)-обогащенные включения в теле зерна и химические составы зернограничной фазы (спектр 1) и частицы в теле зерна (спектр 2); **d** – распределение элементов на рис. 1 b между фазами

pin or the lower surface of the shoulders, while the shear direction is tangential to the tool surface. Thus, the shear geometry varies greatly in different parts of the SZ. To reveal the crystallographic texture in the sample, it is necessary to rotate the EBSD map. Experimental and corrected maps with rotation angles relative to different directions are shown in Fig. 6. Pole figure analysis showed that the entire SZ exhibits the formation of a combination of axial $\langle 110 \rangle$ and limited B/\bar{B} $\{112\} \langle 110 \rangle$ simple shear textures.

Analysis of secondary phases revealed the following features. Both at the top and in the center of the SZ after FSP, contrasting spherical inclusions were observed, which were previously observed in the initial state (Fig. 7). It is worth noting that grain boundary phases were not observed. For visual comparison, the micrographs in Fig. 1 a and Fig. 7 are presented at the same magnification ($\times 500$). The main differences between the top and center of the SZ are that at the top of the stir zone, contrasting white banded

structures elongated along the direction of rotation were observed.

During the initial analysis of the microstructure by the SEM method in the Z-contrast mode at high magnifications, contrasting black bands were observed in the studied zones of the sample (Fig. 8 a, b), the direction of which coincided with the direction of tool rotation. Such bands could have unclear outlines and bend repeatedly. Analysis of the distribution maps of the alloy components (Fig. 8 c, d, e, f, g, h) revealed that these are strongly deformed particles "smeared" between the matrix layers, enriched with Cr. After FSP, Cr particles had a wide variety of morphologies, ranging from large spherical particles to repeatedly bending plates and particles of variable shape, which differed much from the morphology of Cr particles of predominantly spherical shape in the initial state (Fig. 1).

In the microstructure of the studied zones after FSP, a few particles of a new phase enriched in Y were detected

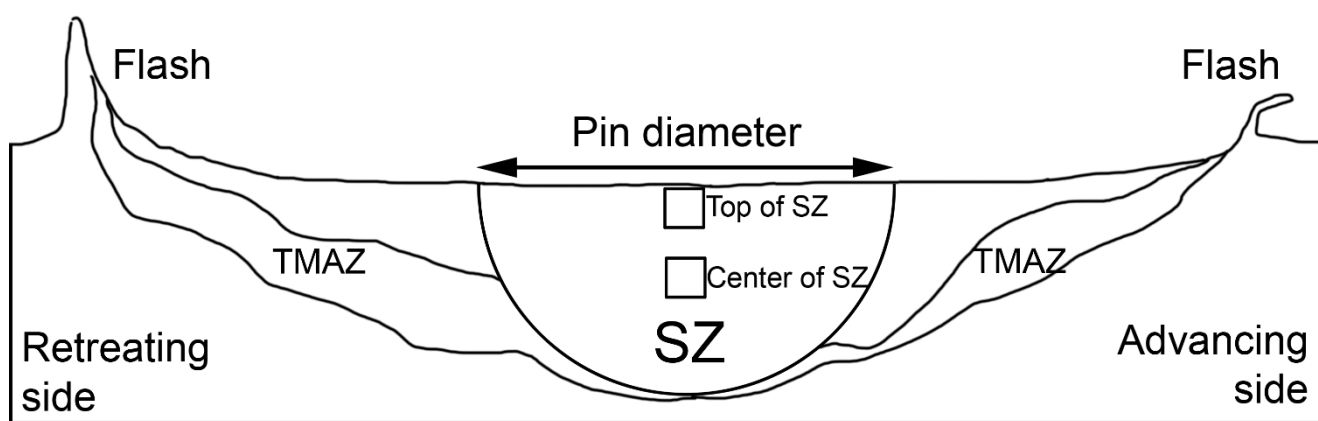
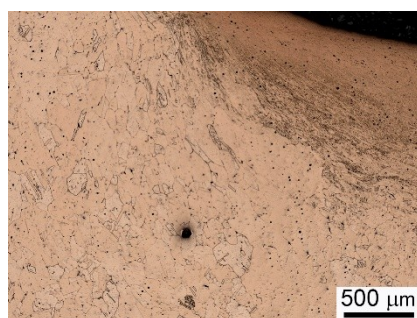
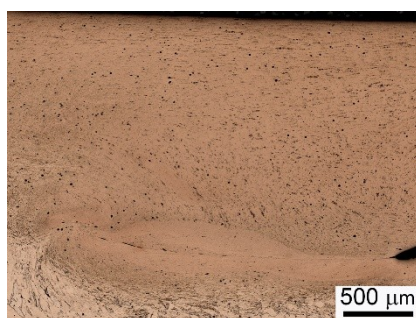
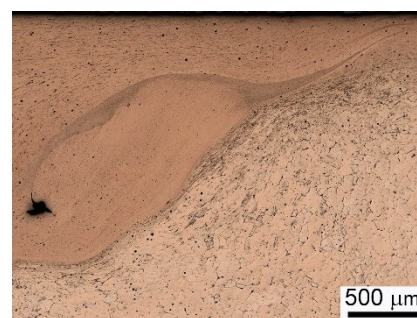
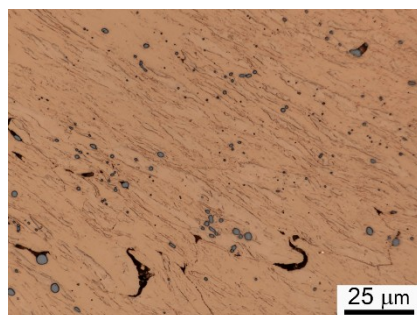
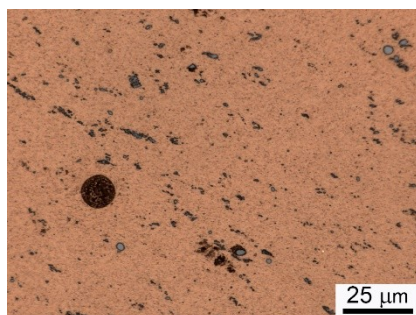
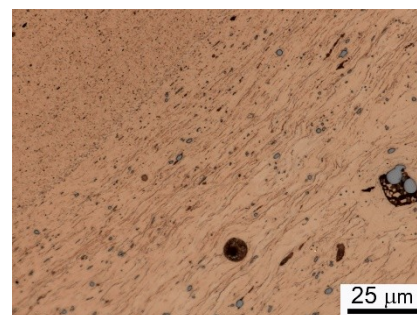
*a**b**c**d**e**f**g*

Fig. 2. Schematic arrangement of macrostructural zones of the studied sample and images of individual zones (optical microscopy):
a – diagram of macrostructural zones; *b, e* – thermo-mechanically affected zones (TMAZ) on the material retreating side at magnifications of $\times 5$ and $\times 100$; *c, f* – stir zones (SZ) at magnifications of $\times 5$ and $\times 100$; *d, g* – TMAZ on the material advancing side at magnifications of $\times 5$ and $\times 100$

Рис. 2. Схема расположения макроструктурных зон исследуемого образца и изображения отдельных зон (оптическая микроскопия): *a* – схема макроструктурных зон; *b, e* – зоны термомеханического влияния (TMAZ) со стороны отвода материала при увеличении $\times 5$ и $\times 100$; *c, f* – зоны перемешивания (SZ) при увеличении $\times 5$ и $\times 100$; *d, g* – TMAZ со стороны набегающего материала при увеличении $\times 5$ и $\times 100$

(Fig. 8 a, b, e, f), while traces of the presence of Zr (Fig. 8 a, b, g, h) were not observed in these particles.

Microhardness and electrical conductivity after friction stir processing

The treated zone was characterized by a non-uniform distribution of microhardness and electrical conductivity (Fig. 9) with a smooth increase in the characteristics in the direction from the material retreating side (RS) to the material advancing side (AS) and their sharp decrease at the boundary of the SZ at the stirring tip interface.

Almost the entire width of the zone of changed microhardness and electrical conductivity corresponds to the diameter of the tool shoulders, which indicates that most of the heat is concentrated under the tool and the heat-affected zone practically does not extend beyond its boundaries.

Extreme values of microhardness and electrical conductivity were observed at the edge of the SZ with AS and reached ≈ 240 HV and ≈ 76 % IACS. In the center of the SZ, the indicators were lower and corresponded to ≈ 167 HV and ≈ 72 % IACS, which is 2.9 and 1.6 times higher than the values in the initial state (≈ 58 HV and ≈ 45 % IACS).

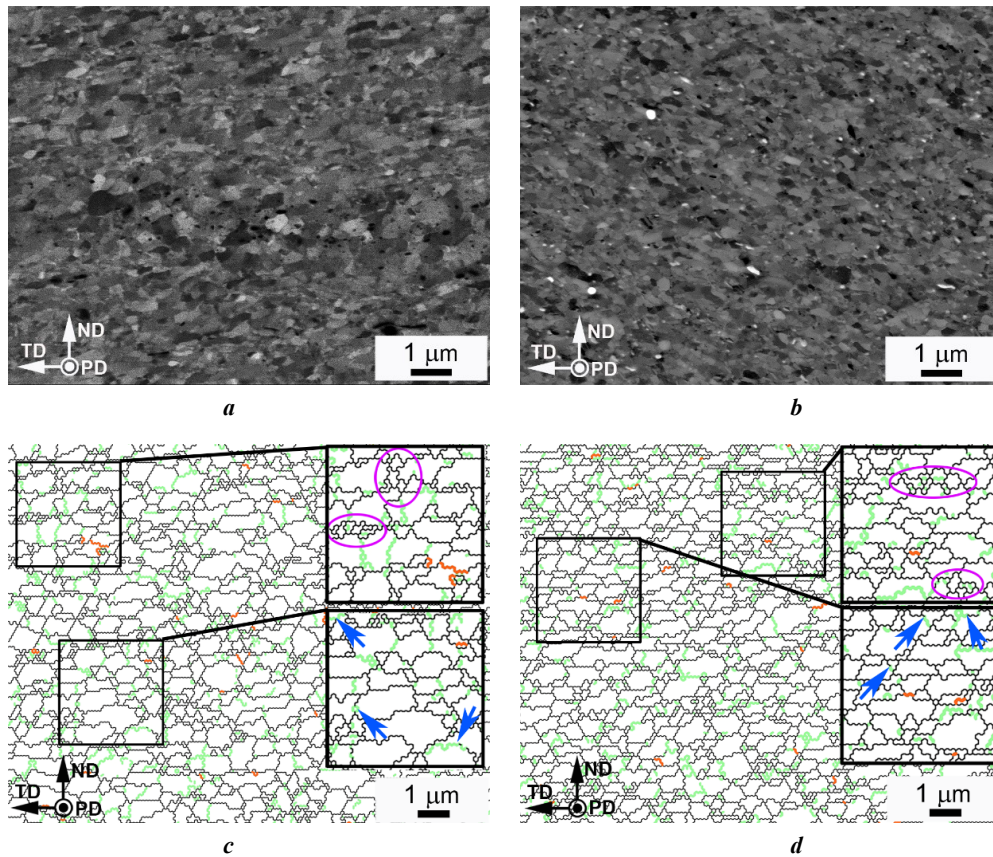


Fig. 3. Microstructure after friction stir processing at the top and center of the stir zone (SZ): SEM micrographs of the top (a) and center of the SZ (b); EBSD maps of the top (c) and center of the SZ (d).

On the maps, low-angle misorientation ($2\text{--}15^\circ$) boundaries are shown in green, high-angle misorientation ($15\text{--}63^\circ$) boundaries are shown in black, and $60^\circ\langle 111 \rangle$ twin boundaries are shown in red.

Blue arrows (c, d) highlight low-angle boundaries that progress in misorientation to high-angle boundaries.

Groups of small grains at the boundaries between relatively large grains are outlined in purple.

The PD, ND, and TD designations correspond to the processing direction, normal direction, and transverse direction

Рис. 3. Микроструктура после обработки трением с перемешиванием сверху и в центре зоны перемешивания (ЗП): микрофотографии РЭМ верха (a) и центра ЗП (b); EBSD-карты верха (c) и центра ЗП (d).

На картах границы малоугловой разориентировки ($2\text{--}15^\circ$) обозначены зеленым цветом, границы большеугловой разориентировки ($15\text{--}63^\circ$) обозначены черным цветом, двойниковые границы $60^\circ\langle 111 \rangle$ обозначены красным цветом. Синими стрелками (c, d) выделены малоугловые границы, набирающие свою разориентировку до большеугловых границ. Фиолетовым цветом обведены группы мелких зерен на границах между относительно крупными зёрнами.

Обозначения PD, ND и TD соответствуют направлению обработки, направлению нормали и поперечному направлению

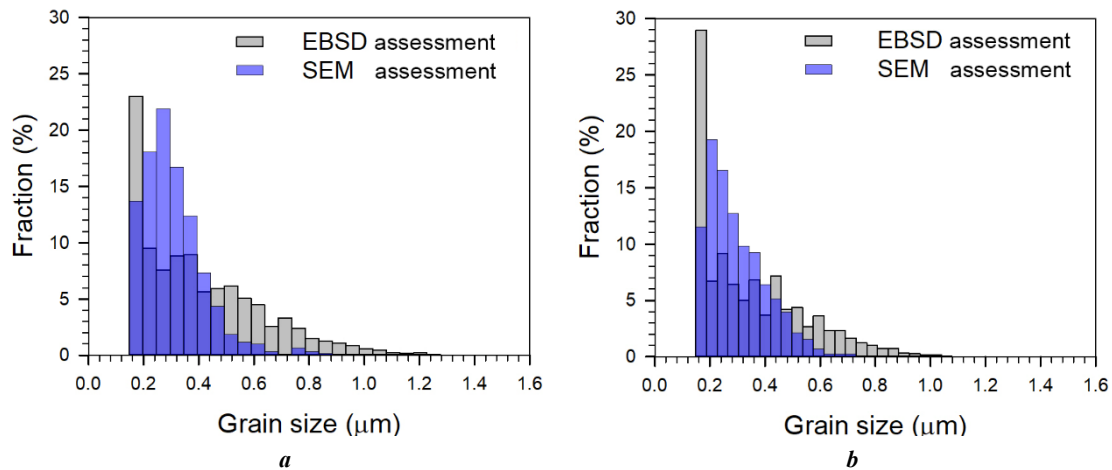


Fig. 4. Grain size distribution after friction stir processing at the top (a) and center (b) of the stir zone

Рис. 4. Размерное распределение зерен после обработки трением с перемешиванием сверху (a) и в центре (b) зоны перемешивания

Table 1. Microstructure parameters after friction stir processing**Таблица 1.** Параметры микроструктуры после обработки трением с перемешиванием

Stir zone area	d_{av} (EBSD) (μm)	d_{av} (SEM) (μm)	SF (SEM)	F_{HAB}/F_{LAB}	θ_{av} (deg)
Top of the stir zone	0.40 ± 0.23	0.28 ± 0.11	1.99	0.86/0.14	36.4
Center of the stir zone	0.35 ± 0.19	0.28 ± 0.11	1.82	0.84/0.16	36.0

Note. d_{av} is average grain size; SF is grain shape factor as the ratio of the maximum size to the minimum one;

F_{HAB} and F_{LAB} are fractions of high-angle and low-angle boundaries; θ_{av} is average angle of misorientation of boundaries.

Примечание. d_{av} – средний размер зерна; SF – коэффициент формы зерна в виде отношения максимального размера к минимальному; F_{HAB} и F_{LAB} – доли большеугловых и малоугловых границ; θ_{av} is средний угол разориентировки границ.

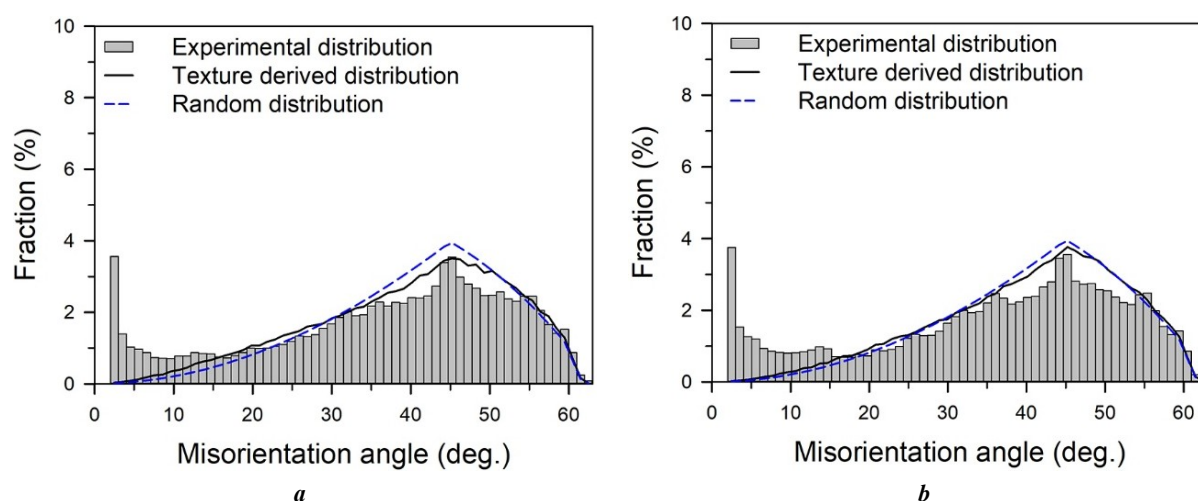
**Fig. 5.** Distribution of misorientation angles after friction stir processing at the top (a) and in the center (b) of the stir zone

Рис. 5. Распределение углов разориентировки после обработки трением с перемешиванием сверху (a) и в центре (b) зоны перемешивания

DISCUSSION

Characteristics of phase composition in the initial state

A phase containing 8–15 at. % of (Y+Zr) designated $\text{Cu}_x(\text{Y,Zr})$ with an x parameter varying from 5.6 to 9.7 was detected in the microstructure of bronze after quenching. According to sources [10; 11], it can be classified as a $\text{Cu}_6\text{Y}/\text{Cu}_7\text{Y}$ -type phase with a hexagonal crystal lattice of the P6/mmm type. This phase can dissolve 12–16 at. % of Y, which is consistent with the total (Y+Zr) content reported in the study. The heterogeneity of the Zr distribution within the grain boundary phase shown in Fig. 1 may be caused by the dendritic heterogeneity in the phase composition or by the presence of multiple phases within the structure of Y- and Zr-rich regions. A similar phenomenon was illustrated in [12] using the example of $\text{Cu}-0.5\text{Y}-(0.05-0.1)\text{Zr}$ alloys, in which particles consisting of metastable $\text{Cu}_5\text{Y}+\text{Cu}_5\text{Zr}$ phases are formed during casting. Considering the fact that the average (Y+Zr) contents determined in the study are also similar to the compositions of the $\text{Cu}_5\text{Y}+\text{Cu}_5\text{Zr}$ phases [12], we cannot exclude the possibility that a metastable phase is observed in the case under consideration.

The second phase observed in the microstructure consists predominantly of Cr. Considering the large size of the particles and the fact that they are observed in the quenched state, they are likely equilibrium particles of the body-centered cubic lattice of Cr [13], which did not dissolve during heating and holding during quenching. The presence of these particles is in good agreement with the equilibrium diagram of Cu–Cr state at a heating temperature for quenching of 920 °C [14].

Characteristics of grain structure and texture formation after FSP

An ultrafine-grained structure with an average grain size of $\approx 0.3 \mu\text{m}$ forms in the upper and central parts of the SZ. To determine the dominant recrystallization mechanism responsible for microstructure formation, we consider the distribution of misorientation angles of the formed grains in different regions of the stir zone (Fig. 5). Comparison with the results of other studies on FSW/FSP of bronzes of the Cu–Cr–Zr system [2–4] indicates that the low fraction of 2–3° of boundaries is associated with a decrease in the process temperature: at a temperature of 790 °C, the relative fraction of such boundaries is $\approx 18\%$ [3], at 440 °C,

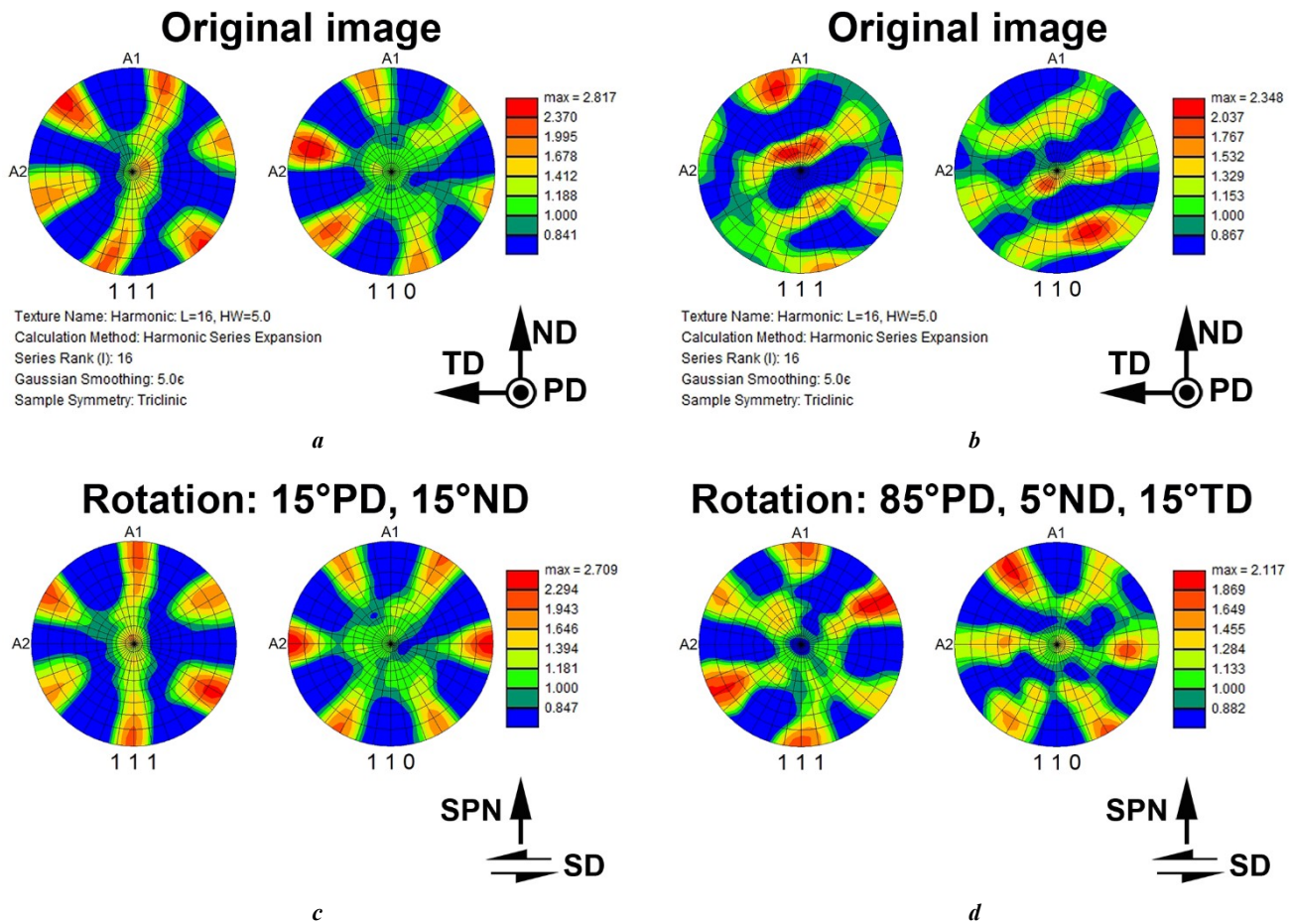


Fig. 6. Experimental (a, b) and corrected (rotated) pole figures (c, d) of {111} and {110} obtained after friction stir processing at the top (a, c) and center (b, d) of the stir zone, illustrating the formed texture. The PD, ND, and TD designations (a, b) correspond to the processing direction, normal direction, and transverse direction. The SD and SPN designations (c, d) correspond to the shear direction and the shear plane normal direction. The rotation angles of the experimental pole figures are indicated at the top of the figure.

Рис. 6. Экспериментальные (a, b) и скорректированные (развернутые) полюсные фигуры (c, d) {111} и {110}, полученные после обработки трением с перемешиванием вверху (a, c)

и в центре (b, d) зоны перемешивания, иллюстрирующие сформировавшуюся текстуру.

Обозначения PD, ND и TD (a, b) соответствуют направлению обработки, направлению нормали и поперечному направлению.

Обозначения SD и SPN (c, d) соответствуют направлению сдвига и направлению нормали к плоскости сдвига.

В верхней части рисунка указаны углы разворота экспериментальных полюсных фигур

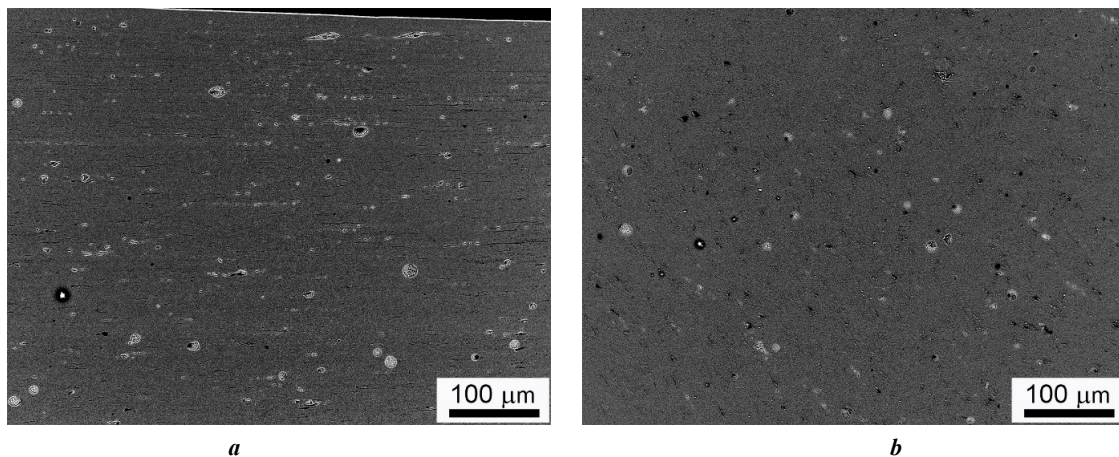


Fig. 7. Microstructure after friction stir processing at the top (a) and center (b) of the stir zone at $\times 500$ magnification

Рис. 7. Микроструктура после обработки трением с перемешиванием вверху (a) и в центре (b) зоны перемешивания при увеличении $\times 500$

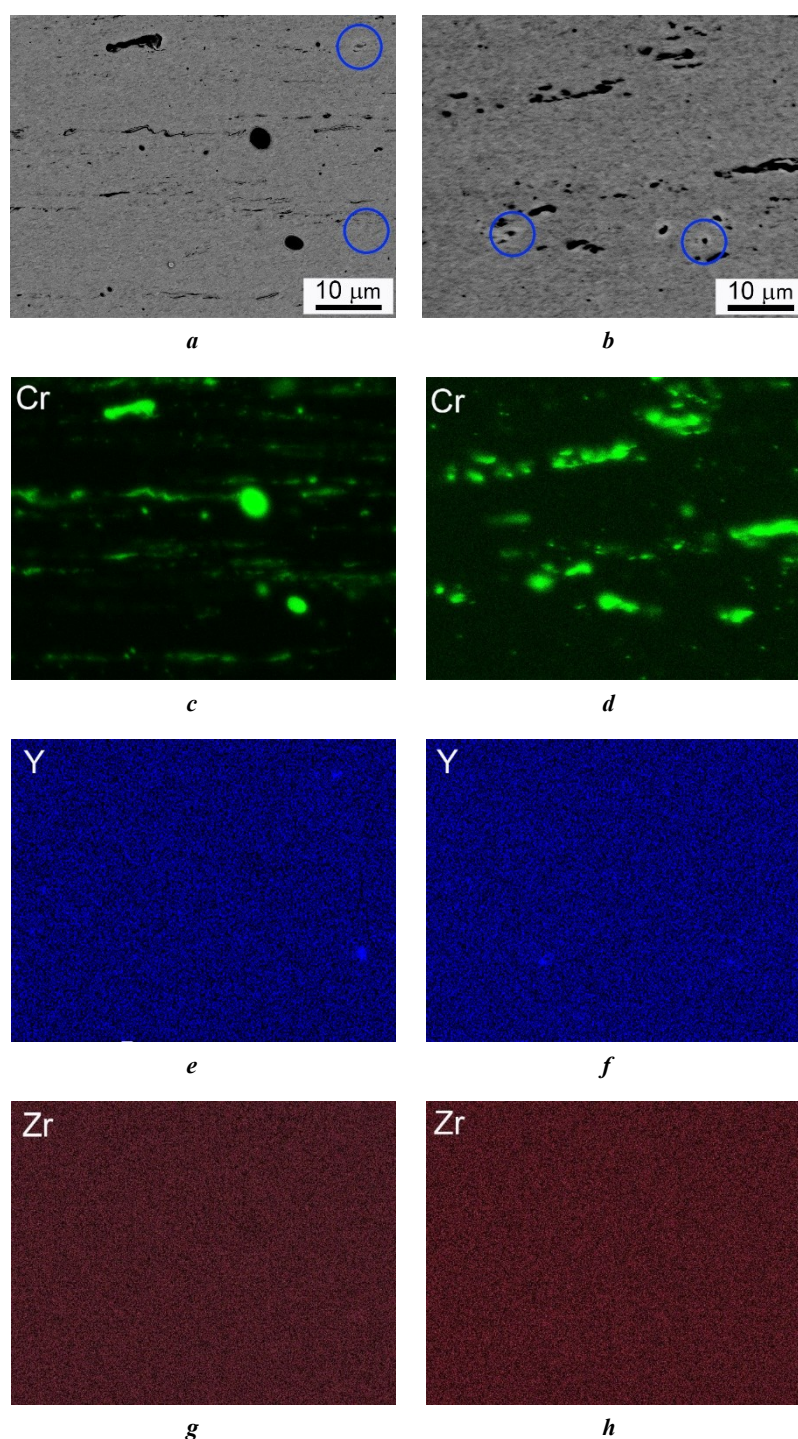


Fig. 8. Secondary phase particles (*a, b*) in combination with the distribution of Cr (*c, d*), Y (*e, f*) and Zr (*g, h*) between the phases after friction stir processing at the top (*a, c, e, g*) and in the center (*b, d, f, h*) of the stir zone

Рис. 8. Частицы вторичных фаз (*a, b*) в сочетании с распределением Cr (*c, d*), Y (*e, f*) и Zr (*g, h*) между фазами после обработки трением с перемешиванием сверху (*a, c, e, g*) и в центре (*b, d, f, h*) зоны перемешивания

a decrease to $\approx 9\%$ [2] is observed, and at a temperature of 240°C , a decrease to $\approx 6\%$ is observed [4]. This is in good agreement with the results presented in Fig. 4.

It is worth noting that the distribution of angle misorientations (Fig. 5) does not show a clearly defined peak of $60^\circ\langle 111 \rangle$ twin boundaries – these boundaries are shown by red lines in Fig. 3. In the initial state, a large number of annealing twin boundaries are observed (Fig. 1 a). As a result, the low fraction of $60^\circ\langle 111 \rangle$ bounda-

ries after FSP can be associated with the low rate of metadynamic recrystallization during plate cooling after processing. The presence of a bimodal distribution (with peaks in the low- and high-angle regions) in Fig. 5 may indicate the dominance of continuous dynamic recrystallization processes. In addition, Fig. 3 c, d show segments of low-angle boundaries that gain their misorientation up to high-angle boundaries, which is also a direct marker of continuous recrystallization. At the same time, Fig. 3 c, d show

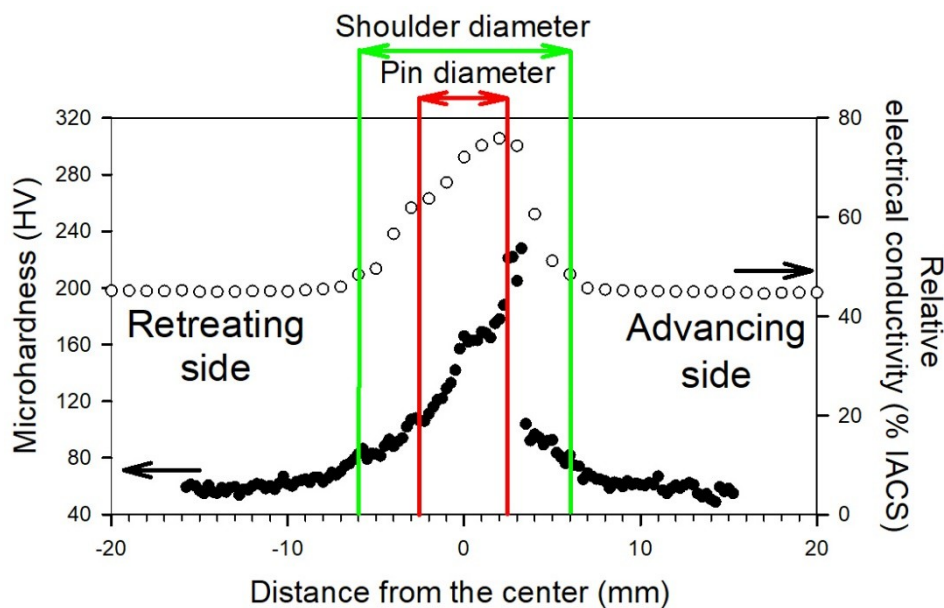


Fig. 9. Distribution of microhardness and relative electrical conductivity in the zone of friction stir processing

Рис. 9. Распределение микротвердости и относительной электропроводности в зоне обработки трением с перемешиванием

configurations of larger grains surrounded by groups of grains an order of magnitude smaller, which may indicate the presence of discontinuous dynamic recrystallization processes. It is likely that two dynamic recrystallization mechanisms compete during the FSP process. However, taking into account the low process temperature, the contribution of the continuous recrystallization mechanism can be considered predominant.

Comparison of the experimental misorientation spectrum with a random distribution (Fig. 5) and a distribution determined by crystallographic texture showed that the texture derived distribution has a smaller discrepancy, indicating that in this case, the emerging angle distribution may be determined by the developing crystallographic texture.

Based on the different rotation angles of the pole figures required to reveal texture at the top and center of the SZ, it is possible to say about the influence of different parts of the stirring tool on texture formation. Thus, small rotation angles were required near the SZ surface, indicating a greater influence of the flat tool shoulders during texture formation than the pin. At the center of the SZ, significant rotation angles were required, indicating a strong influence of the hemispherical pin on the crystallographic texture formation. However, the resulting distributions of misorientation angles (Fig. 5) and crystallographic textures (Fig. 6) in the zones under consideration are qualitatively and quantitatively similar, i.e., the mechanism of the misorientation distribution formation must be the same.

Returning to the relationship between grain misorientation angles near 45° and texture, the CLS boundaries function was used to estimate the fraction of special grain boundaries. Thus, a total of $\approx 2.4\%$ of the $\Sigma 9 -$

$38.9^\circ \langle 110 \rangle$ and $\Sigma 11 - 50.5^\circ \langle 110 \rangle$ boundaries were observed in the structure, the direction of which coincided with the identified predominant texture directions. Moreover, a total of $\approx 2.4\%$ of the $\Sigma 7 - 38.2^\circ \langle 111 \rangle$ and $\Sigma 29a - 43.6^\circ \langle 100 \rangle$ boundaries were observed, the directions of which were not related to texture. It can be assumed that these boundaries form the observed peak, with some of the boundaries associated with the crystallographic texture.

Characteristics of secondary phase changes during FSP

As noted previously, after friction stir processing, spherical inclusions with a Z-contrast were observed in the microstructure, which were identical to $\text{Cu}_x(\text{Y,Zr})$ inclusions observed in the initial state. Their size, however, remained unchanged compared to the initial size. It can be assumed that these inclusions are not deformed during FSP, and the deformed matrix, due to its greater plasticity, “flows” around them during deformation. At the same time, the $\text{Cu}_x(\text{Y,Zr})$ phase located at the original grain boundaries before FSP is ground into smaller fragments, which are arranged in banded structures aligned with the direction of tool rotation. In this case, the phase is arranged as a flat obstacle located at the boundary, which cannot be overcome during copper matrix flow, causing its partial destruction and rotation of the remaining fragments. Thus, the initial morphology of this phase significantly influences its evolution during FSP.

As has been shown, FSP significantly changes the morphology of Cr particles. The presence of elongated, repeatedly bending, plate-like particles is worth noting individually. A similar effect was not observed after FSP at higher temperatures. The authors believe that this particle morphology is associated with the high strain during FSP,

which can reach true values of ≈ 35 units [16]. The following mechanism for the change in Cr particle morphology can be hypothesized: the formation of an ultrafine-grained matrix structure increases the material's ability to resist deformation, thereby increasing internal stresses in the material. The material is heated to a temperature of $\approx 350^\circ\text{C}$, and this combination of thermomechanical conditions likely becomes sufficient for plastic flow of Cr between the matrix grain layers.

During FSP of the Cu–Cr–Zr–Y bronze under study, particles enriched in Y and free of Zr were observed, although in the initial state, there was a phase containing both elements. It is appropriate to consider this phenomenon from the point of view of the analysis of the equilibrium phase diagrams of Cu–Zr and Cu–Y. After treatment with a supersaturated solid solution, Y and Zr can be present in the supersaturated solid solution in accordance with the phase diagram [11; 17]. According to the Cu–Y diagram [11], the closest phase to a given Y content is Cu_7Y , which exists at temperatures below 871°C , whereas according to Cu–Zr diagram [17], the closest phase to a given Zr content is Cu_9Zr_2 , which exists at temperatures below 972°C . One can assume that Zr-enriched phases will precipitate at higher temperatures (a difference of about 100°C). According to differential scanning calorimetry data for quenched Cu–Cr–Zr alloy, the precipitation of the Zr-enriched phase occurs at temperatures of about 490°C [18]. Considering the fact that additional severe plastic deformation in most cases lowers the precipitation temperature of the second phase [18; 19], in combination with the expected difference in the precipitation temperatures of phases with Zr and Y, we naturally observe the precipitation of a Y-enriched phase. Additional thermodynamic modeling of the equilibrium phase composition at temperatures of $350\text{--}1100^\circ\text{C}$ using the Thermo-Calc program predicts the existence of the Cu_5Zr (C15B crystal lattice) and Cu_7Y (P6/mmm crystal lattice) phases in this temperature range. The temperature range of the existence of Cu_5Zr is from 580 to 910°C , while for the Cu_7Y phase it corresponds to temperatures from 350 to 837°C . It is quite natural that after low-temperature FSP, we observe a Y-enriched phase and do not observe phases with Zr. Thus, it can be assumed that the phase observed after FSP is the equilibrium Cu_7Y phase.

The relationship between properties and the forming microstructure during FSP

Having analyzed the observed characteristics of the microstructure, one can identify the relationship between the microstructure evolution and the formation of the distribution of microhardness and electrical conductivity. It is assumed that the asymmetric nature of the distributions combined with the gravitation of extreme values of the quantities to the advancing side (AS), is associated with the uneven distribution of temperature and strain in the deformation zone, shown by the modeling results [20]. In particular, the temperature with AS can be higher than with the retreating side (RS). Considering the fact that we observe a simultaneous increase in microhardness and electrical conductivity, it can be assumed that this phenomenon is associated with both the refinement of the grain structure and the decomposition of the supersaturated solid solution.

The refinement of the grain structure in the stir zone was illustrated in the work. With regard to the decomposition of the supersaturated solid solution, only the precipitation of Y-enriched particles was shown, the amount of which in the microstructure (according to Fig. 8) is small. The maximum electrical conductivity of the treated area reaches 76 % IACS, which is close to the values of aged Cu–Cr–Zr bronze [3], corresponding to the microstructural state after the decomposition (partial or complete) of the solid solution. The high electrical conductivity value indirectly indicates the occurrence of intensive decomposition of the supersaturated solid solution with the release of nanometer-sized Cr and Zr particles during the FSP process. It is likely that the SEM method used in this study is insufficient for the resolution of the nanoscale particles of secondary phases formed at such a low temperature.

CONCLUSIONS

In the work, the following patterns of microstructure formation in Cu–Cr–Zr–Y bronze were identified during low-temperature friction stir processing:

- 1) friction stir processing caused the grain structure refinement to an average grain size of $\approx 0.3\ \mu\text{m}$ with predominantly high-angle boundaries and the formation of a combination of axial $\langle 110 \rangle$ and limited $B/\bar{B}\ \{112\}\langle 110 \rangle$ simple shear textures;
- 2) friction stir processing led to a destruction of the $\text{Cu}_x(\text{Y},\text{Zr})$ phase located along the boundaries of the original grains, but did not destroy this phase with a spherical morphology. FSP altered the morphology of Cr particles due to their deformation and elongation in the direction of tool rotation. FSP was accompanied by the precipitation of a Y-enriched phase not observed in the initial state;
- 3) microstructural changes occurring during FSP led to an increase in the values of microhardness and electrical conductivity in comparison with the quenched state.

REFERENCES

1. Makarov A.V., Lezhnin N.V., Kotelnikov A.B., Vopnuk A.A., Korobov Yu.S., Valiullin A.I., Volkova E.G. Restoration of continuous casting machine mold copper plates made of Cr–Zr bronze using multi-pass friction stir lap welding. *Izvestiya. Non-Ferrous Metallurgy*, 2023, vol. 29, no. 6, pp. 66–83. DOI: [10.17073/0021-3438-2023-6-66-83](https://doi.org/10.17073/0021-3438-2023-6-66-83).
2. Bodyakova A.I., Chistyukhina E.I., Tkachev M.S., Malofeev S.S., Kaibyshev R.O. Effect of Friction Stir Processing on the Structure and Properties of the Low-Doped Cu–Cr–Zr Alloy. *Physics of Metals and Metallography*, 2024, vol. 125, no. 11, pp. 1192–1200. DOI: [10.1134/S0031918X24601677](https://doi.org/10.1134/S0031918X24601677).
3. Bodyakova A., Malopfeev S., Tkachev M., Chistyukhina E., Mironov S., Lezhnin N., Fu Y., Makarov A., Kaibyshev R. Effect of friction-stir processing and subsequent aging treatment on microstructure and service properties of Cu–Cr–Zr alloy. *Materials Characterization*, 2024, vol. 216, article number 114225. DOI: [10.1016/j.matchar.2024.114225](https://doi.org/10.1016/j.matchar.2024.114225).
4. Wang Y.D., Liu M., Yu B.H., Wu L.H., Xue P., Ni D.R., Ma Z.Y. Enhanced combination of mechanical properties

- and electrical conductivity of a hard state Cu–Cr–Zr alloy via one-step friction stir processing. *Journal of Materials Processing Technology*, 2021, vol. 288, article number 116880. DOI: [10.1016/j.jmatprotec.2020.116880](https://doi.org/10.1016/j.jmatprotec.2020.116880).
5. Khomskaya I.V., Zel'dovich V.I., Frolova N.Y., Abdullina D.N., Kheifets A.E. Investigation of Cu₅Zr particles precipitation in Cu–Zr and Cu–Cr–Zr alloys subjected to quenching and high strain rate deformation. *Letters on Materials*, 2019, vol. 9, no. 4, pp. 400–404. DOI: [10.22226/2410-3535-2019-4-400-404](https://doi.org/10.22226/2410-3535-2019-4-400-404).
 6. Ma Yuxia, Chen Huiqin, Li Hui, Dang Shue. Influence Mechanism of Ageing Parameters of Cu–Cr–Zr Alloy on Its Structure and Properties. *Materials*, 2022, vol. 15, no. 21, article number 7605. DOI: [10.3390/ma15217605](https://doi.org/10.3390/ma15217605).
 7. Khomskaya I.V., Zel'dovich V.I., Abdullina D.N., Shorokhov E.V. The Effect of Chromium and Zirconium Alloying on the Structure and Properties of Submicrocrystalline Copper Alloys Obtained by Dynamic Channel-Angular Pressing. *Physics of Metals and Metallography*, 2024, vol. 125, no. 10, pp. 1156–1165. DOI: [10.1134/s0031918x24601434](https://doi.org/10.1134/s0031918x24601434).
 8. Li Yijun, Zhang Jinghua, Fu Ruidong, Wang Jungao, Lv Hongyan, Xing Haizhi. Synergistic improvement of strength and electrical conductivity in Cu–Cr–Zr alloys through prestrain-assisted friction stir processing. *Journal of Materials Research and Technology*, 2023, vol. 27, pp. 564–573. DOI: [10.1016/j.jmrt.2023.09.262](https://doi.org/10.1016/j.jmrt.2023.09.262).
 9. Li Hai-hong, Sun Xue-qin, Zhang Shang-zhou, Zhao Qin-yi, Wang Guang-zhen. Application of rare-earth element Y in refining impure copper. *International Journal of Minerals, Metallurgy, and Materials*, 2015, vol. 22, no. 5, pp. 453–459. DOI: [10.1007/s12613-015-1093-z](https://doi.org/10.1007/s12613-015-1093-z).
 10. Duisemaliev T.U., Duisemaliev U.K. Solubility of yttrium in copper and its effect on the properties of leaded brasses. *Metal Science and Heat Treatment*, 1993, vol. 35, no. 12, pp. 673–676. DOI: [10.1007/BF00707636](https://doi.org/10.1007/BF00707636).
 11. Okamoto H. Cu–Y (Copper–Yttrium). *Journal of Phase Equilibria*, 1992, vol. 13, no. 1, pp. 102–103. DOI: [10.1007/BF02645393](https://doi.org/10.1007/BF02645393).
 12. Liang Dong, Wang Ning, Wang Yuxiang, Liu Zhenjie, Fu Ying. Effects of Zr, Y on the Microstructure and Properties of As-Cast Cu–0.5Y–xZr (wt.%) Alloys. *Metals*, 2019, vol. 9, no. 10, article number 1084. DOI: [10.3390/met9101084](https://doi.org/10.3390/met9101084).
 13. Zel'dovich V.I., Frolova N.Y., Khomskaya I.V., Kheifets A.E., Dobatkin S.V., Shorokhov E.V., Nasonov P.A. Mechanical properties and the structure of chromium–zirconium bronze after dynamic channel-angular pressing and subsequent aging. *Physics of Metals and Metallography*, 2016, vol. 117, no. 1, pp. 74–82. DOI: [10.1134/S0031918X16010129](https://doi.org/10.1134/S0031918X16010129).
 14. Chakrabarti D.J., Laughlin D.E. The Cr–Cu (Chromium–Copper) system. *Bulletin of Alloy Phase Diagrams*, 1984, vol. 5, no. 1, pp. 59–68. DOI: [10.1007/BF02868727](https://doi.org/10.1007/BF02868727).
 15. Fonda R.W., Knipling K.E. Texture development in friction stir welds. *Science and Technology of Welding and Joining*, 2011, vol. 16, no. 4, pp. 288–294. DOI: [10.1179/1362171811Y.0000000010](https://doi.org/10.1179/1362171811Y.0000000010).
 16. Mishin V., Shishov I., Kalinenko A., Vysotskii I., Zuiko I., Malopheyev S., Mironov S., Kaibyshev R. Numerical Simulation of the Thermo-Mechanical Behavior of 6061 Aluminum Alloy during Friction-Stir Welding. *Journal of Manufacturing and Materials Processing*, 2022, vol. 6, no. 4, article number 68. DOI: [10.3390/jmmp6040068](https://doi.org/10.3390/jmmp6040068).
 17. Arias D., Abriata J.P. Cu–Zr (Copper–Zirconium). *Journal of Phase Equilibria*, 1990, vol. 11, no. 5, pp. 452–459. DOI: [10.1007/BF02898260](https://doi.org/10.1007/BF02898260).
 18. Bourezg Y.I., Abib K., Azzeddine H., Bradai D. Kinetics of Cr clustering in a Cu–Cr–Zr alloy processed by equal-channel angular pressing: A DSC study. *Thermochimica Acta*, 2020, vol. 686, article number 178550. DOI: [10.1016/j.tca.2020.178550](https://doi.org/10.1016/j.tca.2020.178550).
 19. Dölling J., Kracun S.F., Prah U., Fehlbier M., Zilly A. A Comparative Differential Scanning Calorimetry Study of Precipitation Hardenable Copper-Based Alloys with Optimized Strength and High Conductivity. *Metals*, 2023, vol. 13, no. 1, article number 150. DOI: [10.3390/met13010150](https://doi.org/10.3390/met13010150).
 20. Venghaus H., Chiumenti M., Baiges J., Juhre D., Dialami N. Embedded technology for enhanced modeling of Friction Stir Welding processes. *Computer Methods in Applied Mechanics and Engineering*, 2025, vol. 435, article number 117539. DOI: [10.1016/j.cma.2024.117539](https://doi.org/10.1016/j.cma.2024.117539).

СПИСОК ЛИТЕРАТУРЫ

1. Макаров А.В., Лежнин Н.В., Котельников А.Б., Вонперук А.А., Коробов Ю.С., Валиуллин А.И., Волкова Е.Г. Восстановление стенок кристаллизаторов машин непрерывного литья заготовок из хромоциркониевой бронзы методом многопроходной сварки трением с перемешиванием // Известия высших учебных заведений. Цветная металлургия. 2023. Т. 29. № 6. С. 66–83. DOI: [10.17073/0021-3438-2023-6-66-83](https://doi.org/10.17073/0021-3438-2023-6-66-83).
2. Bodyakova A.I., Chistyukhina E.I., Tkachev M.S., Malofeev S.S., Kaibyshev R.O. Effect of Friction Stir Processing on the Structure and Properties of the Low-Doped Cu–Cr–Zr Alloy // Physics of Metals and Metallography. 2024. Vol. 125. № 11. P. 1192–1200. DOI: [10.1134/S0031918X24601677](https://doi.org/10.1134/S0031918X24601677).
3. Bodyakova A., Malopfeev S., Tkachev M., Chistyukhina E., Mironov S., Lezhnin N., Fu Y., Makarov A., Kaibyshev R. Effect of friction-stir processing and subsequent aging treatment on microstructure and service properties of Cu–Cr–Zr alloy // Materials Characterization. 2024. Vol. 216. Article number 114225. DOI: [10.1016/j.matchar.2024.114225](https://doi.org/10.1016/j.matchar.2024.114225).
4. Wang Y.D., Liu M., Yu B.H., Wu L.H., Xue P., Ni D.R., Ma Z.Y. Enhanced combination of mechanical properties and electrical conductivity of a hard state Cu–Cr–Zr alloy via one-step friction stir processing // Journal of Materials Processing Technology. 2021. Vol. 288. Article number 116880. DOI: [10.1016/j.jmatprotec.2020.116880](https://doi.org/10.1016/j.jmatprotec.2020.116880).
5. Khomskaya I.V., Zel'dovich V.I., Frolova N.Y., Abdullina D.N., Kheifets A.E. Investigation of Cu₅Zr particles precipitation in Cu–Zr and Cu–Cr–Zr alloys subjected to quenching and high strain rate deformation // Letters on Materials. 2019. Vol. 9. № 4. P. 400–404. DOI: [10.22226/2410-3535-2019-4-400-404](https://doi.org/10.22226/2410-3535-2019-4-400-404).
6. Ma Yuxia, Chen Huiqin, Li Hui, Dang Shue. Influence Mechanism of Ageing Parameters of Cu–Cr–Zr Alloy on Its

- Structure and Properties // Materials. 2022. Vol. 15. № 21. Article number 7605. DOI: [10.3390/ma15217605](https://doi.org/10.3390/ma15217605).
7. Khomskaya I.V., Zel'dovich V.I., Abdullina D.N., Shorokhov E.V. The Effect of Chromium and Zirconium Alloying on the Structure and Properties of Submicrocrystalline Copper Alloys Obtained by Dynamic Channel-Angular Pressing // Physics of Metals and Metallography. 2024. Vol. 125. № 10. P. 1156–1165. DOI: [10.1134/s0031918x24601434](https://doi.org/10.1134/s0031918x24601434).
 8. Li Yijun, Zhang Jinghua, Fu Ruidong, Wang Jungao, Lv Hongyan, Xing Haizhi. Synergistic improvement of strength and electrical conductivity in Cu–Cr–Zr alloys through prestrain-assisted friction stir processing // Journal of Materials Research and Technology. 2023. Vol. 27. P. 564–573. DOI: [10.1016/j.jmrt.2023.09.262](https://doi.org/10.1016/j.jmrt.2023.09.262).
 9. Li Hai-hong, Sun Xue-qin, Zhang Shang-zhou, Zhao Qin-yi, Wang Guang-zhen. Application of rare-earth element Y in refining impure copper // International Journal of Minerals, Metallurgy, and Materials. 2015. Vol. 22. № 5. P. 453–459. DOI: [10.1007/s12613-015-1093-z](https://doi.org/10.1007/s12613-015-1093-z).
 10. Duisemaliev T.U., Duisemaliev U.K. Solubility of yttrium in copper and its effect on the properties of leaded brasses // Metal Science and Heat Treatment. 1993. Vol. 35. № 12. P. 673–676. DOI: [10.1007/BF00707636](https://doi.org/10.1007/BF00707636).
 11. Okamoto H. Cu–Y (Copper–Yttrium) // Journal of Phase Equilibria. 1992. Vol. 13. № 1. P. 102–103. DOI: [10.1007/BF02645393](https://doi.org/10.1007/BF02645393).
 12. Liang Dong, Wang Ning, Wang Yuxiang, Liu Zhenjie, Fu Ying. Effects of Zr, Y on the Microstructure and Properties of As-Cast Cu–0.5Y–xZr (wt.%) Alloys // Metals. 2019. Vol. 9. № 10. Article number 1084. DOI: [10.3390/met9101084](https://doi.org/10.3390/met9101084).
 13. Зельдович В.И., Добаткин С.В., Фролова Н.Ю., Хомская И.В., Хейфец А.Э., Шорохов Е.В., Насонов П.А. Механические свойства и структура хромоциркониевой бронзы после динамического канально-углового прессования и последующего старения // Физика металлов и металловедение. 2016. Т. 117. № 1. С. 79–87. DOI: [10.7868/S0015323016010125](https://doi.org/10.7868/S0015323016010125).
 14. Chakrabarti D.J., Laughlin D.E. The Cr–Cu (Chromium–Copper) system // Bulletin of Alloy Phase Diagrams. 1984. Vol. 5. № 1. P. 59–68. DOI: [10.1007/BF02868727](https://doi.org/10.1007/BF02868727).
 15. Fonda R.W., Knipling K.E. Texture development in friction stir welds // Science and Technology of Welding and Joining. 2011. Vol. 16. № 4. P. 288–294. DOI: [10.1179/1362171811Y.0000000010](https://doi.org/10.1179/1362171811Y.0000000010).
 16. Mishin V., Shishov I., Kalinenko A., Vysotskii I., Zuiko I., Malopheyev S., Mironov S., Kaibyshev R. Numerical Simulation of the Thermo-Mechanical Behavior of 6061 Aluminum Alloy during Friction-Stir Welding // Journal of Manufacturing and Materials Processing. 2022. Vol. 6. № 4. Article number 68. DOI: [10.3390/jmmp6040068](https://doi.org/10.3390/jmmp6040068).
 17. Arias D., Abriata J.P. Cu–Zr (Copper–Zirconium) // Journal of Phase Equilibria. 1990. Vol. 11. № 5. P. 452–459. DOI: [10.1007/BF02898260](https://doi.org/10.1007/BF02898260).
 18. Bourezg Y.I., Abib K., Azzeddine H., Bradai D. Kinetics of Cr clustering in a Cu–Cr–Zr alloy processed by equal-channel angular pressing: A DSC study // Thermochimica Acta. 2020. Vol. 686. Article number 178550. DOI: [10.1016/j.tca.2020.178550](https://doi.org/10.1016/j.tca.2020.178550).
 19. Dölling J., Kracun S.F., Pahl U., Fehlbier M., Zilly A. A Comparative Differential Scanning Calorimetry Study of Precipitation Hardenable Copper-Based Alloys with Optimized Strength and High Conductivity // Metals. 2023. Vol. 13. № 1. Article number 150. DOI: [10.3390/met13010150](https://doi.org/10.3390/met13010150).
 20. Venghaus H., Chiumenti M., Baiges J., Juhre D., Dialami N. Embedded technology for enhanced modeling of Friction Stir Welding processes // Computer Methods in Applied Mechanics and Engineering. 2025. Vol. 435. Article number 117539. DOI: [10.1016/j.cma.2024.117539](https://doi.org/10.1016/j.cma.2024.117539).

УДК 691.73

doi: 10.18323/2782-4039-2025-3-73-5

Особенности формирования микроструктуры в Cu–Cr–Zr–Y бронзе в условиях низкотемпературной обработки трением с перемешиванием

Никитин Иван Сергеевич^{*1}, кандидат технических наук, младший научный сотрудник лаборатории механических свойств наноструктурных и жаропрочных материалов

Калиненко Александр Андреевич², кандидат физико-математических наук, младший научный сотрудник лаборатории механических свойств наноструктурных и жаропрочных материалов

Малофеев Сергей Сергеевич³, кандидат технических наук, старший научный сотрудник лаборатории механических свойств наноструктурных и жаропрочных материалов

Миронов Сергей Юрьевич⁴, доктор физико-математических наук, ведущий научный сотрудник лаборатории механических свойств наноструктурных и жаропрочных материалов

Бодякова Анна Игоревна⁵, кандидат физико-математических наук, научный сотрудник лаборатории механических свойств наноструктурных и жаропрочных материалов

Белгородский государственный национальный исследовательский университет, Белгород (Россия)

*E-mail: nikitin_i@bsuedu.ru

¹ORCID: <https://orcid.org/0000-0002-5417-9857>

²ORCID: <https://orcid.org/0000-0001-7534-0542>

³ORCID: <https://orcid.org/0000-0001-9145-3723>

⁴ORCID: <https://orcid.org/0000-0003-2202-1518>

⁵ORCID: <https://orcid.org/0000-0002-9378-0338>

Поступила в редакцию 15.07.2025

Пересмотрена 26.08.2025

Принята к публикации 09.09.2025

Аннотация: Применение обработки трением с перемешиванием (ОТП) для модификации физических и механических свойств термически упрочняемых низколегированных бронз является перспективной и одновременно сложной задачей по причине широкого температурного интервала его осуществления. Сложность в том, что в результате ОТП бронз могут формироваться кардинально разные типы микроструктур с широким диапазоном размеров зерен и различным сочетанием типов упрочняющих фаз и их разнообразных морфологий. Более того, возможны варианты, при которых ОТП приводит к деградации свойств бронз. Благоприятное сочетание свойств может быть достигнуто в результате осуществления низкотемпературной ОТП. В рамках работы проведен анализ основных микроструктурных изменений перспективной Cu–Cr–Zr–Y бронзы при ОТП со скоростью вращения инструмента 1000 об/мин и скоростью подачи 25 мм/мин (обеспечивающих температуру в зоне перемешивания $\approx 350^\circ\text{C}$) – низкотемпературной ОТП. Методами растровой электронной микроскопии и EBSD-анализа выявлены механизмы формирования ультрамелкозернистой структуры с преимущественно большеугловыми границами, а также развитие двух типов кристаллографических текстур простого сдвига. Показано, что фаза $\text{Cu}_x(\text{Y,Zr})$, наблюдающаяся в исходной структуре, может претерпевать механическое разрушение или же сохранять геометрические параметры в зависимости от своей исходной морфологии и расположения. Впервые показано, что избыточные частицы Cr (равновесная доля при температуре нагрева под закалку) могут не разрушаться, а пластически деформироваться с сильным изменением своей морфологии. При ОТП исследуемой бронзы происходит выделение частиц новой Y-содержащей фазы. Рассмотрена взаимосвязь распределения микротвердости и электропроводности с наблюдаемыми изменениями микроструктуры в новом перспективном материале.

Ключевые слова: обработка трением с перемешиванием; низколегированные бронзы; рекристаллизация; вторичные фазы; электропроводность.

Благодарности: Исследование выполнено за счет гранта Российского научного фонда № 24-29-00628 (<https://rscf.ru/project/24-29-00628/>) с использованием оборудования Центра коллективного пользования «Технологии и Материалы НИУ "БелГУ"».

Статья подготовлена по материалам докладов участников XII Международной школы «Физическое материаловедение» (ШФМ-2025), Тольятти, 15–19 сентября 2025 года.

Для цитирования: Никитин И.С., Калинин А.А., Малофеев С.С., Миронов С.Ю., Бодякова А.И. Особенности формирования микроструктуры в Cu–Cr–Zr–Y бронзе в условиях низкотемпературной обработки трением с перемешиванием // Frontier Materials & Technologies. 2025. № 3. С. 67–80. DOI: 10.18323/2782-4039-2025-3-73-5.

Study of the influence of deformation temperature on the mechanical behaviour and fracturing behaviour of the cast TNM-B1 alloy

Vitaly S. Sokolovskiy*, PhD (Engineering),

researcher of the Laboratory of Bulk Nanostructured Materials

Gennady A. Salishchev¹, Doctor of Sciences (Engineering), Professor,

Head of the Laboratory of Bulk Nanostructured Materials

Belgorod State University, Belgorod (Russia)

*E-mail: sokolovskiy@bsuedu.ru

¹ORCID: <https://orcid.org/0000-0002-0815-3525>

Received 07.07.2025

Revised 25.07.2025

Accepted 20.08.2025

Abstract: The paper covers the study of β -solidifying TiAl-based alloys, which are extremely promising materials for the aviation industry with an operating temperature of up to 850 °C, have high specific strength characteristics. The authors studied the influence of tensile deformation temperature in the range of $T=25\text{--}1000$ °C on the mechanical properties, phase composition and crack formation in the cast β -solidifying TNM-B1 alloy. It is found that the cast TNM-B1 alloy is characterized by a complex microstructure, including $(\alpha_2+\gamma)$ lamellar colonies and interlayers of $\beta(B2)+\omega$ phases, the evolution of which at elevated deformation temperatures determines the material behaviour. It is shown that the ω -phase dissolution and the precipitation of dispersed secondary β -phase particles at $T>950$ °C have a significant influence on the mechanical characteristics. A pronounced temperature dependence of strength and ductility is identified: the maximum strength is observed at 800 °C, while the greatest relative elongation in the studied temperature range is achieved at 1000 °C. The transition from brittle to viscous fracture occurs in the temperature range of about 950 °C. Moreover, a dependence of the crack propagation mechanism on the orientation of lamellar colonies relative to the deformation axis is revealed: with an increase in temperature, the differences are leveled, and at 1000 °C, complete suppression of crack formation with the formation of pores along the boundaries of colonies and clusters of secondary β -phase particles is observed. The obtained results demonstrate the important role of microstructural transformations in the formation of deformation behaviour and mechanical properties of the TNM-B1 alloy based on gamma-titanium aluminide, which is of practical importance for the development of technologies for its thermomechanical processing.

Keywords: TNM-B1 cast alloy; mechanical behaviour; fracturing behaviour; TNM alloy; microstructure; brittle-ductile transition; strength; plasticity.

Acknowledgments: The work was carried out with the financial support of the Russian Science Foundation (agreement No. 19-79-30066) using the equipment of the Common Use Center “Technologies and Materials” of BelSU National Research University, https://rscf.ru/prjcard_int?19-79-30066.

For citation: Sokolovskiy V.S., Salishchev G.A. Study of the influence of deformation temperature on the mechanical behaviour and fracturing behaviour of the cast TNM-B1 alloy. *Frontier Materials & Technologies*, 2025, no. 3, pp. 81–89. DOI: 10.18323/2782-4039-2025-3-73-6.

INTRODUCTION

Intermetallic alloys based on gamma-titanium aluminide (γ -TiAl) are considered as promising materials with an operating temperature of up to 850 °C for use in the aerospace and energy industries, where a combination of heat resistance, low density and oxidation resistance is required [1–3]. Among the γ -TiAl-based alloys, β -solidifying alloys, a typical representative of which is TNM-B1, are of particular interest [4]. The fundamental limitation of the application of γ -TiAl-based intermetallic alloys is their tendency to brittle fracture up to $T=1000$ °C [5–7], which is caused by the nature of the $\gamma(\text{TiAl-L1}_0)$, $\alpha_2(\text{Ti}_3\text{Al-D0}_{19})$ and $\beta(B2)$ phases present in them, characterised by a limited number of active slip/twinning systems, reduced diffusion, difficult trans-

mission of deformation across boundaries and, accordingly, pronounced deformation localisation [8; 9]. As the temperature increases above 650–850 °C, the number of slip/twinning systems increases, diffusion accelerates and dislocation climb is activated [10; 11]. The transition from the brittle to the ductile state also leads to a change in the type of fracture from intercrystallite to transcrystalline in the transition state and dimple in the case of ductile fracture [8]. The orientation of the plates relative to the deformation axis has a significant influence on the development of fracture. It was shown earlier [9; 12] that the orientation of lamellar colonies relative to the external load Φ largely determines their mechanical behaviour. Thus, colonies with an orientation of $15^\circ < \Phi < 75^\circ$ relative to the loading axis are deformed first, in contrast

to colonies with $\Phi < 15^\circ$ and $\Phi > 75^\circ$, in which significantly higher stresses are required to activate slip/twinning systems [12]. This feature should directly influence the propagation of cracks in colonies with different orientations relative to the deformation axis in alloys with a lamellar type of structure. Meanwhile, the effect of the orientation of lamellar colonies on the fracture development in the temperature range of the brittle-ductile transition (BDT) has not been considered in detail in the literature. It is worth noting that in addition to the above phases, TNM alloys may also contain $\omega(\text{Ti}_4\text{Nb}_3\text{Al-B8}_2)$ -phase particles, which are formed in the β -phase interlayers during slow cooling or holding below $T=850^\circ\text{C}$ [13]. During subsequent heating, these particles dissolve, the proportion of the β -phase increases, and the γ -phase particles dissolve/spheroidise, which can significantly affect the fracturing behaviour in the temperature range corresponding to the brittle-ductile transition. However, the assessment of this effect has not been given due attention in the literature [1–3].

The aim of the work is to study the influence of the deformation temperature of cast β -solidifying TNM-B1 alloy with a lamellar structure on its mechanical properties, phase composition, and fracturing behaviour in colonies with different orientations relative to the deformation axis.

METHODS

The starting material was the TNM-B1 intermetallic alloy based on gamma-titanium aluminide with the nominal composition Ti–43.5Al–4Nb–1Mo–0.1B. An ingot with a diameter of 18 mm and a length of 90 mm was produced by die-casting. The chemical composition of the alloy ingot is presented in Table 1.

After mechanical grinding, the cast alloy samples for testing mechanical properties were additionally subjected to electrolytic polishing. An electrolyte of 95 % $\text{C}_2\text{H}_5\text{OH}$ + 5 % HCl was used; the electrolytic polishing temperature was -35°C , and the current density was 0.1 A/m^2 .

Tensile tests were carried out to determine the mechanical properties. An Instron 5882 universal electromechanical testing machine (USA) equipped with a furnace with a maximum heating temperature of 1200°C was used. The tests were carried out in the temperature range from 25 to 1000°C . The deformation rate was 0.96 mm/min ; the initial deformation rate was 10^{-3} s^{-1} . Flat samples with a length of the working part of 16 mm and a cross section of $1.5 \times 3\text{ mm}$ were used. Only samples with visually no pores on the surface were selected for tensile testing.

The microstructure was analysed using a FEI Quanta 600 scanning electron microscope (USA) in the electron backscatter diffraction and secondary backscattered electron mode at an accelerating voltage of 30 kV. The fine structure of the alloy was studied using a JEOL JEM-2100 transmission electron microscope (Japan) at an accelerating voltage of 200 kV. For the research, foils with $\text{Ø}3 \times 0.1\text{ mm}$ were produced, which were subjected to electrolytic thinning on a TenuPol-5 device (Denmark), using electrolyte A2 from Struers (Denmark), the temperature was -32°C , the voltage was 27 V.

RESULTS

Initial microstructure

During the SEM studies in the backscattered electron mode, images of the cast Ti–43.5Al–4.0Nb–1.0Mo–0.1B (TNM-B1) alloy microstructure were obtained; the higher the atomic number of the elements that make up the phases, the greater the image contrast (Fig. 1). It is seen that it is mainly represented by $(\alpha_2+\gamma)$ lamellar colonies, the proportion of which is 85 %, and their average size is $30\text{ }\mu\text{m}$ (Fig. 1 a). Analysis of the fine structure allowed identifying the average interlamellar distance equal to 120 nm (Fig. 1 b). Dark γ -phase particles and light layers of a mixture of $\beta(\text{B2})$ - and ω -phases were located along the boundaries of the colonies, which is confirmed by decoding the electron diffraction patterns from the areas of the corresponding particles (Fig. 1 b, c). The total volume fraction of $\beta(\text{B2})+\omega$ -phases is 10 %, γ -phase – 5 %, the average particle size is 2 and $4\text{ }\mu\text{m}$, respectively (Fig. 1 a, b). The whisker-shaped boride particles are mainly located along the colony boundaries and have an average length of about $15\text{ }\mu\text{m}$ with a diameter of $0.2\text{ }\mu\text{m}$ and a volume fraction of less than 0.1 % (Fig. 1 a). It is worth noting the presence of shrinkage pores in the alloy with a size from 1–10 to $50\text{--}100\text{ }\mu\text{m}$ with a volume fraction of 9 % and dark zones indicating the presence of liquation with a lower content of hard-melting elements (Nb, Mo) located mainly in the area of casting pores (Fig. 1 a).

Mechanical properties

The results of mechanical tensile tests in the temperature range of $25\text{--}1000^\circ\text{C}$ with an initial deformation rate of $\dot{\epsilon}=10^{-3}\text{ s}^{-1}$ are shown in Figs. 2, 3. It is evident that at $T=25^\circ\text{C}$, the cast alloy is destroyed in the elastic region. As the temperature increases to $700\text{--}800^\circ\text{C}$, there is an increase in strength and some increase in ductility to $\delta=0.4\%$. At $T=900^\circ\text{C}$, the strength decreases significantly, while the relative elongation reaches only 0.6 %.

Table 1. Chemical composition of TNM-B1 alloy, at. %
Таблица 1. Химический состав сплава TNM-B1, ат. %

Ti	Al	Nb	Mo	B
51.5	43.6	3.6	1.2	0.1

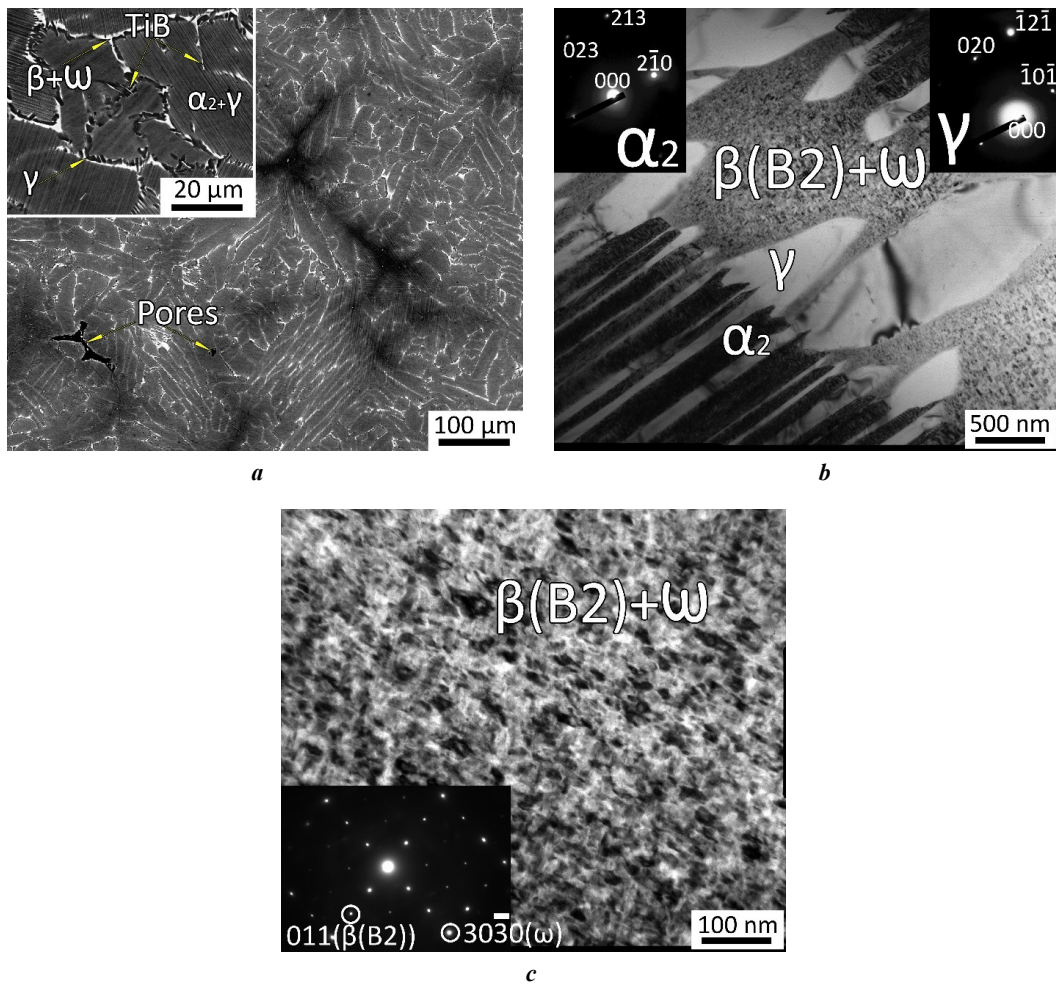


Fig. 1. Microstructure of the TNM-B1 alloy in the as-cast state: overview image and insert with high magnification (a), boundary of lamellar colonies (b), mixture of $\beta(B2)+\omega$ -phases (c).

a – SEM; b, c – TEM with inserts of electron diffraction patterns of the corresponding phases.

Arrows indicate the corresponding phases and structural elements

Рис. 1. Микроструктура сплава TNM-B, в литом состоянии: обзорный снимок и вставка с большим увеличением (a), граница пластинчатых колоний (b), смесь $\beta(B2)+\omega$ -фаз (c).

a – СЭМ; b, c – ПЭМ со вставками электронограмм соответствующих фаз.

Стрелками обозначены соответствующие фазы и структурные элементы

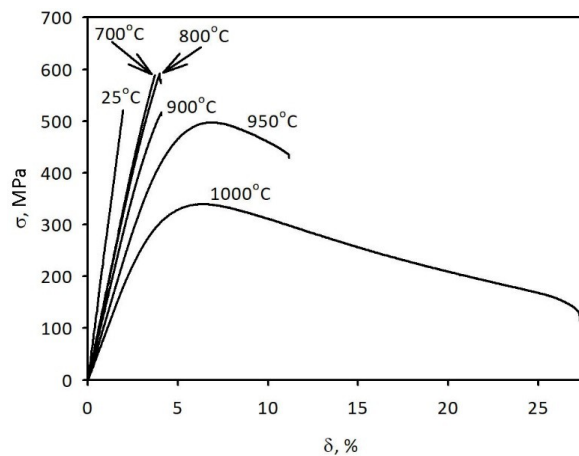


Fig. 2. Stress-strain curves obtained during tensile testing of TNM-B1 alloy in the temperature range of 25–1000 °C ($\dot{\epsilon}=10^{-3} s^{-1}$)

Рис. 2. Кривые «напряжение – деформация», полученные при испытании на растяжение сплава TNM-B1 в интервале температур 25–1000 °C ($\dot{\epsilon}=10^{-3} c^{-1}$)

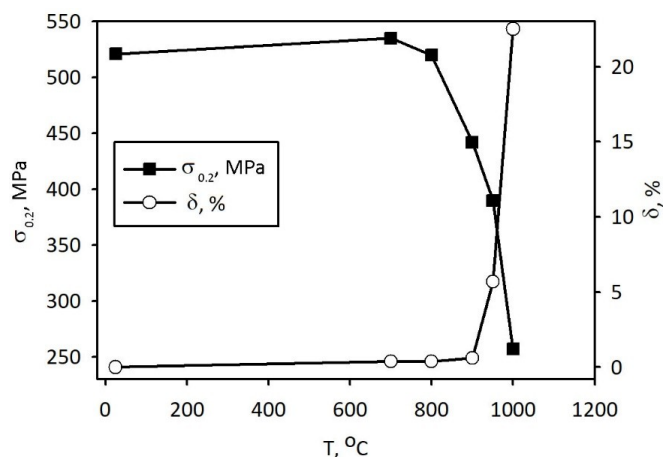


Fig. 3. Dependences of the ultimate strength and relative elongation of cast TNM-B1 alloy on temperature

Рис. 3. Зависимости предела прочности и относительного удлинения литого сплава TNM-B1 от температуры

Increasing the temperature to 950 °C leads to a decrease in the yield strength and a significant increase in ductility to $\delta=5.7\%$. Increasing the deformation temperature to 1000 °C is accompanied by significant softening and an increase in the relative elongation to 22.5 %. Thus, it can be said that stretching at a temperature of 1000 °C corresponds to the viscous temperature range, 950 °C – to the transitional range, and 25–900 °C – to the brittle range (Fig. 3).

Fractography

After tensile tests, the fractures of the samples were examined at temperatures corresponding to the brittle (700 °C), transition (950 °C) and ductile (1000 °C) ranges. After stretching at $T=700$ °C, the fracture is predominantly intercrystallite (Fig. 4 a). The fracture surface is predominantly represented by flat cleavage facets along the α_2/γ interphase boundaries with an orientation close to 75–90° relative to the tensile axis, as well as along the colony boundaries (Fig. 4 a). After testing at $T=950$ °C, traces of the propagation of tortuous cracks are visible on the fracture, the fracture becomes transcrystalline, and the number of secondary cracks increases (Fig. 4 b). The facets are no longer absolutely smooth, while the main area of the fracture is still represented by brittle cleaved areas along the interphase boundaries. It is worth noting the absence of areas indicating fracture along the α_2/γ interphase boundaries, which indicates branching of the main crack inside the colonies. Cardinal changes occur at a temperature of 1000 °C (Fig. 4 c). At low magnification, the fracture looks like a dimple; a more detailed study of the fracture surface confirms the presence of dimples. It is worth noting that spherical formations arising on the fracture surface during localisation of deformation and dynamic recrystallisation/spheroidisation are observed on the fracture surface (Fig. 4 c). Oxidation at $T=1000$ °C of the dimple edges characteristic of the viscous type of fracture can lead to the formation of oxidised spherical formations (Fig. 4 c). The share of the viscous component of the fracture was 70 % (Fig. 4 c).

Changes in microstructure after deformation in the fracture zone

To study crack propagation and microstructure evolution in more detail, during testing, polished side surfaces of samples in fracture zones after tension were examined (Fig. 5). At $T=700$ °C, propagation of main and secondary cracks is observed both along colony boundaries and along α_2/γ interphase boundaries (Fig. 5 a). The length of secondary cracks does not exceed 100 μm . Signs of hindered movement of secondary cracks in favourably oriented ($15^\circ < \Phi < 75^\circ$) lamellar colonies are clearly visible, causing the formation of bridges in the colony body (Fig. 5 a) or the formation of new cracks along colony boundaries, where their propagation is less hindered (Fig. 5 a). Unfavourably oriented ($\Phi < 15^\circ$ and $\Phi > 75^\circ$) colonies are significantly less involved in plastic deformation; cracks propagate along α_2/γ boundaries or along colony boundaries (Fig. 5 a). An increase in the deformation temperature to 950 °C leads to a more active formation of secondary cracks and the formation of bridges even in the case of unfavourably oriented colonies (Fig. 5 b). It is worth noting the complete dissolution of the ω -phase particles at a temperature of 950 °C and an increase in the volume fraction of the β -phase to 15 % due to the formation of particles 0.1–3 μm in size in the body of the lamellar colonies (Fig. 5 b). Fundamental changes are observed upon reaching a temperature of 1000 °C (Fig. 5 c). Active formation of new pores is observed mainly along the colony boundaries, while in unfavourably oriented colonies, cracks form along the α_2/γ interphase boundaries, and in the case of favourably oriented colonies, bending of the plates occurs (Fig. 5 c). Spherical/polygonal particles of the $\gamma/\alpha_2/\beta$ -phases 0.1–3 μm in size are predominantly located along the colony boundaries (Fig. 5 c). It is evident that small pores are formed along the boundaries and in the body of the colonies along the chains of β -phase particles (Fig. 5 c). Moreover, large pores are predominantly located at the boundaries of favourably and unfavourably oriented colonies (Fig. 5 c). The volume fraction of pores near the fracture zone reaches 12 % (Fig. 5 c).

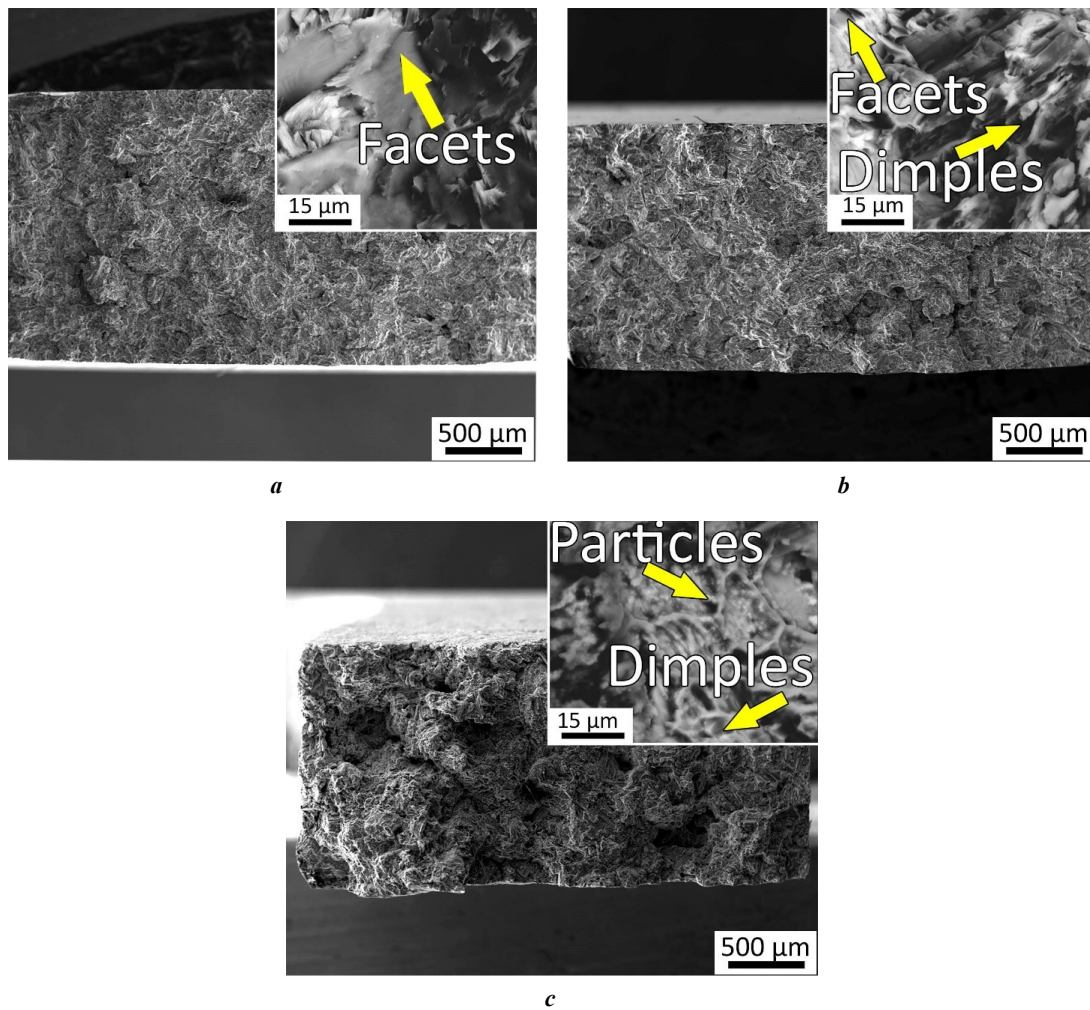


Fig. 4. Fractures of samples after tensile tests of cast TNM-B1 alloy:
a – 700 °C; **b** – 950 °C; **c** – 1000 °C.

In the enlarged areas of the fractures, facets, dimples and particles are visible
Рис. 4. Изломы образцов после испытаний на растяжение литейного сплава TNM-B1:
a – 700 °C; **b** – 950 °C; **c** – 1000 °C.

На увеличенных участках изломов видны фасетки, ямки и частицы

DISCUSSION

The obtained results showed a significant effect of temperature on the mechanical properties of the TNM-B1 alloy, its phase composition and changes in the fracture pattern in colonies with different orientations relative to the deformation axis. Three temperature ranges corresponding to brittle (25–900 °C), transition (950 °C) and ductile (1000 °C) behaviour of the alloy were found. The lamellar type of microstructure, the presence of γ -phase particles, interlayers of $\beta(B2)+\omega$ -phases and borides along the colony boundaries greatly limited the plasticity of the alloy in a wide temperature range. According to [13], at temperatures above 850 °C, the ω -phase particles dissolve, which did not have a noticeable effect on the plasticity level, as a result of which the fracture pattern was predominantly of the intercrystallite type of fracture. Plastic deformation was localised and manifested itself in the formation of bridges in favourably oriented colonies below the temperature of the brittle-ductile transition (Fig. 5 a), which is associated with limited plasticity only in colonies with an orientation

of $15^\circ < \Phi < 75^\circ$ [12]. In the case of unfavourably oriented colonies, the stress level did not reach the values necessary for the plastic deformation onset, which led to the propagation of cracks mainly along the α_2/γ interphase boundaries (Fig. 5 a). This behaviour is associated with the mechanical behaviour anisotropy of colonies with different orientations relative to the deformation axis [8; 9; 12]. According to [10], an increase in the deformation temperature to 950 °C led to the activation of multiple slip and an increase in diffusion, which was expressed in a change in the fracture type from intercrystallite to transcrystalline, the appearance of dimples and the formation of bridges regardless of the orientation of the colonies relative to the deformation axis (Fig. 5). With further increase in temperature, spheroidisation/recrystallisation is activated, which leads to softening and increased plasticity [14]. The formation of new dispersed β -phase particles upon heating to 950–1000 °C is an expected consequence of the increase in the equilibrium β -phase content in the alloy [15], which is typical for TNM alloys when held in the range of 900–1100 °C [15]. As was

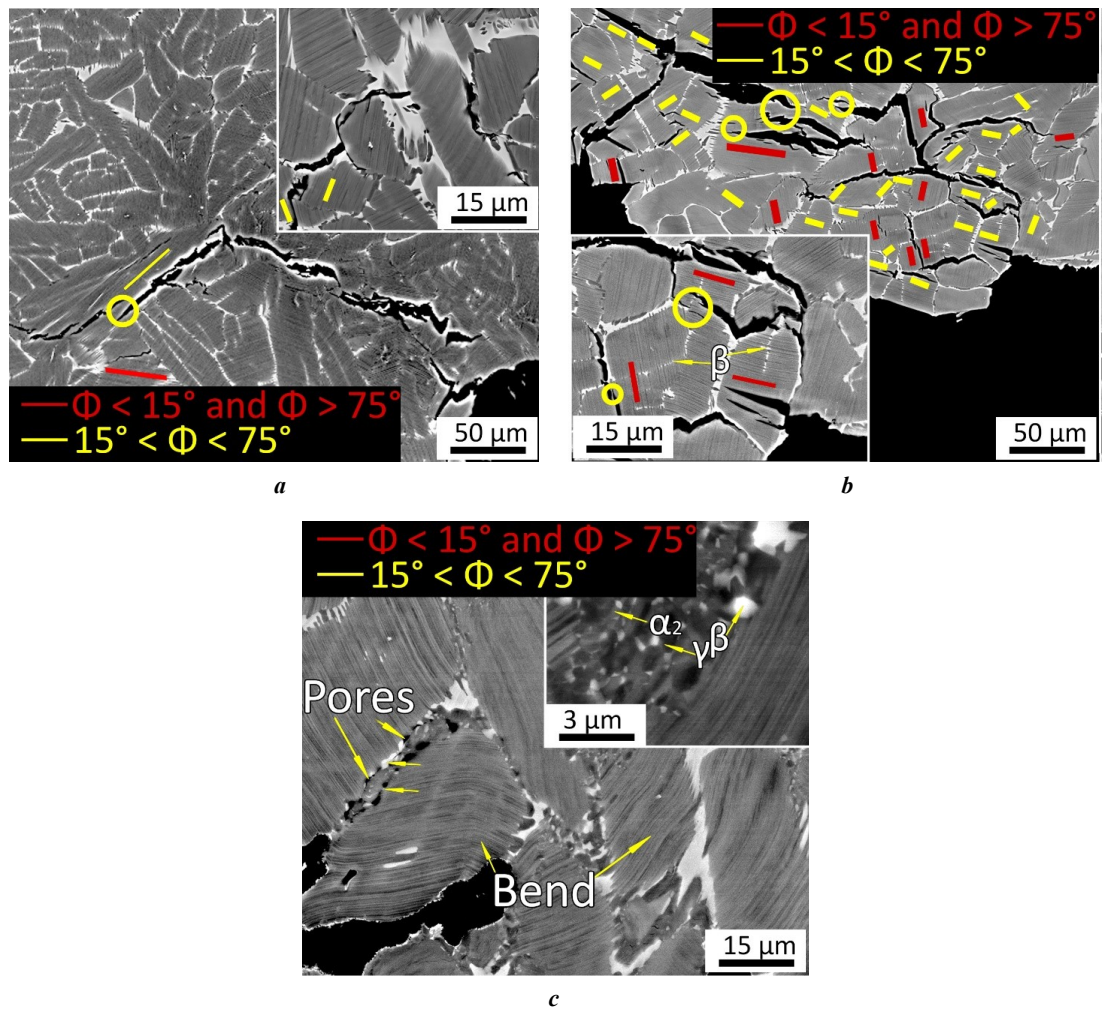


Fig. 5. Microstructure of samples after tensile tests near the fracture zone:

a – 700 °C; **b** – 950 °C; **c** – 1000 °C.

The tensile axis is vertical. The circles indicate the bridges. The arrows indicate the structural elements. The yellow and red lines indicate the colonies favorably and unfavorably oriented relative to the deformation axis, respectively

Рис. 5. Микроструктура образцов после испытаний на растяжение вблизи зоны разрушения: **a** – 700 °C; **b** – 950 °C; **c** – 1000 °C.

Ось растяжения расположена вертикально. Окружностями обозначены перемычки.

Стрелками обозначены структурные элементы.

Желтыми и красными линиями обозначены благоприятно и неблагоприятно ориентированные относительно оси деформации колонии соответственно

shown (Fig. 5), small pores were formed predominantly at the β/γ boundaries, which is consistent with the data [16]. Their formation can be provoked by a higher coefficient of thermal expansion of the β -phase in relation to the γ -phase, leading to local thermal stresses [17].

Particular attention should be paid to the observed mechanism of bridge formation during crack growth. They are formed as a result of plastic deformation between adjacent areas, and their presence correlates with fracture toughness, since it is associated with the work of plastic deformation in the crack propagation zone [18]. The formation of bridges in colonies with different orientations relative to the deformation axis can be affected by microstructural parameters, as well as fracture toughness, which was shown in [18]. Fracture toughness increases with increasing colony size due to the tendency to form larger bridges [19;

20]. As shown in [21], saturation is observed for colonies larger than 600 μm , which can be partly associated with the large colony size, since in such cases only a few colonies are encountered along the crack propagation path. An increase in fracture toughness with a decrease in the interlamellar distance is associated with a hindrance to trans-lamellar cracking, which leads to an increase in the number of bridges [18], a decrease in the interlamellar distance of less than 100 nm leads to the intercrystallite type of fracture due to a decrease in ductility. On the contrary, thick lamellae promote translamellar cracking and facilitated connection of microcracks with the main crack, which leads to the formation of a smaller number of smaller bridges and a decrease in fracture toughness [18]. Previous results [8] confirm those obtained in this work, namely, the formation of bridges only in favourably oriented colonies at room

temperature in the alloy with $\lambda \sim 100$ nm and a decrease in their number at $\lambda \sim 10$ nm, as well as the predominance of translamellar cracking at $\lambda \sim 800$ nm. Most likely, an increase in the colony size will not lead to a change in crack propagation in colonies with different orientations relative to the tensile axis.

The obtained results show that an increase in temperature leads to a change in the phase composition, dissolution of embrittling particles and the development of spheroidisation/recrystallisation, which leads to a change in the behaviour of the alloy from brittle to ductile. The orientation of the lamellae relative to the tensile axis fundamentally affects crack propagation. In the temperature range corresponding to brittle fracture, bridges were formed only in the case of favourable colony orientation; when transition and viscous fracture were reached, bridges were formed regardless of orientation.

CONCLUSIONS

1. The microstructure of the cast TNM-B1 alloy was studied. It was represented mainly by $(\alpha_2 + \gamma)$ -plate colonies with interlayers of a mixture of $\beta(B2) + \omega$ -phases located along the boundaries. At deformation temperatures above 950 °C, dissolution of ω -phase particles and precipitation of dispersed particles of the secondary β -phase were identified.

2. The effect of tensile deformation temperature on mechanical properties was considered. With an increase in deformation temperature, a continuous increase in relative elongation was observed, reaching a maximum of $\delta = 22.5$ % at $T = 1000$ °C, and a nonlinear change in strength with a maximum of $\sigma_B = 592$ MPa at $T = 800$ °C, followed by a decrease to $\sigma_B = 340$ MPa at $T = 1000$ °C. The fracture pattern was predominantly intercrystallite in the brittle, transcrystalline in the transition, and dimple in the ductile temperature range of deformation. The brittle-ductile transition corresponded to a temperature range of about 950 °C, which corresponded to the transition state of the alloy.

3. A study was conducted to investigate the effect of temperature on crack propagation in the alloy structure. A different pattern of crack propagation was found in favourably and unfavourably oriented colonies relative to the deformation axis, which was expressed in the inhibition of crack propagation and the formation of bridges in favourably oriented colonies, in contrast to unfavourably oriented ones. An increase in temperature to 950 °C resulted in no difference in the pattern of crack propagation in colonies with different orientations relative to the axis of tension. When the temperature reached 1000 °C, no cracks were observed, as well as the formation of pores along the boundaries of colonies and along the chains of secondary β -phase particles.

REFERENCES

- Genc O., Unal R. Development of gamma titanium aluminide (γ -TiAl) alloys: A review. *Journal of Alloys and Compounds*, 2022, vol. 929, article number 167262. DOI: [10.1016/j.jallcom.2022.167262](https://doi.org/10.1016/j.jallcom.2022.167262).
- Duan Baohua, Yang Yuchen, He Shiyu et al. History and development of γ -TiAl alloys and the effect of alloying elements on their phase transformations. *Journal of Alloys and Compounds*, 2022, vol. 909, article number 164811. DOI: [10.1016/j.jallcom.2022.164811](https://doi.org/10.1016/j.jallcom.2022.164811).
- Musi M., Graf G., Clemens H., Spoerk-Erdely P. Alloying elements in intermetallic γ -TiAl based alloys – A review on their influence on phase equilibria and phase transformations. *Advanced Engineering Materials*, 2024, vol. 26, no. 4, article number 2300610. DOI: [10.1002/adem.202300610](https://doi.org/10.1002/adem.202300610).
- Tetsui T., Fukuyo T., Mizuta K. Comparison of the impact resistance of TiAl4822 and TNM alloy under expected service conditions of jet engine blades. *Intermetallics*, 2025, vol. 183, article number 108793. DOI: [10.1016/j.intermet.2025.108793](https://doi.org/10.1016/j.intermet.2025.108793).
- Imayev R.M., Kaibyshev O.A., Salishchev G.A. Mechanical behaviour of fine grained TiAl intermetallic compound II. Ductile-brittle transition. *Acta Metallurgica Materialia*, 1992, vol. 40, no. 3, pp. 589–595. DOI: [10.1016/0956-7151\(92\)90408-7](https://doi.org/10.1016/0956-7151(92)90408-7).
- Wu Hao, Zhang Yida, Lu Dong, Gong Xiufang, Lei Liming, Zhang Hong, Liu Yongjie, Wang Qingyuan. Exploring the brittle-to-ductile transition and microstructural responses of TiAl alloy with a crystal plasticity model incorporating dislocation and twinning. *Materials & Design*, 2024, vol. 246, article number 113360. DOI: [10.1016/j.matdes.2024.113360](https://doi.org/10.1016/j.matdes.2024.113360).
- Appel F., Lorenz U., Oehring M., Sparka U., Wagner R. Thermally activated deformation mechanisms in microalloyed two-phase titanium aluminide alloys. *Materials Science and Engineering: A*, 1997, vol. 233, no. 1-2, pp. 1–14. DOI: [10.1016/S0921-5093\(97\)00043-9](https://doi.org/10.1016/S0921-5093(97)00043-9).
- Panov D.O., Sokolovsky V.S., Stepanov N.D., Zhrebtsov S.V., Panin P.V., Volokitina E.I., Nochovnaya N.A., Salishchev G.A. Effect of interlamellar spacing on strength-ductility combination of β -solidified γ -TiAl based alloy with fully lamellar structure. *Materials Science and Engineering: A*, 2023, vol. 862, article number 144458. DOI: [10.1016/j.msea.2022.144458](https://doi.org/10.1016/j.msea.2022.144458).
- Hu D., Loretto M.H. Slip transfer between lamellae in fully lamellar TiAl alloys. *Intermetallics*, 1999, vol. 7, no. 11, pp. 1299–1306. DOI: [10.1016/S0966-9795\(99\)00049-7](https://doi.org/10.1016/S0966-9795(99)00049-7).
- Mishin Y., Herzig Ch. Diffusion in the Ti–Al system. *Acta Materialia*, 2000, vol. 48, no. 3, pp. 589–623. DOI: [10.1016/S1359-6454\(99\)00400-0](https://doi.org/10.1016/S1359-6454(99)00400-0).
- Liu Xin, Liu Hongguang, Shi Shijia, Tang Yuyang, Zhang Jun. On revealing the mechanisms involved in brittle-to-ductile transition of fracture behaviors for γ -TiAl alloy under dynamic conditions. *Journal of Alloys and Compounds*, 2025, vol. 1010, article number 177614. DOI: [10.1016/j.jallcom.2024.177614](https://doi.org/10.1016/j.jallcom.2024.177614).
- Edwards T.E.J., Di Gioacchino F., Goodfellow A.J., Mohanty G., Wehrs J., Michler J., Clegg W.J. Deformation of lamellar γ -TiAl below the general yield stress. *Acta Materialia*, 2019, vol. 163, pp. 122–139. DOI: [10.1016/j.actamat.2018.09.061](https://doi.org/10.1016/j.actamat.2018.09.061).
- Schloffer M., Rashkova B., Schöberl T., Schwaighofer E., Zhang Zhang, Clemens H., Mayer S. Evolution of the ω_o phase in a β -stabilized multi-phase TiAl alloy and

- its effect on hardness. *Acta Materialia*, 2014, vol. 64, pp. 241–252. DOI: [10.1016/j.actamat.2013.10.036](https://doi.org/10.1016/j.actamat.2013.10.036).
14. Molenat G., Galy B., Musi M., Toulalbi L., Thomas M., Clemens H., Monchoux J.Ph., Couret A. Plasticity and brittleness of the ordered β_0 phase in a TNM-TiAl alloy. *Intermetallics*, 2022, vol. 151, article number 107653. DOI: [10.1016/j.intermet.2022.107653](https://doi.org/10.1016/j.intermet.2022.107653).
 15. Kuznetsov A.V., Sokolovskii V.S., Salishchev G.A., Belov N.A., Nochovnaya N.A. Thermodynamic modeling and experimental study of phase transformations in alloys based on γ -TiAl. *Metal Science and Heat Treatment*, 2016, vol. 58, pp. 259–267. DOI: [10.1007/s11041-016-9999-2](https://doi.org/10.1007/s11041-016-9999-2).
 16. Zhu Bin, Xue Xiangyi, Kou Hongchao, Li Xiaolei, Li Jinshan. The cavitation of high Nb-containing TiAl alloys during tensile tests around BDTT. *Materials Science and Engineering: A*, 2018, vol. 729, pp. 86–93. DOI: [10.1016/j.msea.2018.05.028](https://doi.org/10.1016/j.msea.2018.05.028).
 17. Staron P., Stark A., Schell N., Spoerk-Erdely P., Clemens H. Thermal expansion of a multiphase intermetallic Ti-Al-Nb-Mo alloy studied by high-energy X-ray diffraction. *Materials*, 2021, vol. 14, no. 4, article number 727. DOI: [10.3390/ma14040727](https://doi.org/10.3390/ma14040727).
 18. Kim Y.W. Effects of microstructure on the deformation and fracture of γ -TiAl alloys. *Materials Science and Engineering: A*, 1995, vol. 192–193, part 2, pp. 519–533. DOI: [10.1016/0921-5093\(94\)03271-8](https://doi.org/10.1016/0921-5093(94)03271-8).
 19. Liu C.T., Schneibel J.H., Maziasz P.J., Wright J.L., Easton D.S. Tensile properties and fracture toughness of TiAl alloys with controlled microstructures. *Intermetallics*, 1996, vol. 4, no. 6, pp. 429–440. DOI: [10.1016/0966-9795\(96\)00047-7](https://doi.org/10.1016/0966-9795(96)00047-7).
 20. Wang J.N., Xie K. Refining of coarse lamellar microstructure of TiAl alloys by rapid heat treatment. *Intermetallics*, 2000, vol. 8, no. 5–6, pp. 545–548. DOI: [10.1016/S0966-9795\(99\)00153-3](https://doi.org/10.1016/S0966-9795(99)00153-3).
 21. Rogers N.J., Crofts P.D., Jones I.P., Bowen P. Microstructure toughness relationships in fully lamellar γ -based titanium aluminides. *Materials Science and Engineering: A*, 1995, vol. 192–193, part 1, pp. 379–386. DOI: [10.1016/0921-5093\(94\)03222-X](https://doi.org/10.1016/0921-5093(94)03222-X).
- СПИСОК ЛИТЕРАТУРЫ**
1. Genc O., Unal R. Development of gamma titanium aluminide (γ -TiAl) alloys: A review // *Journal of Alloys and Compounds*. 2022. Vol. 929. Article number 167262. DOI: [10.1016/j.jallcom.2022.167262](https://doi.org/10.1016/j.jallcom.2022.167262).
 2. Duan Baohua, Yang Yuchen, He Shiyu et al. History and development of γ -TiAl alloys and the effect of alloying elements on their phase transformations // *Journal of Alloys and Compounds*. 2022. Vol. 909. Article number 164811. DOI: [10.1016/j.jallcom.2022.164811](https://doi.org/10.1016/j.jallcom.2022.164811).
 3. Musi M., Graf G., Clemens H., Spoerk-Erdely P. Alloying elements in intermetallic γ -TiAl based alloys – A review on their influence on phase equilibria and phase transformations // *Advanced Engineering Materials*. 2024. Vol. 26. № 4. Article number 2300610. DOI: [10.1002/adem.202300610](https://doi.org/10.1002/adem.202300610).
 4. Tetsui T., Fukuyo T., Mizuta K. Comparison of the impact resistance of TiAl4822 and TNM alloy under expected service conditions of jet engine blades // *Intermetallics*. 2025. Vol. 183. Article number 108793. DOI: [10.1016/j.intermet.2025.108793](https://doi.org/10.1016/j.intermet.2025.108793).
 5. Imayev R.M., Kaibyshev O.A., Salishchev G.A. Mechanical behaviour of fine grained TiAl intermetallic compound II. Ductile-brittle transition // *Acta Metallurgica Materialia*. 1992. Vol. 40. № 3. P. 589–595. DOI: [10.1016/0956-7151\(92\)90408-7](https://doi.org/10.1016/0956-7151(92)90408-7).
 6. Wu Hao, Zhang Yida, Lu Dong, Gong Xiufang, Lei Liming, Zhang Hong, Liu Yongjie, Wang Qingyuan. Exploring the brittle-to-ductile transition and microstructural responses of TiAl alloy with a crystal plasticity model incorporating dislocation and twinning // *Materials & Design*. 2024. Vol. 246. Article number 113360. DOI: [10.1016/j.matdes.2024.113360](https://doi.org/10.1016/j.matdes.2024.113360).
 7. Appel F., Lorenz U., Oehring M., Sparka U., Wagner R. Thermally activated deformation mechanisms in microalloyed two-phase titanium aluminide alloys // *Materials Science and Engineering: A*. 1997. Vol. 233. № 1–2. P. 1–14. DOI: [10.1016/S0921-5093\(97\)00043-9](https://doi.org/10.1016/S0921-5093(97)00043-9).
 8. Panov D.O., Sokolovsky V.S., Stepanov N.D., Zhreb-tsov S.V., Panin P.V., Volokitina E.I., Nochovnaya N.A., Salishchev G.A. Effect of interlamellar spacing on strength-ductility combination of β -solidified γ -TiAl based alloy with fully lamellar structure // *Materials Science and Engineering: A*. 2023. Vol. 862. Article number 144458. DOI: [10.1016/j.msea.2022.144458](https://doi.org/10.1016/j.msea.2022.144458).
 9. Hu D., Loretto M.H. Slip transfer between lamellae in fully lamellar TiAl alloys // *Intermetallics*. 1999. Vol. 7. № 11. P. 1299–1306. DOI: [10.1016/S0966-9795\(99\)00049-7](https://doi.org/10.1016/S0966-9795(99)00049-7).
 10. Mishin Y., Herzig Ch. Diffusion in the Ti–Al system // *Acta Materialia*. 2000. Vol. 48. № 3. P. 589–623. DOI: [10.1016/S1359-6454\(99\)00400-0](https://doi.org/10.1016/S1359-6454(99)00400-0).
 11. Liu Xin, Liu Hongguang, Shi Shijia, Tang Yuyang, Zhang Jun. On revealing the mechanisms involved in brittle-to-ductile transition of fracture behaviors for γ -TiAl alloy under dynamic conditions // *Journal of Alloys and Compounds*. 2025. Vol. 1010. Article number 177614. DOI: [10.1016/j.jallcom.2024.177614](https://doi.org/10.1016/j.jallcom.2024.177614).
 12. Edwards T.E.J., Di Gioacchino F., Goodfellow A.J., Mohanty G., Wehrs J., Michler J., Clegg W.J. Deformation of lamellar γ -TiAl below the general yield stress // *Acta Materialia*. 2019. Vol. 163. P. 122–139. DOI: [10.1016/j.actamat.2018.09.061](https://doi.org/10.1016/j.actamat.2018.09.061).
 13. Schloffer M., Rashkova B., Schöberl T., Schwaighofer E., Zhang Zhang, Clemens H., Mayer S. Evolution of the ω_0 phase in a β -stabilized multi-phase TiAl alloy and its effect on hardness // *Acta Materialia*. 2014. Vol. 64. P. 241–252. DOI: [10.1016/j.actamat.2013.10.036](https://doi.org/10.1016/j.actamat.2013.10.036).
 14. Molenat G., Galy B., Musi M., Toulalbi L., Thomas M., Clemens H., Monchoux J.Ph., Couret A. Plasticity and brittleness of the ordered β_0 phase in a TNM-TiAl alloy // *Intermetallics*. 2022. Vol. 151. Article number 107653. DOI: [10.1016/j.intermet.2022.107653](https://doi.org/10.1016/j.intermet.2022.107653).
 15. Kuznetsov A.V., Sokolovskii V.S., Salishchev G.A., Belov N.A., Nochovnaya N.A. Thermodynamic modeling and experimental study of phase transformations in alloys based on γ -TiAl // *Metal Science and Heat Treatment*. 2016. Vol. 58. P. 259–267. DOI: [10.1007/s11041-016-9999-2](https://doi.org/10.1007/s11041-016-9999-2).
 16. Zhu Bin, Xue Xiangyi, Kou Hongchao, Li Xiaolei, Li Jinshan. The cavitation of high Nb-containing TiAl

- alloys during tensile tests around BDTT // Materials Science and Engineering: A. 2018. Vol. 729. P. 86–93. DOI: [10.1016/j.msea.2018.05.028](https://doi.org/10.1016/j.msea.2018.05.028).
17. Staron P., Stark A., Schell N., Spoerk-Erdely P., Clemens H. Thermal expansion of a multiphase intermetallic Ti-Al-Nb-Mo alloy studied by high-energy X-ray diffraction // Materials. 2021. Vol. 14. № 4. Article number 727. DOI: [10.3390/ma14040727](https://doi.org/10.3390/ma14040727).
 18. Kim Y.W. Effects of microstructure on the deformation and fracture of γ -TiAl alloys // Materials Science and Engineering: A. 1995. Vol. 192-193. Part 2. P. 519–533. DOI: [10.1016/0921-5093\(94\)03271-8](https://doi.org/10.1016/0921-5093(94)03271-8).
 19. Liu C.T., Schneibel J.H., Maziasz P.J., Wright J.L., Easton D.S. Tensile properties and fracture toughness of TiAl alloys with controlled microstructures // Intermetallics. 1996. Vol. 4. № 6. P. 429–440. DOI: [10.1016/0966-9795\(96\)00047-7](https://doi.org/10.1016/0966-9795(96)00047-7).
 20. Wang J.N., Xie K. Refining of coarse lamellar microstructure of TiAl alloys by rapid heat treatment // Intermetallics. 2000. Vol. 8. № 5-6. P. 545–548. DOI: [10.1016/S0966-9795\(99\)00153-3](https://doi.org/10.1016/S0966-9795(99)00153-3).
 21. Rogers N.J., Crofts P.D., Jones I.P., Bowen P. Microstructure toughness relationships in fully lamellar γ -based titanium aluminides // Materials Science and Engineering: A. 1995. Vol. 192-193. Part 1. P. 379–386. DOI: [10.1016/0921-5093\(94\)03222-X](https://doi.org/10.1016/0921-5093(94)03222-X).

УДК 669.017.165

doi: 10.18323/2782-4039-2025-3-73-6

Исследование влияния температуры деформации на механическое поведение и особенности разрушения литого сплава TNM-B1

Соколовский Виталий Сергеевич*, кандидат технических наук,
научный сотрудник лаборатории объемных наноструктурных материалов
Салищев Геннадий Алексеевич¹, доктор технических наук, профессор,
заведующий лабораторией объемных наноструктурных материалов

Белгородский государственный национальный исследовательский университет, Белгород (Россия)

*E-mail: sokolovskiy@bsuedu.ru

¹ORCID: <https://orcid.org/0000-0002-0815-3525>

Поступила в редакцию 07.07.2025

Пересмотрена 25.07.2025

Принята к публикации 20.08.2025

Аннотация: Статья посвящена β -затвердевающим сплавам на основе TiAl, которые являются крайне перспективными для авиационной промышленности материалами с рабочей температурой до 850 °С, обладают высокими удельными прочностными характеристиками. Исследовано влияние температуры деформации при растяжении в интервале $T=25\text{--}1000$ °С на механические свойства, фазовый состав и трещинообразование в литом сплаве – β -затвердевавшем TNM-B1. Установлено, что литой сплав TNM-B1 характеризуется комплексной микроструктурой, включающей ($\alpha_2+\gamma$)-пластинчатые колонии и прослойки $\beta(B2)+\omega$ -фаз, эволюция которых при повышенных температурах деформации определяет поведение материала. Показано, что растворение ω -фазы и выделение дисперсных частиц вторичной β -фазы при $T>950$ °С оказывают существенное влияние на механические характеристики. Установлена выраженная температурная зависимость прочности и пластичности: максимальная прочность наблюдается при 800 °С, в то время как наибольшее относительное удлинение в исследованном интервале температур достигается при 1000 °С. Переход от хрупкого к вязкому характеру разрушения происходит в интервале температур в области 950 °С. Кроме того, выявлена зависимость механизма распространения трещин от ориентации пластинчатых колоний относительно оси деформации: при повышении температуры различия нивелируются, а при 1000 °С наблюдается полное подавление трещинообразования с формированием пор вдоль границ колоний и скопления частиц вторичной β -фазы. Полученные результаты демонстрируют важную роль микроструктурных превращений в формировании деформационного поведения и механических свойств сплава на основе гамма-алюминидов титана TNM-B1, что имеет практическое значение для разработки технологий его термомеханической обработки.

Ключевые слова: литой сплав TNM-B1; механическое поведение; особенности разрушения; сплав типа TNM; микроструктура; хрупко-вязкий переход; прочность; пластичность.

Благодарности: Работа выполнена при финансовой поддержке Российского научного фонда (соглашение № 19-79-30066) с использованием оборудования Центра коллективного пользования «Технологии и материалы» НИУ «БелГУ», https://rscf.ru/prjcard_int?19-79-30066.

Для цитирования: Соколовский В.С., Салищев Г.А. Исследование влияния температуры деформации на механическое поведение и особенности разрушения литого сплава TNM-B1 // Frontier Materials & Technologies. 2025. № 3. С. 81–89. DOI: 10.18323/2782-4039-2025-3-73-6.



GENERAL PUBLICATION REQUIREMENTS FOR AUTHORS

The journal publishes two versions of papers: in Russian and in English. The data of manuscript has to be original and never submitted or published before in other journals. All submitted papers are checked in the Anti-Plagiarism system ("Antiplagiat" system).

For publication, authors need to submit an application to the editorial office by sending the materials to the e-mail of the journal vektornaukitgu@yandex.ru or by uploading them to their personal account on the website <https://www.vektornaukitech.ru>.

Required structural elements of the manuscript

- *UDC identifier*;
- *the title* of the scientific manuscript;
- *copyright sign and year*;
- *information about the authors*: surname and initials of the author, academic degree, academic status, occupation; company, city, country; ORCID. The author corresponding to the editorial staff should provide his/her E-mail;
- *abstract* (200–250 words) should contain a brief summary of the paper's concept in order to interest a potential reader;
- *keywords* (the main criterion of choosing keywords is their potential value to summarize the content of the document or to help the readers to find the document);
- *acknowledgements* to individuals, granting organizations;
- *the text of the manuscript* structured in accordance with the rules;
- *references* (at least 20 sources).

Article structure

The structure of the article should conform to the IMRAD (Introduction, Methods, Results, and Discussion) standard, applied by Science World Community:

- INTRODUCTION
- METHODS
- RESULTS
- DISCUSSION
- CONCLUSIONS

Tables and figures formatting

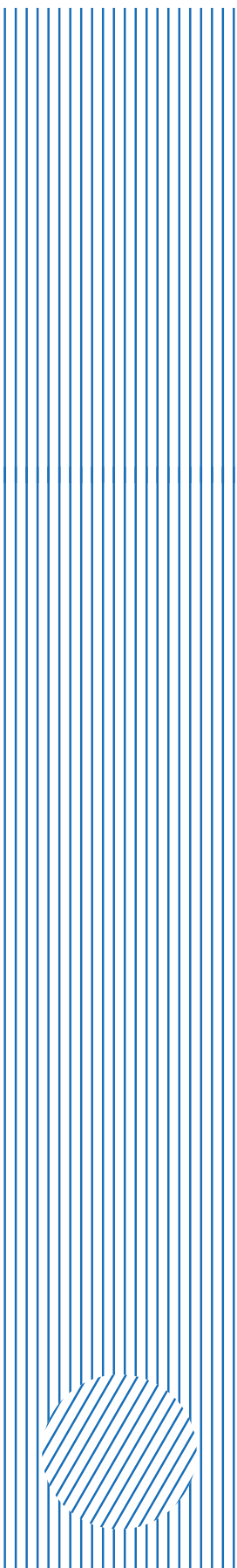
Tables and figures should not fall outside the page layout. The use of landscape pages is not allowed. The titles of the tables and figures captures are required. If the text contains figures, diagrams, and tables from other literary sources, it is necessary to indicate where they were taken from.

Formulas typing

Formulas are edited in Microsoft Equation 3 formula editor. Formulas should not be longer than 80 mm. The size of the formula is 100 %. Converting formulas to figures is not allowed.

References and citations formatting

References are listed in the order of citation in the article. Reference list should not include the sources not cited in the article. In the journal it is not common to cite textbooks and study guides, except the flagship in their respective field, thesis papers and synopsis of a thesis. Not less than a quarter of the sources listed in the reference list should be published in the last 3–5 years. References to print publications only are acceptable (excluding e-journals). References to internet sites are not accepted. Not more than 20 % of the sources can be references on the own author's publications. If a cited source has a DOI, the DOI should be indicated at the end of bibliographic description of this source. All DOIs should be valid links.



Study of the temperature field formed in the process of milling with the use of ultrasonic vibrations under various processing modes

*Aleksandr N. Unyanin**¹, Doctor of Sciences (Engineering), Professor,
professor of Chair “Innovative Technologies in Machine Building”

Aleksandr V. Chudnov, postgraduate student

Ilnaz Z. Dimukhametov, postgraduate student

Ulyanovsk State Technical University, Ulyanovsk (Russia)

*E-mail: a_un@mail.ru

¹ORCID: <https://orcid.org/0000-0002-5557-4197>

Received 14.04.2025

Revised 05.06.2025

Accepted 18.06.2025

Abstract: Study of the temperature field of the milling process with the imposition of ultrasonic vibrations (USV), under various ratios of the vibration amplitude to the depth of tooth penetration into the blank, will allow predicting the efficiency of the milling process with USV under various processing modes. The purpose of this study is to develop physical and mathematical models of the milling process with the imposition of USV, allowing identifying the influence of ultrasonic vibrations on the efficiency of the milling process under various ratios of the vibration amplitude to the depth of tooth penetration. Three sources of heat generation are considered: in the deformation (chip formation) area and in the zones of contact of the chip with the cutting plate (cutter tooth) and the plate with the blank. The authors have developed heat transfer models that take into account, in particular, the change in boundary conditions on the surfaces of the cutting plate and the blank under the USV imposition. When the plate is in contact with the blank, heat flows are directed to the blank, chips and cutter tooth, and the conditions of thermal interaction within the zones of contact of the plate with the chips and the blank are described by boundary conditions of the 2nd type. When the plate leaves the contact with the blank during the ultrasonic imposition and the chip formation process stops, then on all surfaces of the tooth (plate) and the blank that are in contact with the environment (cutting fluid or air), the convective heat transfer is described by the Newton–Richmann law (boundary conditions of the 3rd type). The results of numerical modelling are presented, confirming the assumption that the effect of using ultrasonic vibrations is higher at high values of the ratio of the ultrasonic vibration amplitude to the depth of tooth penetration into the blank.

Keywords: ultrasound; vibrations; milling; heat transfer; numerical modelling.

Acknowledgements: The study was supported by the Russian Science Foundation grant No. 24-2900206, <https://rscf.ru/project/24-29-00206/>.

For citation: Unyanin A.N., Chudnov A.V., Dimukhametov I.Z. Study of the temperature field formed in the process of milling with the use of ultrasonic vibrations under various processing modes. *Frontier Materials & Technologies*, 2025, no. 3, pp. 91–100. DOI: 10.18323/2782-4039-2025-3-73-7.

INTRODUCTION

High temperatures accompanying most machining processes have a significant effect on many physical processes occurring in the machining zone. The temperature of the surface layers of the blanks affects the structural and phase composition of its material [1], residual stresses formed in the surface layer of the machined part [2], and the microhardness of this layer. Defects appear on the machined surfaces of blanks made of materials with low temperatures of decomposition and melting, in particular plastics. It has been found that plastics are easily plastically deformed during machining due to heating [3]. The work [4] confirms that due to the low melting temperature, plastics are prone to undesirable plastic deformation during machining and to the formation of burrs.

The temperature of the tool surfaces in contact with the blanks and chips influences the wear rate, service life and strength of the tool, i.e. its performance [5]. Therefore, re-

search into the patterns of formation of temperature fields of machining processes and the ability to control them are necessary to increase machining productivity and ensure the quality of the machined parts.

The efficiency of cutting processes increases with the use of vibrations, including ultrasonic vibrations (USV), since their use reduces cutting forces and temperatures in the cutting zone, which allows increasing the productivity of processing while ensuring the required quality of parts [6] or increasing the service life of the cutting tool. Analytical and experimental studies of mechanical treatment processes using USV have shown the possibility of reducing, due to their use, cutting forces (up to 2 times) and temperatures in the cutting zone during turning and boring [7], grinding [8] and gear milling [9].

A widely used processing method is milling with cylindrical and end mills. In the milling process, the thickness of the cut per one tooth of the tool changes depending

on the position of the tooth on the trajectory of its contact with the blank. The variable thickness of the cut causes a change in many parameters of the process of treatment, including cutting and friction forces, powers and densities of heat sources. The process of heating the cutter tooth is non-stationary. The tooth heats up in a short period of time while in contact with the blank, then cools down. When modelling this process, the mutual influence of heat sources from successively operating teeth should also be taken into account. Experimental studies indicating an increase in the efficiency of the milling process using USV have been carried out, in particular, when machining non-rigid parts [10] and blanks made of corrosion-resistant steels [11].

The results of numerical modelling of the temperature field of the process of milling using ultrasonic vibrations, carried out on the basis of an analytical study of this process, are given in [12] with varying the pitch of the cutter teeth and in [13] with varying the thermal conductivity of the cutter material. However, these results were obtained with the ratios of the vibration amplitude A to the maximum depth of penetration of the cutter tooth (cutting plate) into the blank a_{mmax} , at which the tooth does not come out of contact with the blank, while at different moments of contact time during processing with ultrasonic vibrations, the depth of tooth penetration can be both greater and less than the depth achieved during processing without vibrations (Fig. 1 a). When the values of these parameters differ insignificantly or the amplitude A exceeds the value a_{mmax} , in certain sections of the trajectory of contact with the blank, the tooth comes out of contact (Fig. 1 b).

When using ultrasonic vibrations in the cutting process, the reduction of thermal and force intensity is ensured by changing the kinematic parameters of the cutting process, reducing the friction coefficients in the cutting zone [7] and changing the mechanical characteristics of the blank material [14]. During the period when the tooth leaves contact with the blank, the cutting and

friction forces, power and density of heat sources are zero, therefore, with an increase in the ratio of the USV amplitude A to the depth of tooth penetration into the blank, the effect of changing the kinematics of the process of treatment should be higher. However, to calculate the temperature field of this process, it is necessary to develop appropriate physical and mathematical models. These models should take into account, in particular, that the boundary conditions on the surfaces of the cutting plate (cutter tooth) and the blank change with USV imposition if the plate leaves contact with the blank. When the cutting plate contacts the blank, heat flows are directed to the blank, chips and plate (milling cutter tooth), i.e. the conditions of thermal interaction within the zones of contact of the plate with the chips and the blank are described by boundary conditions of the 2nd type. When the milling cutter plate comes out of contact with the blank and the chip formation process stops, the heat flows disappear on all surfaces of the plate and the blank that are in contact with the environment (cutting fluid or air), and the convective heat exchange is expressed by the Newton–Richmann law (boundary conditions of the 3rd type).

The purpose of this study is to develop physical and mathematical models of the milling process with the imposition of ultrasonic vibrations (USV), allowing identifying the influence of vibrations on the efficiency of the milling process at different ratios of the vibration amplitude to the depth of tooth penetration into the blank.

METHODS

In the thermophysical analysis of cutting processes, three sources of heat generation are usually taken into account [15]. Therefore, we assume that during milling, heat is generated in the deformation (chip formation) zone and in the zones of contact of the chip with the cutting plate (front surface of the cutter tooth) and the plate (rear surface of the tooth) with the blank, where friction forces act.

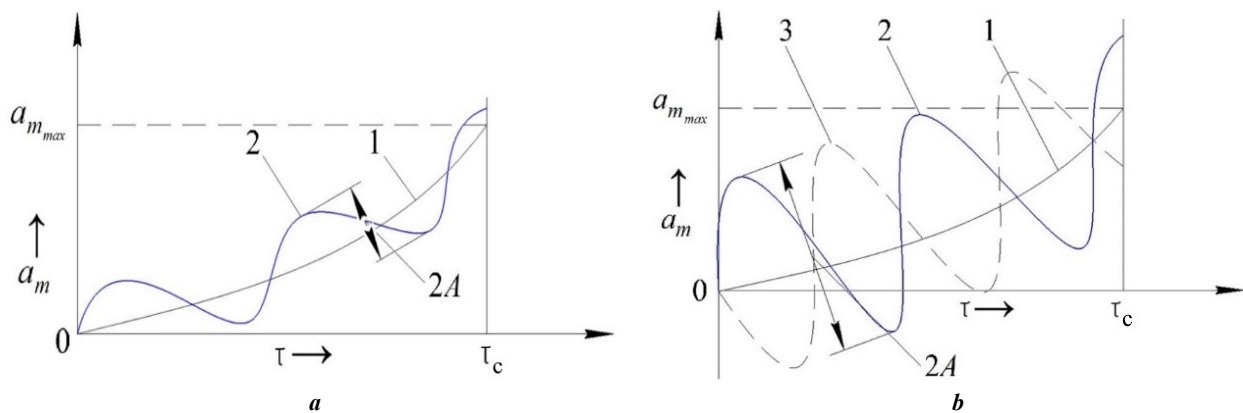


Fig. 1. Dependence of the depth of tooth penetration into the blank a_m on the contact time τ :
 1 – without the use of ultrasonic vibrations; 2 – with the use of ultrasonic vibrations at a phase shift of $\varphi=0^\circ$;
 3 – with the use of ultrasonic vibrations at a phase shift of $\varphi=180^\circ$. **a** – $2A < a_{mmax}$; **b** – $2A = a_{mmax}$

Рис. 1. Зависимость глубины внедрения зуба в заготовку a_m от времени контакта τ :
 1 – без применения УЗК; 2 – с применением УЗК при сдвиге фазы $\varphi=0^\circ$;
 3 – с применением УЗК при сдвиге фазы $\varphi=180^\circ$. **a** – $2A < a_{mmax}$; **b** – $2A = a_{mmax}$

The studies were carried out for the process of counter milling with cylindrical cutters and the periphery of end mills for the case when one tooth (plate) is located on the contact trajectory in the plane perpendicular to the cutter axis. Thermal resistance in the zones of contact of the cutting plate with the chip and the blank is not taken into account. Therefore, it is assumed that the temperature at any point in the contact zones of these objects is the same.

The heat transfer diagram is shown in Fig. 2.

RESULTS

The powers of heat sources in the deformation (chip formation) zone W_g and in the zones of contact of the cutting plate with the chip (W_{1T}), and the blank (W_{2T}) change depending on the position of the tooth on the trajectory of the contact with the blank (contact time τ) and are calculated using the dependencies [16]:

$$W_g(\tau) = P_z(\tau) \cdot V - (W_{1T}(\tau) + W_{2T}(\tau));$$

$$W_{1T}(\tau) = F_1(\tau) \cdot V_1;$$

$$W_{2T}(\tau) = F_2(\tau) \cdot V,$$

where $P_z(\tau)$ is the main component of the cutting force of the cutter plate changing along the contact trajectory, N; $F_1(\tau)$ and $F_2(\tau)$ are the friction forces in the zones of contact of the plate with the chip and the blank, respectively, N; V is the cutting speed, m/s;

V_1 is the speed of chip movement relative to the cutting plate (front surface of the tooth), m/s;

$V_1 = V/k_c$, where k_c is the chip thickening coefficient;

τ is the time, s.

To calculate the main component of the force $P_z(\tau)$ and the friction forces $F_1(\tau)$ and $F_2(\tau)$, the authors transformed the dependencies [17] obtained under the condition that the assessment of the destruction of the blank material is made on the basis of the plastic flow theory ("plastic flow method"). The angle of inclination of the chip groove of the cutter in the calculation dependencies is not taken into account, since the dependence of the force $P_z(\tau)$ and friction forces on this angle is insignificant [18].

Dependencies for calculating the forces:

$$P_z(\tau) = 1.155 \cdot \sigma_{st} \cdot u \cdot a_m(\tau) \cdot b \times \left(D \cdot \cos \gamma + \frac{k_c}{4u \cdot \cos \gamma} + \mu \cdot \sin \gamma + \frac{\mu_2 \cdot l_2(\tau)}{u \cdot a_m(\tau)} + \frac{k_c \cdot a_m(\tau)}{4u \cdot b \cdot \cos \gamma} \right);$$

$$D = \left[1 + \mu_1(1 - \tan \gamma) + \frac{(0.5 + \mu) \cdot u}{2k_c} \right];$$

$$F_1(\tau) = 1.155 \cdot \sigma_{st} \cdot u \cdot a_m(\tau) \cdot b \cdot \left(\mu + \frac{\mu_1(1 - \tan \gamma)}{\sin \gamma} \right);$$

$$F_2 = 1.155 \cdot \mu_2 \cdot \sigma_{st} \cdot l_2(\tau) \cdot b,$$

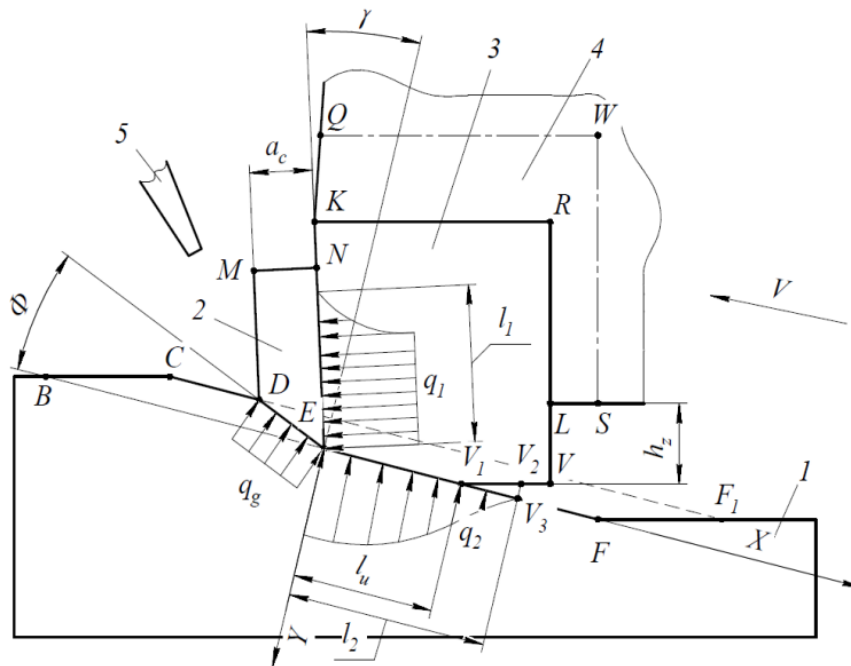


Fig. 2. Diagram of heat transfer during cut-up milling:

1 – blank; 2 – chips; 3 – cutting plate; 4 – cutter body; 5 – cutting fluid supply nozzle

Рис. 2. Схема теплообмена в процессе встречного фрезерования:

1 – заготовка; 2 – стружка; 3 – режущая пластина;

4 – корпус фрезы; 5 – сопло для подачи СОЖ

where σ_{st} is the yield stress of the blank material in the deformation region, determined depending on the temperature in this region, Pa;

μ is the friction coefficient for yield stress;

μ_1, μ_2 are the coefficient of friction of the chip on the plate (front surface of the tooth) and the plate (tooth) on the blank;

γ is the cutting plate rake angle, deg.;

l_2 is the size (length) of the plate-blank contact zone, m;

u is the coefficient;

$a_m(\tau)$ is the depth of plate penetration into the blank depending on contact time τ , m;

b is the size of the machined surface in the direction parallel to the cutter axis, m.

To calculate the $a_m(\tau)$ parameter, a dependence [16] is proposed, the arguments of which are: the amplitude of the ultrasonic vibrations in the direction perpendicular to the machined surface A_u ; the vibration frequency f ; the time of contact of the cutting plate (tooth) with the blank τ ; the depth of plate penetration into the blank a , depending on the feed per cutter tooth S_z and the angle of contact of the plate with the blank.

The length of the contact zone l_2 can be determined by the dependence:

$$l_2 = l_u + \frac{h_u}{tg\alpha},$$

where α is the clearance angle, deg.;

l_u is the size of the wear area on the plate, m;

h_u is the height of the elastic uplift of the blank material [19]:

$$h_u = 1.155 \cdot \frac{\sigma_{sz}}{E_z} \cdot h \cdot B;$$

$$B = \sin^2 \gamma + \mu_1 \cdot (1 - tg\gamma) + \frac{0.5 + \mu}{k_c} - \mu \cdot \sin 2\gamma,$$

where h is the size of the blank in the direction perpendicular to the machined surface, m;

σ_{sz} is the yield stress of the blank material in the deformation zone, Pa;

E_z is the elastic modulus of the blank material in the zone of contact of the plate (tooth) with the blank, determined depending on the temperature in this zone, Pa.

The size of the wear area l_u is related to the radial wear h_u by the dependence:

$$l_u = h_u \cdot (\text{ctg}\alpha - tg\gamma).$$

Since the parameters being the arguments of this dependence depend to a small extent on the τ time of contact of the tooth with the blank, we assume that the friction force F_2 also does not depend on τ . This assumption is confirmed by the results of subsequent numerical modelling.

The yield stress of the blank material in the deformation zone σ_{st} is calculated using the formula [17] depending on the temperature T_d in this zone and the melting temperature T_{melt} of the blank material.

The heat generation density in the chip formation zone with a uniform law of heat source power distribution [15]:

$$q_g(\tau) = \frac{W_g(\tau) \cdot \sin \Phi}{a_m \cdot b},$$

where Φ is the shear angle, deg.

We assume that the power of the heat source in the contact zone of the chip with the front surface of the cutter tooth is distributed according to a combined law, which is a combination of two laws – uniform and exponential [15], and the maximum density of the heat source with this law is:

$$q_{1T}(\tau) = \frac{1.5 \cdot W_{1T}(\tau)}{b \cdot l_1(\tau)}.$$

The size (length) of the zone of contact of the cutting plate with the chip is a variable value on the trajectory of contact of the plate with the blank and can be determined using the formula obtained by transforming the dependence [20]:

$$l_1(\tau) = a_m(\tau) \cdot k_c^{0.1} \cdot [k_c \cdot (1 - tg\gamma) + \sec\gamma].$$

Heat release density in the section located at a distance x_{u1} from the section with the maximum heat release density:

$$q_{1T}(x_{u1}, \tau) = q_{1T}(\tau) \cdot \exp[-k_{01} \cdot x_{u1}],$$

where k_{01} is the coefficient, m^{-1} .

Heat release density (maximum) in the zone of contact of the plate with the blank for an asymmetric normal law of the heat release source power distribution [15]:

$$q_{2T}(\tau) = \frac{2 \cdot W_{2T}(\tau) \cdot \sqrt{k_0}}{b \cdot \sqrt{\pi} \cdot \text{erf}\left[l_2 \sqrt{k_0}\right]},$$

where k_0 is the coefficient;

erf is a function depending on the k_0 and l_2 parameters.

Heat release density in the section located at a distance x_u from the section with the maximum heat release density [16]:

$$q_{2T}(x_u, \tau) = q_{2T}(\tau) \cdot \exp[-k_0 \cdot x_u^2].$$

When machining with a cutter equipped with a replaceable multi-faceted plate, the heat conductivity equations for the blank 1, chip 2, plate 3, and cutter body 4 (Fig. 2) are as follows:

$$\frac{\partial T_1}{\partial \tau} = \left[\frac{\partial}{\partial x} \left(\frac{\lambda_1}{c_1 \cdot \rho_1} \cdot \frac{\partial T_1}{\partial x} \right) + \frac{\partial}{\partial y} \left(\frac{\lambda_1}{c_1 \cdot \rho_1} \cdot \frac{\partial T_1}{\partial y} \right) \right] - V \cdot \frac{\partial T_1}{\partial x};$$

$$\begin{aligned}\frac{\partial T_2}{\partial \tau} &= \left[\frac{\partial}{\partial x} \left(\frac{\lambda_1}{c_1 \cdot \rho_1} \cdot \frac{\partial T_2}{\partial x} \right) + \frac{\partial}{\partial y} \left(\frac{\lambda_1}{c_1 \cdot \rho_1} \cdot \frac{\partial T_2}{\partial y} \right) \right] - \\ &\quad - V_1 \cdot \cos \gamma \frac{\partial T_2}{\partial y} - V_1 \cdot \sin \gamma \frac{\partial T_2}{\partial x}; \\ \frac{\partial T_3}{\partial \tau} &= \left[\frac{\partial}{\partial x} \left(\frac{\lambda_3}{c_3 \cdot \rho_3} \cdot \frac{\partial T_3}{\partial x} \right) + \frac{\partial}{\partial y} \left(\frac{\lambda_3}{c_3 \cdot \rho_3} \cdot \frac{\partial T_3}{\partial y} \right) \right]; \\ \frac{\partial T_4}{\partial \tau} &= \left[\frac{\partial}{\partial x} \left(\frac{\lambda_4}{c_4 \cdot \rho_4} \cdot \frac{\partial T_4}{\partial x} \right) + \frac{\partial}{\partial y} \left(\frac{\lambda_4}{c_4 \cdot \rho_4} \cdot \frac{\partial T_4}{\partial y} \right) \right],\end{aligned}$$

where $\lambda_1, \lambda_3, \lambda_4$ are the coefficients of thermal conductivity of the materials of the blanks (chips), cutting plate and cutter body, respectively, W/(m·K);

$c_1, c_3, c_4; \rho_1, \rho_3, \rho_4$ are the heat capacities (J/(kg·K)) and densities (kg/m³) of the materials of these objects;

T_1, T_2, T_3, T_4 are the temperatures of the blanks, chips, plate and cutter body, respectively, K.

We assume that the thermophysical characteristics of the chips are equal to the corresponding characteristics of the blank ($c_2=c_1, \rho_2=\rho_1, \lambda_2=\lambda_1$).

When machining with a cutter without a plate, the thermophysical characteristics of the cutter body are equal to the corresponding characteristics of the cutter tooth ($c_4=c_3, \rho_4=\rho_3, \lambda_4=\lambda_3$), then the last equation will have the form:

$$\frac{\partial T_4}{\partial \tau} = \left[\frac{\partial}{\partial x} \left(\frac{\lambda_3}{c_3 \cdot \rho_3} \cdot \frac{\partial T_4}{\partial x} \right) + \frac{\partial}{\partial y} \left(\frac{\lambda_3}{c_3 \cdot \rho_3} \cdot \frac{\partial T_4}{\partial y} \right) \right].$$

This form of recording differential equations of thermal conductivity assumes that the physical characteristics of the materials of the blank, cutter body and plate (cutter tooth) depend on temperature.

Initial condition: the temperature of all objects at the initial moment of time $T(x, y, 0)=T_a$, where T_a is the ambient temperature (air and/or coolant).

Within the contact zone EV_3 of blank 1 and plate (tooth) 3, the thermal interaction is expressed by the boundary condition of the 2nd type [16]:

$$\frac{\partial T_1}{\partial y} = -\frac{q'_{2T}(x_u)}{\lambda_1(T_1)}; \quad \frac{\partial T_3}{\partial y} = -\frac{q''_{2T}(x_u)}{\lambda_3(T_3)};$$

$$T_{1k} = T_{3k}; \quad q'_{2T}(x_u) + q''_{2T}(x_u) = q_{2T}(x_u),$$

where $q'_{1T}(x_{u1}), q''_{1T}(x_{u1})$ are the heat flows directed to blank 1 and plate (cutter tooth) 3, respectively, at a distance x_{u1} from the section with the maximum heat release density, W/m²;

T_{1k}, T_{3k} are the temperatures on the surfaces of blank 1 and plate (cutter tooth) 3 within their contact zone, K.

Similar boundary conditions of the 2nd type can express thermal interaction within the contact zone DE of blank 1 with chip 2 and within the contact zone EN of

chip 2 with plate (tooth) 3 in the section with maximum heat generation density.

Boundary condition of the 2nd type within the zone EN in the section with variable heat generation density:

$$\frac{\partial T_2}{\partial n} = -\frac{q'_{1T}(x_{u1})}{\lambda_1(T_2)}; \quad \frac{\partial T_3}{\partial n} = -\frac{q''_{1T}(x_{u1})}{\lambda_3(T_3)};$$

$$T_{2k1}(x_{u1}) = T_{3k1}(x_{u1}); \quad q'_{1T}(x_{u1}) + q''_{1T}(x_{u1}) = q_{1T}(x_{u1}),$$

where $q'_{1T}(x_{u1}), q''_{1T}(x_{u1})$ are heat flows directed to chip 2 and plate (cutter tooth) 3, respectively, at a distance x_{u1} from the section with maximum heat generation density, W/m²;

$T_{2k1}(x_{u1}), T_{3k1}(x_{u1})$ are temperatures on the surfaces of chip 2 and plate (cutter tooth) 3 within the zone of their contact at a distance of x_{u1} from the section with the maximum heat release density, K.

We assume that at the junction of plate 3 with cutter body 4, the thermal resistance is insignificant, therefore the temperatures of the contacting surfaces of the plate T_{3k2} and body T_{4k} are equal (boundary condition of the 4th type): $T_{3k2}=T_{4k}$.

Heat transfer from the surfaces of the objects participating in heat exchange – the cutting plate, cutter body, chip and blank contacting with the environment (cutting fluid or air) is expressed by the Newton–Richmann law (boundary conditions of the 3rd type) [16]. One of the arguments of the dependence describing this law is the coefficient of heat transfer from the surface. The heat transfer coefficients to the environment (cutting fluid and air) depend on the temperatures of these surfaces, which are not known in advance. Therefore, if a preliminary calculation of the coefficients is performed without taking into account the actual surface temperatures, unreliable results can be obtained.

When solving analogues of differential heat conduction equations using the numerical finite element method, the calculation of heat transfer coefficients is performed in parallel with the calculation of heat conduction equations. When calculations are performed using this method, the time, during which the heat exchange process is considered, is divided into finite small intervals $\Delta\tau$. The temperatures of objects determined at the previous moment in time are used to calculate heat transfer coefficients at the current moment, and the obtained values of the coefficients are used to calculate the temperature field at the next moment.

If the surface temperature of the object exchanging heat with the cutting fluid (NK, V_2V and VL of the plate (tooth), MD and MN of the chip, CD, V_3F, BC and FF_1 of the blank, KQ and LS of the cutter body (Fig. 2)) is lower than its boiling point, then the heat transfer coefficient in the cutting fluid is

$$\alpha_g = \frac{Nu_f \cdot \lambda_{gf}}{\ell_x},$$

where Nu_f is the Nusselt criterion;

λ_{gf} is the thermal conductivity coefficient of the cutting fluid, W/(m·K);

ℓ_x is the characteristic surface size, m.

As a characteristic size, we can take: for chips – their thickness a_c , for a blank – the size of the contact trajectory FB of the plate (cutter tooth) with the blank, and for the plate (cutter tooth) – the size h (Fig. 2).

The Nu_f criterion is calculated using the equation:

$$Nu_f = C \cdot Re_f^m \cdot Pr_f^n \cdot (Pr_f / Pr_w)^k,$$

where C , m , n , k are coefficients whose values are determined by the surface shape and the coolant flow mode (laminar, transitional, turbulent); the Prandtl number Pr and Reynolds number Re :

$$Pr_f = \frac{\mu_{gf} \cdot c_{gf}}{\lambda_{gf}};$$

$$Re_f = \frac{V_g \cdot \ell_x}{\nu_{gf}},$$

where μ_g is the dynamic viscosity of the cutting fluid, Pa·s; c_g is the specific heat capacity of the cutting fluid, J/(kg·K); ν_g is kinematic viscosity of the cutting fluid, m²/s;

V_g is the speed of the cutting fluid movement, which can be calculated in cut-up milling as

$$V_g = V_{g1} + V,$$

where V_{g1} is the speed of the cutting fluid flow from the nozzle used to supply it, m/s.

Parameters with f index in their designations are determined based on the temperature of the cutting fluid at the nozzle outlet; if w index is used in the parameter designation, it is determined depending on the average temperature of the corresponding surface.

In most cases, a mixture of cutting fluid and air is present in the cutting zone; therefore, the calculations use the reduced heat transfer coefficients, which depend on the percentage of air in the air-liquid mixture.

If the surface temperature of the object participating in the heat exchange exceeds the boiling point of the liquid, the calculations use the reduced heat transfer coefficient, the value of which depends on the heat transfer coefficient during coolant boiling α_k .

To calculate the α_k coefficient, you can use the equation

$$Nu_k = C_k \cdot Re_k^m \cdot Pr_k^{0.33},$$

where C_k and m are coefficients;

$$Nu_k = \alpha_k \cdot \ell_{x1} / \lambda_{g1};$$

$$Re_k = w_k \cdot \ell_{x1} / \nu_{g1};$$

$$Pr_k = \nu_{g1} / a_{g1},$$

where λ_{g1} , ν_{g1} are physical parameters of the cutting fluid at the saturation temperature;

w_k is conventional boiling speed of cutting fluid vapor, m/s;

a_{g1} is thermal diffusivity coefficient of the cutting fluid at the saturation temperature, m²/s;

ℓ_{x1} is characteristic size of the surface whose temperature exceeds the cutting fluid saturation temperature, m.

Coefficient of heat transfer to air is

$$\alpha_b = \frac{Nu_{bf} \cdot \lambda_{bf}}{\ell_x},$$

where λ_{bf} is thermal conductivity coefficient of air, W/(m·K);

Nu_{bf} is Nusselt criterion calculated using dependencies similar to those for calculating Nu_f .

When applying ultrasonic vibrations, the depth of the plate (tooth) penetration into the blank changes. If the vibration amplitude A_y exceeds the depth of the plate (tooth) penetration into the blank, the plate may come out of contact with the blank. During the absence of contact between the tooth surface and the blank, which were subject to the above boundary conditions of the 2nd type during cutting, heat will be exchanged with the environment (cutting fluid or air), and the boundary conditions will change.

For the surfaces of the blank and the cutter tooth, the boundary conditions of the 3rd type will take the form:

$$-\lambda_1(T_1) \cdot \frac{\partial T_1}{\partial n} = \alpha_1 \cdot (T_{1f} - T_w);$$

$$-\lambda_3(T_3) \cdot \frac{\partial T_3}{\partial n} = \alpha_3 \cdot (T_{3f} - T_w),$$

where α_1 and α_3 are the coefficients of heat transfer to the environment from the surfaces of the blank and the plate (cutter tooth), respectively, W/(m²·K);

T_w is the temperature of the environment (cutting fluid or air), K;

T_{1f} , T_{3f} is the temperature of the flow surface of the blank and the plate (tooth), respectively, K.

To solve the equations of thermal conductivity of the objects participating in the heat exchange, the numerical finite element method is used.

Discrete analogues of differential equations of heat conductivity are obtained based on the fact that the sum of all heat flows entering and leaving the element under consideration over a time interval $\Delta\tau$ is equal to the change in the enthalpy of this element (finite volume). To ensure the stability of the numerical solution of discrete analogues of differential equations of heat conductivity, expressions are obtained for calculating the limitations per a step of the difference grid.

The temperature of the deformable layer is used in the programme when calculating the yield stress of the blank material in the chip formation area.

The adequacy of the above method for calculating the temperature field was assessed by comparing the calculated value of the average temperature in the surface layer of the blank with the results of its measurement by a semi-artificial thermocouple. The difference between the calculated and experimental values does not exceed 12 %, which indicates the possibility of using the proposed method.

Using the developed software, the process of milling polycarbonate blanks was simulated at a cutting speed of

$V=8$ m/s using ultrasonic vibrations with a frequency of 18,600 Hz and an amplitude of $A=10$ μm . The imposition of vibrations in the direction perpendicular to the blank surface being machined was simulated.

The maximum depth of tooth penetration into the blank depends on the elements of the milling mode – the cutting depth t and the feed per tooth S_z . Consequently, with a fixed ultrasonic vibration amplitude, different ratios A/a_{max} can be achieved by varying these elements of the mode.

When machining without ultrasonic vibrations with a cutting depth of $t=0.5$ mm and a feed per tooth of $S_z=0.12$ mm/tooth, the maximum depth of tooth penetration into the blank is $a_{\text{max}}=36$ μm , and when applying ultrasonic vibrations, the ratio A/a_{max} is 0.27. In this case, the tooth comes out of contact only during the initial period of its contact with the blank. With further movement of the tooth along the contact trajectory, the application of vibrations leads to a change in the depth of tooth penetration, both decreasing and increasing. Therefore, changing the kinematics of the milling process due to the use of vibrations at small values of the ratio A/a_{max} does not have a noticeable effect on the efficiency of the process.

In the mode of $t=0.1$ mm and $S_z=0.05$ mm/tooth, when machining without ultrasonic vibrations, the value of a_{max} is 7.6 μm , i.e. less than the vibration amplitude, the ratio A/a_{max} is 1.3. In this case, when vibrations are applied, the contact of the tooth with the blank is interrupted throughout the entire trajectory of the tooth movement relative to the surface being machined. When machining with ultrasonic vibrations in a mode with the ratio $A/a_{\text{max}}=1.3$, compared to machining without vibrations, the force P_z decreased by 45 %, and the temperatures in the contact zones of the tooth with the chips and the blank decreased by 15 %. At lower ratios A/a_{max} , these parameters decreased to a lesser extent.

DISCUSSION

The developed set of mathematical models and dependencies for calculating the main component of cutting force and temperatures during milling has the following differences from the dependencies given in works [6; 15].

1. The change in the depth of tooth (cutting plate) penetration into the blank is taken into account when using ultrasonic vibrations.

2. The change in the boundary conditions on the surfaces of the tooth and the blank is taken into account if, when using ultrasonic vibrations, the plate comes out of contact with the blank. In work [6], heat transfer from the surfaces of objects participating in heat exchange is not taken into account.

3. The models allow taking into account the dependence of the thermophysical properties of objects (milling cutter, blank and chips) on temperature and the effect of the temperature of the deformed layer of the blank material on the deformation stresses and cutting forces of individual milling cutter teeth.

The proposed method for numerically solving analogues of differential equations of heat conductivity with general boundary conditions in the contact zone of objects allows determining the distribution densities of heat flows between the contacting objects (milling cutter, chips and blank).

The developed method and software make it possible to take into account the influence of a larger number of factors on the temperature field than, for example, in [6]: the dimensions of the blank and the milling cutter, including the tooth angles (cutting plate); wear of the milling cutter; thermophysical characteristics of the materials of the blank and the milling cutter (cutting plate); yield strength of the blank material; friction coefficients; elements of the milling mode (cutting depth, cutting speed and feed); thermophysical characteristics of the external environment (cutting fluid and air); the rate of cutting fluid flow through the nozzle for its supply; the number of successively working teeth of the milling cutter, etc., and also to determine both the temperature in the surface layers of the blank and the temperatures in the contact zones of the tooth with the chips and the blank and the temperature of the chips.

The assumption that the effect of using ultrasonic vibrations during milling is higher at higher values of the A/a_{max} ratio was confirmed. Previously conducted studies have found a decrease in cutting forces during turning [7] and grinding [8] with an increase in the vibration amplitude. In [9], it is noted that the efficiency of using ultrasonic vibrations during gear milling increases with an increase in the amplitude. Consequently, the results of numerical modelling indicating a decrease in the thermal and force stress of the milling process correlate with studies conducted using other processing methods.

One of the reasons for the decrease in forces and temperatures is a change in the kinematic parameters of the milling process with an increase in the ultrasonic vibration amplitude, as it has been found in other studies [7; 9].

In the present study, it was found that the use of ultrasonic vibrations during milling leads to a decrease in the milling force to a greater extent (by 45 %) than in temperatures (by 15 %). The obtained result coincides with the study [9], which also recorded that temperatures decrease to a lesser extent than cutting forces.

CONCLUSIONS

1. Analytical studies of the temperature field were performed and software was developed that allows establishing the influence of ultrasonic vibrations on the parameters of the milling process at different ratios of the vibration amplitude to the depth of tooth penetration into the blank.

2. It was found that changing the kinematics of the milling process using ultrasonic vibrations has a more significant effect on the process parameters at a cutting mode that provides a greater ratio of the vibration amplitude to the depth of penetration.

3. The results of the studies will allow predicting the efficiency of the milling process with ultrasonic vibrations at different processing modes.

REFERENCES

1. Khramov A.V., Gorshkov M.G., Nguen Kh.T., Kiselev E.S. Improving the efficiency of turning heat-resistant alloys by introducing the energy of an ultrasonic field into the cutting zone. *Voronezh Scientific and technical Jour-*

- nal*, 2023, vol. 2, no. 2, pp. 4–10. DOI: [10.34220/2311-8873-2023-4-10](#).
 - Evdokimov D.V., Skuratov D.L., Bukatyy A.S. Technological residual deformations prediction of GTE blades by numerical method after end milling. *Izvestia of Samara Scientific Center of the Russian Academy of Sciences*, 2022, vol. 24, no. 1, pp. 11–19. DOI: [10.37313/1990-5378-2022-24-1-11-19](#).
 - Alauddin M., Choudhury I.A., El Baradie M.A., Hashmi M.S.J. Plastics and their machining: A review. *Journal of Materials Processing Technology*, 1995, vol. 54, no. 1-4, pp. 40–46. DOI: [10.1016/0924-0136\(95\)01917-0](#).
 - Jahan M.P., Ma Jianfeng, Hanson C., Chen Xingbang, Arbuckle G.K. Experimental and numerical investigation of cutting forces in micro-milling of polycarbonate glass. *Machining Science and Technology*, 2019, vol. 24, no. 3, pp. 366–397. DOI: [10.1080/10910344.2019.1698608](#).
 - Duan Zhenjing, Li Changhe, Ding Wenfeng et al. Milling Force Model for Aviation Aluminum Alloy: Academic Insight and Perspective Analysis. *Chinese Journal of Mechanical Engineering*, 2021, vol. 34, article number 18. DOI: [10.1186/s10033-021-00536-9](#).
 - Bezazychnyy V.F. The development of the research of thermal processes in mechanical engineering technology. *Spravochnik. Inzhenernyi zhurnal*, 2024, no. 8, pp. 38–48. DOI: [10.14489/hb.2024.08.pp.038-048](#).
 - Kumabe D. *Vibratsionnoe rezanie* [Vibrating cutting]. Moscow, Mashinostroenie Publ., 1985. 424 p.
 - Unyanin A.N., Khazov A.V. Analytical study of grinding forces with the imposition of ultrasonic vibrations with high amplitude. *Izvestia of Samara Scientific Center of the Russian Academy of Sciences*, 2022, vol. 24, no. 1, pp. 37–43. DOI: [10.37313/1990-5378-2022-24-1-37-43](#).
 - Agapov S.I., Prokhvatilov A.S., Bezrukov E.K., Potapov A.A. Peculiarities of the process of ultrasonic vibration machining. *Izvestiya Volgogradskogo gosudarstvennogo tekhnicheskogo universiteta*, 2019, no. 8, pp. 7–10. EDN: [CZJTYT](#).
 - Kiselev E.S., Nazarov M.V. *Osobennosti tekhnologii izgotovleniya nezhestkikh korpusnykh detaley* [Special aspects of the technology of manufacturing non-rigid body parts]. Moscow, RUSAYNS Publ., 2022. 218 p. EDN: [JUSXTL](#).
 - Ivanova T.N. Modern technological techniques improving the efficiency of mechanical processing corrosion-resistant steels, working in aggressive environments. *University proceedings. Volga region. Technical sciences*, 2024, no. 4, pp. 143–156. DOI: [10.21685/2072-3059-2024-4-12](#).
 - Unyanin A.N., Dimukhametov I.Z. Investigation of the Effect of Milling Cutter Tooth Spacing and Milling Mode Features on the Process of Machining Polycarbonate Workpieces Using Ultrasonic Vibrations. *Russian Engineering Research*, 2024, vol. 44, no. 9, pp. 1317–1322. DOI: [10.3103/S1068798X24702010](#).
 - Unyanin A.N., Dimukhametov I.Z. Influence of Tool's Thermal Conductivity on Milling with Ultrasound. *Russian Engineering Research*, 2024, vol. 44, no. 11, pp. 1598–1601. DOI: [10.3103/S1068798X24702617](#).
 - Vologin M.F., Kalashnikov V.V., Nerubay M.S., Shtrikov B.L. *Primenenie ultrazvuka i vzryva pri obrabotke i sborke* [Application of ultrasonic vibrations and explosion when processing and assembling]. Moscow, Mashinostroenie Publ., 2002. 264 p.
 - Reznikov A.N., Reznikov L.A. *Teplovyte protsessy v tekhnologicheskikh sistemakh* [Thermal Processes in Technological Systems]. Moscow, Mashinostroenie Publ., 1990. 288 p. EDN: [SCUAQX](#).
 - Unyanin A.N., Dimukhametov I.Z. Study of the influence of cutter wear and mode on the parameters of the process of milling blanks of polycarbonate parts using ultrasonic vibrations. *Izvestia of Samara Scientific Center of the Russian Academy of Sciences*, 2024, vol. 26, no. 3, pp. 54–62. EDN: [CRNSBF](#).
 - Vorontsov A.L., Sultan-Zade N.M., Albagachiev A.Yu. Development of a new theory of cutting. 9. Practical calculations of cutting parameters in turning. *Russian Engineering Research*, 2008, vol. 28, no. 9, pp. 878–888. DOI: [10.3103/S1068798X08090116](#).
 - Bobrov V.F. *Osnovy teorii rezaniya metallov* [Fundamentals of metal cutting theory]. Moscow, Mashinostroenie Publ., 1975. 344 p.
 - Vorontsov A.L., Sultan-Zade N.M., Albagachiev A.Yu. Development of a new theory of cutting 7. Mathematical description of the formation of different chips, pulsation of the cutting force, and contact parameters of the machined billet surface and the rear cutter surface. *Russian Engineering Research*, 2008, vol. 28, no. 7, pp. 674–680. DOI: [10.3103/S1068798X08070101](#).
 - Vorontsov A.L., Sultan-Zade N.M., Albagachiev A.Yu. Development of a new theory of cutting: 6. Determining the basic parameters of cutting. *Russian Engineering Research*, 2008, vol. 28, no. 6, pp. 571–578. DOI: [10.3103/S1068798X08060129](#).
- ## СПИСОК ЛИТЕРАТУРЫ
- Храмов А.В., Горшков М.Г., Нгуен Х.Т., Киселев Е.С. Повышение эффективности токарной обработки жаропрочных сплавов введением в зону резания энергии ультразвукового поля // Воронежский научно-технический вестник. 2023. Т. 2. № 2. С. 4–10. DOI: [10.34220/2311-8873-2023-4-10](#).
 - Евдокимов Д.В., Скуратов Д.Л., Букатый А.С. Расчетное прогнозирование технологических остаточных деформаций лопаток ГТД на этапе конечного фрезерования // Известия Самарского научного центра РАН. 2022. Т. 24. № 1. С. 11–19. DOI: [10.37313/1990-5378-2022-24-1-11-19](#).
 - Alauddin M., Choudhury I.A., El Baradie M.A., Hashmi M.S.J. Plastics and their machining: A review // Journal of Materials Processing Technology. 1995. Vol. 54. № 1-4. P. 40–46. DOI: [10.1016/0924-0136\(95\)01917-0](#).
 - Jahan M.P., Ma Jianfeng, Hanson C., Chen Xingbang, Arbuckle G.K. Experimental and numerical investigation of cutting forces in micro-milling of polycarbonate glass // Machining Science and Technology. 2019. Vol. 24. № 3. P. 366–397. DOI: [10.1080/10910344.2019.1698608](#).
 - Duan Zhenjing, Li Changhe, Ding Wenfeng et al. Milling Force Model for Aviation Aluminum Alloy: Academic Insight and Perspective Analysis // Chinese Journal of Mechanical Engineering. 2021. Vol. 34. Article number 18. DOI: [10.1186/s10033-021-00536-9](#).

СПИСОК ЛИТЕРАТУРЫ

1. Храмов А.В., Горшков М.Г., Нгуен Х.Т., Киселев Е.С. Повышение эффективности токарной обработки жаропрочных сплавов введением в зону резания энергии ультразвукового поля // Воронежский научно-технический вестник. 2023. Т. 2. № 2. С. 4–10. DOI: [10.34220/2311-8873-2023-4-10](https://doi.org/10.34220/2311-8873-2023-4-10).
2. Евдокимов Д.В., Скуратов Д.Л., Букатый А.С. Расчетное прогнозирование технологических остаточных деформаций лопаток ГТД на этапе конечного фрезерования // Известия Самарского научного центра РАН. 2022. Т. 24. № 1. С. 11–19. DOI: [10.37313/1990-5378-2022-24-1-11-19](https://doi.org/10.37313/1990-5378-2022-24-1-11-19).
3. Alauddin M., Choudhury I.A., El Baradie M.A., Hashmi M.S.J. Plastics and their machining: A review // Journal of Materials Processing Technology. 1995. Vol. 54. № 1-4. P. 40–46. DOI: [10.1016/0924-0136\(95\)01917-0](https://doi.org/10.1016/0924-0136(95)01917-0).
4. Jahan M.P., Ma Jianfeng, Hanson C., Chen Xingbang, Arbuckle G.K. Experimental and numerical investigation of cutting forces in micro-milling of polycarbonate glass // Machining Science and Technology. 2019. Vol. 24. № 3. P. 366–397. DOI: [10.1080/10910344.2019.1698608](https://doi.org/10.1080/10910344.2019.1698608).
5. Duan Zhenjing, Li Changhe, Ding Wenfeng et al. Milling Force Model for Aviation Aluminum Alloy: Academic Insight and Perspective Analysis // Chinese Journal of Mechanical Engineering. 2021. Vol. 34. Article number 18. DOI: [10.1186/s10033-021-00536-9](https://doi.org/10.1186/s10033-021-00536-9).

6. Безъязычный В.Ф. Тепловые процессы в технологии машиностроения // Справочник. Инженерный журнал. 2024. № 8. С. 38–48. DOI: [10.14489/hb.2024.08.pp.038-048](https://doi.org/10.14489/hb.2024.08.pp.038-048).
7. Кумабэ Д. Вибрационное резание. М.: Машиностроение, 1985. 424 с.
8. Унянин А.Н., Хазов А.В. Аналитическое исследование сил шлифования при наложении ультразвуковых колебаний с высокой амплитудой // Известия Самарского научного центра Российской академии наук. 2022. Т. 24. № 1. С. 37–43. DOI: [10.37313/1990-5378-2022-24-1-37-43](https://doi.org/10.37313/1990-5378-2022-24-1-37-43).
9. Агапов С.И., Прохвятилов А.С., Безруков Е.К., Потапов А.А. Особенности процесса ультразвуковой обработки // Известия Волгоградского государственного технического университета. 2019. № 8. С. 7–10. EDN: [CZJTYU](https://www.edn.ru/czjtyy/).
10. Киселев Е.С., Назаров М.В. Особенности технологии изготовления нежестких корпусных деталей. М.: РУСАЙНС, 2022. 218 с. EDN: [JUSXTL](https://www.edn.ru/jusxtl/).
11. Иванова Т.Н. Современные технологические приемы повышения эффективности механической обработки коррозионностойких сталей, работающих в агрессивных средах // Известия высших учебных заведений. Поволжский регион. Технические науки. 2024. № 4. С. 143–156. DOI: [10.21685/2072-3059-2024-4-12](https://doi.org/10.21685/2072-3059-2024-4-12).
12. Unyanin A.N., Dimukhametov I.Z. Investigation of the Effect of Milling Cutter Tooth Spacing and Milling Mode Features on the Process of Machining Polycarbonate Workpieces Using Ultrasonic Vibrations // Russian Engineering Research. 2024. Vol. 44. № 9. P. 1317–1322. DOI: [10.3103/S1068798X24702010](https://doi.org/10.3103/S1068798X24702010).
13. Unyanin A.N., Dimukhametov I.Z. Influence of Tool's Thermal Conductivity on Milling with Ultrasound // Russian Engineering Research. 2024. Vol. 44. № 11. P. 1598–1601. DOI: [10.3103/S1068798X24702617](https://doi.org/10.3103/S1068798X24702617).
14. Вологин М.Ф., Калашников В.В., Нерубай М.С., Штриков Б.Л. Применение ультразвука и взрыва при обработке и сборке. М.: Машиностроение, 2002. 264 с.
15. Резников А.Н., Резников Л.А. Тепловые процессы в технологических системах. М.: Машиностроение, 1990. 288 с. EDN: [SCUAQX](https://www.edn.ru/scuaqx/).
16. Унянин А.Н., Димухаметов И.З. Исследование влияния износа фрезы и режима на параметры процесса фрезерования заготовок деталей из поликарбоната с применением ультразвуковых колебаний // Известия Самарского научного центра Российской академии наук. 2024. Т. 26. № 3. С. 54–62. EDN: [CRNSBF](https://www.edn.ru/crnbsf/).
17. Воронцов А.Л., Султан-заде Н.М., Албагачиев А.Ю. Разработка новой теории резания. 9. Практические расчеты параметров резания при точении // Вестник машиностроения. 2008. № 9. С. 67–76. EDN: [JVNSAD](https://www.edn.ru/jvnrad/).
18. Бобров В.Ф. Основы теории резания металлов. М.: Машиностроение, 1975. 344 с.
19. Воронцов А.Л., Султан-заде Н.М., Албагачиев А.Ю. Разработка новой теории резания. 7. Математическое описание образования стружки разных видов, пульсации сил резания и параметров контакта обработанной поверхности заготовки с задней поверхностью резца // Вестник машиностроения. 2008. № 7. С. 56–60. EDN: [JVNREF](https://www.edn.ru/jvnref/).
20. Воронцов А.Л., Султан-заде Н.М., Албагачиев А.Ю. Разработка новой теории резания. 6. Определение основных параметров процесса резания // Вестник машиностроения. 2008. № 6. С. 64–70. EDN: [JTDHZI](https://www.edn.ru/jtdhzi/).

УДК 621.91

doi: 10.18323/2782-4039-2025-3-73-7

Исследование температурного поля, формирующегося в процессе фрезерования с применением ультразвуковых колебаний, при различных режимах обработки

Унянин Александр Николаевич^{*1}, доктор технических наук, профессор,
профессор кафедры «Инновационные технологии в машиностроении»

Чуднов Александр Владимирович, аспирант

Димухаметов Илназ Зеферович, аспирант

Ульяновский государственный технический университет, Ульяновск (Россия)

*E-mail: a_un@mail.ru

¹ORCID: <https://orcid.org/0000-0002-5557-4197>

Поступила в редакцию 14.04.2025

Пересмотрена 05.06.2025

Принята к публикации 18.06.2025

Аннотация: Исследования температурного поля процесса фрезерования с наложением ультразвуковых колебаний (УЗК) при различных отношениях амплитуды колебаний к глубине внедрения зуба в заготовку позволяют прогнозировать эффективность процесса фрезерования с УЗК при различных режимах обработки. Цель исследования – разработка физических и математических моделей процесса фрезерования с наложением УЗК, позволяющих установить влияние УЗК на эффективность процесса фрезерования при различных отношениях амплитуды колебаний к глубине внедрения зуба. Приняты во внимание три источника тепловыделения: в области деформирования (стружкообразования) и в зонах контакта стружки с режущей пластиной (зубом фрезы) и пластины с заготовкой. Разработаны модели теплообмена, учитывающие, в частности, изменение граничных условий на поверх-

ностях режущей пластины и заготовки при наложении УЗК. Когда пластина находится в контакте с заготовкой, в заготовку, стружку и зуб фрезы направлены тепловые потоки, а условия теплового взаимодействия в пределах зон контакта пластины со стружкой и заготовкой описываются граничными условиями 2-го рода. Когда пластина при наложении УЗК выходит из контакта с заготовкой и процесс стружкообразования прекращается, то на всех поверхностях зуба (пластины) и заготовки, контактирующих с окружающей средой (смазочно-охлаждающей жидкостью или воздухом), конвективный теплообмен описывается законом Ньютона – Рихмана (граничные условия 3-го рода). Приведены результаты численного моделирования, подтвердившие предположение, что эффект от применения УЗК выше при больших значениях отношения амплитуды УЗК к глубине внедрения зуба в заготовку.

Ключевые слова: ультразвук; колебания; фрезерование; теплообмен; численное моделирование.

Благодарности: Исследование выполнено за счет гранта Российского научного фонда № 24-2900206, <https://rscf.ru/project/24-29-00206/>.

Для цитирования: Унянин А.Н., Чуднов А.В., Димухаметов И.З. Исследование температурного поля, формирующегося в процессе фрезерования с применением ультразвуковых колебаний, при различных режимах обработки // Frontier Materials & Technologies. 2025. № 3. С. 91–100. DOI: 10.18323/2782-4039-2025-3-73-7.

Influence of heat treatment on the structure and corrosion properties of microalloyed pipe steels with a chromium content of up to 1 %

Elena A. Chistopoltseva^{*1,5}, PhD (Engineering),
Head of Department of Special Materials Science
Dmitry V. Kudashov^{2,6}, PhD (Engineering), Director
Aleksandr A. Komissarov^{3,7}, PhD (Engineering),
Head of Hybrid Nanostructured Materials Laboratory
Vyacheslav V. Yushchuk^{3,8}, scientific project engineer
*Aleksandr V. Muntin*⁴, PhD (Engineering),
Director of Engineering and Technology Center
*Aleksey V. Chervonniy*⁴, PhD (Engineering),
Head of Research and Development Department
*Egor D. Dolgach*³, scientific project engineer

¹LLC IT Service, Samara (Russia)

²Vyksa branch of MISIS University of Science and Technology, Vyksa (Russia)

³MISIS University of Science and Technology, Moscow (Russia)

⁴JSC Vyksa Metallurgical Plant, Vyksa (Russia)

*E-mail: chistopolceva@its-samara.com

⁵ORCID: <https://orcid.org/0009-0002-5587-287X>

⁶ORCID: <https://orcid.org/0000-0002-7661-1591>

⁷ORCID: <https://orcid.org/0000-0002-8758-5085>

⁸ORCID: <https://orcid.org/0000-0002-3015-1235>

Received 22.04.2025

Revised 20.05.2025

Accepted 17.07.2025

Abstract: The service life of oil pipelines has recently decreased significantly due to severe operating conditions and the increased aggressiveness of the environment, caused by the simultaneous presence of dissolved hydrogen sulfide, carbon dioxide, chlorides, and a high water phase content. Conventional corrosion mitigation methods typically address only one of these factors and therefore fail to provide adequate protection under such combined conditions. This limitation necessitates the use of multiple complementary approaches for corrosion control. This paper proposes microalloying systems for low-carbon steels of grades 10KhB, 10F, 10B, and 15KhF (with chromium content up to 1 %) for seamless pipes, along with optimized heat treatment regimes that provide increased strength, cold resistance, and corrosion resistance in CO₂- and H₂S-containing environments. Mechanical testing after heat treatment demonstrated that the proposed chemical compositions ensure strength classes K52–K56, while also providing high low-temperature toughness. The morphology of carbides in the microstructure depends on the chemical composition and determines the steel's strength, though it does not affect corrosion resistance. The investigated steels showed high resistance to hydrogen-induced cracking (HIC) and sulfide stress cracking (SSC). After exposure to CO₂–H₂S media, a protective iron sulfide film formed on the surface, indicating uniform sulfide corrosion. The corrosion rate and mechanism were found to be governed by the medium composition and the kinetics of iron sulfide film formation. The obtained results allow expanding the scope of application of the proposed steels in multicomponent aggressive environments regardless of the type of microalloying.

Keywords: low-carbon microalloyed steel; heat treatment; corrosion-resistant seamless pipe; CO₂- and H₂S-containing environment; sulfide corrosion of steel; fine-grained structure; oilfield pipelines.

Acknowledgments: The work was carried out within a comprehensive project on the topic “Development and Implementation of Integrated Technologies for the Production of Seamless Pipes from New-Generation Steels with Controlled Corrosion Resistance under Abnormal Operating Conditions for the Fuel and Energy Complex of the Russian Federation” within the agreements No. 075-11-2023-011 dated 10.02.2023 and No. 075-11-2025-017 dated 27.02.2025 in accordance with RF Government Resolution No. 218 dated 09.04.2010.

For citation: Chistopoltseva E.A., Kudashov D.V., Komissarov A.A., Yushchuk V.V., Muntin A.V., Chervonniy A.V., Dolgach E.D. Influence of heat treatment on the structure and corrosion properties of microalloyed pipe steels with a chromium content of up to 1 %. *Frontier Materials & Technologies*, 2025, no. 3, pp. 101–111. DOI: 10.18323/2782-4039-2025-3-73-8.

© Chistopoltseva E.A., Kudashov D.V., Komissarov A.A.,
Yushchuk V.V., Muntin A.V., Chervonniy A.V., Dolgach E.D., 2025

INTRODUCTION

Metal corrosion resulting from the transported medium is the main cause of failures in oil field pipelines. According to [1; 2], the presence of simultaneously dissolved hydrogen sulfide (H_2S) and carbon dioxide (CO_2), even in small concentrations, significantly accelerates corrosion processes, leading to premature wear of equipment, reduced reliability and emergency situations. The partial pressure of gases pH_2S and pCO_2 affects the rate of chemical and electrochemical reactions, the degree of hydrogenation of steel and the likelihood of stress corrosion cracking.

Aggressive environments typical for oil and gas production contain water, dissolved salts, carbon dioxide, hydrogen sulfide and organic acids that actively destroy metal. There are several types of corrosion, the most common of which are general, pitting, crevice, sulfide, and stress corrosion cracking. An integrated approach, including several areas, is required to protect effectively equipment from corrosion. Firstly, it is important to choose the right materials that are resistant to specific operating conditions. Stainless steels and alloys, polymeric materials are widely used in the manufacture of pipes, fittings, tanks and other equipment. Secondly, the use of corrosion inhibitors is an effective way to slow down corrosion processes by forming a protective layer that prevents metal from coming into contact with the environment [3; 4]. In oil and gas fields, the production environments are multicomponent [5; 6], and a mixed corrosion mechanism occurs. The proposed division by corrosion types does not take into account the synergistic effect of the presence of several dissolved gases in the environment. The use of expensive materials or several corrosion protection methods significantly increases the cost of pipeline operation.

Based on the corrosion mechanism, a protection method is selected, for example, the material of oil field pipes. According to [7–9], the chemical composition of steel has a significant effect on the process and rate of corrosion: the presence of various alloying elements in steel can both provoke and slow down its destruction under the influence of an aggressive environment. Depending on the composition of the transported medium and the corrosion mechanism, among the materials used, there are chromium-containing steels [10] resistant to pitting carbon dioxide corrosion and steels resistant to stress-corrosion cracking in H_2S -containing environments [11]. The choice of specific

corrosion-resistant steel depends on factors such as temperature, pressure, concentration of aggressive substances, and the level of mechanical properties. Steels with the addition of chromium, which provides resistance to carbon dioxide corrosion and high strength, are often used for transporting oil and gas.

The behaviour of chromium-containing steel grades in H_2S -containing environments and the effect of microalloying additives on corrosion resistance have been poorly studied. The significance of the influence of the level of strength properties and the type of microstructure of low-alloy steels on corrosion resistance in environments with CO_2 and H_2S is unknown.

Taking into account all the above-mentioned operational features and corrosion protection methods, when developing new steels with increased operational reliability, it is necessary to take into account the effect of the complex impact of a multicomponent corrosive environment [12–14], and the behaviour of steels in these environments over time.

The purpose of the work is to determine the influence of the chemical composition, microstructure, and level of mechanical properties of 10KhB, 10F, 10B, 15KhF steels used for linear oil field pipelines on corrosion resistance in complex aggressive environments containing both CO_2 and H_2S .

METHODS

Research materials

The objects of the study were 10KhB, 10F, 10B, and 15KhF steels (Table 1) after volumetric heat treatment in modes ensuring strength properties at the level of K52–K56. The studied steels are characterised by the presence of chromium in the composition in the range of 0.41–0.64 %, which corresponds to the composition of oil and gas pipes resistant to carbon dioxide corrosion. 10KhB steel is additionally microalloyed with niobium, titanium; 10B steel – with niobium; 10F and 15KhF steels – with vanadium.

The steels were smelted under laboratory conditions in a vacuum induction furnace with a capacity of 60 kg. Commercially pure iron (ARMCO), charge blank and ferroalloys were used as charge materials. After melting and casting, cylindrical ingots with a diameter of 150–160 mm and a length of 300–350 mm were subjected to hot

Table 1. Content of main alloying elements of experimental pipe steels, mass fraction, %
Таблица 1. Содержание основных легирующих элементов опытных трубных сталей, массовая доля, %

Steel grade	C	Cr	Nb	V	Ti
10KhB	0.07	0.64	0.031	0.002	0.011
10B	0.08	0.42	0.029	0.002	0.007
10F	0.07	0.41	0.005	0.070	0.002
15KhF	0.15	0.54	0.004	0.050	0.006

deformation in the temperature range of 900–1200 °C on a MISIS-130D two-roll piercing mill (Russia) and on a DUO-210 universal longitudinal rolling mill (Russia) to obtain strips with a thickness of 12 mm. Hot-rolled blanks were heated in a laboratory furnace, quenched from a temperature of 910 °C in water, and then tempered at 550–680 °C (duration 30 min).

Table 2 shows the strength, impact toughness and ductility properties of the samples of the studied steels after laboratory heat treatment.

Methods

Samples for mechanical tests were cut along the rolling direction. Uniaxial tensile tests were performed on an Instron 150 LX universal testing machine (USA) on cylindrical samples with a diameter of 5 mm. Impact bending tests were carried out at a temperature of –60 °C on Charpy samples with a V-shaped notch and a cross section of 10×10 mm using an Instron SI-1M pendulum impact tester (USA).

The structure of the steels was studied by optical microscopy using a ZEISS Axiovert 40 MAT microscope (Germany); corrosion products were analysed using scanning electron microscopy (SEM) on a Tescan Vega SBH3 electron microscope (Czech Republic). X-ray phase analysis of the corrosion products was carried out on a DRON-3 diffractometer (USSR) in K_{α} –Co radiation.

The steel samples after heat treatment were subjected to corrosion tests, including evaluation of hydrogen-induced cracking resistance according to the NACE TM0284 standard, and sulfide stress-corrosion cracking resistance according to Method A of the NACE TM0177 standard. To evaluate the general corrosion rate, unloaded samples were kept in a model CO₂- and H₂S-containing solution for 240 h. The model environment was a solution containing a 5 % NaCl solution of distilled water saturated with a gas cylinder mixture of CO₂ and H₂S (P_{part} of CO₂ was 0.9 atm and P_{part} of H₂S was 0.1 atm), the test temperature was 20 °C. The pH of the solution during the holding varied in the range of 4.3–5.0, and the H₂S concentration was 93–104 mg/l. The corrosion rate was calculated gravimetrically

by weight loss. The type of corrosion and the form of corrosion damage to the metal were determined using a metallographic method.

RESULTS

Metallographic analysis and mechanical properties

The microstructure of the studied 10KhB, 10B, 10F and 15KhF steels after heat treatment according to the “quenching followed by tempering” mode has noticeable differences. This allows evaluating the influence of the chemical composition, namely microalloying additives, on the microstructure parameters and their combined effect on the mechanical properties and corrosion resistance of steel.

From Fig. 1 a, it is evident that the structure of 10KhB steel after heat treatment according to the “quenching + tempering 550 °C” mode is nonequilibrium and is represented by a mixture of ferrite grains of complex shape with tortuous irregular boundaries and lath bainite grains. The proportion of the carbide component is small. The precipitated carbides are finely dispersed and form chains along the boundaries of bainite laths. This type of structure determines the high level of strength properties of steel, corresponding to K56 strength class. The precipitation of a small amount of second phases preserves the alloying elements in the matrix solid solution, therefore, it has a positive effect on the resistance to carbon dioxide corrosion. An increase in the tempering temperature to 600 °C causes a number of structural transformations both in the ferrite matrix and in the carbide component. The structure of the steel after high-temperature tempering at 600 °C is represented by a homogeneous fine-grained ferrite-carbide mixture (Fig. 1 b). The shape of the ferrite grains is preserved from the bainitic structure after hardening and changes slightly as a result of tempering. The carbide component of the structure is uniformly distributed throughout the volume of the metal and includes finely dispersed precipitates of the cementite type of a rounded shape. Inside the ferrite grains, the carbides form chains along the boundaries of the former bainitic laths.

Table 2. Mechanical properties of experimental steels after quenching from 910 °C and tempering at 550–680 °C
Таблица 2. Механические свойства опытных сталей после закалки от температуры 910 °C и отпуска 550–680 °C

Steel grade	Tempering temperature, °C	σ_B , MPa	σ_T , MPa	δ_5 , %	KCV ⁶⁰ , J/cm ²
10KhB	550	587	476	21.4	373
	600	554	449	20.5	421
10B	550	578	478	22.3	390
	600	541	440	20.7	397
10F	600	533	433	22.5	383
	680	537	465	20.3	409
15KhF	680	578	476	20.9	326

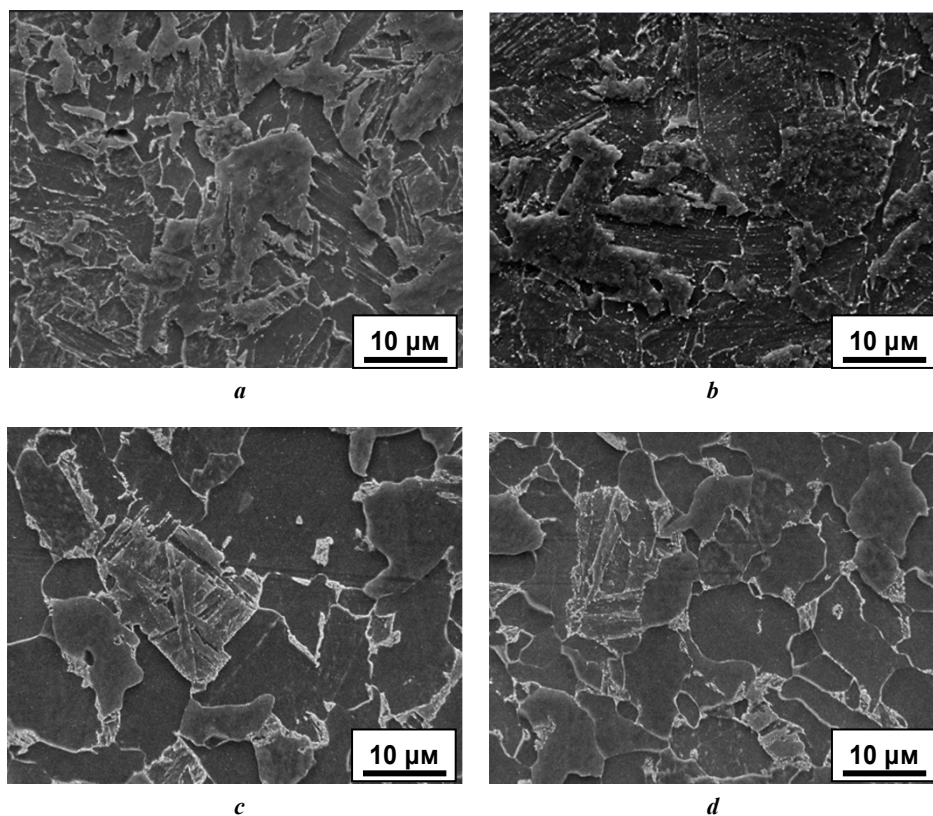


Fig. 1. Microstructure of the studied steels:

a – 10KhB (quenching + tempering 550 °C); *b* – 10KhB (quenching + tempering 600 °C);
c – 10B (quenching + tempering 550 °C); *d* – 10B (quenching + tempering 600 °C)

Рис. 1. Микроструктура исследуемых сталей:

a – 10ХБ (закалка + отпуск 550 °C); *b* – 10ХБ (закалка + отпуск 600 °C);
c – 10Б (закалка + отпуск 550 °C); *d* – 10Б (закалка + отпуск 600 °C)

The revealed structural changes reduced the values of the strength properties from the K56 to K54 level. Based on the results of metallographic analysis of the structure of 10KhB steel, it can be assumed that the dispersed cementite carbides formed during tempering at 600 °C partially contain chromium in their composition, however, the remaining chromium in the ferrite matrix should be sufficient to ensure corrosion resistance in CO₂- and H₂S-containing environments.

The structure of 10B and 10F steels, shown in Fig. 1 c, d and 2 a, b, respectively, differs from that of 10KhB steel and includes a combination of equiaxed excess ferrite grains and grains with a ferrite-carbide mixture. At the same time, if we compare the morphology of the carbide component for 10KhB, 10F and 10B steels after tempering at 600 °C, a difference in shape and size is noticeable. Carbides in 10KhB steel are dispersed and rounded (Fig. 1 b), while in 10B and 10F steels, they are finely dispersed and have an elongated ellipsoid shape (Fig. 1 d, 2 a).

A comparative analysis of the strength properties and microstructure of 10B steel showed that with an increase in the tempering temperature from 550 to 600 °C, the strength decreases, while no noticeable changes in the structure were detected. Consequently, during tempering, transformations occur in the ferrite matrix at the dislocation level and carbonitride precipitates of microalloying elements are formed. Chromium is retained in the ferrite matrix.

An increase in the tempering temperature of 10F steel to 680 °C had the strongest effect on the shape of the carbide component. Due to the processes of spheroidisation and coagulation, cementite-type carbides acquired a larger and rounded shape. In Fig. 2 b, the result of the process of spheroidisation of carbides along grain boundaries is especially noticeable.

According to the results of uniaxial tensile tests, an increase in the tempering temperature from 600 to 680 °C of 10F steel led to a growth in strength properties. This effect is caused by dispersion strengthening during the precipitation of finely dispersed vanadium carbides. The binding of carbon by vanadium retains most of the chromium in solid solution.

The structure of 15KhF steel differs significantly from other studied steels. The ferrite-carbide structure shown in Fig. 2 c is characterised by a large number of rounded cementite-type precipitates uniformly distributed throughout the volume of the ferrite matrix. Chromium can be part of cementite, therefore, the formed type of microstructure of 15KhF steel reduces corrosion resistance in a CO₂-containing environment.

Despite the revealed difference in the type of microstructure and the level of strength properties, laboratory corrosion tests in an H₂S-containing environment using NACE TM0284 and NACE TM0177 standardised methods

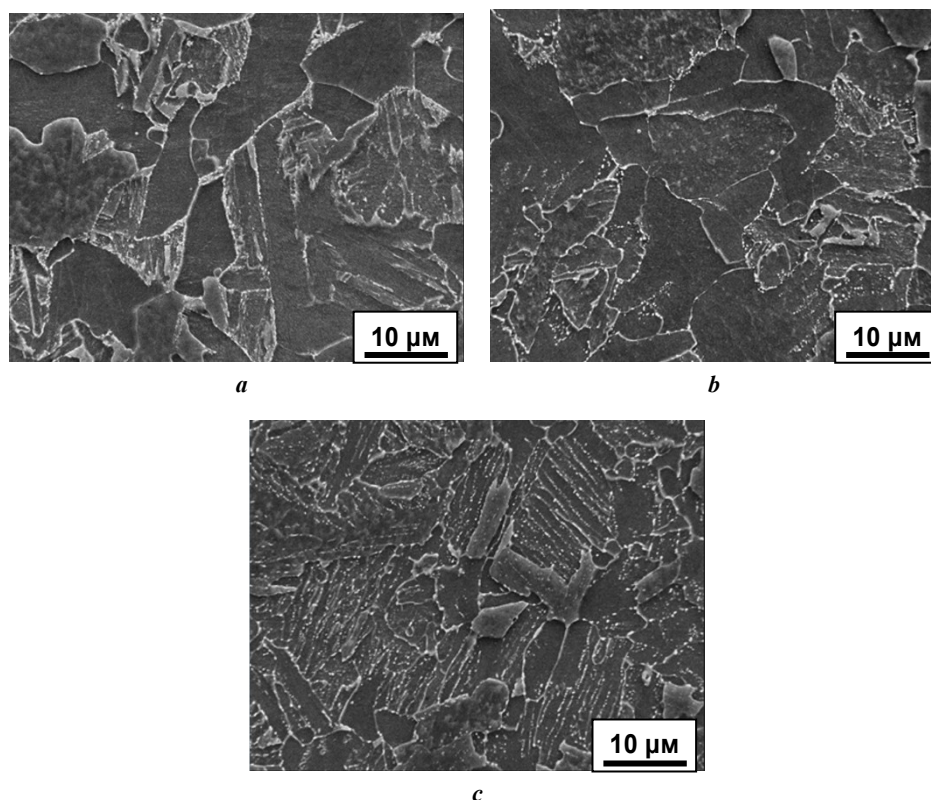


Fig. 2. Microstructure of the studied steels:
a – 10F (quenching + tempering 600 °C); **b** – 10F (quenching + tempering 680 °C);
c – 15KhF (quenching + tempering 680 °C)
Рис. 2. Микроструктура исследуемых сталей:
a – 10Ф (закалка + отпуск 600 °C); **b** – 10Ф (закалка + отпуск 680 °C);
c – 15ХФ (закалка + отпуск 680 °C)

showed that the metal of all the steels studied, regardless of microalloying and strength class, has increased resistance to hydrogen cracking (CLR 0 % and CTR 0 %) and a threshold stress of more than 80 %.

Corrosion properties

The results of corrosion tests of the steel samples in a multicomponent environment containing CO₂ and H₂S presented in Table 3 indicate an insignificant difference in the corrosion resistance of the steels. The obtained values of the general corrosion rate are in the range of 0.11–

0.14 mm/year. 15KhF steel is characterised by the highest values of the general corrosion rate. Probably, the high density and large size of the alloyed cementite precipitates adversely affect the corrosion resistance.

A visual analysis of the steel samples after exposure in a model environment for 240 h showed that all samples were subjected to uniform corrosion. No pitting corrosion, microcracks or blisterings were detected. Consequently, the main mechanism of corrosion of the low-carbon low-alloy steels in a multicomponent CO₂- and H₂S-containing environment is uniform corrosion.

Table 3. Results of the assessment of the general corrosion rate in a multicomponent environment depending on the tempering mode of the quenched steels under study

Таблица 3. Результаты оценки скорости общей коррозии в многокомпонентной среде в зависимости от режима отпуска закаленных исследуемых сталей

Test objects	10KhB		10B		10F		15KhF
	Tempering 550 °C	Tempering 600 °C	Tempering 550 °C	Tempering 600 °C	Tempering 600 °C	Tempering 680 °C	Tempering 680 °C
Corrosion rate, mm/year*	0.12	0.12	0.12	0.12	0.12	0.11	0.14

Note. * The measurement error is equal to the numerical uncertainty and is ± 0.01 mm/year.

Примечание. * Погрешность измерений равна численно неопределенности и составляет $\pm 0,01$ мм/год.

As a result of X-ray phase analysis of corrosion products formed on the surface of the samples, it was found that iron sulfide FeS is the main component of the corrosion products formed during exposure to CO₂- and H₂S-containing environments. In the X-ray diffraction patterns of all the tested samples, lines corresponding to the sample metal matrix were identified – K-lines of the α -Fe phase (BCC lattice) and a low-intensity peak corresponding to FeS sulfide – mackinawite (Fig. 3).

Despite the fact that the gas mixture contains only 10 % of H₂S, its effect on the metal prevails over 90 % of CO₂ and determines the leading corrosion mechanism. The dominance of H₂S in a multicomponent medium is caused by its greater solubility in an aqueous solution under the studied conditions. The content of H₂S in the solution is significantly higher than of CO₂. The product of the interaction of the metal with dissolved H₂S is sulfide FeS, which is less soluble than FeCO₃ and forms a film on the surface of the samples. Dissolved in the model CO₂ solution also interacts with the metal, but the reaction of carbonate formation is slower than that of sulfides.

The appearance of the corrosion products formed on the surface of all the steel samples studied during the holding time of 240 h indicates the unevenness of the layer (Fig. 4). Comparative analysis of the surface layer does not allow establishing the dependence of the thickness and composition of the corrosion products on the structural state and chemical composition of the steels. The uneven nature of the sulfide film distribution on the surface of samples made of 10B and 10F steels is similar to that of 10KhB steel (Fig. 4 b, c, Table 3). Therefore, the proposed

variants of microalloying systems make it possible to achieve an equally high level of corrosion resistance for the studied low-carbon steels in an environment containing H₂S and CO₂. The surface of the samples has an etched relief in which structural elements appear, which indicates the dissolution of iron and the occurrence of corrosion. The etching of the metal by the environment occurs along certain crystallographic planes.

The corrosion products on the surface of 10KhB steel samples after heat treatment using the "quenching and tempering 550 °C" and "quenching and tempering 600 °C" modes are represented by an uneven thin film of iron sulfide. Fig. 5 shows that an increase in the tempering temperature leads to an increase in the number of point corrosion lesions and an increase in the thickness of the corrosion product layer from 2 to 5 μ m. When examining the sections of 10KhB steel samples, an uneven distribution of the surface film of sulfides of non-uniform thickness was found. Single corrosion lesions up to 5–7 μ m deep filled with dense deposits were revealed. The corrosion products are characterised by an increased Cr content of up to 1.5 wt. %, which is 2 times higher than the Cr content in the metal. The concentration of S in the corrosion products does not exceed 1 wt. %.

The uniform corrosion mechanism prevails over the pitting one. The main reasons for the formation of local point lesions are a decrease in the strength of the matrix and the formation of large carbide precipitates of the cementite type. The carbide and ferrite matrix form a local galvanic couple, where the carbide has lower solubility and acts as a cathode, and the ferrite acts as an anode.

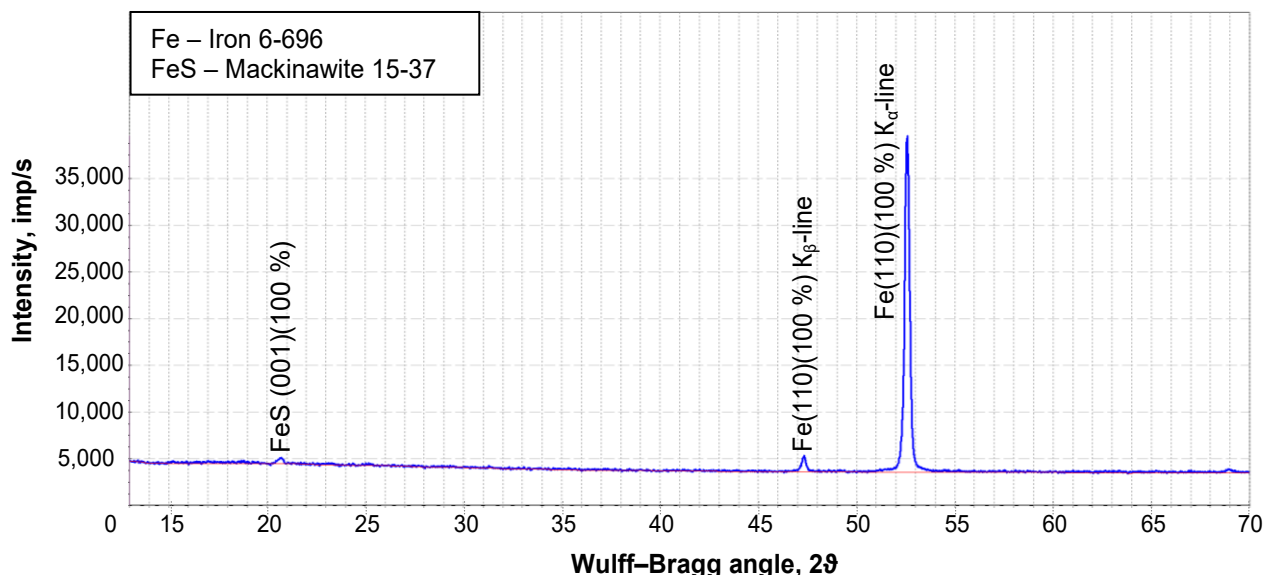
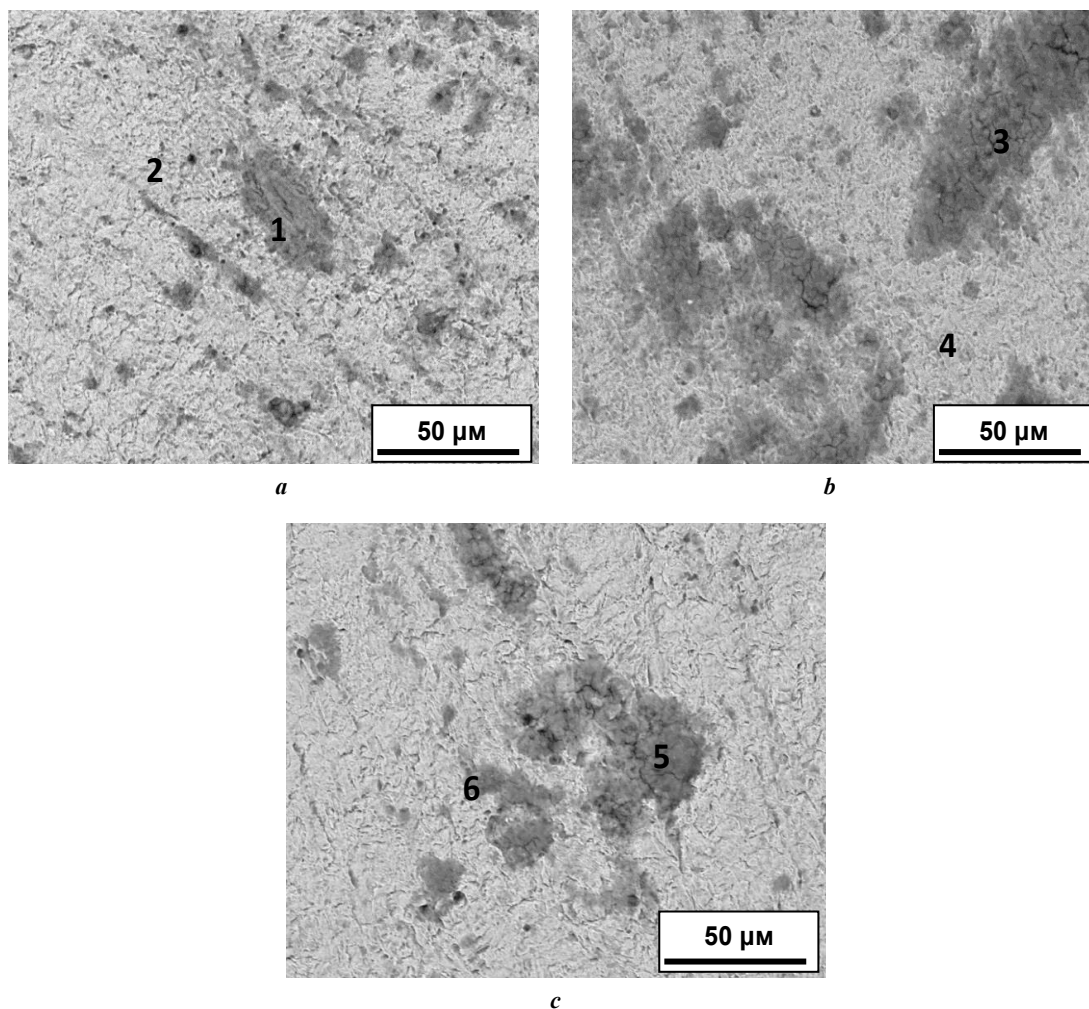


Fig. 3. Results of X-ray phase analysis from the surface of samples after testing in CO₂- and H₂S-containing environment

Рис. 3. Результаты рентгенофазового анализа с поверхности образцов после испытаний в CO₂- и H₂S-содержащей среде



No.	O	Si	S	Cr	Mn	Fe
1	11.34	0.43	13.86	1.18	0.69	The rest
2	3.37	0.56	0.92	0.76	1.14	The rest
3	15.98	0.82	3.78	1.04	1.03	The rest
4	3.62	0.53	0.52	0.60	1.30	The rest
5	20.53	0.48	2.90	0.44	0.63	The rest
6	3.48	0.38	0.44	0.57	1.03	The rest

Fig. 4. Appearance and composition of corrosion products on the surface of the studied samples: **a** is 10KhB (quenching + tempering 550 °C); **b** is 10B (quenching + tempering 600 °C); **c** is 10F (quenching + tempering 680 °C); **d** is chemical composition of corrosion products

Рис. 4. Вид и состав продуктов коррозии на поверхности исследуемых образцов: **a** – 10ХБ (закалка + отпуск 550 °C); **b** – 10Б (закалка + отпуск 600 °C); **c** – 10Ф (закалка + отпуск 680 °C); **d** – химический состав продуктов коррозии

DISCUSSION

The comparative analysis of the nature of corrosion damage and the composition of corrosion products on the samples of the studied steels showed that during holding in an environment containing CO₂ ($P_{\text{CO}_2}=0.9$ atm) and H₂S ($P_{\text{H}_2\text{S}}=0.1$ atm), the predominant mechanism is uniform sulfide corrosion. Regardless of the composition of the studied steels and strength properties, uniform dissolution

of the metal occurs, as evidenced by the formation of an etched surface relief. A thin iron sulfide film is formed on the surface of the samples, which serves as a barrier to further interaction of the metal with the environment and slows down the corrosion process. For comparison: in [15], the rate of general corrosion after holding in a CO₂-containing environment without the addition of H₂S was studied. The obtained values of the rate of general corrosion

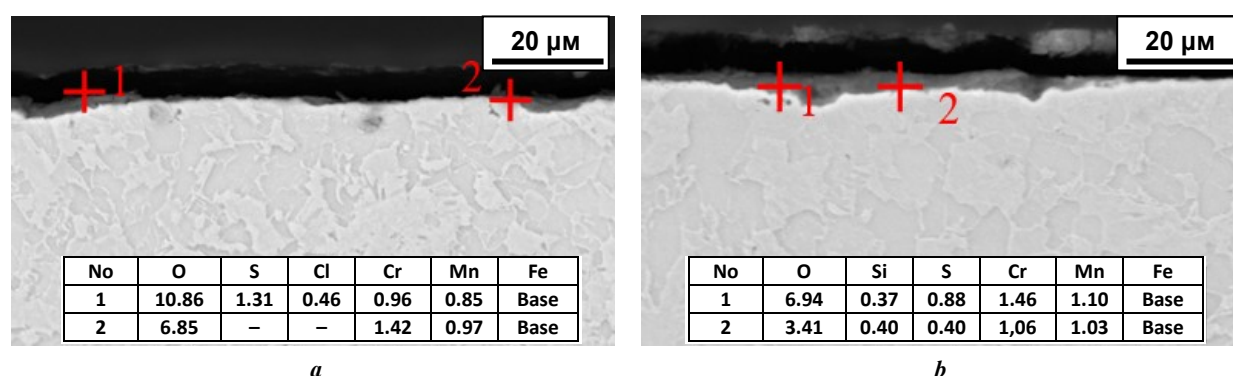


Fig. 5. Cross-section of corrosion products of the studied samples:
a – 10KhB (quenching + tempering 550 °C); *b* – 10KhB (quenching + tempering 600 °C)

Рис. 5. Сечение продуктов коррозии исследуемых образцов:
a – 10ХБ (закалка + отпуск 550 °C); *b* – 10ХБ (закалка + отпуск 600 °C)

in a CO₂-containing environment for low-carbon microalloyed steels in some cases are 2 times higher than the corrosion rates obtained in the presented work. In [16], it is shown that the rate of corrosion developing by the sulfide mechanism is lower than the rate of carbon dioxide corrosion. Accordingly, it will be interesting to assess the effect of different concentrations of CO₂ and H₂S on the corrosion rate. It is important to understand at what H₂S concentrations in a multicomponent environment the transition to the predominant formation of carbonates and the CO₂ corrosion predominance is possible, since there is still no unambiguous opinion in the literature on the influence of H₂S additives on the rate of general corrosion and the predominant mechanism.

The low dependence of the rate of general sulfide corrosion on the chemical composition of steels is confirmed by the obtained values of corrosion rates, which are 0.11–0.14 mm/year. It was found that a decrease in the concentration of carbon in steel reduces the corrosion rate. The revealed dependence is associated with the release of a small amount of carbides, which retain the main alloying elements in the matrix. Moreover, in a corrosive environment, carbides form a galvanic couple with the ferrite matrix accelerating the corrosion of the matrix. At the same time, the influence of microalloying of the studied steels, as well as the tempering mode, which determines the amount of carbonitride precipitation in the structure, on the level of the general corrosion rate of microalloyed steels was not revealed. Consequently, for steel of the same chemical composition, varying the tempering temperature mode and changing the composition of the carbide phase, it is possible to regulate the level of strength properties, maintaining a low corrosion rate. In the works [17–20] dealing with the study of corrosion in environments containing CO₂ and H₂S, only an option for increasing corrosion resistance by introducing microalloying additives is proposed.

Structural transformations occurring in the ferrite matrix during tempering did not affect the rate of general corrosion. Only at the local level by the formation of point lesions with a depth of 5–7 μm was it possible to assess the role of the structural factor in the process of sulfide corrosion. The weak intensity of local corrosion development does not

allow a quantitative comparative assessment of the corrosion resistance of samples with different carbide components. Consequently, at low concentrations of dissolved H₂S and the presence of CO₂ in the environment, the corrosion rate of low-carbon low-alloy steels weakly depends on the structure and properties of the steel and does not exceed 0.14 mm/year, since it is determined by the rate of formation of the surface iron sulfide film.

The studies showed as well that, regardless of the microalloying additives and the strength level achieved due to different tempering temperatures, high resistance to hydrogen cracking and hydrogen sulfide stress cracking can be achieved in low-carbon steels. It is worth noting that various chemical compositions are used to achieve different levels of strength, cold resistance and resistance to hydrogen sulfide cracking in steels obtained by controlled rolling. Manufacturers are forced to simultaneously support several technologies for the production of rolled products, often using complex expensive combinations of microalloying: niobium and titanium or niobium, vanadium and titanium [20]. Moreover, when manufacturing rolled products using controlled rolling methods, achieving a combination of high cold resistance to –60 °C and resistance to hydrogen cracking is only possible with a carbon content of no more than 0.07 %, which requires additional expensive alloying [20]. During unstable supplies of niobium to the Russian market, it is advantageous and advisable to have technologies and concepts of chemical compositions that allow switching to various microalloying systems without losing any properties of the final product, from strength to corrosion resistance in various environments. In addition, the ability to obtain different strength classes with all other equal pipe manufacturing options is important for pipeline components that are produced in small quantities for the construction of special pipelines.

CONCLUSIONS

For the developed steel compositions, appropriate tempering regimes ensure both strength classes K52–K56 and high Charpy impact toughness at –60 °C, despite microstructural variations resulting from different alloying systems.

Corrosion tests in accordance with NACE TM0284 and NACE TM0177 confirmed that all studied steels, regardless of alloying system or strength class, exhibited excellent resistance to hydrogen cracking (CLR 0 %, CTR 0 %) and SSC (threshold stress >80 %).

In a model CO₂-H₂S environment, the general corrosion rate of the steels was 0.11–0.14 mm/year, independent of alloying system, strength class, or microstructure. In all cases, the dominant corrosion mechanism was uniform H₂S corrosion, even though the CO₂ partial pressure was significantly higher than that of H₂S.

REFERENCES

1. Tkacheva V.E., Brikov A.V., Lunin D.A., Markin A.N. *Lokal'naya CO₂-korroziiya neftepromyslovogo oborudovaniya* [Localized CO₂ corrosion of oilfield equipment]. Ufa, RN-BashNIPIneft Publ., 2021. 168 p.
2. Tkacheva V.E., Markin A.N., Kshnyakin D.V., Mal'tsev D.I., Nosov V.V. Corrosion of downhole equipment in hydrogen sulfur-containing environments. *Theory and Practice of Corrosion Protection*, 2021, vol. 26, no. 2, pp. 7–26. DOI: [10.31615/j.corros.prot.2021.100.2-1](https://doi.org/10.31615/j.corros.prot.2021.100.2-1).
3. Bregman Dzh. *Ingibitoriy korrozii* [Corrosion inhibitors]. Moscow, Khimiya Publ., 1966. 312 p.
4. Gonik A.A. *Korroziiya neftepromyslovogo oborudovaniya i mery ee preduprezhdeniya* [Corrosion of Oilfield Equipment and Measures to Prevent it]. Moscow, Nedry Publ., 1976. 192 p.
5. Ulig G.G. *Korroziiya i borba s ney. Vvedenie v korrozi-onnyuyu nauku i tekhniku* [Corrosion and corrosion control. An introduction to corrosion science and engineering]. Leningrad, Khimiya Publ., 1989. 456 p.
6. Vyboyshechik M.A., Zyryanov A.O., Gruzkov I.V., Fedotova A.V. Carbon dioxide corrosion of oilfield casing and tubular goods in media saturated with H₂S and Cl. *Science Vector of Togliatti State University*, 2019, no. 2, pp. 6–17. DOI: [10.18323/2073-5073-2019-2-6-17](https://doi.org/10.18323/2073-5073-2019-2-6-17).
7. Choi Yoon-Seok, Nesic S., Ling Shiun. Effects of H₂S on the CO₂ corrosion of carbon steel in acidic solutions. *Electrochemical Acta*, 2011, vol. 56, no. 4, pp. 1752–1760. DOI: [10.1016/j.electacta.2010.08.049](https://doi.org/10.1016/j.electacta.2010.08.049).
8. Vyboyshechik M.A., Ioffe A.V. The development of steel resistant to carbon dioxide corrosion in oilfield media. *Perspektivnye materialy*. Tolyatti, Tolyatinskiy gosudarstvennyy universitet Publ., 2017. Vol. 7, pp. 115–166. EDN: [HFOONS](https://elibrary.ru/hfonns).
9. Lopez D.A., Perez T., Simison S.N. The influence of microstructure and chemical composition of carbon and low alloy steels in CO₂ corrosion. A state-of-the-art appraisal. *Materials & Design*, 2003, vol. 24, no. 8, pp. 561–575. DOI: [10.1016/S0261-3069\(03\)00158-4](https://doi.org/10.1016/S0261-3069(03)00158-4).
10. Zhao Xuehui, Li Guoping, Liu Junlin, Li Mingxing, Du Quanqing, Han Yan. Corrosion Performance Analysis of Tubing Materials with Different Cr Contents in the CO₂ Flooding Injection–Production Environment. *Coatings*, 2023, vol. 13, no. 10, article number 1812. DOI: [10.3390/coatings13101812](https://doi.org/10.3390/coatings13101812).
11. Ko M., Ingham B., Laycock N., Williams D.E. In situ synchrotron X-ray diffraction study of the effect of chromium additions to the steel and solution on CO₂ corrosion of pipeline steels. *Corrosion Science*, 2014, vol. 80, pp. 237–246. DOI: [10.1016/j.corsci.2013.11.035](https://doi.org/10.1016/j.corsci.2013.11.035).
12. Sun Jianbo, Sun Chong, Lin Xueqiang, Cheng Xiangkun, Liu Huifeng. Effect of chromium on corrosion behavior of P110 steels in CO₂-H₂S environment with high pressure and high temperature. *Materials*, 2016, vol. 9, no. 3, article number 200. DOI: [10.3390/ma9030200](https://doi.org/10.3390/ma9030200).
13. Vagapov R.K., Zapevalov D.N. Aggressive environmental factors causing corrosion at gas production facilities in the presence of carbon dioxide. *Theory and Practice of Corrosion Protection*, 2020, vol. 25, no. 4, pp. 7–17. DOI: [10.31615/j.corros.prot.2020.98.4-1](https://doi.org/10.31615/j.corros.prot.2020.98.4-1).
14. Li Qiang, Jia Wenguang, Yang Kaixiang, Dong Wen-feng, Liu Bingcheng. CO₂ Corrosion Behavior of X70 Steel under Typical Gas-Liquid Intermittent Flow. *Metals*, 2023, vol. 13, no. 7, article number 1239. DOI: [10.3390/met13071239](https://doi.org/10.3390/met13071239).
15. Chen Xuezhong, Yang Xiaomin, Zeng Mingyou, Wang Hu. Influence of CO₂ partial pressure and flow rate on the corrosion behavior of N80 steel in 3.5% NaCl. *International Journal of Electrochemical Science*, 2023, vol. 18, no. 8, article number 100218. DOI: [10.1016/j.ijoes.2023.100218](https://doi.org/10.1016/j.ijoes.2023.100218).
16. Kudashov D.V., Ioffe A.V., Naumenko V.V., Muntin A.V., Udod K.A., Kovtunov S.V. Corrosion resistance of welded tubing of L80 strength group of different chemical composition. *Izvestiya vuzov. Chernaya metallurgiya*, 2022, vol. 65, no. 3, pp. 200–208. DOI: [10.17073/0368-0797-2022-3-200-208](https://doi.org/10.17073/0368-0797-2022-3-200-208).
17. Popkova Yu.I., Grigorev A.Ya. Influence of steel characteristics on the corrosion resistance of tubing under carbon dioxide corrosion conditions. *Bulletin Sukhoi State technical university of Gomel*, 2024, no. 1, pp. 48–62. DOI: [10.62595/1819-5245-2024-1-48-62](https://doi.org/10.62595/1819-5245-2024-1-48-62).
18. Amezhnov A.V., Rodionova I.G., Gladchenkova Yu.S., Zarkova E.I., Stukalova N.A. Comparative assessment of the aggressiveness of various mediums. Influence of medium characteristics on the rate and mechanisms of corrosion processes. *Problems of ferrous metallurgy and materials science*, 2020, no. 3, pp. 62–70. EDN: [HBIWWB](https://elibrary.ru/hbiwwb).
19. Benedito A.V., Torres C.A.B., Silva R.M.C., Krahel P.A., Cardoso D.C.T., Silva F.A., Martins C.H. Effects of niobium addition on the mechanical properties and corrosion resistance of microalloyed steels: a review. *Buildings*, 2024, vol. 14, no. 5, article number 1462. DOI: [10.3390/buildings14051462](https://doi.org/10.3390/buildings14051462).
20. Kholodnyi A.A. Resistance increase to hydrogen-induced sheet cracking for gas and oil pipes based on the structure formation control in the central segregation zone. *Steel in translation*, 2020, vol. 50, no. 1, pp. 53–61. DOI: [10.3103/S0967091220010052](https://doi.org/10.3103/S0967091220010052).

СПИСОК ЛИТЕРАТУРЫ

1. Ткачева В.Э., Бриков А.В., Лунин Д.А., Маркин А.Н. Локальная CO₂-коррозия нефтепромыслового оборудования. Уфа: РН-БашНИПИнефть, 2021. 168 с.
2. Ткачева В.Э., Маркин А.Н., Кшнякин Д.В., Мальцев Д.И., Носов В.В. Коррозия внутрискважинного оборудования в сероводородсодержащих средах // Практика противокоррозионной защиты. 2021. Т. 26. № 2. С. 7–26. DOI: [10.31615/j.corros.prot.2021.100.2-1](https://doi.org/10.31615/j.corros.prot.2021.100.2-1).

3. Брегман Дж. Ингибиторы коррозии. М.: Химия, 1966. 312 с.
4. Гоник А.А. Коррозия нефтепромыслового оборудования и меры ее предупреждения. М.: Недры, 1976. 192 с.
5. Улиг Г.Г. Коррозия и борьба с ней. Введение в коррозионную науку и технику. Л.: Химия, 1989. 456 с.
6. Выбойщик М.А., Зырянов А.О., Грузков И.В., Федотова А.В. Углекислотная коррозия нефтепромысловых труб в средах, насыщенных H_2S и Cl // Вектор науки Тольяттинского государственного университета. 2019. № 2. С. 6–17. DOI: [10.18323/2073-5073-2019-2-6-17](https://doi.org/10.18323/2073-5073-2019-2-6-17).
7. Choi Yoon-Seok, Nesic S., Ling Shiun. Effects of H_2S on the CO_2 corrosion of carbon steel in acidic solutions // *Electrochemical Acta*. 2011. Vol. 56. № 4. P. 1752–1760. DOI: [10.1016/j.electacta.2010.08.049](https://doi.org/10.1016/j.electacta.2010.08.049).
8. Выбойщик М.А., Иоффе А.В. Разработка стали, стойкой к углекислотной коррозии в нефтедобываемых средах // Перспективные материалы. Т. 7. Тольятти: Тольяттинский государственный университет, 2017. С. 115–166. EDN: [HFONNS](https://www.edn.ru/HFONNS).
9. Lopez D.A., Perez T., Simison S.N. The influence of microstructure and chemical composition of carbon and low alloy steels in CO_2 corrosion. A state-of-the-art appraisal // *Materials & Design*. 2003. Vol. 24. № 8. P. 561–575. DOI: [10.1016/S0261-3069\(03\)00158-4](https://doi.org/10.1016/S0261-3069(03)00158-4).
10. Zhao Xuehui, Li Guoping, Liu Junlin, Li Mingxing, Du Quanqing, Han Yan. Corrosion Performance Analysis of Tubing Materials with Different Cr Contents in the CO_2 Flooding Injection–Production Environment // *Coatings*. 2023. Vol. 13. № 10. Article number 1812. DOI: [10.3390/coatings13101812](https://doi.org/10.3390/coatings13101812).
11. Ko M., Ingham B., Laycock N., Williams D.E. In situ synchrotron X-ray diffraction study of the effect of chromium additions to the steel and solution on CO_2 corrosion of pipeline steels // *Corrosion Science*. 2014. Vol. 80. P. 237–246. DOI: [10.1016/j.corsci.2013.11.035](https://doi.org/10.1016/j.corsci.2013.11.035).
12. Sun Jianbo, Sun Chong, Lin Xueqiang, Cheng Xiangkun, Liu Huifeng. Effect of chromium on corrosion behavior of P110 steels in CO_2 - H_2S environment with high pressure and high temperature // *Materials*. 2016. Vol. 9. № 3. Article number 200. DOI: [10.3390/ma9030200](https://doi.org/10.3390/ma9030200).
13. Вагапов Р.К., Запелалов Д.Н. Агрессивные факторы эксплуатационных условий, вызывающие коррозию на объектах добычи газа в присутствии диоксида углерода // Практика противокоррозионной защиты. 2020. Т. 25. № 4. С. 7–17. DOI: [10.31615/j.corros.prot.2020.98.4-1](https://doi.org/10.31615/j.corros.prot.2020.98.4-1).
14. Li Qiang, Jia Wenguang, Yang Kaixiang, Dong Wenfeng, Liu Bingcheng. CO_2 Corrosion Behavior of X70 Steel under Typical Gas-Liquid Intermittent Flow // *Metals*. 2023. Vol. 13. № 7. Article number 1239. DOI: [10.3390/met13071239](https://doi.org/10.3390/met13071239).
15. Chen Xuezhong, Yang Xiaomin, Zeng Mingyou, Wang Hu. Influence of CO_2 partial pressure and flow rate on the corrosion behavior of N80 steel in 3.5% NaCl // *International Journal of Electrochemical Science*. 2023. Vol. 18. № 8. Article number 100218. DOI: [10.1016/j.ijoes.2023.100218](https://doi.org/10.1016/j.ijoes.2023.100218).
16. Кудашов Д.В., Иоффе А.В., Науменко В.В., Мунтин А.В., Удод К.А., Ковтунов С.В. Исследование коррозионной стойкости сварных насосно-компрессорных труб группы прочности L80 различного химического состава // Известия высших учебных заведений. Черная металлургия. 2022. Т. 65. № 3. С. 200–208. DOI: [10.17073/0368-0797-2022-3-200-208](https://doi.org/10.17073/0368-0797-2022-3-200-208).
17. Попкова Ю.И., Григорьев А.Я. Влияние состава стали на коррозионную стойкость насосно-компрессорных труб в условиях углекислотной коррозии // Вестник Гомельского государственного технического университета им. П.О. Сухого. 2024. № 1. С. 48–62. DOI: [10.62595/1819-5245-2024-1-48-62](https://doi.org/10.62595/1819-5245-2024-1-48-62).
18. Амежнов А.В., Родионова И.Г., Гладченкова Ю.С., Заркова Е.И., Стукалова Н.А. Сравнительная оценка агрессивности различных сред. Влияние характеристик среды на скорость и механизмы протекания коррозионных процессов // Проблемы черной металлургии и материаловедения. 2020. № 3. С. 62–70. EDN: [HBIWWB](https://www.edn.ru/HBIWWB).
19. Benedito A.V., Torres C.A.B., Silva R.M.C., Krahel P.A., Cardoso D.C.T., Silva F.A., Martins C.H. Effects of niobium addition on the mechanical properties and corrosion resistance of microalloyed steels: a review // *Buildings*. 2024. Vol. 14. № 5. Article number 1462. DOI: [10.3390/buildings14051462](https://doi.org/10.3390/buildings14051462).
20. Холодный А.А. Повышение сопротивления водородному растрескиванию листов для газо- и нефтепроводных труб на основе управления структурообразованием в центральной сегрегационной зоне // Сталь. 2020. № 1. С. 46–53. EDN: [EMNGDD](https://www.edn.ru/EMNGDD).

Влияние термической обработки на структуру и коррозионные свойства микролегированных трубных сталей с содержанием хрома до 1 %

Чистопольцева Елена Александровна^{1,5}, кандидат технических наук,
руководитель департамента специального материаловедения
Кудашов Дмитрий Викторович^{2,6}, кандидат технических наук, директор
Комиссаров Александр Александрович^{3,7}, кандидат технических наук,
заведующий лабораторией «Гибридные наноструктурные материалы»
Ющук Вячеслав Васильевич^{3,8}, инженер научного проекта
Мунтин Александр Вадимович⁴, кандидат технических наук,
директор инженерно-технологического центра
Червонный Алексей Владимирович⁴, кандидат технических наук,
начальник отдела по исследованиям и разработкам
Долгач Егор Дмитриевич³, инженер научного проекта

¹ООО «ИТ-Сервис», Самара (Россия)

²Выксунский филиал НИТУ «МИСИС», Выкса (Россия)

³Университет науки и технологий МИСИС, Москва (Россия)

⁴АО «Выксунский металлургический завод», Выкса (Россия)

*E-mail: chistopolceva@its-samara.com

⁵ORCID: <https://orcid.org/0009-0002-5587-287X>

⁶ORCID: <https://orcid.org/0000-0002-7661-1591>

⁷ORCID: <https://orcid.org/0000-0002-8758-5085>

⁸ORCID: <https://orcid.org/0000-0002-3015-1235>

Поступила в редакцию 22.04.2025

Пересмотрена 20.05.2025

Принята к публикации 17.07.2025

Аннотация: Осложнение условий эксплуатации, заключающееся в повышении агрессивности сред за счет присутствия одновременно растворенного сероводорода, углекислого газа, хлоридов, увеличения содержания водной фазы, приводит к значительному сокращению продолжительности безаварийной работы трубопроводов. Ограниченность способов защиты вынуждает использовать одновременно несколько антикоррозионных мероприятий для трубопроводов со сложными средами. В работе предложены системы микролегирования низкоуглеродистых марок сталей 10ХБ, 10Ф, 10Б, 15ХФ с содержанием хрома до 1 % для бесшовных труб и режимы термической обработки, позволяющие достичь одновременно повышенную прочность, хладостойкость и коррозионную стойкость в средах, содержащих CO_2 и H_2S . По результатам механических испытаний сталей после термической обработки установлено, что предложенные варианты микролегирования гарантируют прочностные свойства классов прочности К52–К56 и хладостойкость одновременно. Морфология карбидной составляющей структуры зависит от микролегирующего элемента и определяет уровень прочности стали, но не оказывает влияния на коррозионную стойкость. Исследуемые стали обладают повышенной стойкостью к водородному растрескиванию и сульфидному коррозионному растрескиванию под напряжением. После выдержки в многокомпонентной CO_2 - и H_2S -содержащей среде формируется поверхностная пленка сульфида железа, свидетельствующая о протекании равномерной сульфидной коррозии. Скорость коррозии исследуемых сталей и тип коррозии определяются составом агрессивной среды и скоростью формирования поверхностной пленки сульфида железа. Полученные результаты позволяют расширить область применения предлагаемых сталей в многокомпонентных агрессивных средах независимо от вида микролегирования.

Ключевые слова: низкоуглеродистая микролегированная сталь; термическая обработка; коррозионно-стойкая бесшовная труба; CO_2 - и H_2S -содержащая среда; сульфидная коррозия стали; мелкозернистая структура; нефтепромысловые трубопроводы.

Благодарности: Работа выполнена в рамках комплексного проекта по теме «Разработка и внедрение комплексных технологий производства бесшовных труб из сталей нового поколения с управляемой коррозионной стойкостью при осложненных условиях эксплуатации для топливно-энергетического комплекса Российской Федерации» в рамках соглашений № 075-11-2023-011 от 10.02.2023 и № 075-11-2025-017 от 27.02.2025 по постановлению Правительства РФ № 218 от 09.04.2010.

Для цитирования: Чистопольцева Е.А., Кудашов Д.В., Комиссаров А.А., Ющук В.В., Мунтин А.В., Червонный А.В., Долгач Е.Д. Влияние термической обработки на структуру и коррозионные свойства микролегированных трубных сталей с содержанием хрома до 1 % // Frontier Materials & Technologies. 2025. № 3. С. 101–111. DOI: 10.18323/2782-4039-2025-3-73-8.

The influence of rotary swaging and subsequent annealing on the structure and mechanical properties of L68 single-phase brass

Eleonora I. Chistyukhina^{*1,2,4}, research engineer

at the Laboratory of Physical Metallurgy of Non-Ferrous and Light Metals
named by Academician A.A. Bochvar, graduate student of Chair of Metal Science and Physics of Strength

Natalia S. Martynenko^{1,5}, PhD (Engineering), senior researcher
at the Laboratory of Physical Metallurgy of Non-Ferrous and Light Metals named by Academician A.A. Bochvar

Olga V. Rybalchenko^{1,6}, PhD (Engineering), leading researcher
at the Laboratory of Physical Metallurgy of Non-Ferrous and Light Metals named by Academician A.A. Bochvar

Ivan S. Nikitin^{3,7}, PhD (Engineering), junior researcher
at the Laboratory of Mechanical Properties of Nanostructured Materials and Superalloys

Elena A. Lukyanova^{1,8}, PhD (Engineering), senior researcher
at the Laboratory of Physical Metallurgy of Non-Ferrous and Light Metals named by Academician A.A. Bochvar

Artem D. Gorbenko^{1,9}, research engineer
at the Laboratory of Strength and Plasticity of Metallic and Composite Materials and Nanomaterials

Diana R. Temralieva^{1,10}, research engineer
at the Laboratory of Physical Metallurgy of Non-Ferrous and Light Metals named by Academician A.A. Bochvar

Petr B. Straumal^{1,11}, PhD (Physics and Mathematics), senior researcher
at the Laboratory of Physical Metallurgy of Non-Ferrous and Light Metals named by Academician A.A. Bochvar

Vladimir A. Andreev^{1,12}, PhD (Engineering), leading researcher
at the Laboratory of Plastic Deformation of Metallic Materials

Sergey V. Dobatkin^{1,13}, Doctor of Science (Engineering), Professor, Head
of the Laboratory of Physical Metallurgy of Non-Ferrous and Light Metals named by Academician A.A. Bochvar

¹*A.A. Baikov Institute of Metallurgy and Materials Science of RAS, Moscow (Russia)*

²*University of Science and Technology "MISIS", Moscow (Russia)*

³*Belgorod State University, Belgorod (Russia)*

*E-mail: e.chistyukhina@mail.ru

⁴ORCID: <https://orcid.org/0009-0009-2192-3246>

⁵ORCID: <https://orcid.org/0000-0003-1662-1904>

⁶ORCID: <https://orcid.org/0000-0002-0403-0800>

⁷ORCID: <https://orcid.org/0000-0002-5417-9857>

⁸ORCID: <https://orcid.org/0000-0001-7122-6427>

⁹ORCID: <https://orcid.org/0000-0002-3357-4049>

¹⁰ORCID: <https://orcid.org/0000-0002-8392-7826>

¹¹ORCID: <https://orcid.org/0000-0001-6192-5304>

¹²ORCID: <https://orcid.org/0000-0003-3937-1952>

¹³ORCID: <https://orcid.org/0000-0003-4232-927X>

Received 30.06.2025

Revised 18.07.2025

Accepted 25.08.2025

Abstract: Copper alloys based on the Cu–Zn system, in particular L68 brass, are promising structural materials. However, to improve their reliability and expand the scope of application, it is necessary to enhance their strength characteristics. In this work, the influence of a combination of rotary swaging (RS) and subsequent annealing on the structure, strength and ductility of L68 brass was studied. For this purpose, the alloy microstructure was studied in the quenched and deformed states, mechanical tests for uniaxial tension, a Brinell hardness study, and an assessment of structural and phase transitions using differential scanning calorimetry were carried out. It was found that during rotary swaging, both α -phase grains elongated along the deformation direction and an ultrafine-grained structure inside them consisting of subgrains, deformation twins and shear bands are formed. Subsequent annealing at 450 °C leads to an increase in the grain size to 3–5 μm due to static recrystallization. After rotary swaging, an increase in the offset yield strength ($\sigma_{0.2}$) and ultimate tensile stress limit (σ_B) by ~ 10 and ~ 3.5 times, respectively, is observed with a decrease in the relative elongation value by more than 6 times. Subsequent annealing at 450 °C, which caused the formation of a recrystallised structure, led to a decrease in the strength characteristics of L68 brass relative to the deformed state with a simultaneous increase in the relative elongation value compared to both the deformed and the initial state of the alloy. However, it is worth noting that $\sigma_{0.2}$ and σ_B of L68 brass after rotary swaging

© Chistyukhina E.I., Martynenko N.S., Rybalchenko O.V.,
Nikitin I.S., Lukyanova E.A., Gorbenko A.D.,
Temralieva D.R., Straumal P.B., Andreev V.A., Dobatkin S.V., 2025

and subsequent annealing at 450 °C exceed the values for the quenched alloy by an average of ~2.5 and ~1.7 times, respectively, and exceed the values regulated by GOST 494-90, GOST 1066-2015, GOST 931-90, and GOST 5362-78.

Keywords: L68 brass; rotary swaging; ultrafine-grained structure; recrystallization; strength; ductility.

Acknowledgments: The work was carried out with the financial support of state assignment No. 075-00319-25-00.

The paper was written on the reports of the participants of the XII International School of Physical Materials Science (SPM-2025), Togliatti, September 15–19, 2025.

For citation: Chistyukhina E.I., Martynenko N.S., Rybalchenko O.V., Nikitin I.S., Lukyanova E.A., Gorbenko A.D., Temralieva D.R., Straumal P.B., Andreev V.A., Dobatkin S.V. The influence of rotary swaging and subsequent annealing on the structure and mechanical properties of L68 single-phase brass. *Frontier Materials & Technologies*, 2025, no. 3, pp. 113–124. DOI: 10.18323/2782-4039-2025-3-73-9.

INTRODUCTION

Copper and its alloys are widely used in the electrical industry due to their excellent electrical conductivity [1]. However, copper alloys, in particular alloys of the Cu–Zn system, are also used as structural materials in shipbuilding and aircraft construction, the petrochemical industry, in the production of pipes and plumbing products, as well as refrigeration equipment and military products [2]. This use of brasses is caused by their high corrosion resistance, non-magnetic nature and good formability, as well as by a balance of strength and ductility [3]. Brass with a zinc content of up to 37 % is single-phase and is an α -solid solution with a face-centered cubic lattice [4]. Single-phase α -brass with a low zinc content is more resistant to corrosion and dezincification processes compared to two-phase (α + β)-brasses [5; 6]. However, the main disadvantage of single-phase brasses is their low strength characteristics. Precipitation hardening and grain refinement by deformation treatment can improve the mechanical properties and, consequently, expand the scope of application of brass. In this case, by refining the microstructure to an ultrafine-grained (UFG) and/or nanosized structure, it is possible to achieve a significant increase in the strength of copper alloys. Nano- and UFG structures in metals and alloys can be formed by the severe plastic deformation (SPD) methods [7]. The most popular SPD methods applied to copper alloys are high-pressure torsion [8], equal-channel angular pressing (ECAP) [9], multi-axial forging [10], etc. Thus, in [11], the authors managed to achieve a combination of relatively high strength and ductility in the Cu–30Zn alloy treated with ECAP. In this case, the ultimate tensile stress limit of the alloy was 565 MPa, the yield strength was 250 MPa, and the relative elongation was 20 %. In another work, after ECAP, it was possible to achieve significant strengthening of the Cu–30Zn alloy ($\sigma_{0.2}$ =542 MPa, σ_B =692 MPa) accompanied by a strong drop in ductility (up to δ =5.6 %) [11]. However, despite the advantages of SPD methods for strengthening metals and alloys, their application in industry is still hindered. Therefore, the development of processing modes that allow obtaining a UFG structure in copper alloys without using SPD methods is an urgent task.

In copper alloys, it is possible to obtain a UFG structure by using traditional deformation methods. For example, in work [12], a UFG structure was obtained in Cu–30Zn brass using cryogenic rolling followed by recrystallization annealing. In this case, a decrease in the average grain size to 0.5 μ m with a proportion of high-angle boundaries equal to 90 % made it possible to double the strength of the original alloy. Another traditional de-

formation method successfully used to improve the physical and mechanical properties of materials by creating a UFG structure is rotary swaging (RS). Traditionally, this method is used to manufacture hollow and solid, cylindrical and stepped shafts and axles with a round and faceted cross-section, therefore, its manufacturing application is not difficult, unlike SPD methods [13]. Currently, rotary swaging is successfully used to refine the structure of structural titanium [14; 15] and aluminium [16] alloys, steels [17] and other materials. Previously, we have already demonstrated the potential of rotary swaging for producing a UFG structure in copper alloys: thus, studies were conducted on the influence of rotary swaging on the microstructure, mechanical properties and electrical conductivity of Cu–0.8%Hf [18], Cu–0.77%Cr–0.86%Hf [19] and Cu–0.5%Cr–0.08%Zr [20; 21] alloys. In these alloys, due to the formed UFG structure, as well as the deposition of particles rich in Cr, Zr and Hf, the strength and electrical conductivity increase significantly with a simultaneous decrease in ductility.

The aim of the work is to study the influence of rotary swaging and subsequent annealing on the structure and mechanical properties of single-phase L68 brass. It is expected that the combination of rotary swaging and subsequent annealing will allow producing an alloy with improved strength and ductility.

METHODS

The material of the study was L68 grade brass. For smelting the studied alloy, M0b grade copper and Ts0 grade zinc were used as charge materials. The alloy was smelted in an induction furnace; casting was carried out in a water-cooled cast-iron mold with a diameter of 52 mm and a height of 200 mm. The chemical composition was determined using X-ray fluorescence analysis on a BRUKER S8 Tiger (series 2, Germany) sequential X-ray fluorescence wave-dispersive spectrometer in a vacuum according to the standard technique using the QUANT-EXPRESS software (Bruker, Germany). According to the analysis, the studied alloy consisted of 68±0.21 wt. % of Cu and 32±0.13 wt. % of Zn. Then, the resulting ingot was subjected to hot pressing at a temperature of 630 °C to a final diameter of 20 mm. Then, the rod was annealed at 800 °C for 2 h, followed by quenching in water.

Rotary swaging was performed at room temperature using an RKM 2129.02 two-die rotary swaging machine. Before rotary swaging, the rod was mechanically turned to 19 mm (initial diameter). Rotary swaging was performed in 10 passes with an intermediate reduction in the rod diame-

ter from 0.6 to 1.5 mm, depending on the stage of deformation to a final diameter of 6 mm.

The degree of deformation (ε) was determined by the formula

$$\varepsilon = \ln \frac{A_0}{A_f},$$

where A_0 is the initial cross-sectional area of the blank;

A_f is the final cross-sectional area of the blank.

Therefore, the degree of deformation corresponding to the final diameter of the rod of 6 mm was equal to 2.31.

The microstructure before and after rotary swaging was studied at low magnifications using an ADF I350 optical microscope (ADF OPTICS Co. LTD, China). The microstructure after rotary swaging was analysed in the longitudinal section of the rod, parallel to the deformation direction. The microstructure after rotary swaging was studied using transmission electron microscopy (TEM). TEM analysis was performed using a JEOL JEM 2100 microscope (Japan) at an accelerating voltage of 200 kV. Samples for transmission microscopy were prepared by electrolytic polishing on a TenuPol 5 installation (Denmark) using an electrolyte containing HNO_3 and CH_3OH at a voltage of 19.5 V and a temperature of -25°C . The size of the structural components was determined by the random linear intercept method in the Digimizer software environment.

The structural phase transitions were studied by differential scanning calorimetry (DSC) on a NETZSCH DSC 404 F3 Pegasus device (NETZSCH, Germany) with linear heating in the temperature range of $150\text{--}700^\circ\text{C}$ in a protective argon atmosphere at a rate of 10 K/min in corundum crucibles. To understand better the reactions occurring during heating of the studied samples, overlapping peaks were separated. The obtained experimental data were described as a superposition of Gaussian peaks, or Gaussians, meaning the addition of several Gaussian functions. Origin Pro 2021 software was used to perform peak separation analysis. The resulting function was obtained,

which had several maxima describing the transformations occurring during heating.

For uniaxial tensile tests, flat samples with a working part length of 5.75 mm, a width of 2 mm and a thickness of 1 mm were prepared. Mechanical tests were carried out at room temperature on an Instron 3382 testing machine (UK) at a constant loading rate of 1 mm/min. At least three samples were tested for each alloy state. Hardness was measured by the Brinell method on an IT 5010-01 testing machine (Russia) with a steel indenter diameter of 2.5 mm under a load of 62.5 kg, holding time of 30 s.

RESULTS

Fig. 1 shows that the structure of L68 brass in the quenched state consists of large α -phase grains $500\text{--}600\ \mu\text{m}$ in size and annealing twins $10\text{--}70\ \mu\text{m}$ in size. The microstructure is significantly transformed during rotary swaging. After rotary swaging, bands about $45\ \mu\text{m}$ wide elongated along the swaging direction are formed.

After rotary swaging, a UFG structure is formed inside the elongated α -phase grains (Fig. 2 a). This UFG structure consists of deformation twins from several tens to 200 nm in width (Fig. 2 b), subgrains $300\text{--}400\ \text{nm}$ in size, the boundaries of which are lined up with wide dislocation walls (Fig. 2 c), and shear bands $400\text{--}500\ \text{nm}$ in width (Fig. 2 a). It should also be noted that the formation of subgrains occurs mostly inside the shear bands (Fig. 2 a).

Fig. 3 combines the original experimental data, the individual obtained approximation peaks for the studied alloys, and a new resulting line (cumulative curve) of the approximation of overlapping peaks based on the estimated values. One can see that the new fitted profile is almost identical to the experimental one (Fig. 3), which reflects the accuracy of the peak separation procedure used in this analysis.

The DSC analysis of the alloy curve revealed the presence of five heat absorption peaks: two small peaks corresponding to temperatures of ~ 213 and $\sim 301^\circ\text{C}$, the maximum peak at $\sim 433^\circ\text{C}$, and peaks at ~ 560 and $\sim 626^\circ\text{C}$

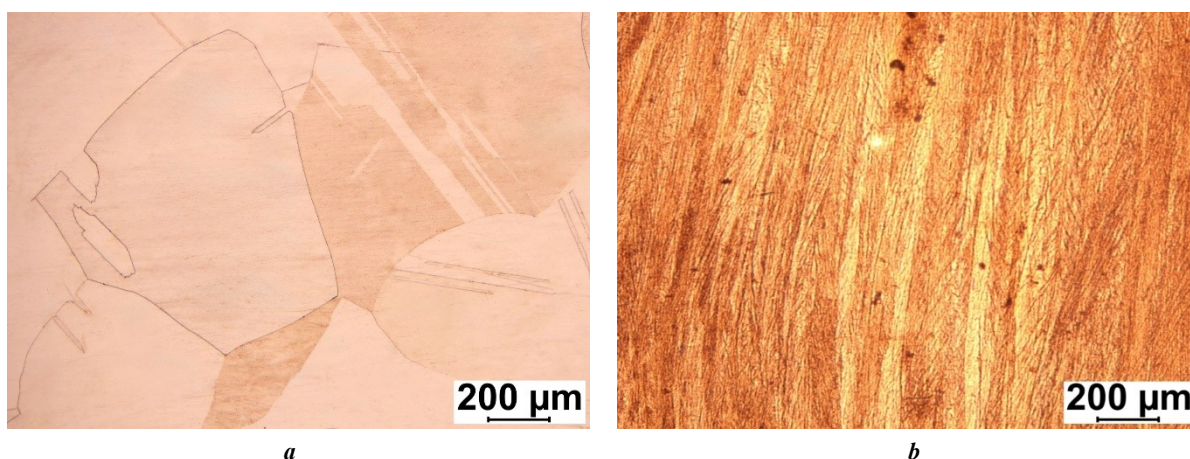


Fig. 1. Microstructure of L68 brass in the quenched state (a) and after rotary swaging at room temperature (b)

Рис. 1. Микроструктура латуни Л68 в закаленном состоянии (a) и после ротационнойковки при комнатной температуре (b)

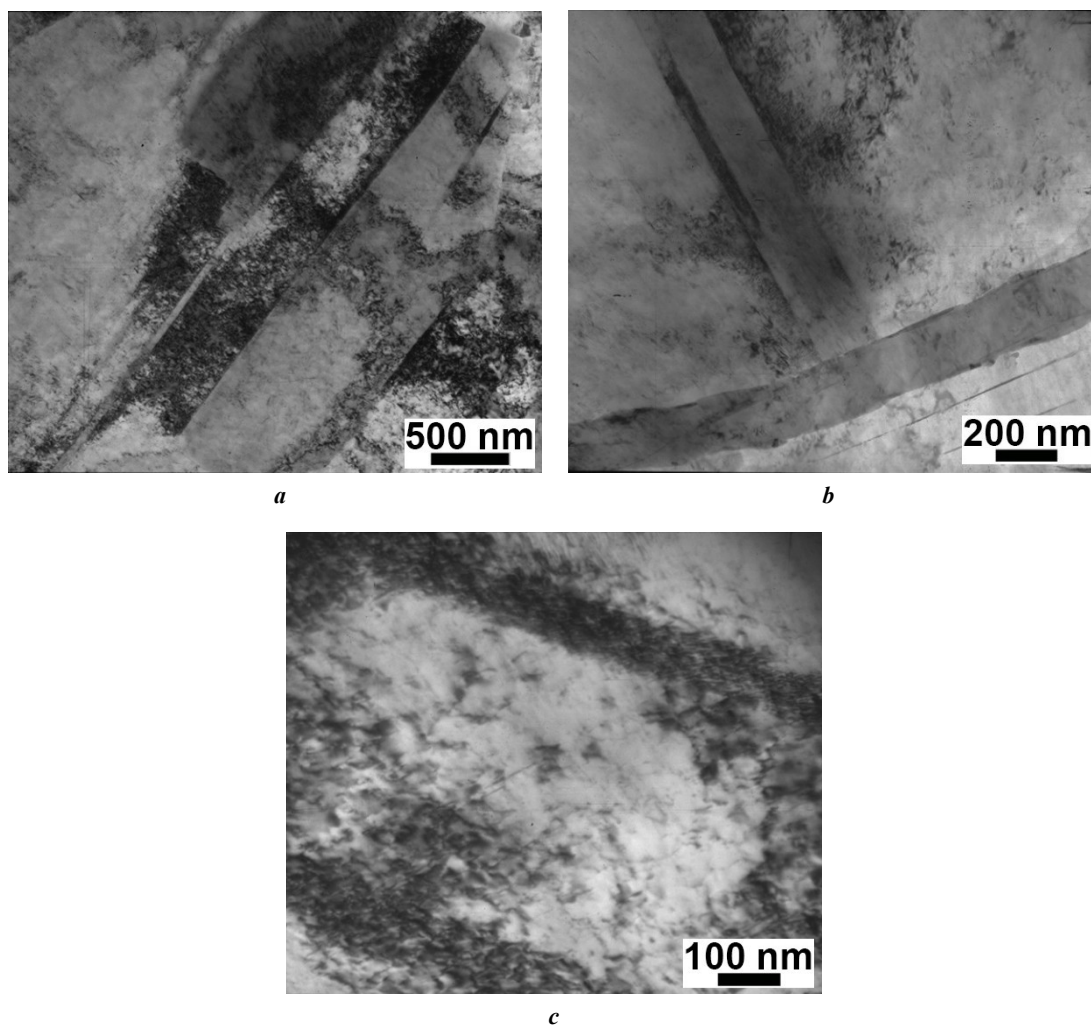


Fig. 2. TEM images of L68 brass after rotary swaging: alloy structure at magnifications of $\times 25,000$ (a), $\times 50,000$ (b) and $\times 100,000$ (c)

Рис. 2. ПЭМ-изображения латуни Л68 после ротационнойковки: структура сплава при увеличениях $\times 25\,000$ (a), $\times 50\,000$ (b) и $\times 100\,000$ (c)

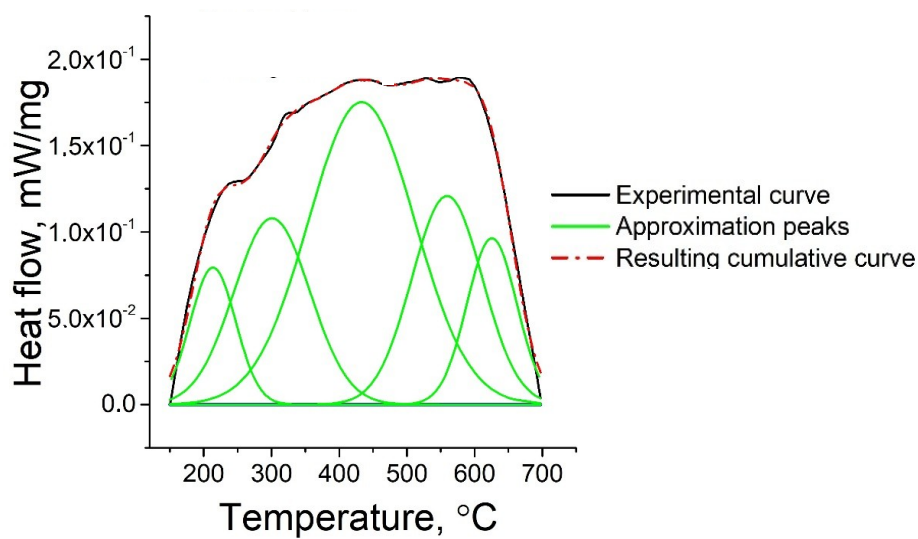


Fig. 3. Dependence of heat flow on heating temperature for L68 brass after rotary swaging

Рис. 3. Зависимость теплового потока от температуры нагрева для латуни Л68 после ротационнойковки

(Fig. 3). Based on the obtained results, the temperature regimes of 450, 500, and 550 °C were determined for subsequent annealing of L68 brass after rotary swaging. The choice of temperatures was based on the fact that structural and phase transformations should already occur at these temperatures. In this case, temperatures above 550 °C were not taken into account to avoid rapid grain growth.

It can be seen from Fig. 4 that additional annealing of the alloy after rotary swaging leads to a decrease in hardness, the higher the heating temperature. At the same time, in the range of 30–240 min, the holding time does not have a significant effect on the hardness values.

After quenching, the alloy demonstrates high ductility values with relatively low strength properties (Fig. 5). Carrying out rotary swaging with a degree of deformation of 2.31 significantly increases the values of strength characteristics, while the elongation decreases. After additional annealing, the strength characteristics decrease compared to the values after rotary swaging, but relative to the quenched state, the ultimate tensile stress limit, offset yield strength and elongation increase.

Table 1 shows that rotary swaging at $\epsilon=2.31$ resulted in a significant increase in strength with an increase in the values of $\sigma_{0.2}$ and σ_B by more than 10 and 3 times, respectively, while δ decreased by more than 6 times.

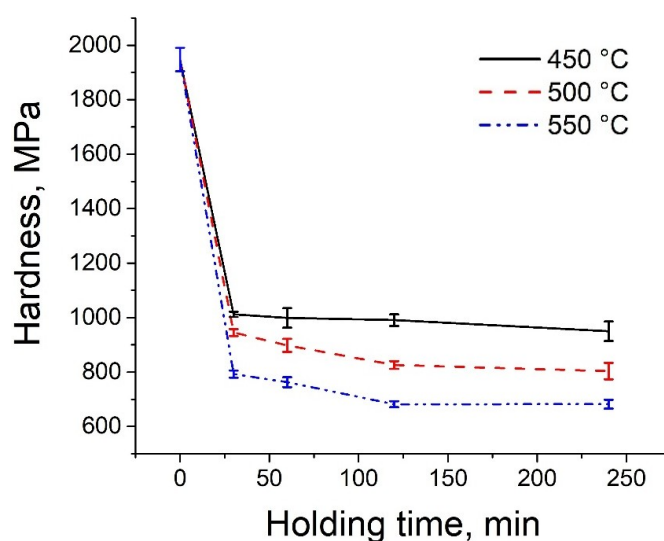


Fig. 4. Dependence of the hardness of L68 brass after rotary swaging on the temperature and heating time
Рис. 4. Зависимость твердости латуни Л68 после ротационной ковки от температуры и времени нагрева

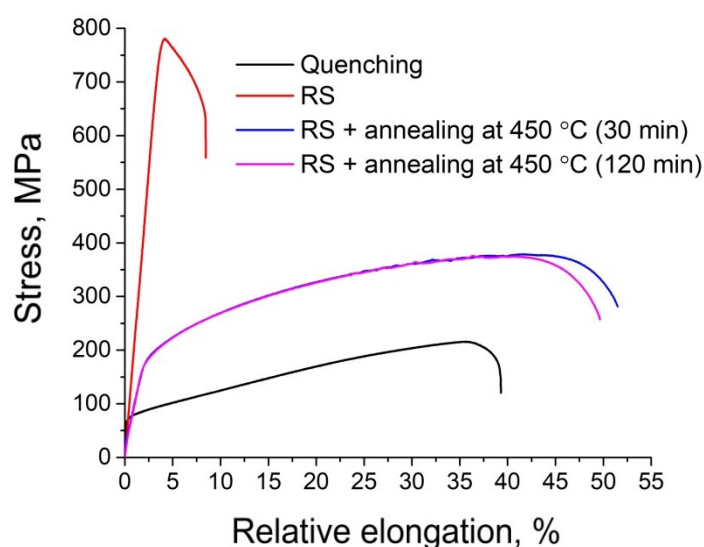


Fig. 5. Stress-strain curves of L68 brass in different states
Рис. 5. Кривые растяжения латуни Л68 в различных состояниях

Table 1. Mechanical properties of L68 brass in different states
Таблица 1. Механические свойства латуни Л68 в различных состояниях

State		$\sigma_{0.2}$, MPa	σ_B , MPa	δ , %
Quenching		72±4	222±13	39.9±3.8
Rotary swaging at $\epsilon=2.31$	before heating	754±5	775±6	6.3±0.4
	450 °C (30 min)	180±2	382±4	49.1±1.4
	450 °C (2 h)	172±3	374±4	49.9±2.8

Additional annealing at 450 °C for 30 and 120 min after rotary swaging contributed to a decrease in strength properties and an increase in ductility. However, relative to the initial state (after quenching), the offset yield strength increased on average by ~ 2.5 times, the ultimate tensile stress limit by ~ 1.7 times, and the elongation increased by 10. The properties after annealing for 30 and 120 min were approximately equal.

The structure of L68 brass after rotary swaging and additional annealing consists predominantly of fine equiaxed grains (Fig. 5). After annealing for 30 min, the average size is $3.1 \pm 0.4 \mu\text{m}$; with an increase in the heating duration to 120 min, the grains increase slightly to $4.5 \pm 0.8 \mu\text{m}$. It should also be noted that individual twins no more than $1 \mu\text{m}$ wide are formed inside the recrystallized grains (Fig. 6).

DISCUSSION

The study of the influence of cold rotary swaging and subsequent annealing on the structure and mechanical properties of L68 brass showed that rotary swaging leads to the formation of a microstructure in the alloy, which is

elongated along the direction of deformation (Fig. 1), as well as to the formation of a UFG microstructure inside the elongated grains and a significant increase in the density of crystal lattice defects (Fig. 2). Such a change in the microstructure leads to a significant increase in the strength of the alloy (yield strength and ultimate tensile stress limit increase by ~ 10 and ~ 3.5 times, respectively), but greatly reduces its ductility (δ decreases from 39.9 ± 3.8 to 6.3 ± 0.4 %).

The conducted DSC analysis showed that all the identified transformations occur with energy absorption (Fig. 3). Thus, the first peaks on swaged brass (~ 213 and ~ 301 °C) probably correspond to the ongoing processes of polygonisation and recovery. Similar results were obtained during the DSC analysis of cold-formed wire made of LS59-1 lead brass, where the authors revealed the occurrence of these processes in the temperature range of 115–235 °C [22]. The next peak on the curve for the swaged alloy, corresponding to ~ 433 °C, is probably associated with the onset of recrystallization processes. It is known that in deformed pure copper, the recrystallization process begins to occur at 250–350 °C [23; 24]. The recrystallisation onset temperature

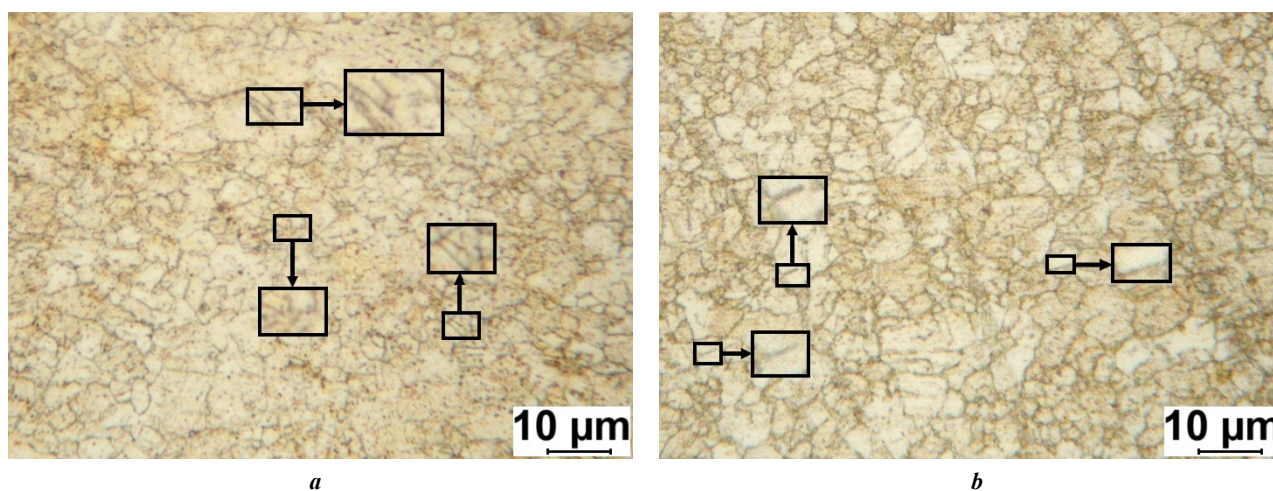


Fig. 6. Microstructure of L68 brass after rotary swaging at room temperature and subsequent annealing for 30 min (a) and 2 h (b). Arrows indicate twins

Рис. 6. Микроструктура латуни Л68 после ротационной ковки при комнатной температуре и последующего отжига в течение 30 мин (a) и 2 ч (b). Стрелки указывают на двойники

in this case depends on the purity of copper, the degree of deformation and the heating rate of the samples during the study. The addition of alloying elements increases the recrystallization temperature, in this case to ~ 433 °C. The fact that recrystallization occurs at this temperature is also confirmed by microstructural studies (Fig. 6). Thus, annealing of the alloy at 450 °C causes the formation of small equiaxed grains with individual twins. In this case, increasing the annealing time from 30 min to 2 h has little effect on the size of the forming grain, causing only a slight increase from 3.1 ± 0.4 to 4.5 ± 0.8 μm . In this case, the peaks corresponding to ~ 560 and ~ 626 °C are apparently associated either with the further course of primary recrystallization, or with the onset of collective and secondary recrystallization.

The formation of a recrystallized structure after annealing caused a significant decrease in the strength of L68 brass relative to the swaged state (Fig. 5, Table 1). Thus, the modulus of rupture in this case decreased by ~ 4.2 times and the ultimate tensile stress limit – by ~ 2 times. However, it is worth noting that the obtained values of the strength characteristics significantly exceed the values obtained for the quenched alloy: by ~ 2.5 and ~ 1.7 times for $\sigma_{0.2}$ and σ_B , respectively. In this case, the relative elongation values increase both in comparison with the swaged state (by ~ 7.9 times) and with respect to the quenched state (by ~ 10 %). It is worthy of note that the mechanical properties of L68 brass annealed for 30 min and 2 h are practically the same. The increase in the alloy strength after rotary swaging is largely related to the refinement of the alloy microstructure and an increase in the dislocation density.

As is known, the increase in the strength of metals and alloys is mainly influenced by such factors as grain size, the presence of second-phase particles, an increase in the density of crystal lattice defects, in particular dislocations, and the formation of a solid solution [25]. In the study, the presence of second-phase particles was not detected in any of the alloy states, so the contribution of this mechanism can be neglected. On the other hand, the alloy contains 32 ± 0.13 wt. % of Zn, which is completely dissolved in the copper matrix, forming a solid solution. The presence of zinc increases the strength characteristics of pure copper. However, as was said above, the alloy structure in all three states (quenched, swaged and annealed) consists of grains of a solid solu-

tion of zinc in copper of different sizes. This means that the contribution of the solid-solution mechanism to strengthening has a similar value for different states of the alloy. At the same time, rotary swaging leads to a significant grain refinement relative to the quenched state. Moreover, rotary swaging, like any deformation treatment, causes an increase in the dislocation density. For example, in [26] it was shown that during rotary swaging of the Cu–3.11Cr copper alloy, an increase in the dislocation density was observed from $3.87 \times 10^{11} \text{ m}^{-2}$ in the quenched state to $1.22 \times 10^{15} \text{ m}^{-2}$ after rotary swaging. Therefore, a significant increase in the dislocation density should also be expected in this experiment. Subsequent annealing at 450 °C leads both to an increase in the grain size to 3–5 μm due to the recrystallization and to a decrease in the dislocation density. In [26], the dislocation density of the Cu–3.11Cr alloy after rotary swaging with subsequent aging in the temperature range from 400 to 550 °C was also calculated. It was shown that heating in this temperature range leads to a slight decrease in the dislocation density to $9.41 \times 10^{14} \text{ m}^{-2}$. Grain growth and a decrease in dislocation density lead to a decrease in the contribution of these mechanisms to strengthening, which results in a decrease in the strength characteristics. At the same time, the formation of small, recrystallized grains and a decrease in dislocation density lead to a significant improvement in the ductility of the alloy. A similar picture was observed in [27] during annealing at various temperatures of the Cu–4.5 wt. % Al alloy subjected to rotary swaging. The authors showed that an increase in the temperature and duration of annealing leads to grain growth due to recrystallization, which has a positive effect on ductility.

Summarizing the obtained data, one can conclude that rotary swaging significantly increases the strength characteristics of L68 brass with a decrease in its ductility, while subsequent annealing allows obtaining a state with improved strength and ductility values relative to the quenched state. At the same time, both swaged and annealed alloys can be successfully used in the national economy to solve various tasks, since the mechanical characteristics obtained in the work are not inferior to the values regulated by GOST 494-90, GOST 1066-2015, GOST 931-90 and GOST 5362-78 or even exceed them (Table 2). For example, brass after rotary swaging can be used in

Table 2. Comparison of the requirements for processed L68 brass with the data obtained in the work
Таблица 2. Сравнение требований, предъявляемых к обработанной латуни Л68, с полученными в работе данными

Application / processing technique	σ_B , MPa	δ , %	Source
Soft wire (diameter 0.18–0.75 mm)	340	25	GOST 1066-2015
Hard-drawn wire (diameter 0.18–0.75 mm)	690–930	–	GOST 1066-2015
Cold-rolled hard band	430–540	10	GOST 931-90
Cold-rolled band	290–370	42	GOST 931-90
Cold-rolled band	290–340	50	GOST 5362-78

Table 2 continued
Продолжение таблицы 2

Application / processing technique	σ_B , MPa	δ , %	Source
Soft pipe	290	40	GOST 494-90
Half-hard pipe	340	35	GOST 494-90
Rotary swaging ($\epsilon=2.31$)	775 \pm 6	6.3 \pm 0.4	Current study
Rotary swaging ($\epsilon=2.31$) + heating 450 °C (30 min)	382 \pm 4	49.1 \pm 1.4	Current study

the manufacture of products that require high strength indicators, for example, those operating under abrasion conditions. L68 brass annealed after rotary swaging can be used in the manufacture of products for which a combination of strength and ductility is important, for example, plumbing products. Moreover, rotary swaging processing can be easily combined with other deformation methods, for example, with drawing. It is assumed that such a combination can lead to an additional improvement in mechanical characteristics.

CONCLUSIONS

1. Rotary swaging of L68 brass leads to the formation of α -phase grains elongated along the deformation direction, within which a UFG structure is formed consisting of subgrains 300–400 nm in size, deformation twins from several tens to 200 nm in width, and shear bands 400–500 nm in width.

2. After annealing at 450 °C, a recrystallised microstructure with a grain size of 3.1 \pm 0.4 and 4.5 \pm 0.8 μ m is formed for 30 min and 2 h of holding, respectively.

3. The formation of a UFG structure after rotary swaging leads to an increase in $\sigma_{0.2}$ and σ_B by ~ 10 and ~ 3.5 times, respectively, with a decrease in ductility from 39.9 \pm 3.8 to 6.3 \pm 0.4 %. Subsequent annealing at 450 °C resulted in a decrease in the strength characteristics of L68 brass due to recrystallization with a simultaneous increase in the relative elongation value to ~ 49 %.

4. The duration of annealing at 450 °C did not affect the value of the mechanical characteristics of the alloy.

REFERENCES

- Yang Kuo, Wang Yihan, Guo Mingxing, Wang Hu, Mo Yongda, Dong Xueguang, Lou Huafen. Recent development of advanced precipitation-strengthened Cu alloys with high strength and conductivity: a review. *Progress in Materials Science*, 2023, vol. 138, article number 101141. DOI: [10.1016/j.pmatsci.2023.101141](https://doi.org/10.1016/j.pmatsci.2023.101141).
- Mousavi S.E., Sonboli A., Naghshehkesh N., Meratian M., Salehi A., Sanayei M. Different behavior of alpha and beta phases in a Low Stacking Fault Energy copper alloy under severe plastic deformation. *Materials Science and Engineering: A*, 2020, vol. 788, article number 139550. DOI: [10.1016/j.msea.2020.139550](https://doi.org/10.1016/j.msea.2020.139550).
- Imai H., Li S., Atsumi H., Kosaka Y., Kojima A., Umeda J., Kondoh K. Mechanical Properties and Machinability of Extruded Cu-40% Zn Brass Alloy with Bismuth via Powder Metallurgy Process. *Transactions of JWRI*, 2009, vol. 38, no. 1, pp. 25–30. DOI: [10.18910/5502](https://doi.org/10.18910/5502).
- Basori I., Gadhu R., Sofyan B.T. Effects of deformation and annealing temperature on the microstructures and mechanical properties of Cu-32% Zn Brass. *ARNP Journal of Engineering and Applied Sciences*, 2016, vol. 11, no. 4, pp. 2741–2745. DOI: [10.4028/www.scientific.net/KEM.748.218](https://doi.org/10.4028/www.scientific.net/KEM.748.218).
- Galai M., Ouassir J., Ebn Touhami M., Nassali H., Benqlilou H., Belhaj T., Berrami K., Mansouri I., Oauki B. α -Brass and ($\alpha+\beta$) Brass Degradation Processes in Azrou Soil Medium Used in Plumbing Devices. *Journal of Bio-and Tribo-Corrosion*, 2017, vol. 3, no. 3, article number 30. DOI: [10.1007/s40735-017-0087-y](https://doi.org/10.1007/s40735-017-0087-y).
- Pelto-Huikko A., Salonen N., Latva M. Dezincification of faucets with different brass alloys. *Engineering Failure Analysis*, 2025, vol. 169, article number 109202. DOI: [10.1016/j.engfailanal.2024.109202](https://doi.org/10.1016/j.engfailanal.2024.109202).
- Valiev R.Z., Islamgaliev R.K., Alexandrov I.V. Bulk nanostructured materials from severe plastic deformation. *Progress in materials science*, 2000, vol. 45, no. 2, pp. 103–189. DOI: [10.1016/S0079-6425\(99\)00007-9](https://doi.org/10.1016/S0079-6425(99)00007-9).
- Vidilli A.L., Machado I.F., Edalati K., Botta W.J., Bolfarini C., Koga G.Y. Wear-resistant ultrafine severely deformed brass (Cu-30Zn). *Materials Letters*, 2024, vol. 377, article number 137465. DOI: [10.1016/j.matlet.2024.137465](https://doi.org/10.1016/j.matlet.2024.137465).
- Chen Jianqing, Su Yehan, Zhang Qiyu, Sun Jiapeng, Yang Donghui, Jiang Jinghua, Song Dan, Ma Aibin. Enhancement of strength-ductility synergy in ultrafine-grained Cu-Zn alloy prepared by ECAP and subsequent annealing. *Journal of Materials Research and Technology*, 2022, vol. 17, pp. 433–440. DOI: [10.1016/j.jmrt.2022.01.026](https://doi.org/10.1016/j.jmrt.2022.01.026).
- Shahriyari F., Shaeri M.H., Dashti A., Zarei Z., Noghani M.T., Cho Jae Hyung, Djavanroodi F. Evolution of mechanical properties, microstructure and texture and of various brass alloys processed by multi-directional forging. *Materials Science and Engineering: A*, 2022, vol. 831, article number 142149. DOI: [10.1016/j.msea.2021.142149](https://doi.org/10.1016/j.msea.2021.142149).
- Radhi H.N., Mohammed M.T., Aljassani A.M.H. Influence of ECAP processing on mechanical and wear properties of brass alloy. *Materials Today: Proceedings*, 2021, vol. 44, pp. 2399–2402. DOI: [10.1016/j.matpr.2020.12.461](https://doi.org/10.1016/j.matpr.2020.12.461).
- Konkova T., Mironov S., Korznikov A., Korznikova G., Myshlyayev M., Semiatin L. A two-step approach for producing an ultrafine-grain structure in Cu–30Zn brass.

- Materials Letters. *Materials Letters*, 2015, vol. 161, pp. 1–4. DOI: [10.1016/j.matlet.2015.08.025](https://doi.org/10.1016/j.matlet.2015.08.025).
13. Mao Qingzhong, Liu Yanfang, Zhao Yonghao. A review on mechanical properties and microstructure of ultrafine grained metals and alloys processed by rotary swaging. *Journal of Alloys and Compounds*, 2022, vol. 896, article number 163122. DOI: [10.1016/j.jallcom.2021.163122](https://doi.org/10.1016/j.jallcom.2021.163122).
 14. Naydenkin E.V., Mishin I.P., Zabudchenko O.V., Lykova O.N., Manisheva A.I. Structural-phase state and mechanical properties of β titanium alloy produced by rotary swaging with subsequent aging. *Journal of Alloys and Compounds*, 2023, vol. 935, article number 167973. DOI: [10.1016/j.jallcom.2022.167973](https://doi.org/10.1016/j.jallcom.2022.167973).
 15. Chuvil'deev V.N., Kopylov V.I., Nokhrin A.V. et al. Enhancement of the Strength and the Corrosion Resistance of a PT-7M Titanium Alloy Using Rotary Forging. *Russian Metallurgy (Metally)*, 2021, vol. 2021, no. 5, pp. 600–610. DOI: [10.1134/S0036029521050050](https://doi.org/10.1134/S0036029521050050).
 16. Mao Qingzhong, Wang Long, Nie Jinfeng, Zhao Yonghao. Optimizing strength and electrical conductivity of 6201 aluminum alloy wire through rotary swaging and aging processes. *Journal of Materials Processing Technology*, 2024, vol. 331, article number 118497. DOI: [10.1016/j.jmatprotec.2024.118497](https://doi.org/10.1016/j.jmatprotec.2024.118497).
 17. Dedyulina O.K., Salishchev G.A. Formation of ultrafine-grained structure in medium-carbon steel 40HGNM by swaging and its influence on mechanical properties. *Fundamental research*, 2013, no. 1-3, pp. 701–706. EDN: [PUUUVF](https://www.eidn.org/PUUUVF).
 18. Martynenko N.S., Bocharov N.R., Rybalchenko O.V., Prosvirnin D.V., Rybalchenko G.V., Kolmakov A.G., Morozov M.M., Yusupov V.S., Dobatkin S.V. Increase in the strength and electrical conductivity of a Cu–0.8 Hf alloy after rotary swaging and subsequent aging. *Russian Metallurgy (Metally)*, 2023, vol. 2023, no. 4, pp. 466–474. DOI: [10.1134/S0036029523040158](https://doi.org/10.1134/S0036029523040158).
 19. Martynenko N., Rybalchenko O., Straumal P. et al. Increasing strength and electrical conductivity of Cu–0.77% Cr–0.86% Hf alloy by rotary swaging and subsequent aging. *Journal of Materials Science*, 2024, vol. 59, pp. 5944–5955. DOI: [10.1007/s10853-024-09332-x](https://doi.org/10.1007/s10853-024-09332-x).
 20. Martynenko N., Rybalchenko O., Bodyakova A., Prosvirnin D., Rybalchenko G., Morozov M., Yusupov V., Dobatkin S. Effect of Rotary Swaging on the Structure, Mechanical Characteristics and Aging Behavior of Cu–0.5%Cr–0.08%Zr Alloy. *Materials*, 2023, vol. 16, no. 1, article number 105. DOI: [10.3390/ma16010105](https://doi.org/10.3390/ma16010105).
 21. Martynenko N.S., Bocharov N.R., Rybalchenko O.V., Bodyakova A.I., Morozov M.M., Leonova N.P., Yusupov V.S., Dobatkin S.V. Effect of rotary swaging and subsequent aging on the structure and mechanical properties of a Cu–0.5% Cr–0.08% Zr alloy. *Russian metallurgy (Metally)*, 2022, vol. 2022, no. 5, pp. 512–519. DOI: [10.1134/S0036029522050081](https://doi.org/10.1134/S0036029522050081).
 22. Illarionov A.G., Loginov Y.N., Stepanov S.I., Illarionova S.M., Radaev P.S. Variation of the Structure-and-Phase Condition and Physical and Mechanical Properties of Cold-Deformed Leaded Brass Under Heating. *Metal Science and Heat Treatment*, 2019, vol. 61, pp. 243–248. DOI: [10.1007/s11041-019-00408-z](https://doi.org/10.1007/s11041-019-00408-z).
 23. Chen Jian, Ma Xiao-guang, Li Jun, Yao Yu-hong, Yan Wen, Fan Xin-hui. New method for analyzing recrystallization kinetics of deformed metal by differential scanning calorimeter. *Journal of Central South University*, 2015, vol. 22, pp. 849–854. DOI: [10.1007/s11771-015-2592-9](https://doi.org/10.1007/s11771-015-2592-9).
 24. Benchabane G., Boumerzoug Z., Thibon I., Gloriant T. Recrystallization of pure copper investigated by calorimetry and microhardness. *Materials Characterization*, 2008, vol. 59, no. 10, pp. 1425–1428. DOI: [10.1016/j.matchar.2008.01.002](https://doi.org/10.1016/j.matchar.2008.01.002).
 25. Sitdikov V.D., Khafizova E.D., Polenok M.V. Microstructure and properties of the Zn–1%Li–2%Mg alloy subjected to severe plastic deformation. *Frontier Materials & Technologies*, 2023, no. 2, pp. 117–130. DOI: [10.18323/2782-4039-2023-2-64-7](https://doi.org/10.18323/2782-4039-2023-2-64-7).
 26. Mao Qingzhong, Wang Long, Nie Jinfeng, Zhao Yonghao. Enhancing strength and electrical conductivity of Cu–Cr composite wire by two-stage rotary swaging and aging treatments. *Composites Part B: Engineering*, 2022, vol. 231, article number 109567. DOI: [10.1016/j.compositesb.2021.109567](https://doi.org/10.1016/j.compositesb.2021.109567).
 27. Li Xingfu, Li Cong, Sun Lele, Gong Yulan, Pan Hongjiang, Tan Zhilong, Xu Lei, Zhu Xinkun. Enhancing strength-ductility synergy of Cu alloys with heterogeneous microstructure via rotary swaging and annealing. *Materials Science and Engineering: A*, 2025, vol. 920, article number 147501. DOI: [10.1016/j.msea.2024.147501](https://doi.org/10.1016/j.msea.2024.147501).

СПИСОК ЛИТЕРАТУРЫ

1. Yang Kuo, Wang Yihan, Guo Mingxing, Wang Hu, Mo Yongda, Dong Xueguang, Lou Huafen. Recent development of advanced precipitation-strengthened Cu alloys with high strength and conductivity: a review // *Progress in Materials Science*. 2023. Vol. 138. Article number 101141. DOI: [10.1016/j.pmatsci.2023.101141](https://doi.org/10.1016/j.pmatsci.2023.101141).
2. Mousavi S.E., Sonboli A., Naghshehkish N., Meratian M., Salehi A., Sanayei M. Different behavior of alpha and beta phases in a Low Stacking Fault Energy copper alloy under severe plastic deformation // *Materials Science and Engineering: A*. 2020. Vol. 788. Article number 139550. DOI: [10.1016/j.msea.2020.139550](https://doi.org/10.1016/j.msea.2020.139550).
3. Imai H., Li S., Atsumi H., Kosaka Y., Kojima A., Umeda J., Kondoh K. Mechanical Properties and Machinability of Extruded Cu–40% Zn Brass Alloy with Bismuth via Powder Metallurgy Process // *Transactions of JWRI*. 2009. Vol. 38. № 1. P. 25–30. DOI: [10.18910/5502](https://doi.org/10.18910/5502).
4. Basori I., Gadhu R., Sofyan B.T. Effects of deformation and annealing temperature on the microstructures and mechanical properties of Cu–32% Zn Brass // *ARPN Journal of Engineering and Applied Sciences*. 2016. Vol. 11. № 4. P. 2741–2745. DOI: [10.4028/www.scientific.net/KEM.748.218](https://doi.org/10.4028/www.scientific.net/KEM.748.218).
5. Galai M., Ouassir J., Ebn Touhami M., Nassali H., Benqlilou H., Belhaj T., Berrami K., Mansouri I., Oauki B. α -Brass and $(\alpha+\beta)$ Brass Degradation Processes in Azrou Soil Medium Used in Plumbing Devices // *Journal of Bio-and Tribo-Corrosion*. 2017. Vol. 3. № 3. Article number 30. DOI: [10.1007/s40735-017-0087-y](https://doi.org/10.1007/s40735-017-0087-y).
6. Peltto-Huikko A., Salonen N., Latva M. Dezincification of faucets with different brass alloys // *Engineering Failure Analysis*. 2025. Vol. 169. Article number 109202. DOI: [10.1016/j.engfailanal.2024.109202](https://doi.org/10.1016/j.engfailanal.2024.109202).

7. Valiev R.Z., Islamgaliev R.K., Alexandrov I.V. Bulk nanostructured materials from severe plastic deformation // *Progress in materials science*. 2000. Vol. 45. № 2. P. 103–189. DOI: [10.1016/S0079-6425\(99\)00007-9](https://doi.org/10.1016/S0079-6425(99)00007-9).
8. Vidilli A.L., Machado I.F., Edalati K., Botta W.J., Bolfarini C., Koga G.Y. Wear-resistant ultrafine severely deformed brass (Cu-30Zn) // *Materials Letters*. 2024. Vol. 377. Article number 137465. DOI: [10.1016/j.matlet.2024.137465](https://doi.org/10.1016/j.matlet.2024.137465).
9. Chen Jianqing, Su Yehan, Zhang Qiyu, Sun Jiapeng, Yang Donghui, Jiang Jinghua, Song Dan, Ma Aibin. Enhancement of strength-ductility synergy in ultrafine-grained Cu-Zn alloy prepared by ECAP and subsequent annealing // *Journal of Materials Research and Technology*. 2022. Vol. 17. P. 433–440. DOI: [10.1016/j.jmrt.2022.01.026](https://doi.org/10.1016/j.jmrt.2022.01.026).
10. Shahriyari F., Shaeri M.H., Dashti A., Zarei Z., Noghani M.T., Cho Jae Hyung, Djavanroodi F. Evolution of mechanical properties, microstructure and texture and of various brass alloys processed by multi-directional forging // *Materials Science and Engineering: A*. 2022. Vol. 831. Article number 142149. DOI: [10.1016/j.msea.2021.142149](https://doi.org/10.1016/j.msea.2021.142149).
11. Radhi H.N., Mohammed M.T. Aljassani A.M.H. Influence of ECAP processing on mechanical and wear properties of brass alloy // *Materials Today: Proceedings*. 2021. Vol. 44. P. 2399–2402. DOI: [10.1016/j.matpr.2020.12.461](https://doi.org/10.1016/j.matpr.2020.12.461).
12. Konkova T., Mironov S., Korznikov A., Korznikova G., Myshlyaev M., Semiatin L. A two-step approach for producing an ultrafine-grain structure in Cu–30Zn brass. *Materials Letters*. 2015. Vol. 161. P. 1–4. DOI: [10.1016/j.matlet.2015.08.025](https://doi.org/10.1016/j.matlet.2015.08.025).
13. Mao Qingzhong, Liu Yanfang, Zhao Yonghao. A review on mechanical properties and microstructure of ultrafine grained metals and alloys processed by rotary swaging // *Journal of Alloys and Compounds*. 2022. Vol. 896. Article number 163122. DOI: [10.1016/j.jallcom.2021.163122](https://doi.org/10.1016/j.jallcom.2021.163122).
14. Naydenkin E.V., Mishin I.P., Zabudchenko O.V., Lykova O.N., Manisheva A.I. Structural-phase state and mechanical properties of β titanium alloy produced by rotary swaging with subsequent aging // *Journal of Alloys and Compounds*. 2023. Vol. 935. Article number 167973. DOI: [10.1016/j.jallcom.2022.167973](https://doi.org/10.1016/j.jallcom.2022.167973).
15. Chuvil'deev V.N., Kopylov V.I., Nokhrin A.V. et al. Enhancement of the Strength and the Corrosion Resistance of a PT-7M Titanium Alloy Using Rotary Forging // *Russian Metallurgy (Metally)*. 2021. Vol. 2021. № 5. P. 600–610. DOI: [10.1134/S0036029521050050](https://doi.org/10.1134/S0036029521050050).
16. Mao Qingzhong, Wang Long, Nie Jinfeng, Zhao Yonghao. Optimizing strength and electrical conductivity of 6201 aluminum alloy wire through rotary swaging and aging processes // *Journal of Materials Processing Technology*. 2024. Vol. 331. Article number 118497. DOI: [10.1016/j.jmatprotec.2024.118497](https://doi.org/10.1016/j.jmatprotec.2024.118497).
17. Дедюлина О.К., Салищев Г.А. Формирование ультрамелкозернистой структуры в среднеуглеродистой стали 40ХГНМ ротационной ковкой и ее влияние на механические свойства // *Фундаментальные исследования*. 2013. № 1-3. С. 701–706. EDN: [PUUIVF](https://www.edn.ru/PUUIVF).
18. Martynenko N.S., Bochvar N.R., Rybalchenko O.V., Prosvirnin D.V., Rybalchenko G.V., Kolmakov A.G., Morozov M.M., Yusupov V.S., Dobatkin S.V. Increase in the strength and electrical conductivity of a Cu–0.8 Hf alloy after rotary swaging and subsequent aging // *Russian Metallurgy (Metally)*. 2023. Vol. 2023. № 4. P. 466–474. DOI: [10.1134/S0036029523040158](https://doi.org/10.1134/S0036029523040158).
19. Martynenko N., Rybalchenko O., Straumal P. et al. Increasing strength and electrical conductivity of Cu–0.77% Cr–0.86% Hf alloy by rotary swaging and subsequent aging // *Journal of Materials Science*. 2024. Vol. 59. P. 5944–5955. DOI: [10.1007/s10853-024-09332-x](https://doi.org/10.1007/s10853-024-09332-x).
20. Martynenko N., Rybalchenko O., Bodyakova A., Prosvirnin D., Rybalchenko G., Morozov M., Yusupov V., Dobatkin S. Effect of Rotary Swaging on the Structure, Mechanical Characteristics and Aging Behavior of Cu–0.5%Cr–0.08%Zr Alloy // *Materials*. 2023. Vol. 16. № 1. Article number 105. DOI: [10.3390/ma16010105](https://doi.org/10.3390/ma16010105).
21. Мартыненко Н.С., Бочвар Н.Р., Рыбальченко О.В., Бодякова А.И., Морозов М.М., Леонова Н.П., Юсупов В.С., Добаткин С.В. Влияние ротационнойковки и последующего старения на структуру и механические свойства сплава Cu–0,5%Cr–0,08%Zr // *Металлы*. 2022. № 3. С. 56–64. EDN: [MQEZDH](https://www.edn.ru/MQEZDH).
22. Illarionov A.G., Loginov Y.N., Stepanov S.I., Illarionova S.M., Radaev P.S. Variation of the Structure-and-Phase Condition and Physical and Mechanical Properties of Cold-Deformed Lead Brass Under Heating // *Metal Science and Heat Treatment*. 2019. Vol. 61. P. 243–248. DOI: [10.1007/s11041-019-00408-z](https://doi.org/10.1007/s11041-019-00408-z).
23. Chen Jian, Ma Xiao-guang, Li Jun, Yao Yu-hong, Yan Wen, Fan Xin-hui. New method for analyzing recrystallization kinetics of deformed metal by differential scanning calorimeter // *Journal of Central South University*. 2015. Vol. 22. P. 849–854. DOI: [10.1007/s11771-015-2592-9](https://doi.org/10.1007/s11771-015-2592-9).
24. Benchabane G., Boumerzoug Z., Thibon I., Gloriant T. Recrystallization of pure copper investigated by calorimetry and microhardness // *Materials Characterization*. 2008. Vol. 59. № 10. P. 1425–1428. DOI: [10.1016/j.matchar.2008.01.002](https://doi.org/10.1016/j.matchar.2008.01.002).
25. Ситдииков В.Д., Хафизова Э.Д., Поленок М.В. Микроструктура и свойства сплава Zn–1%Li–2%Mg, подвергнутого интенсивной пластической деформации // *Frontier Materials & Technologies*. 2023. № 2. С. 117–130. DOI: [10.18323/2782-4039-2023-2-64-7](https://doi.org/10.18323/2782-4039-2023-2-64-7).
26. Mao Qingzhong, Wang Long, Nie Jinfeng, Zhao Yonghao. Enhancing strength and electrical conductivity of Cu–Cr composite wire by two-stage rotary swaging and aging treatments // *Composites Part B: Engineering*. 2022. Vol. 231. Article number 109567. DOI: [10.1016/j.compositesb.2021.109567](https://doi.org/10.1016/j.compositesb.2021.109567).
27. Li Xingfu, Li Cong, Sun Lele, Gong Yulan, Pan Hongjiang, Tan Zhilong, Xu Lei, Zhu Xinkun. Enhancing strength-ductility synergy of Cu alloys with heterogeneous microstructure via rotary swaging and annealing // *Materials Science and Engineering: A*. 2025. Vol. 920. Article number 147501. DOI: [10.1016/j.msea.2024.147501](https://doi.org/10.1016/j.msea.2024.147501).

Влияние ротационнойковки и последующегоотжига на структуру и механические свойства однофазной латуни Л68

Чистюхина Элеонора Ивановна^{*1,2,4}, инженер-исследователь

лаборатории металловедения цветных и легких металлов

им. академика А.А. Бочвара, магистрант кафедры металловедения и физики прочности

Мартыненко Наталья Сергеевна^{1,5}, кандидат технических наук, старший научный сотрудник

лаборатории металловедения цветных и легких металлов им. академика А.А. Бочвара

Рыбалченко Ольга Владиславовна^{1,6}, кандидат технических наук, ведущий научный сотрудник

лаборатории металловедения цветных и легких металлов им. академика А.А. Бочвара

Никитин Иван Сергеевич^{3,7}, кандидат технических наук, младший научный сотрудник

лаборатории механических свойств наноструктурных и жаропрочных материалов

Лукьянова Елена Александровна^{1,8}, кандидат технических наук, старший научный сотрудник

лаборатории металловедения цветных и легких металлов им. академика А.А. Бочвара

Горбенко Артем Дмитриевич^{1,9}, инженер-исследователь лаборатории

прочности и пластичности металлических и композиционных материалов и наноматериалов

Темралиева Диана Ривовна^{1,10}, инженер-исследователь

лаборатории металловедения цветных и легких металлов им. академика А.А. Бочвара

Страумал Петр Борисович^{1,11}, кандидат физико-математических наук, старший научный сотрудник

лаборатории металловедения цветных и легких металлов им. академика А.А. Бочвара

Андреев Владимир Александрович^{1,12}, кандидат технических наук, ведущий научный сотрудник

лаборатории пластической деформации металлических материалов

Добаткин Сергей Владимирович^{1,13}, доктор технических наук, профессор,

заведующий лабораторией металловедения цветных и легких металлов им. академика А.А. Бочвара

¹Институт металлургии и материаловедения им. А.А. Байкова РАН, Москва (Россия)

²Университет науки и технологий МИСИС, Москва (Россия)

³Белгородский государственный национальный исследовательский университет, Белгород (Россия)

*E-mail: e.chistyuhina@mail.ru

⁴ORCID: <https://orcid.org/0009-0009-2192-3246>

⁵ORCID: <https://orcid.org/0000-0003-1662-1904>

⁶ORCID: <https://orcid.org/0000-0002-0403-0800>

⁷ORCID: <https://orcid.org/0000-0002-5417-9857>

⁸ORCID: <https://orcid.org/0000-0001-7122-6427>

⁹ORCID: <https://orcid.org/0000-0002-3357-4049>

¹⁰ORCID: <https://orcid.org/0000-0002-8392-7826>

¹¹ORCID: <https://orcid.org/0000-0001-6192-5304>

¹²ORCID: <https://orcid.org/0000-0003-3937-1952>

¹³ORCID: <https://orcid.org/0000-0003-4232-927X>

Поступила в редакцию 30.06.2025

Пересмотрена 18.07.2025

Принята к публикации 25.08.2025

Аннотация: Медные сплавы на основе системы Cu–Zn, в частности латунь Л68, являются перспективными конструкционными материалами. Однако для повышения их надежности и расширения области применения необходимо повышать их прочностные характеристики. В работе изучалось влияние комбинации ротационнойковки (РК) и последующего отжига на структуру, прочность и пластичность латуни Л68. Для этого проведены исследования микроструктуры сплава в закаленном и деформированном состояниях, механические испытания на одноосное растяжение, исследование твердости по методу Бринелля, а также оценка структурно-фазовых переходов методом дифференциальной сканирующей калориметрии. Установлено, что в процессе РК происходит формирование не только вытянутых вдоль направления деформации зерен α -фазы, но и ультрамелкозернистой структуры внутри них, состоящей из субзерен, двойников деформации и полос сдвига. Последующий отжиг при 450 °С приводит к росту размера зерна до 3–5 мкм за счет протекания статической рекристаллизации. После РК наблюдается рост условного предела текучести ($\sigma_{0,2}$) и предела прочности (σ_B) в ~10 и ~3,5 раза соответственно при снижении значения относительного удлинения более чем в 6 раз. Последующий отжиг при 450 °С, вызвавший формирование рекристаллизованной структуры, привел к снижению прочностных характеристик латуни Л68 относительно деформированного состояния при одновременном росте значения относительного удлинения по сравнению как с деформированным, так и с исходным состоянием сплава. Однако стоит отметить, что $\sigma_{0,2}$ и σ_B латуни Л68 после РК и последующего отжига при 450 °С превышают значения для зака-

ленного сплава в среднем в $\sim 2,5$ и в $\sim 1,7$ раза соответственно и превышают значения, регламентированные ГОСТ 494-90, ГОСТ 1066-2015, ГОСТ 931-90 и ГОСТ 5362-78.

Ключевые слова: латунь Л68; ротационная ковка; ультрамелкозернистая структура; рекристаллизация; прочность; пластичность.

Благодарности: Работа выполнена при финансовой поддержке государственного задания № 075-00319-25-00.

Статья подготовлена по материалам докладов участников XII Международной школы «Физическое материаловедение» (ШФМ-2025), Тольятти, 15–19 сентября 2025 года.

Для цитирования: Чистюхина Э.И., Мартыненко Н.С., Рыбальченко О.В., Никитин И.С., Лукьянова Е.А., Горбенко А.Д., Темралиева Д.Р., Страумал П.Б., Андреев В.А., Добаткин С.В. Влияние ротационной ковки и последующего отжига на структуру и механические свойства однофазной латуни Л68 // Frontier Materials & Technologies. 2025. № 3. С. 113–124. DOI: 10.18323/2782-4039-2025-3-73-9.

Strength of joints produced by ultrasonic spot welding of copper plates using tools with different tooth heights

Elvina R. Shayakhmetova, junior researcher

Institute for Metals Superplasticity Problems of RAS, Ufa (Russia)

E-mail: elvinar@imsp.ru

ORCID: <https://orcid.org/0000-0002-1659-9922>

Received 30.06.2025

Revised 21.07.2025

Accepted 12.08.2025

Abstract: Ultrasonic welding of metals is an energy-efficient, environmentally friendly technology that allows producing solid-state joints between thin blanks. The widespread use of this technology is hampered by the low strength of the resulting joints and the instability of their properties. One of the ways to improve strength characteristics is to develop a welding tool that ensures stable transmission of ultrasonic vibration energy to the joint zone. For this purpose, a relief with teeth or pyramids of different shapes and heights is applied to the surface of the welding tip and anvil. This paper presents data on the fracture load and fracture energy of lap joints produced by ultrasonic spot welding of copper plates using tools with a tooth height of 0.1 and 0.4 mm. Ultrasonic welding was carried out with a frequency of 20 kHz and a vibration amplitude of 18–20 μm , the welding duration was 2 and 3 s, the clamping force was 2.5 kN. The paper considers the features of the fracture of the produced joints and the distribution of normal strains in the weld spot, and results of calculation of stress intensity factors in its vicinity. It is shown that after ultrasonic welding for 3 s, the strength characteristics of the joints produced with different tools reach the highest values, they are close in magnitude, but the experimental data scatter is half as much after welding with a tool with small teeth. The joints produced with such a tool fractured along the interface of the joint, and after welding with a tool with large teeth, the fracture developed with nugget pull-out, which is explained by an increase in the stress intensity factor at the tip of the concentrator surrounding the weld spot.

Keywords: copper; ultrasonic welding of metals; solid-state joint; joint strength; welding tool relief; stress intensity factor.

Acknowledgments: This work was carried out within the state assignment of IMSP RAS (No. 124022900006-2). Part of experimental data was obtained during the accomplishment of a project supported by the Russian Science Foundation (grant No. 22-19-00617, <https://rscf.ru/project/22-19-00617/>). Electron microscopic studies and mechanical tests were carried out on the facilities of shared services center of IMSP RAS “Structural and Physical-Mechanical Studies of Materials”.

The author expresses deep gratitude to M.A. Murzinova, PhD (Engineering), and A.A. Nazarov, Doctor of Sciences (Physics and Mathematics), for their assistance in conducting the research and a discussion of the results obtained.

The paper was written on the reports of the participants of the XII International School of Physical Materials Science (SPM-2025), Togliatti, September 15–19, 2025.

For citation: Shayakhmetova E.R. Strength of joints produced by ultrasonic spot welding of copper plates using tools with different tooth heights. *Frontier Materials & Technologies*, 2025, no. 3, pp. 125–136. DOI: 10.18323/2782-4039-2025-3-73-10.

INTRODUCTION

Ultrasonic welding (USW) of metals is an energy-efficient, environmentally friendly technology used primarily to produce electrical contacts in the automotive and electrical industries [1]. Currently, the USW method is used to produce joints of metal blanks made of sheets, tapes, foils, and wires with a cross-section of up to 3 mm.

Despite a number of advantages, the widespread use of ultrasonic welding of metals is limited due to the low strength of the resulting joints and the wide scatter of mechanical test results [2; 3]. This is largely associated with the small magnitude and uneven distribution of strains over the area of the weld spot, which are necessary to form and increase the area of microwelds [4; 5].

The distribution and magnitude of strain depend on the temperature in the joint zone, the thickness of the welded blanks, their thermophysical and mechanical properties, and conditions of USW, primarily, the input welding energy, which is proportional to the time of USW, and the compressive pressure [6–8]. At the selected pressure at initial stages of ultrasonic welding, the upper plate should slide over the lower one, ensuring the removal of oxide films and contaminants from contacting surfaces, as well as their heating due to friction. At final stages of the process, the same pressure should be sufficient to heal discontinuities in the joint zone of metals heated to 0.4–0.8 of melting temperature [1; 3].

To transmit the ultrasonic vibration energy from the sonotrode to the joining zone, knurls of different shapes

and depths are applied to the surface of the welding tip and anvil [1; 9–11]. A relief formed by pyramids or teeth, the height and periodicity of which amount fractions of a millimeter, is created on the tool surface. The penetration of teeth/pyramids into the blanks to be joined ensures their contact with the tool, but is accompanied by extrusion of the metal into the valleys on the tool surface. As a result, the distribution of strains in the weld spot area becomes periodic [1; 5; 11].

In [5], a clear correlation was found between the distribution of normal strains in the central cross section of the weld spot and the linear weld density. In the described experiments, a satisfactory density of at least 70 % was observed in those areas where the sample was subjected to compression by 15 % or more. At the same time, in neighbouring areas, where the metal was extruded into the tool valleys, tensile strains were recorded, and the linear weld density decreased to 5 %. Compressive strains sufficient for healing defects can be achieved after the tool teeth completely penetrated into the surface of the plates being joined and the valleys are completely filled with metal [4], which can lead to an increase in the strength of the joints. One can expect that with a decrease in the height of the teeth, their penetration into the surface of the plates will occur faster, and, all other conditions being equal, the USW sample in the weld spot will experience compressive strains sufficient to form high-strength welded joints.

The aim of this work is to analyse the reasons for changes in the fracture load and the fracture mode of cop-

per lap joints produced by ultrasonic spot welding using a tool with different tooth heights.

METHODS

The experiments were performed on copper plates with dimensions $50 \times 20 \text{ mm}^2$ cut from 0.8 mm thick sheets manufactured by LLC Degtyarsk Metallurgical Plant, Yekaterinburg (Russia). The chemical composition of the sheets, specified in the manufacturer's certificate, is presented in Table 1.

Before welding, the plates were ground on abrasive paper of P240 grit at an angle of 45° to the long side of the plate and degreased with alcohol and acetone. Such preparation allows distinguishing reliably traces of sliding that occur during ultrasonic welding and scratches that appear during mechanical tests on the fracture surfaces from traces of preliminary surface treatment of the plates.

Ultrasonic welding was performed on a laboratory facility manufactured at the Institute for Metals Superplasticity Problems of the Russian Academy of Sciences (Russia) and successfully used in welding titanium [12], nickel [13], and copper [14] plates. Welding tips with identical sizes, $6 \times 6 \text{ mm}^2$, and a relief in the form of teeth of different heights were used: $H=0.4 \text{ mm}$ and $H=0.1 \text{ mm}$ (Fig. 1). The relief of the anvil corresponded to the relief of the tip. Hereinafter in the text, the tool with a tooth height of $H=0.1 \text{ mm}$ is called the tool with small teeth or fine ones,

Table 1. Chemical composition of the investigated material according to GOST 859-2014, wt. %
Таблица 1. Химический состав исследованного материала по ГОСТ 859-2014, мас. %

Cu	O	Zn	Fe	Pb	S	Ni	Others
99.96	0.02	0.004	0.003	0.003	0.002	0.001	<0.03

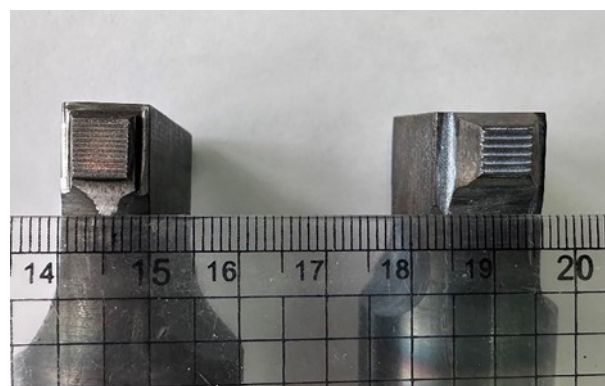


Fig. 1. Photograph of welding tips used in ultrasonic welding:
on the left – a tip with teeth of $H=0.1 \text{ mm}$, on the right – with teeth of $H=0.4 \text{ mm}$
Рис. 1. Фотография сварочных наконечников, использованных при УЗС:
слева – наконечник с зубцами $H=0,1 \text{ мм}$, справа – с зубцами $H=0,4 \text{ мм}$

and the tool with a tooth height of $H=0.4$ mm is called the tool with large teeth or coarse ones.

Ultrasonic welding was performed with a frequency of 20 kHz and a vibration amplitude of the sonotrode of 18–20 μm . The direction of vibrations was parallel to the short side of the plates. The clamping force was 2.5 kN, the time of ultrasound exposure was 2 and 3 s.

The strength properties of the joints were assessed based on the results of tensile lap shear tests in accordance with the recommendations of GOST 6996-66. The tests were carried out on an Instron 5982 universal testing machine (England) at room temperature with a crosshead speed of 1 mm/min. During the tests, the crosshead displacement (l , mm) and the corresponding loading force (F , N) were recorded. The maximum (peak) value $F=F_{\max}$ was considered the sample fracture load. The area under the $F(l)$ curve limited by the F_{\max} value was taken as the fracture energy of the joints (A , J). The average values of fracture load (\bar{F}_{\max}) and the fracture energy (\bar{A}) of joints produced by ultrasonic welding with different tools for each mode were obtained based on the test results of at least 4 samples. The standard deviation was taken as the value of statistical error.

The fracture surfaces of the tested samples were examined on a TESCAN MIRA 3 LMH FEG scanning electron microscope (Czech Republic) in the secondary electron mode at magnifications from $\times 20$ to $\times 2000$.

The depth of penetration of the tip teeth was measured on an instrumental microscope in the central section of the weld spot parallel to the direction of vibration of the tip. When performing the measurements, the coordinates of the centre of the imprint of each tooth and the tip valley (x_i ; y_i), as well as the thickness of the welded sample at this point (h_i) were recorded. The magnitude of the normal strain of the sample (e_{ni} , %) at each point was calculated as $e_{ni}=100 \times (h_i - h_0)/h_0$, where h_0 is the thickness of the two initial plates. Based on the calculation results, distributions of normal strains and the depth of penetration of the tool teeth in the central section of the welded sample were constructed. The technique for

these measurements and the construction of distributions of normal strains of the sample is described in detail and illustrated in [5]. Additionally, the depth of penetration of the teeth was measured in the peripheral sections of the weld spots, as well as by the imprints of the tips on the welded samples, recording the change in the focal length when focusing on the surface of the plate and the bottom of the imprint of each tooth. The measurements performed showed that the depth of penetration of the teeth decreased equally in the directions parallel and perpendicular to the tip vibration.

RESULTS

Mechanical tests

Changing the height of the tool teeth does not significantly affect the fracture load and fracture energy of the joints produced under the same USW conditions (Table 2). However, the scatter of experimental values of \bar{F}_{\max} and \bar{A} is twice as large after welding with the coarse tool. All samples produced by USW for 2 s fractured along the interface of the joint (Fig. 2 a). Increasing the welding time from 2 to 3 s did not change the type (mode) of fracture of the samples produced with the tool with small teeth, but caused an increase in the values of \bar{F}_{\max} and \bar{A} (Table 2).

In contrast, increasing the time of welding with the tool with large teeth did not affect \bar{F}_{\max} and \bar{A} of the joints, but led to a change in their fracture mode, which occurred with a partial nugget pull-out of the weld spot (Fig. 2 b, c). The crack initiated on the side of the weld spot perpendicular to the direction of the tensile force and propagated along this side. Further fracture of the samples occurred in different ways. In some cases, the crack extended beyond the weld spot and grew in the plate, opening under the action of the tensile load (Fig. 2 b). In this case, the free edges of the plates were bent around the weld spot. In other cases, the crack continued to propagate along the sides of the spot,

Table 2. Properties of joints of copper plates produced by ultrasonic welding with a tool with different tooth heights
Таблица 2. Свойства соединений пластин меди, полученных УЗС инструментом с разной высотой зубцов

Properties of joints	Teeth height (H); USW time (t)			
	$H=0.1$ mm; $t=2$ s	$H=0.1$ mm; $t=3$ s	$H=0.4$ mm; $t=2$ s	$H=0.4$ mm; $t=3$ s
\bar{F}_{\max} , N	1593 \pm 101	2075 \pm 100	1814 \pm 294	1918 \pm 241
k_F , %	6	5	16	12
\bar{A} , J	0.46 \pm 0.18	1.76 \pm 0.61	0.99 \pm 0.64	1.91 \pm 1.06
k_A , %	39	34	64	66
Fracture mode	Interface fracture			Nugget pull-out

Note. \bar{F}_{\max} is average values of fracture load; k_F is a coefficient of variation of experimental \bar{F}_{\max} values; \bar{A} is average values of fracture energy; k_A is a coefficient of variation of experimental \bar{A} values.

Примечание. \bar{F}_{\max} – средние значения усилий разрушения; k_F – коэффициент вариации экспериментальных значений \bar{F}_{\max} ; \bar{A} – средние значения работы разрушения; k_A – коэффициент вариации экспериментальных значений \bar{A} .

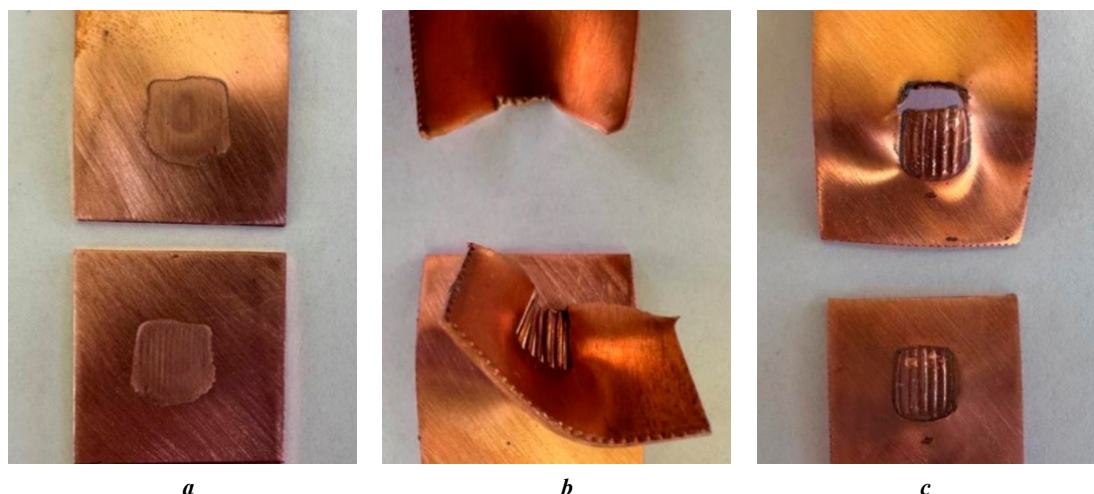


Fig. 2. Photographs of samples after testing:
a – interfacial fracture; *b, c* – partial nugget pull-out fracture
Рис. 2. Фотографии образцов после испытаний:
a – разрушение по поверхности соединения; *b, c* – разрушение с частичным отрывом сварной точки

parallel to the tensile force. However, the closure of the cracks growing towards each other was not observed. It was preceded by bending of the free edges of the plates and fracture along the interface of the joint (Fig. 2 c).

Fractographic analysis

In all cases, the fracture surface had a wavy macrorelief created by the teeth of the welding tool (Fig. 3 a, c and 4 a, c). The features of the microrelief under the tooth imprints and between them depended on the USW time and the height of the teeth.

On the fracture surfaces of the samples welded with a tool with small teeth ($H=0.1$ mm) for 2 s, a uniform microrelief is observed, the height of the irregularities of which is comparable to the depth of the scratches from preliminary grinding (Fig. 3 b). Both under the tooth imprints and between them, small dimples are observed, slightly elongated in the direction of the tip vibration. On the fracture surfaces of these samples, neither microwelds with a developed dimple microrelief nor areas with smoothed tops of scratches from preliminary grinding are observed, which indicates tight contact of the plates during ultrasonic welding. After welding with the same tool for 3 s, under the imprints of all the teeth there are microwelds consisting of many dimples elongated in the direction of shear (Fig. 3 d).

The microrelief on the fracture surfaces of samples produced with the tool with a tooth height of $H=0.4$ mm is very heterogeneous. After welding for 2 s, numerous microwelds are observed under the tooth imprints, while traces of preliminary grinding are observed between them (Fig. 4 b). In these areas, the tops of the scratches from preliminary grinding are crushed (smoothed), and there are almost no areas with small dimples. Increasing the USW time to 3 s leads to a significant expansion of the areas occupied by microwelds and to the appearance of a microrelief with small dimples between the tooth imprints in the areas where traces of preliminary grinding are preserved (Fig. 4 d).

Results of measuring normal strains

The noted features of the location of microwelds on the fracture surfaces are associated with different distributions of strains in the weld spots, which, in turn, largely depend on the penetration of the tool teeth into the joined plates. The tip teeth with a height of $H=0.1$ mm penetrated into the welded plate relatively uniformly over the entire area of the weld spot to a depth of 0.07–0.08 mm after USW for 2 s (Fig. 5 a). After USW for 3 s, the relief height on the plate surface reached 0.1 mm, and the size of the weld spot reached the size of the welding tip (Fig. 5 a, c). Along the entire cross-section of the weld spot, compressive strains were observed, the value of which reached 12 % under the tooth imprints and decreased to 3 % under the tip valleys (Fig. 5 b, blue line). It is evident that the normal strains of the sample varied according to a periodic law. The period value is uniquely determined by the distance between the tool tooth tops and is 0.6 mm for a tool with $H=0.1$ mm.

The depth of penetration of the coarse tip teeth ($H=0.4$ mm) was noticeably greater in the centre of the weld spot and decreased toward its periphery (Fig. 5 a, d, e). After ultrasonic welding for 2 and 3 s, the greatest penetration depth in the centre of the weld spot was 0.25 and 0.37 mm, respectively, and the smallest one at the periphery of the spot was 0.17 and 0.28 mm. Since the tip teeth were not completely penetrated into the plate surface, the weld spot size remained smaller than the size of the welding tip. The period of change in normal strains of the samples welded with the tool with a tooth height of $H=0.4$ mm was 0.9 mm, which corresponds to the distance between the tool tooth tops. In this case, periodically changing compressive strains of 7–14 % across the entire cross-section of the weld spot (Fig. 5 b, red solid line) were observed if the tip teeth were located above the anvil valleys, as shown in Fig. 5 d. With any other relative position of the tool teeth and valleys (Fig. 5 e), compressive strains were replaced by tensile strains (red dotted line in Fig. 5 b). In the absence of control

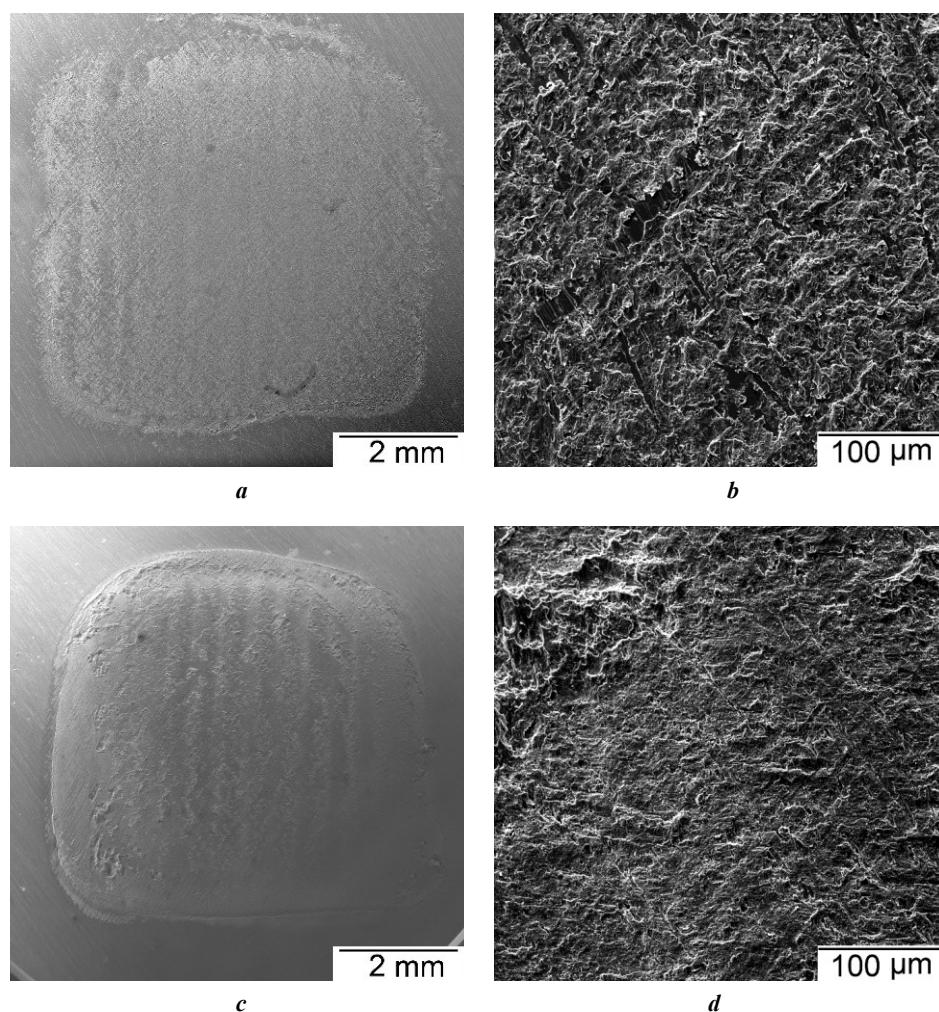


Fig. 3. Typical images of fracture surfaces of samples produced by ultrasonic welding with a tool with a tooth height of $H=0.1$ mm:

a, b – welding time of 2 s; *c, d* – welding time of 3 s; *a, c* – macrorelief; *b, d* – microrelief

Рис. 3. Типичные изображения поверхностей разрушения образцов, полученных УЗС инструментом с высотой зубцов $H=0,1$ мм:

a, b – время воздействия ультразвука 2 с; *c, d* – время воздействия ультразвука 3 с; *a, c* – макрорельеф; *b, d* – микрорельеф

over the relative position of the 0.4 mm high tool teeth, the distribution of strains in the samples produced under the same welding conditions differed significantly, which caused a significant scatter in the fracture load value.

DISCUSSION

Tensile shear tests are the simplest and therefore the most common method for assessing the quality of spot welded joints. The value of \bar{F}_{\max} characterises the load-bearing capacity of welded samples, and the value of \bar{A} characterises their ability to resist elastic and plastic deformations [1]. At the same time, the question of the sufficiency of these data for assessing the performance of joints and the possibility of comparing strength characteristics remains debatable.

It follows from the data obtained that under the selected USW conditions, the use of a welding tool with a tooth height of 0.1 and 0.4 mm allows producing joints of copper plates

with a thickness of 0.8 mm, which demonstrate the same (within the statistical error) values of fracture load and fracture energy. In this case, the scatter of experimental data is half as much after welding with a tool with 0.1 mm high teeth.

During ultrasonic welding, teeth with a height of $H=0.1$ mm completely penetrate into the joined plates, which ensures 1) the occurrence of normal compressive strains at the weld spot; 2) equality of the weld spot dimensions to the dimensions of the welding tip; 3) reduction in the thickness of the plates at the weld spot periphery by no more than 0.1 mm.

With an uncontrolled mutual arrangement of the teeth of the welding tip and anvil with a height of $H=0.4$ mm, their incomplete/partial penetration into the plate caused 1) the occurrence of both compressive and tensile normal strains at the weld spot, which is consistent with the results of work [5]; 2) the formation of a weld spot whose size is smaller than the tip size; 3) a reduction in the thickness of the plates at the weld spot periphery by 0.17–0.28 mm.

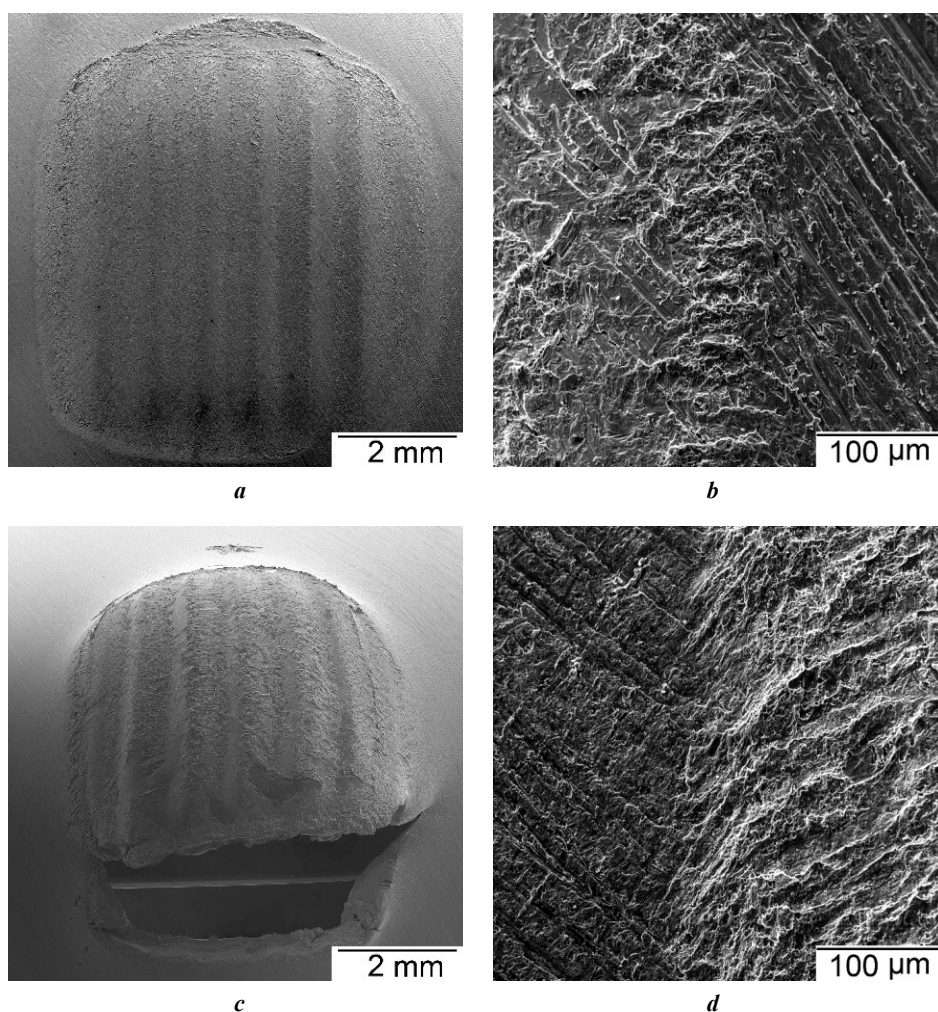


Fig. 4. Typical images of fracture surfaces of samples produced by ultrasonic welding with a tool with a tooth height of $H=0.4$ mm:

a, b – welding time of 2 s; **c, d** – welding time of 3 s; **a, c** – macrorelief; **b, d** – microrelief
Рис. 4. Типичные изображения поверхностей разрушения образцов, полученных УЗС инструментом с высотой зубцов $H=0,4$ мм:

a, b – время воздействия ультразвука 2 с; **c, d** – время воздействия ультразвука 3 с;
a, c – макрорельеф; **b, d** – микрорельеф

Due to the difference in the sizes of the weld spots (Fig. 5), the comparison of the \bar{F}_{\max} values (Table 2) becomes not entirely correct. The results of assessment of the weld joint strength σ as the ratio of \bar{F}_{\max} to the weld spot area S measured by the tooth imprints (Fig. 5 a) showed that σ is somewhat higher after ultrasonic welding with a coarse tool (Table 3). However, these results are difficult to interpret unambiguously, since during tensile shear tests the weld spot is in a complex stress-strain state [15–17]. Under the action of the tensile force F , shear stresses arise in the plane of the joint, which are balanced by two bending moments. In this case, maximum tensile and compressive stresses arise on the opposite edges (sides) of the weld spot perpendicular to the direction of tension, as shown in Fig. 6. Moreover, a narrow gap – a sharp concentrator located along the perimeter of the weld spot always remains between the overlap-welded plates (Fig. 5 d, e). Attempts are made to take into account the influence of the concentrator on the properties of welded joints, for example, by estimat-

ing the value of the critical equivalent stress intensity factor. The results of such an assessment are important in predicting the performance of spot welded joints and structures under the action of cyclic alternating loads and allow partially replacing labour-intensive tests [15; 16]. However, no generally accepted methodology for such assessments has been proposed; different approaches are used [18].

In [15], simple equations were proposed for calculating the critical equivalent stress intensity factor K_{eq} at the tip of a sharp concentrator of spot welded joints–produced by resistance spot welding:

$$K_{eq} = \sqrt{K_I^2 + K_{II}^2} = \frac{\sqrt{19}F_{\max}}{2\pi d\sqrt{h}},$$

where K_I and K_{II} are the stress intensity factors near the tips of the tensile and transverse shear cracks, respectively; K_{eq} is the critical equivalent stress intensity factor in tensile shear tests;

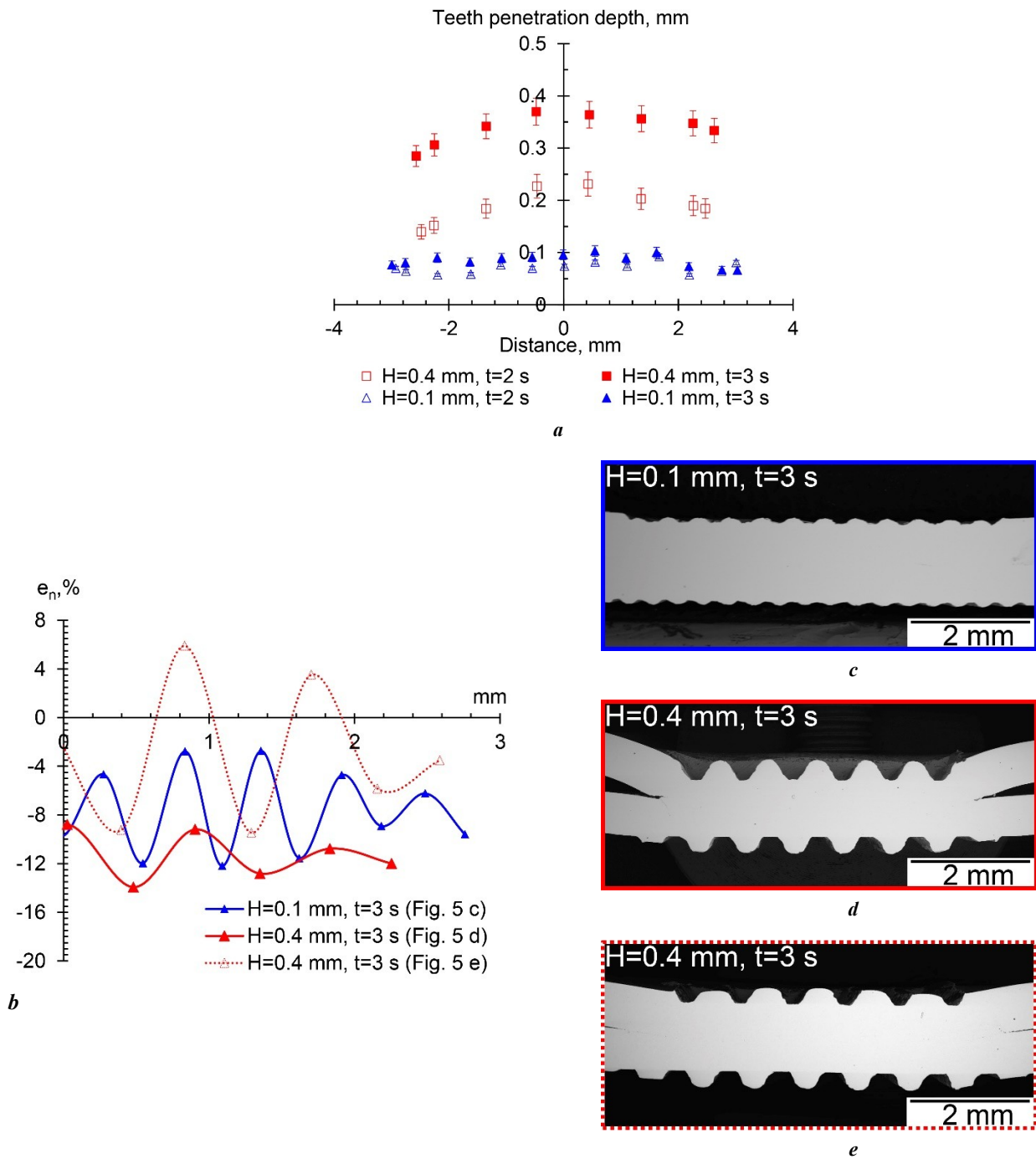


Fig. 5. Influence of the height of the welding tool teeth on the deformation at the weld spot:

a – depth of teeth penetration into the plates being joined;

b – distribution of normal deformations of the samples along the joint lines.

Cross-sections of samples produced by the ultrasonic welding using the tool with the height of the teeth: **c** – H=0.1 mm; **d, e** – H=0.4 mm

Рис. 5. Влияние высоты зубцов сварочного инструмента на деформацию в сварной точке:

a – глубина внедрения наконечника в соединяемые пластины;

b – распределение нормальных деформаций образцов вдоль линий соединений.

Поперечные сечения образцов, полученных УЗС инструментом с высотой зубцов: **c** – H=0,1 мм; **d, e** – H=0,4 мм

F_{max} is the maximum loading forces in such tests;
 d is the diameter of the weld spot;
 h is the thickness of the plates.

This approach has been successfully used to calculate the stress intensity factors arising during testing of joints produced by friction stir spot welding [19; 20]

and ultrasonic welding [18; 21–24]. In the latter case, $d=d^*$ is the equivalent diameter of a circle whose area is equal to the area of the weld spot formed by a rectangular welding tip. Obviously, $d^* = \sqrt{4S/\pi}$, where S is the area of the weld spot. When performing assessments,

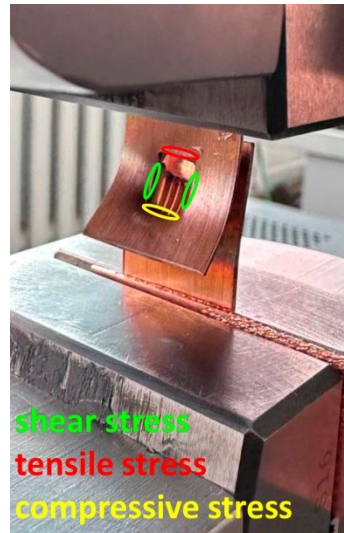


Fig. 6. Welded sampe in wedge grips of the testing machine during tensile lap shear tests.

Scheme of maximum stress distributions near of the welded spot according to [15]

Рис. 6. Сварной образец в клиновых захватах машины во время испытаний на сдвиг растяжением.

Схема распределения максимальных напряжений вблизи сварной точки по данным [15]

Table 3. Initial data and results of the assessment of the critical equivalent stress intensity factor and strength of joints

Таблица 3. Исходные данные и результаты оценки критического эквивалентного коэффициента интенсивности напряжений и прочности соединений

Characteristics of joints	Teeth height (H); USW time (t)			
	$H=0.1\text{ mm};$ $t=2\text{ s}$	$H=0.1\text{ mm};$ $t=3\text{ s}$	$H=0.4\text{ mm};$ $t=2\text{ s}$	$H=0.4\text{ mm};$ $t=3\text{ s}$
$S, \text{ mm}^2$	35.21	35.99	24.53	27.03
$h, \text{ mm}$	0.71	0.69	0.62	0.49
$\bar{F}_{\max}, \text{ N}$	1593	2075	1814	1918
$K_{eq}, \text{ MPa}\sqrt{\text{m}}$	6.2	8.1	9.1	10.3
$\sigma, \text{ MPa}$	45	58	74	71

Note. $S, \text{ mm}^2$ is a weld spot area; $h, \text{ mm}$ is the thickness of plates around the weld spot perimeter;

\bar{F}_{\max} is average values of fracture load; K_{eq} is an equivalent stress intensity factor; σ is the strength of welded joint.

Примечание. $S, \text{ мм}^2$ – площадь сварной точки; $h, \text{ мм}$ – толщина пластин по периметру сварной точки;

\bar{F}_{\max} – средние значения усилий разрушения; K_{eq} – эквивалентный коэффициент интенсивности напряжений;

σ – прочность сварного соединения.

the authors of [21–24] did not take into account the effect of the ultrasonic welding conditions on the size of the weld spot and the change in the plate thickness, taking the area of the spot S to be equal to the area of the welding tip, and the thickness of the plates of the welded sample h to be equal to the thickness of the initial sheet.

Unlike [21–24], in this work, K_{eq} was calculated taking into account changes in S and h , which are caused by the use of a tool with different tooth heights and different USW durations (Table 3). This approach allowed showing that an increase in the welding time with a tool with small and large teeth leads to an increase in the K_{eq} values by ap-

proximately 30 and 13 %, respectively. In the first case, the increase in K_{eq} is associated with an increase in \bar{F}_{\max} , and in the second – with a decrease in the size of the weld spot S and the thickness of the plates h along its edges. A decrease in these geometric dimensions of the samples is accompanied by a rapid decrease in fatigue life [18], despite the increase in critical stresses in the vicinity of the crack tip, causing its rapid propagation. A decrease in h also leads to a change in the fracture mode of the samples, which develops not along the interface of the joint (Fig. 2 a), but with a nugget pull-out (Fig. 2 b, c), and

the crack initiates and grows in the area of action of maximum tensile stresses (Fig. 6).

It is often believed [4; 17] that fracture with nugget pull-out is typical for high-quality joints, since the resistance to the applied load of the welded joint is higher than the cross-section of the plate along its edge. However, even in this case, the microwelds with a developed dimple relief do not cover the entire fracture surface and are located mainly under the tooth imprints (Fig. 4 c). Consequently, the quality of the joints can be improved by optimising the ultrasonic welding parameters and improving the tool relief. For example, some increase in \bar{F}_{\max} , \bar{A} and K_{eq} can occur after increasing the clamping force and/or the welding time when welding with a tool with small teeth. However, this will inevitably lead to its accelerated wear. Such measures are not advisable when welding with a tool with large teeth, since they will cause thinning of the plates along the perimeter of the spot. Therefore, improving the relief of the welding tool, taking into account the height of the knurls and the thickness of the plates being joined, seems to be a promising direction for further research.

CONCLUSIONS

The results of a comparative study of joints of 0.8 mm thick copper plates produced by ultrasonic welding at a frequency of 20 kHz and a vibration amplitude of 18–20 μm for 2 and 3 s under the action of a clamping force of 2.5 kN by a tool with a tooth height of 0.1 and 0.4 mm showed that an increase in the ultrasonic welding time to 3 s leads to an increase in the fracture load and fracture energy of the produced joints. The height of the tool teeth did not have a significant effect on the average values of these magnitudes, while the variation coefficient of the experimental values was two times smaller if the ultrasonic welding was performed with a tool with small teeth. Therefore, to improve the stability of the properties of welded joints, it is advisable to use a welding tool with a tooth height of 0.1 mm. After ultrasonic welding with this tool, the weld spot area is larger, and the thinning of the plates is less than after using a tool with 0.4 mm teeth. This can increase the fatigue life, despite the lower values of strength and critical stress intensity factor. However, under the selected USW conditions, its capabilities are not fully realised. To improve the properties of joints and their stability, work is required to further optimise the tool relief and ultrasonic welding modes.

REFERENCES

- De Leon M., Shin H.S. Review of the advancements in aluminum and copper ultrasonic welding in electric vehicles and superconductor applications. *Journal of Materials Processing Technology*, 2022, vol. 307, article number 117691. DOI: [10.1016/j.jmatprotec.2022.117691](https://doi.org/10.1016/j.jmatprotec.2022.117691).
- Müller F.W., Mirz C., Schiebahn A., Reisgen U. Influence of quality features, disturbances, sensor data, and measurement time on quality prediction for ultrasonic metal welding. *Welding in the World*, 2025, vol. 69, pp. 1961–1989. DOI: [10.1007/s40194-025-01959-x](https://doi.org/10.1007/s40194-025-01959-x).
- Yang Jingwei, Xie Chuhaio, Zhang Jie, Qiao Jian. Design strategies for enhancing strength and toughness in ultrasonic welding of dissimilar metals: A review. *Materials Today Communications*, 2025, vol. 42, article number 111502. DOI: [10.1016/j.mtcomm.2025.111502](https://doi.org/10.1016/j.mtcomm.2025.111502).
- Yang Jingwei, Cao Diao, Lu Qinghua. The effect of welding energy on the microstructural and mechanical properties of ultrasonic-welded copper joints. *Materials*, 2017, vol. 10, no. 2, article number 193. DOI: [10.3390/ma10020193](https://doi.org/10.3390/ma10020193).
- Murzinova M.A., Shayakhmetova E.R., Mukhametgalina A.A., Sarkeeva A.A., Nazarov A.A. Local plastic deformation and quality of Cu–Cu joints obtained by ultrasonic welding. *Metals*, 2023, vol. 13, no. 10, article number 1661. DOI: [10.3390/met13101661](https://doi.org/10.3390/met13101661).
- Chen Kunkun, Zhang Yansong, Wang Hongze. Study of plastic deformation and interface friction process for ultrasonic welding. *Science and Technology of Welding and Joining*, 2016, vol. 22, no. 3, pp. 208–216. DOI: [10.1080/13621718.2016.1218601](https://doi.org/10.1080/13621718.2016.1218601).
- Huang Hui, Chen Jian, Lim Yong Chae, Hu Xiaohua, Cheng Jiahao, Feng Zhili, Sun Xin. Heat generation and deformation in ultrasonic welding of magnesium alloy AZ31. *Journal of Materials Processing Technology*, 2019, vol. 272, pp. 125–136. DOI: [10.1016/j.jmatprotec.2019.05.016](https://doi.org/10.1016/j.jmatprotec.2019.05.016).
- Jedrasiak P., Shercliff H.R. Finite element analysis of heat generation in dissimilar alloy ultrasonic welding. *Materials & Design*, 2018, vol. 158, pp. 184–197. DOI: [10.1016/j.matdes.2018.07.041](https://doi.org/10.1016/j.matdes.2018.07.041).
- Kim Jisun, Kim Jeawoong, Kim Inju. Analysis of welding properties using various horn-tip patterns in the ultrasonic metal welding process. *Mechanics & Industry*, 2020, vol. 21, no. 1, article number 102. DOI: [10.1051/meca/2019078](https://doi.org/10.1051/meca/2019078).
- Du Pengfei, Chen Weishan, Deng Jie, Li Kai, Liu Yingxiang. Effects of knurl tooth angle on mechanical and thermal behaviors of aluminum ultrasonic welding. *Ultrasonics*, 2020, vol. 108, article number 106207. DOI: [10.1016/j.ultras.2020.106207](https://doi.org/10.1016/j.ultras.2020.106207).
- Ni Z.L., Li B.H., Liu Y., Huang L., Nazarov A., Wang X.X., Yuan Z.P., Ye F.X. Numerical analysis of ultrasonic spot welding of metal sheets: A review. *Science and Technology of Welding and Joining*, 2023, vol. 28, no. 9, pp. 841–864. DOI: [10.1080/13621718.2023.2260625](https://doi.org/10.1080/13621718.2023.2260625).
- Mukhametgalina A.A., Murzinova M.A., Nazarov A.A. Microstructure of a titanium sample produced by ultrasonic consolidation. *Letters on materials*, 2022, vol. 12, no. 2, pp. 153–157. DOI: [10.22226/2410-3535-2022-2-153-157](https://doi.org/10.22226/2410-3535-2022-2-153-157).
- Shayakhmetova E.R., Murzinova M.A., Mukhametgalina A.A., Nazarov A.A. Structure evolution in ultrafine-grained nickel induced by ultrasonic welding. *Letters on materials*, 2024, vol. 14, no. 1, pp. 91–96. DOI: [10.48612/letters/2024-1-91-96](https://doi.org/10.48612/letters/2024-1-91-96).
- Mukhametgalina A.A., Shayakhmetova E.R., Murzinova M.A., Nazarov A.A., Sarkeeva A.A. Effect of surface state on the quality of copper joints produced by ultrasonic welding. *Letters on materials*, 2024, vol. 14, no. 3, pp. 190–197. DOI: [10.48612/letters/2024-3-190-197](https://doi.org/10.48612/letters/2024-3-190-197).
- Zhang Shicheng. Stress intensities at spot welds. *International Journal of Fracture*, 1997, vol. 88, pp. 167–185. DOI: [10.1023/A:1007461430066](https://doi.org/10.1023/A:1007461430066).

16. Zhang Shicheng. Stress intensities derived from stresses around a spot weld. *International Journal of Fracture*, 1999, vol. 99, pp. 239–257. DOI: [10.1023/A:1018608615567](https://doi.org/10.1023/A:1018608615567).
17. Radakovic D.J., Tumuluru M. Predicting resistance spot weld failure modes in shear tension tests of advanced high-strength automotive steels. *Welding Journal*, 2008, vol. 87, pp. 96s–105s.
18. Patel V.K., Bhole S.D., Chen D.L. Fatigue life estimation of ultrasonic spot welded Mg alloy joints. *Materials & Design*, 2014, vol. 62, pp. 124–132. DOI: [10.1016/j.matdes.2014.05.008](https://doi.org/10.1016/j.matdes.2014.05.008).
19. Rosendo T., Tier M., Mazzaferro J., Mazzaferro C., Strohaecker T.R., Dos Santos J.F. Mechanical performance of AA6181 refill friction spot welds under lap shear tensile loading. *Fatigue & Fracture of Engineering Materials & Structures*, 2015, vol. 38, no. 12, pp. 1443–1455. DOI: [10.1111/ffe.12312](https://doi.org/10.1111/ffe.12312).
20. Zou Yangfan, Li Wenya, Yang Xiawei et al. Characterizations of dissimilar refill friction stir spot welding 2219 aluminum alloy joints of unequal thickness. *Journal of Manufacturing Processes*, 2022, vol. 79, pp. 91–101. DOI: [10.1016/j.jmapro.2022.04.062](https://doi.org/10.1016/j.jmapro.2022.04.062).
21. Peng He, Chen Daolun, Jiang Xianguan. Microstructure and mechanical properties of an ultrasonic spot welded aluminum alloy: the effect of welding energy. *Materials*, 2017, vol. 10, no. 5, article number 449. DOI: [10.3390/ma10050449](https://doi.org/10.3390/ma10050449).
22. Mohammed S.M.A.K., Dash S.S., Jiang Xianquan, Li Dongyang, Chen Daolun. Ultrasonic spot welding of 5182 aluminum alloy: evolution of microstructure and mechanical properties. *Materials Science and Engineering: A*, 2019, vol. 56, pp. 417–429. DOI: [10.1016/j.msea.2019.04.059](https://doi.org/10.1016/j.msea.2019.04.059).
23. Ma Qiuchen, Ma Jingyuan, Zhou Jianli, Ji Hongjun. Intrinsic dependence of welding quality and recrystallization on the surface-contacted micro-asperity scale during ultrasonic welding of Cu–Cu joints. *Journal of Materials Research and Technology*, 2022, vol. 17, pp. 353–364. DOI: [10.1016/j.jmrt.2022.01.011](https://doi.org/10.1016/j.jmrt.2022.01.011).
24. Bajaj D., Mehavarnam R., Fang Xingfan, Ma Ninshu Xu, Li Dongyang, Chen Daolun. Achieving superior aluminum-steel dissimilar joining via ultrasonic spot welding: microstructure and fracture behavior. *Materials Science and Engineering: A*, 2025, vol. 919, article number 147489. DOI: [10.1016/j.msea.2024.147489](https://doi.org/10.1016/j.msea.2024.147489).
1. De Leon M., Shin H.S. Review of the advancements in aluminum and copper ultrasonic welding in electric vehicles and superconductor applications // *Journal of Materials Processing Technology*. 2022. Vol. 307. Article number 117691. DOI: [10.1016/j.jmatprotec.2022.117691](https://doi.org/10.1016/j.jmatprotec.2022.117691).
2. Müller F.W., Mirz C., Schiebahn A., Reisgen U. Influence of quality features, disturbances, sensor data, and measurement time on quality prediction for ultrasonic metal welding // *Welding in the World*. 2025. Vol. 69. P. 1961–1989. DOI: [10.1007/s40194-025-01959-x](https://doi.org/10.1007/s40194-025-01959-x).
3. Yang Jingwei, Xie Chuhao, Zhang Jie, Qiao Jian. Design strategies for enhancing strength and toughness in ultrasonic welding of dissimilar metals: A review // *Materials Today Communications*. 2025. Vol. 42. Article number 111502. DOI: [10.1016/j.mtcomm.2025.111502](https://doi.org/10.1016/j.mtcomm.2025.111502).
4. Yang Jingwei, Cao Diao, Lu Qinghua. The effect of welding energy on the microstructural and mechanical properties of ultrasonic-welded copper joints // *Materials*. 2017. Vol. 10. № 2. Article number 193. DOI: [10.3390/ma10020193](https://doi.org/10.3390/ma10020193).
5. Murzinova M.A., Shayakhmetova E.R., Mukhametgalina A.A., Sarkeeva A.A., Nazarov A.A. Local plastic deformation and quality of Cu–Cu joints obtained by ultrasonic welding // *Metals*. 2023. Vol. 13. № 10. Article number 1661. DOI: [10.3390/met13101661](https://doi.org/10.3390/met13101661).
6. Chen Kunkun, Zhang Yansong, Wang Hongze. Study of plastic deformation and interface friction process for ultrasonic welding // *Science and Technology of Welding and Joining*. 2016. Vol. 22. № 3. P. 208–216. DOI: [10.1080/13621718.2016.1218601](https://doi.org/10.1080/13621718.2016.1218601).
7. Huang Hui, Chen Jian, Lim Yong Chae, Hu Xiaohua, Cheng Jiahao, Feng Zhili, Sun Xin. Heat generation and deformation in ultrasonic welding of magnesium alloy AZ31 // *Journal of Materials Processing Technology*. 2019. Vol. 272. P. 125–136. DOI: [10.1016/j.jmatprotec.2019.05.016](https://doi.org/10.1016/j.jmatprotec.2019.05.016).
8. Jedrasiak P., Shercliff H.R. Finite element analysis of heat generation in dissimilar alloy ultrasonic welding // *Materials & Design*. 2018. Vol. 158. P. 184–197. DOI: [10.1016/j.matdes.2018.07.041](https://doi.org/10.1016/j.matdes.2018.07.041).
9. Kim Jisun, Kim Jeawoong, Kim Inju. Analysis of welding properties using various horn-tip patterns in the ultrasonic metal welding process // *Mechanics & Industry*. 2020. Vol. 21. № 1. Article number 102. DOI: [10.1051/meca/2019078](https://doi.org/10.1051/meca/2019078).
10. Du Pengfei, Chen Weishan, Deng Jie, Li Kai, Liu Yingxiang. Effects of knurl tooth angle on mechanical and thermal behaviors of aluminum ultrasonic welding // *Ultrasonics*. 2020. Vol. 108. Article number 106207. DOI: [10.1016/j.ultras.2020.106207](https://doi.org/10.1016/j.ultras.2020.106207).
11. Ni Z.L., Li B.H., Liu Y., Huang L., Nazarov A., Wang X.X., Yuan Z.P., Ye F.X. Numerical analysis of ultrasonic spot welding of metal sheets: A review // *Science and Technology of Welding and Joining*. 2023. Vol. 28. № 9. P. 841–864. DOI: [10.1080/13621718.2023.2260625](https://doi.org/10.1080/13621718.2023.2260625).
12. Mukhametgalina A.A., Murzinova M.A., Nazarov A.A. Microstructure of a titanium sample produced by ultrasonic consolidation // *Letters on materials*. 2022. Vol. 12. № 2. P. 153–157. DOI: [10.22226/2410-3535-2022-2-153-157](https://doi.org/10.22226/2410-3535-2022-2-153-157).
13. Shayakhmetova E.R., Murzinova M.A., Mukhametgalina A.A., Nazarov A.A. Structure evolution in ultrafine-grained nickel induced by ultrasonic welding // *Letters on materials*. 2024. Vol. 14. № 1. P. 91–96. DOI: [10.48612/letters/2024-1-91-96](https://doi.org/10.48612/letters/2024-1-91-96).
14. Mukhametgalina A.A., Shayakhmetova E.R., Murzinova M.A., Nazarov A.A., Sarkeeva A.A. Effect of surface state on the quality of copper joints produced by ultrasonic welding // *Letters on materials*. 2024. Vol. 14. № 3. P. 190–197. DOI: [10.48612/letters/2024-3-190-197](https://doi.org/10.48612/letters/2024-3-190-197).
15. Zhang Shicheng. Stress intensities at spot welds // *International Journal of Fracture*. 1997. Vol. 88. P. 167–185. DOI: [10.1023/A:1007461430066](https://doi.org/10.1023/A:1007461430066).
16. Zhang Shicheng. Stress intensities derived from stresses around a spot weld // *International Journal*

СПИСОК ЛИТЕРАТУРЫ

- of Fracture. 1999. Vol. 99. P. 239–257. DOI: [10.1023/A:1018608615567](https://doi.org/10.1023/A:1018608615567).
17. Radakovic D.J., Tumuluru M. Predicting resistance spot weld failure modes in shear tension tests of advanced high-strength automotive steels // *Welding Journal*. 2008. Vol. 87. P. 96s–105s.
 18. Patel V.K., Bhole S.D., Chen D.L. Fatigue life estimation of ultrasonic spot welded Mg alloy joints // *Materials & Design*. 2014. Vol. 62. P. 124–132. DOI: [10.1016/j.matdes.2014.05.008](https://doi.org/10.1016/j.matdes.2014.05.008).
 19. Rosendo T., Tier M., Mazzaferro J., Mazzaferro C., Strohaecker T.R., Dos Santos J.F. Mechanical performance of AA6181 refill friction spot welds under lap shear tensile loading // *Fatigue & Fracture of Engineering Materials & Structures*. 2015. Vol. 38. № 12. P. 1443–1455. DOI: [10.1111/ffe.12312](https://doi.org/10.1111/ffe.12312).
 20. Zou Yangfan, Li Wenya, Yang Xiawei et al. Characterizations of dissimilar refill friction stir spot welding 2219 aluminum alloy joints of unequal thickness // *Journal of Manufacturing Processes*. 2022. Vol. 79. P. 91–101. DOI: [10.1016/j.jmapro.2022.04.062](https://doi.org/10.1016/j.jmapro.2022.04.062).
 21. Peng He, Chen Daolun, Jiang Xianguan. Microstructure and mechanical properties of an ultrasonic spot welded aluminum alloy: the effect of welding energy // *Materials*. 2017. Vol. 10. № 5. Article number 449. DOI: [10.3390/ma10050449](https://doi.org/10.3390/ma10050449).
 22. Mohammed S.M.A.K., Dash S.S., Jiang Xianquan, Li Dongyang, Chen Daolun. Ultrasonic spot welding of 5182 aluminum alloy: evolution of microstructure and mechanical properties // *Materials Science and Engineering: A*. 2019. Vol. 56. P. 417–429. DOI: [10.1016/j.msea.2019.04.059](https://doi.org/10.1016/j.msea.2019.04.059).
 23. Ma Qiuchen, Ma Jingyuan, Zhou Jianli, Ji Hongjun. Intrinsic dependence of welding quality and recrystallization on the surface-contacted micro-asperity scale during ultrasonic welding of Cu–Cu joints // *Journal of Materials Research and Technology*. 2022. Vol. 17. P. 353–364. DOI: [10.1016/j.jmrt.2022.01.011](https://doi.org/10.1016/j.jmrt.2022.01.011).
 24. Bajaj D., Mehavarnam R., Fang Xingfan, Ma Ninshu Xu, Li Dongyang, Chen Daolun. Achieving superior aluminum-steel dissimilar joining via ultrasonic spot welding: microstructure and fracture behavior // *Materials Science and Engineering: A*. 2025. Vol. 919. Article number 147489. DOI: [10.1016/j.msea.2024.147489](https://doi.org/10.1016/j.msea.2024.147489).

УДК 534-8; 621.791.16

doi: 10.18323/2782-4039-2025-3-73-10

Прочность соединений пластин меди, полученных точечной ультразвуковой сваркой инструментом с разной высотой зубцов

Шаяхметова Эльвина Рафитовна, младший научный сотрудник

Институт проблем сверхпластичности металлов РАН, Уфа (Россия)

E-mail: elvinar@imsp.ruORCID: <https://orcid.org/0000-0002-1659-9922>

Поступила в редакцию 30.06.2025

Пересмотрена 21.07.2025

Принята к публикации 12.08.2025

Аннотация: Ультразвуковая сварка (УЗС) металлов позволяет получать твердофазные соединения между тонкими заготовками и относится к энергоэффективным экологически чистым технологиям. Широкое использование этой технологии сдерживает невысокая прочность получаемых соединений и нестабильность их свойств. Одним из способов повышения прочностных характеристик является разработка сварочного инструмента, обеспечивающего стабильную передачу энергии ультразвуковых колебаний в зону соединения. Для этого на поверхность сварочного наконечника и наковальни наносят рельеф с зубцами или пирамидками разной формы и высоты. В работе представлены данные об усилиях и работе разрушения нахлесточных соединений, полученных точечной ультразвуковой сваркой пластин меди инструментом с высотой зубцов 0,1 и 0,4 мм. УЗС проводили с частотой 20 кГц и амплитудой колебаний 18–20 мкм, длительность сварки составляла 2 и 3 с, величина сжимающей нагрузки 2,5 кН. В работе рассмотрены особенности разрушения полученных соединений и распределения нормальных деформаций в сварной точке, рассчитаны коэффициенты интенсивности напряжений в ее окрестностях. Показано, что после УЗС в течение 3 с показатели прочности соединений, полученных разным инструментом, достигают наибольших значений, они близки по величине, однако разброс экспериментальных данных вдвое меньше после сварки инструментом с мелкими зубцами. Соединения, полученные таким инструментом, разрушаются по поверхности соединения, а после сварки инструментом с крупными зубцами – с отрывом сварной точки, что объясняется увеличением коэффициента интенсивности напряжений в вершине концентратора, окружающего сварную точку.

Ключевые слова: медь; ультразвуковая сварка металлов; твердофазное соединение; прочность соединений; рельеф сварочного инструмента; коэффициент интенсивности напряжений.

Благодарности: Исследование выполнено в рамках государственного задания ИПСМ РАН (регистрационный номер 124022900006-2). Часть экспериментальных данных получена при выполнении гранта РНФ № 22-19-00617

(<https://rscf.ru/project/22-19-00617/>). Микроструктурные исследования проводились на базе ЦКП ИПСМ РАН «Структурные и физико-механические исследования материалов».

Автор выражает глубокую благодарность к.т.н. М.А. Мурзиновой и д.ф.-м.н. А.А. Назарову за помощь при проведении исследований и обсуждение полученных результатов.

Статья подготовлена по материалам докладов участников XII Международной школы «Физическое материаловедение» (ШФМ-2025), Тольятти, 15–19 сентября 2025 года.

Для цитирования: Шаяхметова Э.Р. Прочность соединений пластин меди, полученных точечной ультразвуковой сваркой инструментом с разной высотой зубцов // Frontier Materials & Technologies. 2025. № 3. С. 125–136. DOI: 10.18323/2782-4039-2025-3-73-10.

OUR AUTHORS

Andreev Vladimir Aleksandrovich, PhD (Engineering),
leading researcher at the Laboratory of Plastic Deformation of Metallic Materials.
Address: A.A. Baikov Institute of Metallurgy and Materials Science of the RAS,
119334, Russia, Moscow, Leninskiy Prospekt, 49.
E-mail: vandreev@imet.ac.ru

Belonogov Savely Olegovich, engineer
of the Laboratory of Destructive Inspection Methods.
Address: LLC Middle Volga Certification and Diagnostic Center “Delta”,
445009, Russia, Togliatti, Pobedy Street, 22/1.
E-mail: savelij.belonogov.2001@mail.ru

Bochkarev Aleksandr Gennadievich, PhD (Engineering),
assistant professor of Chair “Welding, Pressure Material Treatment and Related Processes”.
Address: Togliatti State University,
445020, Russia, Togliatti, Belorusskaya Street, 14.
E-mail: a.bochkarev5@tltsu.ru

Bodyakova Anna Igorevna, PhD (Physics and Mathematics),
researcher of the Laboratory of Mechanical Properties
of Nanostructured Materials and Superalloys.
Address: Belgorod State University,
308015, Russia, Belgorod, Pobedy Street, 85.
E-mail: morozova_ai@bsuedu.ru

Bushueva Natalia Igorevna, postgraduate student,
research engineer of scientific laboratory “Metal Forming”.
Address: Ural Federal University named after the first President of Russia B.N. Yeltsin,
620002, Russia, Yekaterinburg, Mira Street, 19.
E-mail: n.i.bushueva@urfu.ru

Chervonnyy Aleksey Vladimirovich, PhD (Engineering),
Head of Research and Development Department.
Address: JSC Vyksa Metallurgical Plant,
607061, Russia, Vyksa, Brat'yev Batashyovyykh Street, 45.
E-mail: chervonnyj_av@vsw.ru

Chistopoltseva Elena Aleksandrovna, PhD (Engineering),
Head of Department of Special Materials Science.
Address: LLC IT Service,
443001, Russia, Samara, Yarmaroch'naya Street, 52/55.
E-mail: chistopolceva@its-samara.com

Chistyukhina Eleonora Ivanovna, research engineer
at the Laboratory of Physical Metallurgy of Non-Ferrous
and Light Metals named by Academician A.A. Bochvar,
graduate student of Chair of Metal Science and Physics of Strength.
Address 1: A.A. Baikov Institute of Metallurgy and Materials Science of the RAS,
119334, Russia, Moscow, Leninskiy Prospekt, 49.
Address 2: University of Science and Technology “MISIS”,
119049, Russia, Moscow, Leninskiy Prospekt, 4.
E-mail: e.chistyuhina@mail.ru

Chudnov Aleksandr Vladimirovich, postgraduate student.
Address: Ulyanovsk State Technical University,
432027, Russia, Ulyanovsk, Severny Venets Street, 32.
E-mail: chudnov73ru@gmail.com

Dimukhametov Ilnaz Zeferovich, postgraduate student.

Address: Ulyanovsk State Technical University,
432027, Russia, Ulyanovsk, Severny Venets Street, 32.
E-mail: iln-d@yandex.ru

Dobatkin Sergey Vladimirovich, Doctor of Science (Engineering), Professor,
Head of the Laboratory of Physical Metallurgy of Non-Ferrous
and Light Metals named by Academician A.A. Bochvar.

Address: A.A. Baikov Institute of Metallurgy and Materials Science of the RAS,
119334, Russia, Moscow, Leninskiy Prospekt, 49.
E-mail: dobatkin.sergey@gmail.com

Dolgach Egor Dmitrievich, scientific project engineer.

Address: MISIS University of Science and Technology,
119049, Russia, Moscow, Leninsky Prospekt, 4.
E-mail: edolgach@gmail.com

Gorbenko Artem Dmitrievich, research engineer
at the Laboratory of Strength and Plasticity of Metallic
and Composite Materials and Nanomaterials.

Address: A.A. Baikov Institute of Metallurgy and Materials Science of the RAS,
119334, Russia, Moscow, Leninskiy Prospekt, 49.
E-mail: artemgorbenk@yandex.ru

Kalinenko Aleksandr Andreevich, PhD (Physics and Mathematics),
junior researcher of the Laboratory of Mechanical Properties
of Nanostructured Materials and Superalloys.

Address: Belgorod State University,
308015, Russia, Belgorod, Pobedy Street, 85.
E-mail: kalinenko@bsuedu.ru

Khokhlov Yuri Yurievich, Head of the Laboratory
of Chair “Welding, Pressure Material Treatment and Related Processes”.

Address: Togliatti State University,
445020, Russia, Togliatti, Belorusskaya Street, 14.
E-mail: y.y.khokhlov@rambler.ru

Komissarov Aleksandr Aleksandrovich, PhD (Engineering),

Head of Hybrid Nanostructured Materials Laboratory.
Address: MISIS University of Science and Technology,
119049, Russia, Moscow, Leninsky Prospekt, 4.
E-mail: komissarov@misis.ru

Kovtunov Aleksandr Ivanovich, Doctor of Sciences (Engineering),
professor of Chair “Welding, Pressure Material Treatment and Related Processes”.

Address: Togliatti State University,
445020, Russia, Togliatti, Belorusskaya Street, 14.
E-mail: akovtunov@rambler.ru

Kudashov Dmitry Viktorovich, PhD (Engineering), Director.

Address: Vyksa branch of MISIS University of Science and Technology,
607036, Russia, Vyksa, Shimorskoe workers settlement, Kalinin Street, 206.
E-mail: kudja@mail.ru

Lebedev Yuri Anatolyevich, PhD (Physics and Mathematics),
senior researcher.

Address: Institute of Physics of Molecules and Crystals
of Ufa Federal Research Center of RAS,
450054, Russia, Ufa, Prospekt Oktyabrya, 71.
E-mail: lebedev@anrb.ru

Levashkin Denis Gennadyevich, PhD (Engineering), Associate Professor, assistant professor of Chair “Equipment and Technologies of Machinery Production”.
Address: Togliatti State University,
445020, Russia, Togliatti, Belorusskaya Street, 14.
E-mail: denis.levden@yandex.ru

Loginov Yuri Nikolaevich, Doctor of Science (Engineering), professor of Chair of Metal Forming.
Address: Ural Federal University
named after the first President of Russia B.N. Yeltsin,
620002, Russia, Yekaterinburg, Mira Street, 19.
E-mail: j.n.loginov@urfu.ru

Lukyanova Elena Aleksandrovna, PhD (Engineering), senior researcher at the Laboratory of Physical Metallurgy of Non-Ferrous and Light Metals named by Academician A.A. Bochvar.
Address: A.A. Baikov Institute of Metallurgy and Materials Science of the RAS,
119334, Russia, Moscow, Leninskiy Prospekt, 49.
E-mail: helenelukyanova@gmail.com

Malinin Andrey Vladimirovich, PhD (Engineering), Deputy General Director for Research.
Address: LLC RN-BashNIPIneft,
450006, Russia, Ufa, Lenin Street, 86/1.
E-mail: MalininAV@bnipi.rosneft.ru

Malopheyev Sergey Sergeevich, PhD (Engineering), senior researcher of the Laboratory of Mechanical Properties of Nanostructured Materials and Superalloys.
Address: Belgorod State University,
308015, Russia, Belgorod, Pobedy Street, 85.
E-mail: malofeev@bsuedu.ru

Martynenko Natalia Sergeevna, PhD (Engineering), senior researcher at the Laboratory of Physical Metallurgy of Non-Ferrous and Light Metals named by Academician A.A. Bochvar.
Address: A.A. Baikov Institute of Metallurgy and Materials Science of the RAS,
119334, Russia, Moscow, Leninskiy Prospekt, 49.
E-mail: nata_roug@mail.ru

Mironov Sergey Yurievich, Doctor of Sciences (Physics and Mathematics), leading researcher of the Laboratory of Mechanical Properties of Nanostructured Materials and Superalloys.
Address: Belgorod State University,
308015, Russia, Belgorod, Pobedy Street, 85.
E-mail: mironov@bsuedu.ru

Muntin Aleksandr Vadimovich, PhD (Engineering), Director of Engineering and Technology Center.
Address: JSC Vyksa Metallurgical Plant,
607061, Russia, Vyksa, Bratyev Batashyovykh Street, 45.
E-mail: muntin_av@omk.ru

Nikitin Ivan Sergeevich, PhD (Engineering), junior researcher of the Laboratory of Mechanical Properties of Nanostructured Materials and Superalloys.
Address: Belgorod State University,
308015, Russia, Belgorod, Pobedy Street, 85.
E-mail: nikitin_i@bsuedu.ru

Plakhotny Denis Ivanovich, senior lecturer
of Chair “Welding, Pressure Material Treatment and Related Processes”.
Address: Togliatti State University,
445020, Russia, Togliatti, Belorusskaya Street, 14.
E-mail: d01125@mail.ru

Rastorguev Dmitry Aleksandrovich, PhD (Engineering), Associate Professor,
assistant professor of Chair “Equipment and Technologies of Machinery Production”.
Address: Togliatti State University,
445020, Russia, Togliatti, Belorusskaya Street, 14.
E-mail: rast_73@mail.ru

Rybalchenko Olga Vladislavovna, PhD (Engineering),
leading researcher at the Laboratory of Physical Metallurgy of Non-Ferrous
and Light Metals named by Academician A.A. Bochvar.
Address: A.A. Baikov Institute of Metallurgy and Materials Science of the RAS,
119334, Russia, Moscow, Leninskiy Prospekt, 49.
E-mail: rybalch@mail.ru

Salishchev Gennady Alekseevich, Doctor of Sciences (Engineering), Professor,
Head of the Laboratory of Bulk Nanostructured Materials.
Address: Belgorod State University,
308015, Russia, Belgorod, Pobedy Street, 85.
E-mail: salishchev_g@bsuedu.ru

Shayakhmetova Elvina Rafitovna, junior researcher.
Address: Institute for Metals Superplasticity Problems of RAS,
450001, Russia, Ufa, Stepan Khalturin Street, 39.
E-mail: elvinar@imsp.ru

Sitdikov Vil Dayanovich, Doctor of Sciences (Physics and Mathematics),
senior expert.
Address: LLC RN-BashNIPIneft,
450006, Russia, Ufa, Lenin Street, 86/1.
E-mail: SitdikovVD@bnipi.rosneft.ru

Sokolovskiy Vitaly Sergeevich, PhD (Engineering),
researcher of the Laboratory of Bulk Nanostructured Materials.
Address: Belgorod State University,
308015, Russia, Belgorod, Pobedy Street, 85.
E-mail: sokolovskiy@bsuedu.ru

Straumal Petr Borisovich, PhD (Physics and Mathematics),
senior researcher at the Laboratory of Physical Metallurgy of Non-Ferrous
and Light Metals named by Academician A.A. Bochvar.
Address: A.A. Baikov Institute of Metallurgy and Materials Science of the RAS,
119334, Russia, Moscow, Leninskiy Prospekt, 49.
E-mail: straumal.peter@yandex.ru

Temralieva Diana Rivovna, research engineer
at the Laboratory of Physical Metallurgy of Non-Ferrous
and Light Metals named by Academician A.A. Bochvar.
Address: A.A. Baikov Institute of Metallurgy and Materials Science of the RAS,
119334, Russia, Moscow, Leninskiy Prospekt, 49.
E-mail: diana4-64@mail.ru

Unyanin Aleksandr Nikolaevich, Doctor of Sciences (Engineering), Professor,
professor of Chair “Innovative Technologies in Machine Building”.
Address: Ulyanovsk State Technical University,
432027, Russia, Ulyanovsk, Severny Venets Street, 32.
E-mail: a_un@mail.ru

Vedeneev Ivan Vyacheslavovich, engineer
of the Laboratory of Non-Destructive Inspection.
Address: LLC Middle Volga Certification and Diagnostic Center “Delta”,
445009, Russia, Togliatti, Pobedy Street, 22/1.
E-mail: cool.vedeneev@inbox.ru

Voronov Roman Dmitrievich, teacher
of Chair “Equipment and Technologies of Machinery Production”.
Address: Togliatti State University,
445020, Russia, Togliatti, Belorusskaya Street, 14.
E-mail: smr.rom@yandex.ru

Yushchuk Vyacheslav Vasilievich, scientific project engineer.
Address: MISIS University of Science and Technology,
119049, Russia, Moscow, Leninsky Prospekt, 4.
E-mail: slava_yushchuk@mail.ru

НАШИ АВТОРЫ

Андреев Владимир Александрович, кандидат технических наук,
ведущий научный сотрудник
лаборатории пластической деформации металлических материалов.
Адрес: Институт металлургии и материаловедения им. А.А. Байкова РАН,
119334, Россия, г. Москва, Ленинский пр-т, 49.
E-mail: vandreev@imet.ac.ru

Белоногов Савелий Олегович, инженер
лаборатории разрушающих методов контроля.
Адрес: ООО «Средневожский сертификационно-диагностический центр «Дельта»,
445009, Россия, г. Тольятти, ул. Победы, 22/1.
E-mail: savelij.belonogov.2001@mail.ru

Бодякова Анна Игоревна, кандидат физико-математических наук,
научный сотрудник лаборатории механических свойств наноструктурных
и жаропрочных материалов.
Адрес: Белгородский государственный национальный исследовательский университет,
308015, Россия, г. Белгород, ул. Победы, 85.
E-mail: morozova_ai@bsuedu.ru

Бочкарев Александр Геннадьевич, кандидат технических наук,
доцент кафедры «Сварка, обработка материалов давлением
и родственные процессы».
Адрес: Тольяттинский государственный университет,
445020, Россия, г. Тольятти, ул. Белорусская, 14.
E-mail: a.bochkarev5@tltsu.ru

Бушуева Наталья Игоревна, аспирант,
инженер-исследователь научной лаборатории «Обработка металлов давлением».
Адрес: Уральский федеральный университет
имени первого Президента России Б.Н. Ельцина,
620002, Россия, г. Екатеринбург, ул. Мира, 19.
E-mail: n.i.bushueva@urfu.ru

Веденеев Иван Вячеславович, инженер лаборатории неразрушающего контроля.
Адрес: ООО «Средневожский сертификационно-диагностический центр «Дельта»,
445009, Россия, г. Тольятти, ул. Победы, 22/1.
E-mail: cool.vedeneev@inbox.ru

Воронов Роман Дмитриевич, преподаватель
кафедры «Оборудование и технологии машиностроительного производства».
Адрес: Тольяттинский государственный университет,
445020, Россия, г. Тольятти, ул. Белорусская, 14.
E-mail: smr.rom@yandex.ru

Горбенко Артем Дмитриевич, инженер-исследователь
лаборатории прочности и пластичности металлических
и композиционных материалов и наноматериалов.
Адрес: Институт металлургии и материаловедения им. А.А. Байкова РАН,
119334, Россия, г. Москва, Ленинский пр-т, 49.
E-mail: artemgorbenk@yandex.ru

Димухаметов Илназ Зеферович, аспирант.
Адрес: Ульяновский государственный технический университет,
432027, Россия, г. Ульяновск, ул. Северный Венец, 32.
E-mail: iln-d@yandex.ru

Добаткин Сергей Владимирович, доктор технических наук, профессор, заведующий лабораторией металловедения цветных и легких металлов им. академика А.А. Бочвара.
Адрес: Институт металлургии и материаловедения им. А.А. Байкова РАН, 119334, Россия, г. Москва, Ленинский пр-т, 49.
E-mail: dobatkin.sergey@gmail.com

Долгач Егор Дмитриевич, инженер научного проекта.
Адрес: Университет науки и технологий МИСИС, 119049, Россия, г. Москва, Ленинский пр-т, 4.
E-mail: edolgach@gmail.com

Калиненко Александр Андреевич, кандидат физико-математических наук, младший научный сотрудник лаборатории механических свойств наноструктурных и жаропрочных материалов.
Адрес: Белгородский государственный национальный исследовательский университет, 308015, Россия, г. Белгород, ул. Победы, 85.
E-mail: kalinenko@bsuedu.ru

Ковтунов Александр Иванович, доктор технических наук, профессор кафедры «Сварка, обработка материалов давлением и родственные процессы».
Адрес: Тольяттинский государственный университет, 445020, Россия, г. Тольятти, ул. Белорусская, 14.
E-mail: akovtunov@rambler.ru

Комиссаров Александр Александрович, кандидат технических наук, заведующий лабораторией «Гибридные наноструктурные материалы».
Адрес: Университет науки и технологий МИСИС, 119049, Россия, г. Москва, Ленинский пр-т, 4.
E-mail: komissarov@misis.ru

Кудашов Дмитрий Викторович, кандидат технических наук, директор.
Адрес: Выксунский филиал НИТУ «МИСИС», 607036, Россия, г. Выкса, р. п. Шиморское, ул. Калинина, 206.
E-mail: kudja@mail.ru

Лебедев Юрий Анатольевич, кандидат физико-математических наук, старший научный сотрудник.
Адрес: Институт физики молекул и кристаллов Уфимского федерального исследовательского центра РАН, 450054, Россия, г. Уфа, пр-т Октября, 71.
E-mail: lebedev@anrb.ru

Левашкин Денис Геннадьевич, кандидат технических наук, доцент, доцент кафедры «Оборудование и технологии машиностроительного производства».
Адрес: Тольяттинский государственный университет, 445020, Россия, г. Тольятти, ул. Белорусская, 14.
E-mail: denis.levden@yandex.ru

Логинов Юрий Николаевич, доктор технических наук, профессор кафедры обработки металлов давлением.
Адрес: Уральский федеральный университет имени первого Президента России Б.Н. Ельцина, 620002, Россия, г. Екатеринбург, ул. Мира, 19.
E-mail: j.n.loginov@urfu.ru

Лукьянова Елена Александровна, кандидат технических наук, старший научный сотрудник лаборатории металловедения цветных и легких металлов им. академика А.А. Бочвара.
Адрес: Институт металлургии и материаловедения им. А.А. Байкова РАН, 119334, Россия, г. Москва, Ленинский пр-т, 49.
E-mail: helenelukyanova@gmail.com

Малинин Андрей Владимирович, кандидат технических наук,
заместитель генерального директора по исследованиям.
Адрес: ООО «РН-БашНИПИнефть»,
450006, Россия, г. Уфа, ул. Ленина, 86/1.
E-mail: MalininAV@bnipi.rosneft.ru

Малофеев Сергей Сергеевич, кандидат технических наук,
старший научный сотрудник лаборатории механических свойств
наноструктурных и жаропрочных материалов.
Адрес: Белгородский государственный национальный исследовательский университет,
308015, Россия, г. Белгород, ул. Победы, 85.
E-mail: malofeev@bsuedu.ru

Мартыненко Наталья Сергеевна, кандидат технических наук,
старший научный сотрудник лаборатории металловедения цветных
и легких металлов им. академика А.А. Бочвара.
Адрес: Институт металлургии и материаловедения им. А.А. Байкова РАН,
119334, Россия, г. Москва, Ленинский пр-т, 49.
E-mail: nata_roug@mail.ru

Миронов Сергей Юрьевич, доктор физико-математических наук,
ведущий научный сотрудник лаборатории механических свойств
наноструктурных и жаропрочных материалов.
Адрес: Белгородский государственный национальный исследовательский университет,
308015, Россия, г. Белгород, ул. Победы, 85.
E-mail: mironov@bsuedu.ru

Мунтин Александр Вадимович, кандидат технических наук,
директор инженерно-технологического центра.
Адрес: АО «Выксунский металлургический завод»,
607061, Россия, г. Выкса, ул. Братьев Баташёвых, 45.
E-mail: muntin_av@omk.ru

Никитин Иван Сергеевич, кандидат технических наук,
младший научный сотрудник лаборатории механических свойств
наноструктурных и жаропрочных материалов.
Адрес: Белгородский государственный национальный исследовательский университет,
308015, Россия, г. Белгород, ул. Победы, 85.
E-mail: nikitin_i@bsuedu.ru

Плахотный Денис Иванович, старший преподаватель
кафедры «Сварка, обработка материалов давлением
и родственные процессы».
Адрес: Тольяттинский государственный университет,
445020, Россия, г. Тольятти, ул. Белорусская, 14.
E-mail: d01125@mail.ru

Расторгуев Дмитрий Александрович, кандидат технических наук, доцент,
доцент кафедры «Оборудование и технологии машиностроительного производства».
Адрес: Тольяттинский государственный университет,
445020, Россия, г. Тольятти, ул. Белорусская, 14.
E-mail: rast_73@mail.ru

Рыбальченко Ольга Владиславовна, кандидат технических наук,
ведущий научный сотрудник лаборатории металловедения цветных
и легких металлов им. академика А.А. Бочвара.
Адрес: Институт металлургии и материаловедения им. А.А. Байкова РАН,
119334, Россия, г. Москва, Ленинский пр-т, 49.
E-mail: rybalch@mail.ru

Салищев Геннадий Алексеевич, доктор технических наук, профессор, заведующий лабораторией объемных наноструктурных материалов.
Адрес: Белгородский государственный национальный исследовательский университет, 308015, Россия, г. Белгород, ул. Победы, 85.
E-mail: salishchev_g@bsuedu.ru

Ситдиков Виль Даянович, доктор физико-математических наук, старший эксперт.
Адрес: ООО «РН-БашНИПИнефть», 450006, Россия, г. Уфа, ул. Ленина, 86/1.
E-mail: SitdikovVD@bnipi.rosneft.ru

Соколовский Виталий Сергеевич, кандидат технических наук, научный сотрудник лаборатории объемных наноструктурных материалов.
Адрес: Белгородский государственный национальный исследовательский университет, 308015, Россия, г. Белгород, ул. Победы, 85.
E-mail: sokolovskiy@bsuedu.ru

Страумал Петр Борисович, кандидат физико-математических наук, старший научный сотрудник лаборатории металловедения цветных и легких металлов им. академика А.А. Бочвара.
Адрес: Институт металлургии и материаловедения им. А.А. Байкова РАН, 119334, Россия, г. Москва, Ленинский пр-т, 49.
E-mail: straumal.peter@yandex.ru

Темралиева Диана Ривовна, инженер-исследователь лаборатории металловедения цветных и легких металлов им. академика А.А. Бочвара.
Адрес: Институт металлургии и материаловедения им. А.А. Байкова РАН, 119334, Россия, г. Москва, Ленинский пр-т, 49.
E-mail: diana4-64@mail.ru

Унянин Александр Николаевич, доктор технических наук, профессор, профессор кафедры «Инновационные технологии в машиностроении».
Адрес: Ульяновский государственный технический университет, 432027, Россия, г. Ульяновск, ул. Северный Венец, 32.
E-mail: a_un@mail.ru

Хохлов Юрий Юрьевич, заведующий лабораторией кафедры «Сварка, обработка материалов давлением и родственные процессы».
Адрес: Тольяттинский государственный университет, 445020, Россия, г. Тольятти, ул. Белорусская, 14.
E-mail: y.y.khokhlov@rambler.ru

Червонный Алексей Владимирович, кандидат технических наук, начальник отдела по исследованиям и разработкам.
Адрес: АО «Выксунский металлургический завод», 607061, Россия, г. Выкса, ул. Братьев Баташёвых, 45.
E-mail: chervonnyj_av@vsw.ru

Чистопольцева Елена Александровна, кандидат технических наук, руководитель департамента специального материаловедения.
Адрес: ООО «ИТ-Сервис», 443001, Россия, г. Самара, ул. Ярмарочная, д. 52/55.
E-mail: chistopolceva@its-samara.com

Чистюхина Элеонора Ивановна, инженер-исследователь, лаборатории металловедения цветных и легких металлов им. академика А.А. Бочвара, магистрант кафедры металловедения и физики прочности.
Адрес 1: Институт металлургии и материаловедения им. А.А. Байкова РАН, 119334, Россия, г. Москва, Ленинский пр-т, 49.
Адрес 2: Университет науки и технологий МИСИС, 119049, Россия, г. Москва, Ленинский пр-т, 4.
E-mail: e.chistyuhina@mail.ru

Чуднов Александр Владимирович, аспирант.

Адрес: Ульяновский государственный технический университет,
432027, Россия, г. Ульяновск, ул. Северный Венец, 32.

E-mail: chudnov73ru@gmail.com

Шаяхметова Эльвина Рафитовна, младший научный сотрудник.

Адрес: Институт проблем сверхпластичности металлов РАН,
450001, Россия, г. Уфа, ул. Степана Халтурина, 39.

E-mail: elvinar@imsp.ru

Ющук Вячеслав Васильевич, инженер научного проекта.

Адрес: Университет науки и технологий МИСИС,
119049, Россия, г. Москва, Ленинский пр-т, 4.

E-mail: slava_yushchuk@mail.ru

On the cover: Image of the fracture surface of a sample after tensile lap shear testing (the sample was obtained by ultrasonic welding with a tool with a tooth height of $H=0.4$ mm, the welding time is 2 s). Author of the photo: E.R. Shayakhmetova, junior researcher (Laboratory of Modern Welding Methods, Institute for Metals Superplasticity Problems, Russian Academy of Sciences, Ufa, Russia).

На обложке: Изображение поверхности разрушения образца после испытаний на сдвиг растяжением (образец получен ультразвуковой сваркой инструментом с высотой зубцов $H=0,4$ мм, время воздействия ультразвука – 2 с). Автор фото: Э.Р. Шаяхметова, младший научный сотрудник (лаборатория «Современные методы сварки», Институт проблем сверхпластичности металлов РАН, Уфа, Россия).